

# Solid state quantum optics: Control of electrons, photons and phonons

---

Vorgelegt von  
Diplom-Physikerin  
**Julia Kabuß**  
aus Mönchengladbach

von der Fakultät II – Mathematik und Naturwissenschaften  
der Technischen Universität Berlin

zur Erlangung des akademischen Grades

Doktor der Naturwissenschaften

— **Dr. rer. nat.** —

genehmigte Dissertation

## Promotionsausschuss

- Vorsitzende : Prof. Dr. rer. nat. Birgit Kanngießer, TU Berlin  
1. Gutachter : Prof. Dr. rer. nat. Andreas Knorr, TU Berlin  
2. Gutachter : Prof. Dr. rer. nat. Oliver Benson, HU Berlin

Tag der wissenschaftlichen Aussprache: 04. Dezember 2013

Berlin 2014  
D 83



# Abstract

Technological progress in the manufacturing of solid state based nanostructures, such as photonic devices, quantum phononic structures and coupled electronic and nanomechanical hybrid systems, enables the transfer of quantum optics and vibrational phenomena to systems, that are scalable by design. In contrast to atom physics, these systems often strongly interact with their solid state surroundings, which leads to modified dynamics and optical features. To properly address these features in solid state quantum optics, the applied theoretical methods extent from a quantum mechanical treatment of higher order quantum correlations to effective and semiclassical frameworks, employing Heisenberg's formalism.

The first part of this work is focused on interesting effects and possible applications arising from the interaction of a typical semiconductor quantum dot (QD) with acoustic and optical phonons. In the comparably new field of nanophononics, a QD as the active medium, coupled to a high-Q acoustic cavity phonon mode is proposed as a phonon laser. Within a detuned optical excitation scheme, this type of phonon laser exploits an induced Raman process for the generation of coherent and non equilibrium phonons. Besides solving the full quantum correlated dynamics of the phonon laser system, simple semiclassical phonon laser equations are derived, allowing for a straightforward analytical discussion of the operational regimes of the QD-phonon laser. Further, as a possible mean of characterization of a particular nanostructure, the light emission of a QD is investigated. As an addition to the regime of weak excitation and the famous Mollow triplet, the emission spectrum of a semiconductor QD can exhibit a third striking spectral scenario, emerging from the coupling to longitudinal optical (LO) phonons. The spectrum is again dramatically changed, where the electron-phonon coupling strength can be extracted via the spectral positions of the emission peaks.

In the second part of this work intrinsic and coherent quantum control is explored. Specifically, a feedback setup that stabilizes a cavity quantum electrodynamics (cQED) is investigated with respect to the quantum limit of single photon feedback. By a particular design of its environment, a typical cQED system exhibits surprising Rabi-oscillations also at weak coupling conditions. In order to implement delayed single photon feedback, the cQED couples to a continuum of distinctively environmentally shaped photon modes.

Further, as an example of coherent quantum control in the solid state, the generation of entanglement between radiatively coupled nitrogen-vacancy (NV) centers is proven to be possible, even at strong cavity loss rates. The calculations are based on an effective analytical treatment and also full quantum mechanical description, that involves the cavity mediated interaction between the NV-centers. In contrast to previous models, the calculations here predict a counterintuitive asymmetry towards the detuning of frequencies.

---

# Abstrakt

Der technologische Fortschritt in Bezug auf die Herstellung von Festkörper basierten Nanostrukturen, wie photonische Bauteile, phononische Strukturen oder elektronische und nanomechanische Hybridsysteme, ermöglichen es, typische Phänomene der Quantenoptik und Nanomechanik auf das Feld dieser baubedingt skalierbaren Systeme auszuweiten. Im Gegensatz zu atomaren Systemen kommt es in Festkörperstrukturen zu verstärkten Wechselwirkungen mit dem umliegenden Material. Diese dadurch bedingten spezifischen Eigenschaften angemessen beschreiben zu können, erfordert oftmals eine voll quantenmechanische Behandlung der Quantenkorrelationen höherer Ordnung, hier basierend auf der Heisenberg Bewegungsgleichungsmethode, die zusätzlich semiklassische Näherungen ermöglicht. Der erste Teil meiner Arbeit befasst sich mit den interessanten Effekten und möglichen Anwendungen, die aus der Wechselwirkung zwischen einem Halbleiterquantenpunkt (QP) mit akustischen und optischen Phononen hervorgehen. Eingebettet in das vergleichsweise neue Feld der Nanophononik wird ein QP Phononlaser vorgeschlagen, der durch die Kopplung an eine akustische Phononmode mit hohem Q-Faktor realisiert werden kann. Dieser Phononlaser nutzt zur Erzeugung von kohärenten Phononen den induzierten Ramanprozess unter frequenzverstimmter optischer Anregung. Neben einer voll quantenmechanischen Beschreibung der quantenkorrelierten Dynamik und Statistik werden auch einfach semiklassische Phononlasergleichungen hergeleitet. So kann der stationäre Phononlaser analytisch in einfachen Formeln beschrieben werden.

Zusätzlich wird die zur Charakterisierung verwendete Lichtemission eines QP untersucht. Neben der schwachen und starken Anregung mit der berühmten Mollowtriplett-Emission liegt der Fokus hier auf einem dritten Anregungszenario. Dieses stellt sich ein, wenn die Rabi-Frequenz des Lasers mit der optischen Phononfrequenz übereinstimmt. Das Spektrum weist dann eine dramatische Veränderung auf. Mithilfe der ermittelten spektralen Informationen kann die Elektron-Phonon-Kopplung bestimmt werden.

Der zweite Teil der Arbeit behandelt die Quantenkontrolle typischer Systeme der Quantenelektrodynamik (QED). Mittels intrinsischer Kontrolle durch ein Quantenfeedback kann ein gekoppeltes Resonator-Emitter-System im Limes der schwachen Kopplung Rabi-Oszillationen aufweisen. Die Beschreibung des Feedbacks fußt auf einer kontinuierlichen Behandlung eines strukturierten photonischen Reservoirs. Als weiteres Beispiel der Quantenkontrolle befasst sich die Arbeit abschließend mit einem kohärenten Besetzungstransfer zwischen zwei radiativ gekoppelten Stickstoffstörstellen in Diamant. Mithilfe eines numerischen und effektiven analytischen Modells kann die Möglichkeit von Grundzustandsverschränkung auch für starke Photonenverluste bestätigt werden. Im Gegensatz zu bisherigen Ergebnissen wird hier eine kontraintuitive Abhängigkeit von den verschiedenen Frequenzverstimmlungen vorhergesagt.

---

# Contents

<b>List of Figures</b>	<b>IX</b>
<b>1. Introduction</b>	<b>1</b>
1.1. Motivation . . . . .	1
1.2. Structure of the work . . . . .	4
<b>2. Theoretical Framework</b>	<b>5</b>
2.1. Solid state Hamilton-operator . . . . .	5
2.1.1. Quantum confinement . . . . .	6
2.2. Formulation of the solid state Hamiltonian in second quantization . . . . .	7
2.2.1. Electric dipole representation . . . . .	8
2.2.2. Electron-photon interaction . . . . .	8
2.2.3. Coupling to a classical laser field . . . . .	9
2.2.4. Electron phonon interaction . . . . .	9
2.3. Quantum and phonon optics . . . . .	10
2.4. Statistics – Photon and phonon number probabilities . . . . .	10
2.4.1. Observables of the cavity statistics . . . . .	10
2.5. Calculating the statistics . . . . .	11
2.6. Jaynes Cummings model–Equation of motion method . . . . .	13
2.6.1. Solution of the Jaynes-Cummings model . . . . .	14
2.6.2. Treatment of the JCM within the equation of motion approach . . . . .	15
<b>3. A Quantum dot phonon laser</b>	<b>19</b>
3.1. Nanophononics – acoustic cavities . . . . .	19
3.2. Acoustic cavity coupled QD – a phonon laser scheme . . . . .	20
3.2.1. Model system – quantum mechanical treatment . . . . .	20
3.2.2. Equations of motion . . . . .	23
3.2.3. Dynamics . . . . .	24
3.2.4. Stationary domain . . . . .	25
3.3. QD-Cavity acousto dynamics . . . . .	25
3.3.1. Symmetric phonon assisted Rabi-oscillations by induced Raman in the lossless case . . . . .	26
3.3.2. Phonon lasing by a two level system . . . . .	28
3.4. Classical to quantum regimes of a single quantum dot phonon laser . . . . .	31
3.4.1. Steady-state properties . . . . .	31
3.4.2. Damping and loss . . . . .	34

3.5. Effective phonon laser . . . . .	36
3.5.1. Effective Hamiltonian approach . . . . .	36
3.5.2. Effective spontaneous emission . . . . .	39
3.5.3. Semiclassical limit of the effective phonon laser equations . . . . .	39
3.5.4. Semiclassical Model in the Stationary Limit . . . . .	41
3.5.4.1. Phonon number . . . . .	42
3.5.4.2. Laser frequency . . . . .	42
3.5.4.3. Threshold behavior . . . . .	43
3.5.5. Comparison of the analytics with the full quantum model: – Input-output behavior . . . . .	45
3.5.6. Influence of pure dephasing . . . . .	46
3.5.7. Influence of phonon- and radiative decay . . . . .	48
3.5.8. High phonon number regime . . . . .	49
3.6. Quantum theory of the effective phonon laser . . . . .	50
3.6.1. Stationary limit of the effective quantum model . . . . .	51
3.6.2. Verification of the effective phonon laser Hamiltonian . . . . .	53
3.6.3. Conclusion . . . . .	53
<b>4. Phonon-assisted Mollow triplet</b> . . . . .	<b>55</b>
4.1. Input-laser field and emitted light field . . . . .	57
4.1.1. Hamilton-operator and equations of motion . . . . .	58
4.1.2. Treatment of the multi-mode phonon system . . . . .	58
4.1.3. Treatment of the multi-mode photon system . . . . .	59
4.2. Stationary spectrum:–Mollow triplet . . . . .	61
4.2.1. Without phonon interaction . . . . .	62
4.2.2. The power spectrum and the quantum regression theorem . . . . .	64
4.3. Phonon-assisted Mollow triplet . . . . .	65
4.3.1. Anti-crossings of the Mollow-sidebands and the Mollow-triplet centers	67
4.3.2. Strength of the anticrossings of the sidebands and the splittings of the phonon satellites . . . . .	70
4.4. Time-resolved light emission from semiconductor quantum dots . . . . .	73
4.4.1. Time-resolved signal . . . . .	73
4.4.2. Temporal emission dynamics . . . . .	75
4.4.2.1. Time-resolved spectrum in the weak excitation regime . . .	75
4.4.2.2. Time-resolved spectrum in the strong excitation regime . .	77
4.4.2.3. Evolution of the different spectral contributions . . . . .	79
4.5. Excitation frequency dependence of the emission dynamics of semiconductor quantum dots . . . . .	81
4.5.1. Quantum dot modeled as a three level system . . . . .	81
4.5.2. Dynamics: Factorizing approach to the equations of motion . . . . .	84
4.6. Excitation dependent emission dynamics . . . . .	86
4.6.1. Time-resolved spectrum of a quantum dot . . . . .	86
4.6.2. Emission dynamics . . . . .	87
4.7. Conclusion . . . . .	90

<b>5. Quantum control: Single photon delayed feedback</b>	<b>93</b>
5.1. Model for the cQED with quantum feedback . . . . .	93
5.1.1. Quantum approach to the external optical feedback . . . . .	94
5.1.2. Equations of motion . . . . .	95
5.2. Single photon feedback . . . . .	96
5.2.1. Feedback induced restoration of strong coupling signatures . . . . .	98
5.2.2. Conclusion . . . . .	100
<b>6. Coherent control and entanglement of radiatively coupled <math>\Lambda</math>-systems</b>	<b>101</b>
6.1. Introduction . . . . .	101
6.2. Cavity-QED of an optically driven $\Lambda$ -system . . . . .	102
6.2.1. Equations of motion for the single $\Lambda$ -system . . . . .	103
6.2.2. Effective two level system . . . . .	105
6.2.3. Coherent population transfer in a cavity-coupled $\Lambda$ -system – Ideal case	107
6.2.4. Influence of photon loss . . . . .	110
6.2.5. Influence of the cavity statistics on the population transfer efficiency	110
6.3. Cavity QED of two radiatively coupled $\Lambda$ -systems . . . . .	113
6.3.1. Equations of motion for the coupled $\Lambda$ -systems: Full model . . . . .	113
6.3.2. Effective two-level system . . . . .	115
6.4. Deterministic entanglement of distant NV-centers at weak coupling conditions	119
6.4.1. NV centers . . . . .	120
6.4.2. Entanglement at strong coupling conditions:– Ideal case . . . . .	120
6.5. Influence of dissipation on the entanglement between the NV centers . . . . .	123
6.5.1. Influence of photon decay and coupling strength on the concurrence	125
6.5.2. The dependence of the entanglement generation on the detuning strengths: - - The interplay between detuning and dissipative pro- cesses . . . . .	126
6.5.3. Conclusion . . . . .	128
<b>7. Conclusion and outlook</b>	<b>129</b>
<b>A. Appendix</b>	<b>i</b>
A.1. Parameters of an InGaAs/GaAs-QD . . . . .	i
A.2. Jaynes-Cummings-model . . . . .	i
A.3. Equations for the emission spectrum of a quantum dot . . . . .	ii
A.4. Quantum regression theorem . . . . .	iii
A.5. Coherent population transfer . . . . .	iv
A.6. Effective coupling between two $\Lambda$ -systems . . . . .	iv
A.6.1. Cavity-coupling . . . . .	iv
<b>Bibliography</b>	<b>vii</b>
<b>Danksagung</b>	<b>xxiii</b>



# List of Figures

1.1. Phonon-induced anticrossing . . . . .	3
2.1. Jaynes-Cummings model . . . . .	13
2.2. Dynamics of the inversion in the Jaynes-Cummings model . . . . .	17
3.1. Level scheme of the quantum dot phonon laser . . . . .	21
3.2. Scheme of a two level quantum dot, coupled to an acoustic cavity (ideal case)	26
3.3. Phonon-assisted Rabi-oscillations . . . . .	27
3.4. Dynamics of the phonon-phonon correlation function in the ideal case . . .	27
3.5. Dynamics of the phonon system in the case of dissipative processes . . . . .	28
3.6. Dynamics of the phonon probability distribution . . . . .	29
3.7. Scheme of a two-level quantum dot, coupled to an acoustic cavity . . . . .	30
3.8. Input-output behavior of the quantum dot phonon laser . . . . .	32
3.9. Evolution of the phonon statistics with the optical pump strength . . . . .	33
3.10. Influence of the radiative decay on phonon lasing . . . . .	34
3.11. Influence of the acoustic cavity lifetime on phonon lasing . . . . .	35
3.12. The phonon number, Mandel $Q$ parameter and the inversion versus phonon decay rate . . . . .	36
3.13. Scheme of the effective subsystem to the quantum dot phonon laser . . . . .	39
3.14. Comparison between the effective semiclassical- and the full model in the steady state . . . . .	45
3.15. Influence of pure dephasing on the emission properties of the phonon laser .	47
3.16. Phonon probability distribution at different pure dephasing strengths . . . .	48
3.17. Evolution of the thresholds versus phonon- and radiative decay . . . . .	49
3.18. Phonon number and threshold behavior in the many phonon limit . . . . .	50
3.19. Input-output behavior according to the effective quantum mechanical model	54
4.1. Level scheme of a quantum dot in the strong and the weak excitation regime	56
4.2. Level scheme of the Mollow triplet . . . . .	63
4.3. Emission spectrum of a two-level system in the weak and the Mollow-triplet regime . . . . .	64
4.4. Level scheme of the phonon assisted Mollow triplet . . . . .	66
4.5. Emission spectrum of a quantum dot in the weak and the strong excitation regime . . . . .	66
4.6. LO-phonon induced anticrossings in the emission spectrum of a quantum dot	68
4.7. Emission spectrum of a quantum dot versus varying excitation strength . .	69
4.8. Spectral positions of the phonon assisted features during the anticrossings .	70

4.9. Relative peak positions during the anticrossings . . . . .	71
4.10. Emission spectrum in the anticrossing regime versus frequency detuning of the laser . . . . .	73
4.11. Scheme of the measurement setup for the time-resolved emission spectrum . . . . .	74
4.12. Time-resolved emission spectrum at weak optical excitation . . . . .	76
4.13. Time-resolved emission spectrum at strong optical excitation . . . . .	78
4.14. Temporal evolution of the spectrum at selected spectral positions . . . . .	79
4.15. Temporal evolution of the Mollow-triplet features . . . . .	80
4.16. Excitonic $V$ -type level structure and decay channels of a quantum dot . . . . .	83
4.17. Time-resolved spectrum at different optical excitation frequencies . . . . .	86
4.18. Temporal evolution of the emission features at close to resonant optical excitation . . . . .	88
4.19. Temporal evolution of the emission features at different temperatures and excitation between the first and the second resonance . . . . .	89
4.20. Dynamics of the fluorescence contributions at different excitation frequencies . . . . .	90
4.21. Evolution of the phonon assisted fluorescence in comparison with experimental data . . . . .	91
5.1. Feedback scheme . . . . .	94
5.2. Dynamics in the single excitation limit . . . . .	97
5.3. Stabilization of Rabi-oscillations via quantum feedback . . . . .	99
5.4. Rabi-oscillation at a fluctuating number of excitations . . . . .	100
6.1. Scheme of a $\Lambda$ -system inside a single mode cavity . . . . .	103
6.2. Effective level scheme of the $\Lambda$ -system . . . . .	105
6.3. Rabi-oscillations in the effective Jaynes-Cummings model . . . . .	108
6.4. Detuning effects in the effective Jaynes-Cummings model . . . . .	109
6.5. The effective Jaynes-Cummings model in the weak coupling regime . . . . .	110
6.6. Rabi-oscillations of the inversion at thermal cavity statistics . . . . .	111
6.7. Temporal evolution of the photon probability distribution . . . . .	112
6.8. Temporal evolution of the lower order photon probabilities at thermally doped cavity statistics . . . . .	113
6.9. Scheme of two radiatively coupled $\Lambda$ -systems . . . . .	114
6.10. Effective subsystem of two radiatively coupled $\Lambda$ -systems . . . . .	117
6.11. Interaction timescales in the effective subsystem . . . . .	118
6.12. Illustration of two NV centers nanodiamonds integrated into a photonic crystal cavity . . . . .	119
6.13. Dynamics of the populations and the concurrence . . . . .	121
6.14. Evolution of the target state population at different detuning strengths . . . . .	122
6.15. Dependence of the effective subsystem on the different detunings . . . . .	123
6.16. Population- and concurrence dynamics in the presence of dissipative processes . . . . .	124
6.17. Concurrence and entanglement time versus photon decay rate . . . . .	125
6.18. Evolution of the concurrence and transfer time with the photon decay rate at different detunings . . . . .	126
6.19. Concurrence and transfer time versus cavity- and laser detuning . . . . .	127

6.20. Robustness of the concurrence against the change of the transition frequency 128

*"Und jedem Anfang wohnt ein Zauber inne"*

HERMANN HESSE

# 1

## Introduction

### 1.1. Motivation

Advances in nanoengineering yield the possibility of adapting typical quantum optical effects, such as single photon emission, Rabi-oscillations or entanglement for quantum information, to the field of semiconductor and solid state physics. Technologically grown low dimensional structures, such as quantum dots (QDs), carbon nanotubes (CNTs), Nitrogen vacancy (NV) centers, etc. are already well established in nanoscience, as they inherit the elemental benefit of tunable device properties. Within the manufacturing process, coupling strengths, transition frequencies or sites can be determined by design, making future investigations and the search for novel nanostructures indispensable for nanotechnologies. In contrast to atomic systems, these designed nanostructures often strongly interact with phonons or impurities, present in the solid state surroundings. Characteristic to the fabricated material system, such interactions lead for example to an altered and more complex emission behavior, strong dephasing mechanisms or even constitute their applicability as technological component. Although often understood as an obstacle, to be overcome by the device modeling, these effects can as well be reversed into new technologically utilizable effects, inherent only to the solid state.

### Phonon lasers

A comparably new and currently intense research field is the nanophononics and optomechanics, with the aim of exploiting structures, that allow for the quantum manipulation of single harmonic oscillator modes [AR13, SKH<sup>+</sup>12, RH13], phonon lasing [GLPV10, VHK<sup>+</sup>09, KPSR12] and cooling [KBP<sup>+</sup>13, SRA<sup>+</sup>08] or just the investigation of a sound based analogue (cavity quantum acousto dynamics (cQAD)) [SRT11, RWJ<sup>+</sup>09, TBF<sup>+</sup>02] to the optical cavity quantum electrodynamics (cQED). In the field of optomechanics, breakthrough techniques allow for the fabrication of very high mechanical quality factors,

as in single-crystal diamond nanomechanical oscillators [TBMD12]. Such devices are the foundation to the vibrant research field of cavity optomechanics, that allow the study of the radiation pressure force in the quantum regime [SNCH<sup>+</sup>12], cooling and coherent vibrational motion [KBP<sup>+</sup>13]. These devices are based on the cavity-enhanced phonon-photon coupling [KV08, GHV<sup>+</sup>09] and have further been realized in micro disk-systems [JLR<sup>+</sup>09], optical microtoroid resonators [KV07] or in Fabry-Perot cavities [MK04].

To manipulate the respective harmonic oscillator mode of the mechanical device, the light directly couples the mechanical motion via radiation pressure force [WRI02] or is mediated via an emitter-oscillator coupling [AR13, KBP<sup>+</sup>13]. In both cases, external manipulation of the oscillator motion can result in either optical cooling [CKJ<sup>+</sup>11] or vibrational amplification. The latter can be achieved in a stimulated phonon emission process, generating phonon emission in the gigahertz [GLPV10] or terahertz regime [BAHK10] and is experimentally demonstrated as a mechanical pendulum to an optical laser [KPSR12].

However, the generation of coherent phonons and monochromatic acoustic waves has also been observed and proposed for typical semiconductor nanostructures (semiconductor quantum wells, quantum dots or carbon nanotubes [LSW<sup>+</sup>03, FLKJP13, GMM<sup>+</sup>06, KCBK12, SRT11]). In these cases, the light field mostly couples to the electronic transitions of nanostructures (e.g. in quantum dots) rather, than to the resonator mode itself. Similar to the case of a trapped ion [VHK<sup>+</sup>09], the phonon system is controlled by optical excitation, exploiting a band diagonal emitter-phonon coupling in an induced Raman process [KCBK12, KWH<sup>+</sup>10]. The laser mechanism is realized via a  $\Lambda$ -type three-level laser structure or effectively an inverse incoherently pumped two level laser.

As demonstrated for the case of various optomechanical systems, the here proposed phonon laser is realized for a two-level quantum dot-acoustic cavity-system [KCBK12, SRT11, RWJ<sup>+</sup>09, TBF<sup>+</sup>02]. The coupled system is triggered into coherent phonon generation by excitation with a frequency detuned optical laser. Such a setup adds additional degrees of freedom to the phonon laser architecture due to the advances in semiconductor nanotechnology and phononics and the possible scalability of semiconductor nanostructures [BIZR00].

## Phonon-assisted Mollow triplet

In order to characterize a semiconductor nanostructure, a useful tool is nonlinear optical spectroscopy as it reveals the systems resonances and interactions within the emission and scattering spectrum. Due to multi-particle interactions and the presence of phonons in the solid state, such structures exhibit a variety of different spectral features. In particular, phonons have been reported to strongly modify the emission properties of quantum light emitters [TBF<sup>+</sup>02, FLKJP13, TBF<sup>+</sup>02], with respect to homogeneous broadening and dephasing times, the appearance of extra phonon-assisted peaks in the spectrum, but also a modified cQED.

The great progress in the field of phonon engineering towards the generation of non-equilibrium phonons [SDR<sup>+</sup>10, WRZI04], cavity phonons and coherent phonons [GLPV10, FLKJP13] highly motivates the study of phonon coupling- and multi-phonon-features

[CFC<sup>+</sup>10, MKH08] in solid state based quantum light emitters [VAK02, MVTG06, BJS<sup>+</sup>07] such as quantum dots (QDs), nanolayers, nanotubes, quantum wells, etc]. Stationary or time dependent laser fields, applied to the quantum light and phonon emitters, serve as external control of the phonon statistics [KCBK12] and therefore the emission properties of the device.

The emission spectrum of an atom is known to be sensitive to the optical excitation regime, exhibiting Rayleigh scattering and fluorescence emission in the weak excitation regime and the famous Mollow triplet [Mol69, SZ97] for strong optical excitation. A similar behavior is predicted and reported for the artificial atom (like QDs) [UAR<sup>+</sup>11, UWU<sup>+</sup>12, VLT09, GTVC<sup>+</sup>10], as it inherits a quasi discrete level structure due to quantum confinement. The coupling to phonons, however, leads to additional phonon-assisted contributions to the spectrum, such as Raman scattering, phonon satellites [KWH<sup>+</sup>10, MVA12] and also phonon-assisted Mollow triplets in the high driving regime [RH11, KCRK11]. Next to the strong driving regime (Mollow-regime), an additional strong excitation scenario can be provoked for the QD, that occurs for coinciding Rabi- and (here LO-)phonon frequencies  $\Omega_R = \omega_{LO}$ . In this third excitation regime, the spectrum is changed drastically, resulting from the formation of quasi-particles between the electronic, the exciting light field and the phonon system. These predicted spectral features are proposed to serve as an emission intensity independent mean of measuring the electron-phonon coupling strength [HR50, KCRK11].

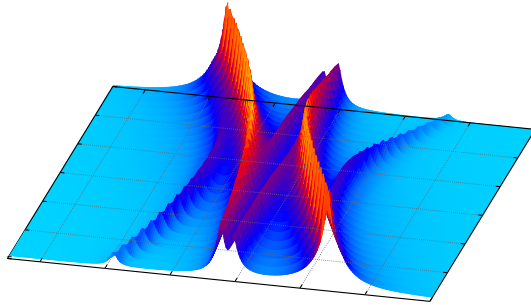


Figure 1.1.: Phonon-induced anticrossing in the calculated emission spectrum of a QD.

### Single photon feedback

In classical self-feedback setups, the stabilization of semiconductor lasers can be achieved by placing an external mirror in front of a cavity-emitter system. This well-known scheme is described with the Lang-Kobayashi model [LK80, HDY<sup>+</sup>11, MMT90], being a reliable tool in the regime of classical light fields. With focus on quantum information processing and the realization of quantum networks, the stabilization of particular quantum states is highly desired. Usually, this control is realized in the form of a repeated action sensor-controller-actuator loop [ZDP<sup>+</sup>12, VMS<sup>+</sup>12, WM10].

In particular few emitter systems, such as QD-microcavity systems exhibit a deviating behavior with respect to the Lang-Kobayashi case. Involving an intrinsic quantum feedback by a particular design of the environment, a microcavity-few-quantum dot laser is demonstrating quantum chaos [AHR<sup>+</sup>11]. This feature is further accompanied by a drastic modification of the cavity photon statistics, leading to considerable intensity fluctuations (bunching). In this transition area of classical- and quantum emission, models surpassing

the classical Lang-Kobayashi-type systems have to be consulted.

Further considerations of quantum feedback are settled in the true quantum limit, i.e. the single photon regime, where quantum fluctuations explicitly dominate the emission properties. Previous proposals for photon feedback involved a self-feedback of a laser driven atom, placed in front of a half-cavity [DZ02]. Based on a similar approach, the cavity-quantum electrodynamics involving self-photon feedback [CKS<sup>+</sup>13] is investigated here. Such a feedback scheme enables a recovery of Rabi-oscillations for emitter-cavity coupling constants small compared with the outcoupling strength.

## Radiatively coupled NV-centers

Among the variety of quantum confined solid state nanostructures, the negatively charged nitrogen-vacancy (NV) center strikes with deliberately long coherence times [BNT<sup>+</sup>09, BCR<sup>+</sup>12, HA08, WSSB13]. Further, its level structure, basically providing a  $\Lambda$ -type level structure with two separately addressable optical transitions onto an excited state manifold, makes it an ideal candidate for coherent control [STN<sup>+</sup>06, TCT<sup>+</sup>10, MGT<sup>+</sup>11]. Next to the coupling to high-Q mechanical oscillator modes [TBMD12], as mentioned above, there has been significant technological progress in the integration of single NV-centers within photonic crystal cavities [FSH<sup>+</sup>12, ML08, WSK<sup>+</sup>10]. Next to probabilistic entanglement schemes [BHP<sup>+</sup>13], involving entanglement between spatially distanced NV-centers, the particular level structure offers the possibility of coherently control the entanglement via the effective coupling by a photonic crystal cavity mode [YXFD10]. In a scheme, priorly proposed for a QD-microcavity system [IAB<sup>+</sup>99], a coherent population switch via a ground state entanglement between two distant (uncoupled) NV-centers can be effectuated. Via strong laser detunings towards the optical transition, the population switch can be realized even for large ratios of the photon loss rate and the cavity coupling.

## 1.2. Structure of the work

Chapter 2 briefly introduces the considered material systems and applied theoretical methods. In chapter 3, a proposal for a semiconductor QD phonon laser is discussed, involving a full quantum mechanical treatment as well as a semiclassical level of description. The third chapter deals with novel high driving field induced phonon features in the spectrum of a QD, that give access to the electron-phonon coupling strength. Further phonon related emission characteristics are investigated on the basis of the time-resolved spectrum. The description is based on an equation of motion approach, that includes higher order non-Markovian phonon-phonon correlations to describe the phonon features. Chapter 5 contains the single-photon self-feedback in cavity QED, theoretically demonstrating the recovery of Rabi-oscillations for typical weak coupling conditions. In chapter 6, the coherent control of two radiatively coupled  $\Lambda$ -systems is studied under the influence of strong photon loss out of the photonic crystal cavity. The theoretical description is considered with an effective analytical model and a full systems treatment. Finally, a brief summary collects the results and contains proposals for future research. Some complementary derivations and formulas can be found in the appendix.

# 2

## Theoretical Framework

In this chapter, an introductory outline of the material systems of interest and the basics of the applied theoretical methods will be presented in a compact manner. Further, this introduction will cover (as a foundation to quantum electrodynamics) a brief discussion of the Jaynes-Cummings model, which will frequently be referred to in this thesis.

### 2.1. Solid state Hamilton-operator

The basic starting point for the following theoretical considerations is a typical solid state Hamilton operator, composed of the multi particle interactions present in the solid state system:

$$H = H_e + H_i + H_{e-i}, \quad (2.1)$$

with the electronic  $e$  and the ionic  $i$  part and interaction between them. The usual approach is to treat the kinetic energy of the ions as a perturbation for the system. Within the so called Born-Oppenheimer approximation, the electrons are assumed to move in the static potential of the nuclei  $V_{e-i}(\{\vec{R}_0\})$  that are located at fixed positions  $\{\vec{R}_0\}$  [Czy00, Hak93]. On the other hand, the nuclei's motion is considered within an effective potential  $V_{i-i}(\{\vec{R}\})$ , given by the electronic eigen-energies, i.e the approximation leads to a decoupling of the electron- and ion dynamics. A correction to this approximation involves for example the electron-phonon interaction  $V_{e-i}(\{\vec{r}\} - \{\vec{R}\})$ . Including the light matter interaction (in

Coulomb gauge) given by the minimal coupling Hamiltonian [VW94], the different contributions to the Hamiltonian now read [Czy00]:

$$H_e = \sum_l \left\{ \frac{1}{2m_e} [\vec{p}_l + e\vec{A}]^2 \right\} + \int d^3r \left\{ \epsilon_0 \vec{E}_\perp^2 + \mu_0^{-1} \vec{B}^2 \right\} + V_{e-i}(\{\vec{r}\} - \{\vec{R}_0\}), \quad (2.2)$$

$$H_i = \sum_l \frac{P_l}{2m_l} + V_{i-i}(\{\vec{R}\}), \quad (2.3)$$

$$H_{e-i} = V_{e-i}(\{\vec{r}\} - \{\vec{R}\}), \quad (2.4)$$

where the braces stand for the whole set of coordinates of the electron  $\vec{r}$  and ion  $\vec{R}$  coordinates. Equation (2.2) describes the motion of the electrons within the lattice potential of the nuclei  $V_{e-i}(\{\vec{R}_0\})$ , which later on will be treated within the effective mass approximation. Further, it contains the electron-light interaction as well as the free radiation part of the Hamiltonian (second term in Eq. (2.2)). The ion part of the Hamilton operator  $H_{i-i}$  will be reformulated into the free phonon Hamilton-operator, while  $H_{e-i}$  accordingly is the electron-phonon interaction. Within the formulation of second quantization of particles and fields, these interactions will be introduced in more explicit form in the following section. The carrier part of the Hamiltonian  $H_c$  can further be simplified in the effective mass approximation [Czy00]. Here, the motion of the electrons within the periodic ion potential  $V_{e-i}(\{\vec{r}\} - \{\vec{R}_0\})$  is mimicked by a modified effective carrier mass  $m_e \rightarrow m_e^*$ , such that Eq. (2.2) reduces to:

$$H_e = \sum_l \left\{ \frac{1}{2m_e^*} [\vec{p}_l + e\vec{A}]^2 \right\} + \int d^3r \left\{ \epsilon_0 \vec{E}_\perp^2 + \mu_0^{-1} \vec{B}^2 \right\}. \quad (2.5)$$

### 2.1.1. Quantum confinement

The solid state nanostructures considered here (quantum dots, NV-centers) spatially confine the electrons in all three dimensions, leading to a discrete atom like level structure. Theoretically, this confinement is introduced via postulating electronic wave functions composed of the periodic Bloch factor  $u_{si}$  and an envelope function  $\xi_i(\vec{r})$  [HK94]:

$$\varphi_i(\vec{r}) = \xi_i(\vec{r}) u_{s \approx 0i}(\vec{r}), \quad (2.6)$$

where  $i$  denotes the band index. These confinement function are determined through the confinement potential  $V_{\text{conf}}$ , fulfilling

$$\left\{ -\frac{\hbar^2}{2m^*} \nabla^2 + V_{\text{conf}}(\vec{r}) \right\} \xi_i(\vec{r}) = \hbar\omega_i \xi_i(\vec{r}). \quad (2.7)$$

Due to the confinement induced spatial determination of the electron within the nanostructure, the momentum index  $s$  can be skipped in the following. In this work, the confinement potential will be described via a harmonic potential, leading to Gaussian envelope functions [FWDK03, KWH<sup>+</sup>10].

## 2.2. Formulation of the solid state Hamiltonian in second quantization

Throughout the thesis, the different fields (Schrödinger, Maxwell) are treated within the formalism of second quantization. Within canonical quantization, the crucial step towards quantization is the postulation of commutation relations for the canonic field variables according to the respective wave equations (Hamilton function).

**Schrödinger's field:**– In the case of the Schrödinger equation, this Hamilton function is given by:

$$H = \int \psi^\dagger(\vec{r}) \left\{ -\frac{\hbar^2}{2m} \nabla^2 + V(\vec{r}) \right\} \psi(\vec{r}), \quad (2.8)$$

with the fermionic commutation relations for the field variables

$$[\pi(\vec{r}), \psi(\vec{r}')]_+ = \frac{\hbar}{i} \delta(\vec{r} - \vec{r}'), \quad [\psi(\vec{r}), \psi^*(\vec{r}')]_+ = \delta(\vec{r} - \vec{r}'), \quad [\psi^{(*)}(\vec{r}), \psi^{(*)}(\vec{r}')]_+ = 0, \quad (2.9)$$

where the conjugate momentum  $\pi \equiv \frac{L}{\dot{\psi}} = -\frac{\hbar}{i} \psi^*$  is derived from the Lagrangian  $L$ , fulfilling Schrödinger's equation [Hak93]. Solving Schrödinger's equations, the commutation relations of Eq. (2.9) also effectuate commutation relations for the evolution coefficients to its solution. With:

$$\psi = \sum_i \varphi_i^{(*)}(\vec{r}) a_i^{(\dagger)} \quad \Rightarrow \quad [a_i, a_j^\dagger]_+ = \delta_{ij}, \quad [a_i^{(\dagger)}, a_j^{(\dagger)}]_+ = 0. \quad (2.10)$$

In this formalism, the operators  $a_i^\dagger$  and  $a_i$  describe the creation and annihilation of a particle in the state  $|i\rangle$ . Using Dirac notation, the state of the system is given by the product state, as follows:

$$|\{n\}\rangle = \prod_\alpha a_i^{\dagger n_\alpha} |0\rangle, \quad \text{with } n_\alpha \in \{0, 1\} \quad (2.11)$$

With this, Eq. (2.8) can be cast into the simple form

$$H = \sum_i \hbar\omega_i a_i^\dagger a_i \equiv \sum_i \hbar\omega_i \hat{n}_i, \quad (2.12)$$

where  $\hat{n}_i$  denotes the occupation number operator.

**Maxwell's field:**– In a similar procedure, now starting from Maxwell's equations [Hak93], the electromagnetic field can be quantized according to:

$$\vec{A}(\vec{r}, t) = \sum_k \left\{ \vec{\lambda}_k(\vec{r}) c_k(t) - \vec{\lambda}_k^*(\vec{r}) c_k^\dagger(t) \right\}, \quad \vec{\lambda}_k = \frac{i\vec{e}_k e^{ik\cdot\vec{r}}}{\sqrt{2\epsilon_0 \hbar \omega_k V}}, \quad (2.13)$$

with the bosonic commutation relations for the photonic creation and annihilation operators

$$[c_k, c_{k'}^\dagger]_- = \delta_{kk'}, \quad [c_k^{(\dagger)}, c_{k'}^{(\dagger)}]_- = 0. \quad (2.14)$$

Here, the state of the photon system is created as:

$$|\{n\}\rangle = \prod_{\alpha} \frac{1}{\sqrt{n_{\alpha}!}} a^{\dagger n_{\alpha}} |0\rangle \quad (2.15)$$

### 2.2.1. Electric dipole representation

Before fully representing the Hamiltonian in second quantization, including the quantization of Schrödinger's field, a long wavelength approximation is performed in Eq. (2.5). Here, the vector potential is assumed to be spatially independent  $\vec{A}(\vec{r}, t) \approx \vec{A}(\vec{0}, t)$ , as the optical wavelengths can be expected to be large compared with the dimension of the here considered small nanostructures. First, applying now the electromagnetic field quantization to Eq. (2.5),  $H_e$  is given by:

$$H_e = \sum_l \left\{ \frac{1}{2m_e^*} [\vec{p}_l + e\vec{A}(0, t)]^2 \right\} + \sum_k \hbar\omega_k c_k^\dagger c_k. \quad (2.16)$$

In order to explicitly express the Hamiltonian in the form of an electric dipole interaction, the following (time-independent) unitary transformation  $T$  is applied to the full Hamiltonian [CT92]:

$$H' = THT^\dagger, \quad \text{with } T = \exp\left[\frac{i}{\hbar} \vec{d} \cdot \vec{A}(0, t)\right] \equiv \exp\left[\vec{d} \cdot (\vec{\lambda}_k(0)c_k(t) - \vec{\lambda}_k^*(0)c_k^\dagger(t))\right], \quad (2.17)$$

with  $\vec{d} = \sum_l q_l \vec{r}_l$  being the electric dipole moment. As the Coulomb parts Eqs. (2.3) and (2.4) of the Hamiltonian only depend on  $\vec{r}$ , they remain unaffected by  $T$ .  $H_e$  however results in:

$$H'_e = \sum_l \frac{1}{2m_e^*} \vec{p}_l + \sum_k \hbar\omega_k c_k^\dagger c_k - \vec{d} \cdot \sum_k \left\{ \vec{\mathcal{E}}_k c_k - \vec{\mathcal{E}}_k^* c_k^\dagger \right\}, \quad \vec{\mathcal{E}}_k = \omega_k \vec{\lambda}_k. \quad (2.18)$$

### 2.2.2. Electron-photon interaction

Now applying also the quantization for Schrödinger's field and considering the atom like electronic level structure in accordance with Sec. 2.1.1 Eq. (2.5) is finally reduced to:

$$\begin{aligned} H'_e &= H_{el}^0 + H_{pt}^0 + H_{el-pt}^I \\ &= \sum_i \hbar\omega_i a_i^\dagger a_i + \sum_k \hbar\omega_k c_k^\dagger c_k + \sum_{k,ij} \left\{ M_k^{ij} c + M_k^{ij*} c^\dagger \right\} a_i^\dagger a_j, \end{aligned} \quad (2.19)$$

describing the quasi free motion of the quantum confined electrons  $H_{el}^0$  within the bands denoted by  $i$ , the free part of the quantized radiation field  $H_{pt}^0$  and the interaction between

the photonic- and the electronic system  $H_{el-pt}^I$ . The electron-photon coupling strength  $M_k^{ij} = \langle i | \vec{d} \cdot \vec{\mathcal{E}}_k | j \rangle$  involves the wavefunctions of the respective nanostructure, for the quantum dot given by Eq. (2.6).

### 2.2.3. Coupling to a classical laser field

For the coupling of the QD with a single mode laser field, the photon system is assumed to be in the coherent state  $|\alpha\rangle$ . Via applying a unitary transformation onto  $H_e$ , the electron-light interaction is represented by a coupling of the electronic system with a classical laser field [CT92]. Corresponding with  $H_{el-pt}^I$ , in the classical limit, the electron-light interaction is simplified to:

$$H_{el-pt}^{I'} = H_{el-L}^I = -\vec{d} \cdot \vec{E}_L \sum_{ij} a_i^\dagger a_j, \quad \text{with} \quad E_L = \vec{\mathcal{E}}_L \alpha e^{-i\omega_L t} + \vec{\mathcal{E}}_L^* \alpha^* e^{i\omega_L t}, \quad (2.20)$$

where  $\alpha$  is the complex amplitude of the coherent light field with  $\langle n \rangle = \alpha^2$  being the intensity (average photon number) of the field. The interaction strength is often given in units of the Rabi-frequency, given by  $\Omega_R = 2\Omega \equiv -\frac{\vec{d} \cdot \vec{E}_L \alpha}{\hbar}$ .

### 2.2.4. Electron phonon interaction

Considering Eqs. (2.3) and (2.4), the ion part of the particle density is treated classically  $\rho_i(\vec{r}) = \psi_i(\vec{r})\psi_i(\vec{r}) \approx \sum_n \delta(\vec{r} - \vec{R}_n)$ . For quantizing the ionic system, the spatially dependent part of the ion potential  $V_{i-i}(\{\vec{R}\})$  is expanded to second order from the equilibrium positions  $\vec{R}_{0n} = \vec{u}_n - \vec{R}_n$  [Czy00]:

$$V_{i-i}\{\vec{R}\} \approx V_{i-i}\{\vec{R}_0\} + \frac{1}{2} \sum_{l,m,\mu,\nu} \frac{\partial^2 V_{i-i}}{\partial R_{l\mu} \partial R_{m,\nu}} \Big|_{\vec{R}_0} u_{l\mu} u_{m,\nu} \quad (2.21)$$

where  $\vec{u}_n$  are the ionic displacement coordinates. Introducing normal coordinates  $\{\tilde{u}, \tilde{p}\}$  for the ionic displacement vectors and the ion momenta via a unitary coordinate transformation, Eq. (2.3) can be brought into the form of uncoupled harmonic oscillators:

$$H_{i-i} = \frac{1}{2} \sum_l \left\{ \tilde{p}_l^2 + \omega_l^2 \tilde{u}_l^2 \right\}. \quad (2.22)$$

Following the usual quantization procedure for the harmonic oscillator, quantizing the actual ionic coordinates, Eqs. (2.3) and (2.4) yield the free phonon Hamiltonian  $H_{pn}^0$  and the electron phonon interaction  $H_{el-pn}^I$ :

$$H_i + H_{e-i} = H_{pn}^0 + H_{el-pn}^I = \sum_q \hbar \omega_q b_q^\dagger b_q + \sum_{q,i} \left\{ g_q^{i*} b_q^\dagger + g_q^i b_q \right\} a_i^\dagger a_i, \quad (2.23)$$

where the phonon creation-  $b_q^\dagger$  and annihilation operators  $b_q$  exhibit the same bosonic commutation relations such as the photon operators in Eq. (2.14). In Eq. (2.23) it was already

assumed, that the interaction between the electrons and the phonons is band diagonal, i.e. no transitions between the different electronic states are induced via the phonon system. In the solid state, there are different possibilities for the coupled ionic motion, leading to different types of phonon modes. In this thesis, two coupling mechanisms will be considered. The first is the coupling to longitudinal acoustic (LA) phonons, introduced via a deformation potential coupling and the second is the coupling to longitudinal optical (LO) phonons via the Fröhlich coupling [Mah81, Hau70]:

$$g_{q,LO}^i = \sqrt{\frac{e^2 \hbar \omega_{LO}}{2V \epsilon_0 \epsilon_r}} \langle i | e^{iqr} | i \rangle, \quad \text{with} \quad \epsilon_r = \left( \frac{1}{\epsilon_s} - \frac{1}{\epsilon_\infty} \right)^{-1}, \quad (2.24)$$

$$g_{q,LA}^i = \sqrt{\frac{\hbar q}{2\rho_m v_L V}} D_i \langle i | e^{iqr} | i \rangle. \quad (2.25)$$

In Eq. (2.24), the Einstein approximation, assuming a constant dispersion relation for the LO-phonons was applied.

### 2.3. Quantum and phonon optics

Applying the broad spectrum of concepts, known from quantum optics to the field of quantum phononics, is a convenient and often useful method in order to describe similar effects and applications in phonon optics. Although this procedure is not generally legitimate, as for example, the phonon potential cannot always be assumed to be harmonic, it is applicable in a broad range of domains. As outlined above, usually the difference between photons and phonons is the way of quantization, respectively. In the photon case, hermitian field operators are associated with the classical field variables by postulating a quantization of the radiation field. In contrast, the phononic commutation relations are directly gained from first quantization of the atomic position and momentum operators.

### 2.4. Statistics – Photon and phonon number probabilities

Dealing with cavity quantum electrodynamics (CQED) in quantum optics and cavity quantum acousto dynamics (CQAD) in nano-phononics, the evaluation of the cavity field statistics provides basic insight and information about the emission properties of the considered quantum system. In the following chapters 3 and 6, the phonon- and photon statistics of the system will be calculated via the higher order (photon/phonon) coherences. Here in this section, a short introduction of photon statistics is given and the used method, based on an inductive equation of motion scheme, is presented [CRCK10, KCR<sup>+</sup>11].

#### 2.4.1. Observables of the cavity statistics

There are several quantities, which are used for the characterization of the cavity field statistics. The Discrimination of different types of light, with diverging coherence properties

to be determined with a second order correlation setup (Hanbury-Brown-Twiss interferometer) gives the crucial information about the operational regime of an optical device. Within this measurement, the quantum field statistics are revealed via an intensity-intensity correlation, in quantum optics given by:

$$g^{(2)}(0) = \frac{\langle c^\dagger c^\dagger c c \rangle}{\langle c^\dagger c \rangle^2}. \quad (2.26)$$

In Eq. (2.26), the photon-photon correlation is given for a single mode quantum light field, measured at equal time-and location, as will be considered in the following. Its value states the conditioned measurement of two photons, i.e the regularity of the photons within a light beam. This quantity is normalized to the case of a coherent light field. Other types of statistics can then be referred to this benchmark value:

$$g^{(2)}(0) = 1 + \frac{(\Delta n)^2 - \langle n \rangle}{\langle n \rangle^2} \rightarrow \begin{cases} = 1, & \text{random (coherent)} \\ > 1, & \text{correlated (bunched)} \\ < 1, & \text{anti-correlated (anti-bunched),} \end{cases}$$

These values are calculated via the respective state of the system  $\rho$ . The extrema of light statistics are (i) the coherent state  $\rho = |\alpha\rangle\langle\alpha|$  with the Glauber state defined as  $|\alpha\rangle \equiv e^{-\frac{1}{2}|\alpha|^2} \sum_n \frac{\alpha^n}{\sqrt{n!}}$ , (ii) the photon number state (Fock)  $\rho = |n\rangle\langle n|$  and (iii) the thermal state  $\rho = \sum_n P_n |n\rangle\langle n|$ .

Evaluating the photon statistics of a cavity, another important parameter is the photon number probability distribution  $P_n(t)$  [Lou90, RCSK09] as occurring within the density matrix of the photon system. Same as for the  $g^{(2)}$ -function, it can be benchmarked with the coherent case, in this particular case exhibiting a Poissonian shape:

$$P_n = \begin{cases} |\langle n|\alpha\rangle|^2 = \frac{\langle n \rangle^n e^{-\langle n \rangle}}{n!}, & \text{coherent} \\ \frac{\langle n \rangle^n}{(1+\langle n \rangle)^{n+1}}, & \text{thermal} \\ \delta_{nm} \text{ for } m = \langle n \rangle, & \text{Fock.} \end{cases} \quad (2.27)$$

Thus, a correlated cavity field will exhibit a broader distribution  $P_n$  (super-Poissonian), than for the coherent case, while anti-correlated photons show a narrower probability distribution (sub-Poissonian).

## 2.5. Calculating the statistics

In this thesis, the quantities of interest will be calculated on the basis of an equation of motion approach, developed in Refs [CRCK10, KCR<sup>+</sup>11]. Within this approach, higher order quantum correlations  $\langle c^{\dagger n} c^m \rangle$ , that determine the statistics are directly accessible. With those, quantities, such as the average photon number  $N = \langle n \rangle = \langle c^\dagger c \rangle$  or the second

order correlation function  $g^{(2)}(0)$  can be determined. These correlation quantities can be given as an expansion of the photon number probability distribution:

$$\langle c^{\dagger m} c^m \rangle = \sum_{n=m}^{\infty} \frac{n!}{(n-m)!} P_n(t). \quad (2.28)$$

Here,  $m$  is the power of photonic creation  $c_{\nu}^{\dagger}$  and annihilation  $c_{\nu}$  operators. In the usual cases, i.e. a coherent, thermal or Fock statistics, the probabilities converge to zero for large enough photon numbers  $P_n \rightarrow 0$ , ( $n \rightarrow n_{\infty}$ ). This justifies the truncation of the sum at a critical value  $n_{\infty}$ . Additionally rearranging Eq. (2.28), the probabilities can be expressed in terms of the photon-correlations  $\langle c^{\dagger m} c^m \rangle$ :

$$\begin{aligned} \langle c^{\dagger m} c^m \rangle &= \sum_{n=m}^{\infty} \frac{n!}{(n-m)!} P_n = m! P_m + \sum_{n=1}^{\infty} \frac{(m+n)!}{n!} P_{m+n} \\ \underbrace{\Rightarrow}_{P_{n_{\infty}} \approx 0} P_m &= \frac{1}{m!} \left[ \langle c^{\dagger m} c^m \rangle - \sum_{n=1}^{n_{\infty}} \frac{(m+n)!}{n!} P_{m+n} \right], \end{aligned} \quad (2.29)$$

and the photon probabilities can be calculated in an iterative procedure, if the photon correlations are known up to a critical order  $n_{\infty}$  with the start-value  $P_{n_{\infty}} = \frac{1}{n_{\infty}!} \langle c^{\dagger n_{\infty}} c^{n_{\infty}} \rangle$ . As an example, in the case of  $n_{\infty} = 3$  (corresponding to a extremely small average photon number or a Fock statistics with  $\langle n \rangle = 3$  at the max), the photon-probabilities are given by:

$$\begin{aligned} P_3 &= \frac{1}{3!} \langle c^{\dagger} c^{\dagger} c^{\dagger} c c c \rangle, \\ P_2 &= \frac{1}{2!} \langle c^{\dagger} c^{\dagger} c c \rangle - \frac{3! P_3^{\nu}}{2!}, \\ P_1 &= \langle c^{\dagger} c \rangle - 2! P_2^{\nu} - \frac{3! P_3^{\nu}}{2!}. \end{aligned}$$

The choice of the order  $n_{\infty}$  is strongly dependent on the mean photon number, the photon statistics or the integration time. In the case of a Fock-state with  $\bar{n}_{\nu} = 1$  and the electronic system in the ground state  $|c\rangle$ , only the first order photon correlation  $\langle c^{\dagger} c \rangle$  exists. There is only the probability of finding 1 or 0 photons.

In general, however, especially in the case of a coherent or a thermal statistics, truncation at  $n_{\infty} = 3$  cannot be justified, even at low average photon numbers. The inductive method, used in this thesis generates the higher order correlations up to converging orders also at high  $\langle n \rangle$ . However, in the high photon number regime the calculation may be numerically very demanding and other methods for calculating the statistics are more adequate [SZ97, RCSK09]. Considering in particular Eq. (2.29) in the case of a thermal statistics, where according to Wick's theorem for boson operators  $\langle c^{\dagger m} c^m \rangle = m! \langle c^{\dagger} c \rangle^m$  [Lou90] the limit of this method is revealed. In this case, the start value is  $P_{n_{\infty}} > 1$  for  $\langle c^{\dagger} c \rangle > 0$ , i.e. a truncation of the sum in Eq. (2.28) leads to a severe error. However, for the here considered optical (and acoustic) frequencies in the range of meV-eV, the average thermal

boson number calculated with the Bose-Einstein distribution  $N \equiv \langle c^\dagger c \rangle = 1/[\exp[\frac{\hbar\omega}{k_B T}] - 1]$  results in values well below 1.

Note, that Eqs. (2.28) and (2.29) reflect the fact, that the photon-probability of the quantum state is evaluated, using the respective Fock-state as the absolute benchmark.

## 2.6. Jaynes Cummings model–Equation of motion method

In this section, the method for calculating the expectation values, including the bosonic operator correlations introduced in the previous section, is shortly reviewed on the standard example of cavity-QED. But first, an analytical solution will be presented, as given in Ref. [SZ97].

The Jaynes-Cummings model (JCM) corresponds to the electron-photon part of the Hamiltonian of Eq. (2.19) in a Rotating wave approximation (RWA), keeping only energy conserving terms. Further, it treats the lines of a two level system  $i, j \in \{b, a\}$  containing only one electron and a single photon mode  $k = k_0$ :

$$H_{JC} = \hbar\omega_a a_a^\dagger a_a + \hbar\omega_b a_b^\dagger a_b + \hbar\omega_0 c^\dagger c + \hbar g (a_b^\dagger a_a c^\dagger + a_a^\dagger a_b c). \quad (2.30)$$

This Hamilton operator basically describes the interaction of a single two-level emitter with a single cavity mode, as visualized in Fig. 2.1. Via the interaction of the electronic system with the quantum light field (or cavity vacuum), transitions between the two levels can be induced. Starting for example in the excited state with an initially empty cavity, the two-level systems decays into the lower state, emitting a photon into the cavity in a cavity induced spontaneous emission process. Since this model is by definition a closed system. The emitted phonon is subsequently reabsorbed on the time scale given by  $g$ , leading to the well-known effect of Rabi-oscillations.

It is useful reviewing this model, since it is contained within more complex systems with

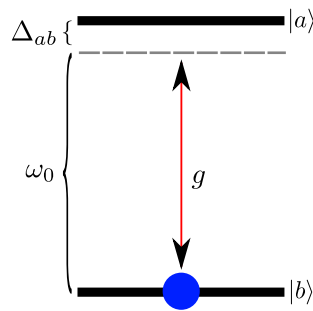


Figure 2.1.: Scheme of a two-level system with the unperturbed ground-  $|b\rangle$  and excited state  $|a\rangle$ , interacting with a single cavity mode with frequency  $\omega_0$ . The levels are separated with the energy  $\omega_a - \omega_b = \omega_{ab}$ . The two level system contains a single electron.

more than just one interaction as an effective subsystem. With respect selecting such an

effective JCM-like subsystem, it will be referred to, when dealing for example with the phonon laser in Chaps. 3 and 6.

### 2.6.1. Solution of the Jaynes-Cummings model

Due to the simplicity of the electronic structure in the JCM, the Hamiltonian is usually expanded in the electronic subspace  $|b\rangle\langle b| + |a\rangle\langle a| = \hat{1}$ . Within the interaction picture, Eq. (2.30) can be given in the compact form:

$$H'_{JC} = \hbar g |v\rangle\langle c| c^\dagger e^{-i\Delta_{ab}t} + h.c., \quad (2.31)$$

where  $\Delta_{ab} = \omega_{ab} - \omega_0$ . As this system is lossless, it is most convenient, solving it in Schrödinger's picture  $i\hbar \frac{\partial |\psi\rangle}{\partial t} = H'_{JC} |\psi\rangle$ , where the systems state is generally given as  $|\psi(t)\rangle = \sum_n [\alpha_{b,n}(t) |b, n\rangle + \alpha_{a,n}(t) |a, n\rangle]$ , where the first index denotes the electronic state and the second index the photon number state. Applying Schrödinger's equation and Eqs. (2.30), within a rotating frame  $\alpha_{i,n} \rightarrow \alpha_{i,n} e^{i(\omega_i - \omega_0)t}$ , this leads to the following equations of motion for the coefficients:

$$\dot{\alpha}_{a,n} = -ig\sqrt{n+1} e^{i\Delta_{ab}t} \alpha_{b,n+1}, \quad (2.32)$$

$$\dot{\alpha}_{b,n+1} = -ig\sqrt{n+1} e^{i\Delta_{ab}t} \alpha_{a,n}. \quad (2.33)$$

The solution can straightforward be calculated as:

$$\begin{aligned} \alpha_{a,n}(t) &= \left[ \alpha_{a,n}(0) \left[ \cos\left(\frac{\Omega_{G,n}t}{2}\right) - \frac{i\Delta_{ab}}{\Omega_{G,n}} \sin\left(\frac{\Omega_{G,n}t}{2}\right) \right] \right. \\ &\quad \left. - \frac{i\Omega_{R,n}}{\Omega_{G,n}} \alpha_{b,n+1}(0) \sin\left(\frac{\Omega_{G,n}t}{2}\right) \right] e^{\frac{i\Delta_{ab}t}{2}}, \end{aligned} \quad (2.34)$$

$$\begin{aligned} \alpha_{b,n+1}(t) &= \left[ \alpha_{b,n+1}(0) \left[ \cos\left(\frac{\Omega_{G,n}t}{2}\right) + \frac{i\Delta_{ab}}{\Omega_{G,n}} \sin\left(\frac{\Omega_{G,n}t}{2}\right) \right] \right. \\ &\quad \left. - \frac{i\Omega_{R,n}}{\Omega_{G,n}} \alpha_{a,n}(0) \sin\left(\frac{\Omega_{G,n}t}{2}\right) \right] e^{-\frac{i\Delta_{ab}t}{2}}, \end{aligned} \quad (2.35)$$

with the photon-manifold dependent bare Rabi frequency  $\Omega_{R,n} = 2g\sqrt{n+1}$  and generalized Rabi-frequency  $\Omega_{G,n} = \sqrt{\Omega_{R,n}^2 + \Delta_{ab}^2}$  determining the dynamics. For the case an initial excitation of the two-level system, the initial values for the coefficients are simply  $\alpha_{a,n}(0) = \alpha_n(0)$  and  $\alpha_{b,n+1}(0) = 0$ . For this special case, the inversion and the photon probabilities can be calculated by:

$$R(t) = \sum_{n=0}^{\infty} [|\alpha_{a,n}|^2 - |\alpha_{b,n}|^2] = \sum_{n=0}^{\infty} P_n(0) \left[ \frac{\Delta_{ab}^2}{\Omega_{G,n}^2} + \frac{\Omega_{R,n}^2}{\Omega_{G,n}^2} \cos\left(\frac{\Omega_{G,n}t}{2}\right) \right], \quad (2.36)$$

$$\begin{aligned} P_n(t) &= |\alpha_{a,n}|^2 + |\alpha_{b,n}|^2 = P_n(0) \left[ \cos^2\left(\frac{\Omega_{G,n}t}{2}\right) + \left(\frac{\Delta_{ab}}{\Omega_{G,n}}\right)^2 \sin^2\left(\frac{\Omega_{G,n}t}{2}\right) \right] \\ &\quad + P_{n-1}(0) \frac{\Omega_{R,n-1}}{\Omega_{G,n-1}} \sin^2\left(\frac{\Omega_{G,n-1}t}{2}\right). \end{aligned} \quad (2.37)$$

Apparently, with an initially empty cavity  $P_0(0) = 1$  and zero detuning of the cavity mode from the electronic resonance  $\Delta_{ab} = 0$ , the probabilities and the inversion just perform simple sinusoidal Rabi-oscillations, as shortly discussed before. However, at different initial statistics  $P_n(0)$ , the oscillatory behavior can be drastically changed. In particular the photon probabilities each rotate at different frequencies.

### 2.6.2. Treatment of the JCM within the equation of motion approach

While the JCM is limited to the most simple lossless case of CQED, additional interactions and dissipative processes in a quantum system demand other methods of description. In this thesis, the quantities of interest are calculated on the basis of an equations of motion approach. Within this approach, the inclusion of losses, several interactions between different quantum systems as well as many particle interactions is straight forward using Heisenberg's equation of motion.

$$\langle \dot{O} \rangle = \frac{i}{\hbar} \langle [H, O] \rangle + Tr \{ O \mathcal{L} \rho \}, \quad (2.38)$$

where  $H$  includes the interactions and the Lindblad-operator  $\mathcal{L}$  introduces the dissipative processes on the basis of a second order Markovian treatment of the interactions with the dissipative degrees of freedom [Car99, BP02]. Within this approach, a naturally emerging problem is the so called hierarchy-problem. This means, that an operator quantity of the order  $n$  in a quantum system (here photon system) couples to a quantity of the order  $n + 1$  and so on. A method to overcome this problem, frequently used for solid state systems is the cluster expansion [Fri96, KK08]. However, this method is valid only in the limes of many emitter/photon systems. Transitions from the quantum- to the classical regime require non perturbative treatments.

The inductive equation of motion method [CRCK10, KCR<sup>+</sup>11], here demonstrated for the photon coherences, generates a set of equations which is formally identical for each photon manifold. In the case of the JCM [Eq. (2.30)] (at resonance  $\omega_{ab} = 0$ ) the equation for the first- and second order photon correlations  $N = \langle c^\dagger c \rangle$  and  $g^{(2)}(0) \langle c^\dagger c \rangle^2 = \langle c^\dagger c^\dagger c c \rangle$  read:

$$\partial_t \langle c^\dagger c \rangle = i [M a_b^\dagger a_a c^\dagger - M^* a_a^\dagger a_b c], \quad (2.39)$$

and

$$\partial_t \langle c^\dagger c^\dagger c c \rangle = 2i [M a_b^\dagger a_a c^\dagger c^\dagger c - M^* a_a^\dagger a_b c^\dagger c c]. \quad (2.40)$$

From these two equations, the general equation of motion for the  $m$ -th order can be guessed:

$$\partial_t \langle c^{\dagger m} c^m \rangle = i m [M a_b^\dagger a_a c^{\dagger m} c^{m-1} - M^* a_a^\dagger a_b c^{\dagger m-1} c^m]. \quad (2.41)$$

This assumption is to be proven by mathematical induction.

$$\begin{aligned}
 \partial_t(c^{\dagger m+1}c^{m+1}) &= \partial_t(c^\dagger c^{\dagger m}c^m c) \\
 &= (\partial_t c^\dagger)c^{\dagger m}c^m c + c^\dagger \partial_t(c^{\dagger m}c^m)c \\
 &+ c^\dagger(c^{\dagger m}c^m)\partial_t c.
 \end{aligned} \tag{2.42}$$

Now, using the result for  $\partial_t(c^{\dagger m}c^{\dagger m})$  of Eq. (2.41) and considering the equations of motion for  $c^\dagger$  and for  $c$ :

$$\partial_t c^\dagger = -iM^{\nu*}a_a^\dagger a_b, \quad \partial_t c = +iM^\nu a_b^\dagger a_a, \tag{2.43}$$

This gives the general form for the equations of motion for the photon correlations, now resulting in:

$$\partial_t(c^{\dagger m+1}c^{m+1}) = i(m+1)[Ma_b^\dagger a_a c^{\dagger m+1}c^m - M^* a_a^\dagger a_b c^{\dagger m}c^{m+1}], \tag{2.44}$$

In order to reproduce the analytical solution to the JCM in Eqs. (2.36) and (2.37), a set of equations for the photon-assisted electronic quantities, such as the population densities and the polarizations are derived in the same manner. Starting with the  $(n+m)$ -th order photon assisted electronic density, the respective set of equations results in:

$$\partial_t \langle a_a^\dagger a_a c^{\dagger n} c^m \rangle = iM [\langle a_b^\dagger a_a c^{\dagger n+1} c^m \rangle - \langle a_a^\dagger a_b c^{\dagger n} c^{m+1} \rangle], \tag{2.45}$$

$$\partial_t \langle a_b^\dagger a_a c^{\dagger n} c^m \rangle = niM \langle a_b^\dagger a_a c^{\dagger n-1} c^m \rangle + iM [2\langle a_a^\dagger a_a c^{\dagger n} c^{m+1} \rangle - \langle c^{\dagger n} c^{m+1} \rangle], \tag{2.46}$$

$$\partial_t \langle c^{\dagger m} c^m \rangle = iM [m \langle a_b^\dagger a_a c^{\dagger m} c^{m-1} \rangle - n \langle a_a^\dagger a_b c^{\dagger n-1} c^m \rangle]. \tag{2.47}$$

These three general EOM, describing the dynamics of the JCM is solved numerically. To compare this approach with the analytics, the dynamics of the inversion (here given as  $R(t) = 2\langle a_a^\dagger a_a \rangle - 1$ ) are calculated for different initial photon statistics. While in Eqs. (2.36) and (2.37), the statistics enter via the photon probability distribution  $P_n$ , it is here incorporated via the initial values for the expectation values of the operator correlations. These are determined under the assumption of a factorizing state  $\rho(t=0) = \rho_{el} \otimes \rho_{pt}$  with respect to the electronic and the photonic system at  $t=0$ . With this, the initial conditions are given as:

$$\langle a_i^\dagger a_j c^{\dagger n} c^n \rangle = \langle a_i^\dagger a_j \rangle \langle c^{\dagger n} c^n \rangle = \langle a_i^\dagger a_j \rangle \times \begin{cases} N^n, & \text{(coherent)} \\ n!N^n, & \text{(thermal)} \\ \frac{N!}{(N-n)!}, & \text{(Fock)}, \end{cases} \tag{2.48}$$

where  $N$  is the average photon number.

In Fig. 2.2, the dynamics of the inversion  $R(t)$ , as calculated with the analytical formula of Eq. (2.36) is depicted together the results from Eqs. (2.45)-(2.47) at three different initial cavity statistics: (a) For an initially empty cavity with  $N(0) = 0$  (Fock), (b) a coherent state with  $N(0) = 5$  and a thermal state with  $N(0) = 0.3$ . In all three cases, the emitter is assumed to be excited at the beginning  $R(0) = 1$ . The fat grey curves correspond to

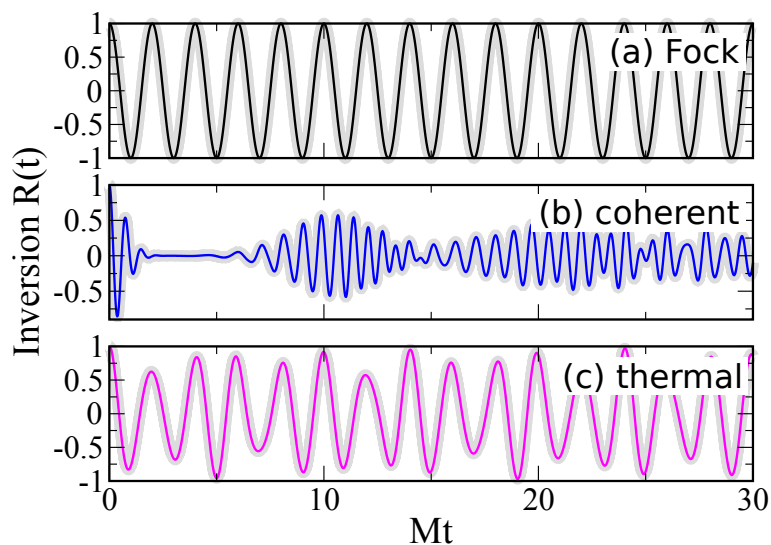


Figure 2.2.: Dynamics of the inversion  $R$  according to the Jaynes-Cummings model at different initial conditions for the photon field: (a) Fock state with  $N(0) = 0$ , (b) coherent state with  $N(0) = 6$  and (c) thermal statistics with  $N(0) = 0.3$ . The fat grey curves corresponds to the analytical Jaynes-Cummings solution and the thin colored curves are calculated with the inductive equation of motion method.

the analytics, while the thin colored curves are calculated numerically with Eqs. (2.45)-(2.47). Obviously, both solutions are in perfect agreement, proving the equation of motion approach to be a reliable tool for calculating the dynamics involving higher order photon assisted processes at different types of statistics. This makes this method in particular useful for the description of transition between different regimes, which states an advantage in comparison with the cluster expansion method or a Born factorization.

For the Fock case in In Fig. 2.2(a), the inversion  $R$  is performing symmetric Rabi-oscillations on timescale given by the electron-photon coupling element  $M$ . Due to this coupling induced spontaneous emission, the inversion decays, emitting a photon into the cavity, which is subsequently reabsorbed again. In the case of the coherent statistics Fig. 2.2(b), however, the dynamics exhibits the well-known collapse, beating and following revival of the oscillations [RWK87]. In contrast to (a), where the oscillations are determined by a single Rabi-frequency  $\Omega_{R,0}$ , there are also higher order Rabi-frequencies  $\Omega_{R,n}$  ( $n > 0$ ) involved. The different orders of the photon correlations lead to an interference, causing these features. In order to reach convergence with the analytics, the photon correlations had to be included up to  $n = 35$ th order. For the thermal statistics in Fig. 2.2(c), the inversion is performing chaotic oscillations. As here, the photon probability distribution is peaked about zero, the time scale of the oscillations is more comparable to the Fock case. Although there are several orders of photon correlations (Rabi-frequencies) involved in the dynamics as well, such as for the coherent case, there are no periodic collapses/revivals present in the temporal evolution. In the Poissonian (coherent) case, the Rabi-frequencies are distributed

much narrower, than in the super Poissonian thermal case, giving rise to constructive and destructive interference.

The systems, that will theoretically be examined in the following sections are treated, making use of the above introduced method. Within this approach, it is possible to incorporate several interactions and losses, while still retaining an arbitrary accuracy in the description of higher order effects. Further theoretical framework will be introduced in the respective sections, as needed.

# 3

## A Quantum dot phonon laser

The foundation of a broad spectrum of laser applications is the coherent beam amplification. While this optical feature is well understood, the feasibility of highly coherent beams of sound by translating the laser mechanism to the generation of coherent phonons is currently explored in experimental [VHK<sup>+</sup>09, GLPV10, BAHK10] and theoretical works [CMPFT01, CK03, KCBK12, KPSR12]. To generalize the concept of stimulated emission onto phononic systems establishes new possibilities to improve imaging resolutions in tomography or non-demolishing measurement techniques, but is also an interesting effect for fundamental science itself.

The phonon laser, as an acoustic pendant to a usual optical laser, constitutes a new and promising device, regarding its multiple possible applications and fundamental properties. Usually operated in the sub-MHz domain, the acoustic laser gives access to a frequency range, that is often hardly accessible in the optical regime. Besides the fact, that a phonon laser states a new way of coupling quantum systems, the comparably large wavelengths and the slower speeds makes coherent phonons and controlled phonon devices suitable for several areas of application.

### 3.1. Nanophononics – acoustic cavities

The research area of *nanophononics* involves the investigation and the engineering of phononic devices in order to control and manipulate the spectral and spatial properties of phonons in, for example, semiconductors, solids and optomechanics. Designed to confine a single acoustic phonon mode, acoustic nanocavities constitute the basis for applications such as phonon laser action [VHK<sup>+</sup>09, GLPV10, BAHK10, KCBK12] and acousto-luminescence [AMK07], control of phonon statistics [SDR<sup>+</sup>10] or modification of the electron-phonon interaction [TBF<sup>+</sup>02, CKM02]. Phonon cavities have been proposed [LKFBJ07, SRT11] and realized in several cases. In analogy to two Bragg reflectors (BRs), enclosing a stop band spacer of thickness  $d_\lambda$  corresponding to a multiple of the favored

cavity frequency  $\lambda$ , an acoustic cavity can be build of a semiconductor multilayer nanostructure. In the acoustic case, two superlattices enclose a spacer of the thickness  $d_{\lambda_a} = n\lambda_a/2$  of a multiple of the acoustical phonon wavelength [TBF<sup>+</sup>02, LKFBJ07]. Thus, changing the cavity design leads to a modification in the electron-phonon coupling and further can lead to a modulation of the light-sound interaction [LFJTM04]. In the case of the above described superlattice based nano-cavity structure, fundamental properties, such as the sound velocity, the position and width of the cavity frequency as well as the phonon lifetime can be controlled by the characteristics of the acoustic BRs [TBF<sup>+</sup>02].

## 3.2. Acoustic cavity coupled QD – a phonon laser scheme

In this chapter, a scheme for a possible realization of a phonon laser and non-equilibrium phonon source is presented, including the coherent optical control of a single acoustic phonon mode (acoustic cavity). In the suggested scheme [Fig. 3.1], a quantum dot, coupled to an acoustic cavity mode serves as the acoustic medium. The internal cavity statistics can be adjusted by the input power of an external laser drive and chosen to be either bunched, coherent or even nonclassical. The following discussions and results will show, that the emission properties and the threshold behavior of this system have similarities to photonic lasing of single atoms [MS92, C. 93, MBB<sup>+</sup>03, DRB<sup>+</sup>10].

The problem will first be addressed via a full quantum mechanical description, with respect to the cavity phonon system. Subsequently, a semiclassical treatment of the subject is developed, based on an effective Hamiltonian-approach. This effective approach yields a set of simple phonon laser equations, which are benchmarked with the full quantum mechanical treatment. Third, the effective system is treated quantum mechanically, giving access to analytical formulas for the higher order phonon-phonon quantum correlations and phonon probability distributions. This approach serves as an additional verification of the validity for the effective description. Parts of the here presented findings of this chapter have been published in Refs. [KCBK12, KCK13].

### 3.2.1. Model system – quantum mechanical treatment

The basis of the phonon laser proposal is a two-level semiconductor QD (conduction  $|c\rangle$  and valence band  $|v\rangle$  states), which is coupled to a single acoustic cavity mode [KCBK12]. The system is excited by a coherent optical laser field, driving the QD at the anti-Stokes resonance. This means, that the laser is blue detuned from the bare electronic transition  $\omega_{cv} = \omega_c - \omega_v$  with one phonon frequency  $\omega_L = \omega_{cv} + \omega_{ph}$  (straight yellow arrow), cp. Fig. 3.1. In a stimulated Raman process (curved black arrow), this excitation scheme leads to a light induced emission of phonons into the cavity mode (curly green arrow).

The system is described by a laser driven two-level system (electron-light coupling  $\Omega$ ), which is coupled to a single harmonic oscillator mode (electron-phonon coupling  $g$ ):

$$\mathcal{H}_0 = -\frac{\hbar\omega_{cv}}{2}\sigma_z + \hbar\omega_{ph}b^\dagger b, \quad (3.1)$$

$$\mathcal{H}_I(t) = \hbar\Omega(t)e^{i\omega_L t}\sigma + \hbar g\sigma^\dagger\sigma b^\dagger + h.c., \quad (3.2)$$

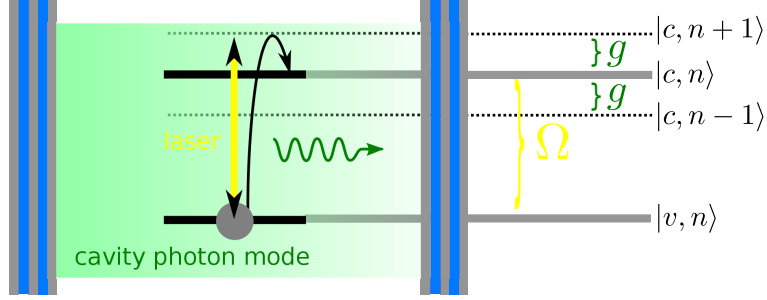


Figure 3.1.: Semiconductor QD, coupled to a single acoustic cavity mode (green area), indicated by the layered structure. An external laser field (yellow arrow) drives the QD's dipole transition, with Rabi-frequency  $\Omega$ . The coupling to the single acoustic cavity mode leads to a discrete phonon assisted level structure, as illustrated on the right. The QD is assumed as a two level system with a valence band state  $|v\rangle$  and a conduction band state  $|c\rangle$ .

where  $\sigma_z \equiv |v\rangle\langle v| - |c\rangle\langle c|$ ,  $\sigma \equiv |v\rangle\langle c|$  are the Pauli-operators [SZ97] and  $b^{(\dagger)}$  are the phononic ladder operators [Mah00]. The laser field with Rabi-frequency  $\Omega_R \equiv 2\Omega(t)$  is treated classically [See Eq. (2.20)].

**Losses .** – The inclusion of losses and damping, such as a phonon lifetime  $\kappa^{-1}$ , a radiative damping  $\Gamma_r$  and pure dephasing  $\gamma_{pd}$  of the electronic transition  $|c\rangle \rightarrow |v\rangle$  is crucial for the consideration of the proposed system. Within the discussion to Sec. 3.4.1, it will become apparent, that these conflicting types of damping have several and also counterintuitive effects to phonon lasing. On the one hand they can state a limit to the efficiency of the device as a phonon laser or coherent phonon source, but on the other hand they represent a necessary condition. These losses are assumed to originate from couplings to Markovian multi-mode photon and phonon bath modes and can therefore be incorporated in the typical Lindblad form [Car02]:

$$\dot{\rho} = -\frac{i}{\hbar}[\mathcal{H}(t), \rho] + 2\kappa\mathcal{D}[b]\rho + 2\Gamma_r\mathcal{D}[\sigma]\rho + \frac{\gamma_{pd}}{2}\mathcal{P}[\sigma_z]\rho, \quad (3.3)$$

with

$$\mathcal{D}[x]\rho \equiv x\rho x^\dagger - \frac{1}{2}\{x^\dagger x, \rho\} \quad \text{and} \quad \mathcal{P}[x]\rho = x\rho x - \rho \quad (3.4)$$

For the studies in this thesis the environment is assumed to be kept in the low temperature regime. Within such an assumption, a back action of the external Markovian baths can be neglected. Thus, the inverse phonon lifetime  $\kappa$ , the radiative decay  $\Gamma_r$  and the pure dephasing  $\gamma_{pd}$  are held constant.

**Damping of the expectation values:**– For determining the effect of Eq. (3.3) on the

damping of expectation values, first the expectation values are expressed by the density matrix:

$$\begin{aligned} \langle |\alpha\rangle \langle \beta| b^{\dagger n} b^m \rangle &= \text{Tr}[\rho |\alpha\rangle \langle \beta| b^{\dagger n} b^m] = \sum_{\mu, l} [\langle \mu | \langle l | \rho | \alpha \rangle \langle \beta | b^{\dagger n} b^m | \mu \rangle | l \rangle] \\ &= \sum_l [\langle \beta | \langle l | \rho b^{\dagger n} b^m | \alpha \rangle | l \rangle] = \sum_{l \geq m} \frac{\sqrt{l!} \sqrt{(l - (m - n))!}}{(l - m)!} \rho_{\beta, \alpha}^{l, (l - (m - n))} \end{aligned} \quad (3.5)$$

Here, Greek indices correspond to the electronic-, while the Latin indices correspond to the phononic system. Differentiation of Eq. (3.5) and inserting the Lindblad terms from Eq. (3.3) into the time derivative of  $\rho$  results in:

$$\frac{d}{dt} \langle |\alpha\rangle \langle \beta| b^{\dagger n} b^m \rangle = \sum_{l \geq m} \frac{\sqrt{l!} \sqrt{(l - (m - n))!}}{(l - m)!} \dot{\rho}_{\beta, \alpha}^{l, (l - (m - n))} \quad (3.6)$$

with

$$\begin{aligned} \underbrace{\dot{\rho}_{\beta, \alpha}^{l, (l - (m - n))}}_{(3.3)} &\equiv \langle \beta | \langle l | 2\Gamma_r \mathcal{D}[\sigma] \rho + \frac{\gamma_{pd}}{2} \mathcal{P}[\sigma_z] \rho | \alpha \rangle | (l - (m - n)) \rangle \\ &\quad + \langle \beta | \langle l | 2\kappa \mathcal{D}[b] \rho | \alpha \rangle | (l - (m - n)) \rangle \\ &\equiv \dot{\rho}_{el} + \dot{\rho}_{ph}. \end{aligned} \quad (3.7)$$

Here,  $\dot{\rho}_e$  and  $\dot{\rho}_{ph}$  denotes the damping of the electronic and the phononic degrees of freedom. Evaluating the phonon related part of Eq. (3.6) gives:

$$\begin{aligned} \frac{d}{dt} \langle |\alpha\rangle \langle \beta| b^{\dagger n} b^m \rangle_{ph} &\equiv \sum_{l \geq m} \frac{\sqrt{l!} \sqrt{(l - (m - n))!}}{(l - m)!} \dot{\rho}_{el} \\ &\stackrel{(3.7)}{=} 2\kappa \sum_{l \geq m} \frac{\sqrt{(l+1)!} \sqrt{(l - (m - n) + 1)!}}{(l - m)!} \rho_{\beta, \alpha}^{(l+1), (l - (m - n) + 1)} \\ &\quad - \underbrace{\kappa \sum_{l \geq m} \frac{\sqrt{l!} \sqrt{(l - (m - n))!}}{(l - m)!} (l + l - m + n) \rho_{\beta, \alpha}^{l, (l - (m - n))}}_{(*)}, \end{aligned} \quad (3.8)$$

where the last term of Eq. 3.8 can be rewritten, adding a zero:

$$\begin{aligned} (*) &= -\kappa(n + m) \langle |\alpha\rangle \langle \beta| b^{\dagger n} b^m \rangle - 2\kappa \sum_{l \geq m+1} \frac{\sqrt{l!} \sqrt{(l - (m - n))!}}{(l - m - 1)!} \rho_{\beta, \alpha}^{l, (l - (m - n))} \\ &= -\kappa(n + m) \langle |\alpha\rangle \langle \beta| b^{\dagger n} b^m \rangle - 2\kappa \sum_{l \geq m} \frac{\sqrt{(l+1)!} \sqrt{(l - (m - n) + 1)!}}{(l - m)!} \rho_{\beta, \alpha}^{(l+1), (l - (m - n) + 1)}. \end{aligned} \quad (3.9)$$

The second term of Eq. 3.10 cancels with the first term in Eq. 3.8, so that the phonon related part of the damping to the quantity  $\langle |i\rangle\langle j|b^{\dagger n}b^m\rangle$  is simply given by [See also Eq. (2.38)]:

$$\frac{d}{dt}\langle |i\rangle\langle j|b^{\dagger n}b^m\rangle_{ph} = -\kappa(n+m)\langle |i\rangle\langle j|b^{\dagger n}b^m\rangle. \quad (3.10)$$

Now, also evaluating the electronic part of Eq. (3.7) results in:

$$\begin{aligned} \dot{\rho}_{el} &= \delta_{\beta,v}\delta_{\alpha,c}\Gamma_r\rho_{c,c}^{l,(l-(m-n))} - \delta_{\alpha,c}\frac{\Gamma_r}{2}\rho_{c,j}^{l,(l-(m-n))} - \delta_{\beta,c}\frac{\Gamma_r}{2}\rho_{\alpha,c}^{l,(l-(m-n))} \\ &- \delta_{\alpha,c}\delta_{\beta,v}\frac{\gamma_{pd}}{2}\rho_{c,v}^{l,(l-(m-n))} - \delta_{\alpha,v}\delta_{\beta,c}\frac{\gamma_{pd}}{2}\rho_{v,c}^{l,(l-(m-n))}. \end{aligned} \quad (3.11)$$

For a more compact notation, the following abbreviations for the operator (here phonon) assisted electronic densities, polarizations and the (phonon) correlations are introduced and used throughout this chapter:

$$C^{(n|m)} \equiv \langle |c\rangle\langle c|b^{\dagger n}b^m\rangle, \quad (3.12)$$

$$V^{(n|m)} \equiv \langle |v\rangle\langle v|b^{\dagger n}b^m\rangle, \quad (3.13)$$

$$P^{(n|m)} \equiv \langle |v\rangle\langle c|b^{\dagger n}b^m\rangle, \quad (3.14)$$

$$N^{(n|m)} \equiv C^{(n|m)} + V^{(n|m)} = \langle b^{\dagger n}b^m\rangle. \quad (3.15)$$

Inserting the respective operators for  $\alpha$  and  $\beta$  in Eqs. (3.7), (3.10) and Eq. (3.11), the damping terms for the equations of motion of the expectation values  $\text{Tr}\{O\mathcal{L}\rho\}$  are here given by:

$$\dot{C}^{(n|m)} = -[2\Gamma_r + (n+m)\kappa]C^{(n|m)}, \quad (3.16)$$

$$\dot{V}^{(n|m)} = 2\Gamma_r C^{(n|m)} - (n+m)\kappa V^{(n|m)}, \quad (3.17)$$

$$\dot{P}^{(n|m)} = -[\Gamma_r + \gamma_{pd} + (n+m)\kappa]P^{(n|m)}, \quad (3.18)$$

$$\dot{N}^{(n|m)} = -(n+m)\kappa N^{(n|m)}. \quad (3.19)$$

### 3.2.2. Equations of motion

This chapter is focused on the generation of coherent and non-equilibrium phonons. In order to evaluate the phonon emission properties, the input-output behavior and the dynamics of the system, the average phonon number  $N \equiv \langle b^{\dagger}b \rangle$  is calculated. Further, the quantum statistical properties of the internal phonon cavity field is reflected in the value of the phonon-phonon correlation function, in the used notation represented as:

$$g^{(2)}(0) = \frac{N^{(2|2)}}{(N^{(1|1)})^2}. \quad (3.20)$$

Alternatively as well as supportingly, the phonon number probabilities  $p_n(t)$ , as introduced for the photon case in Eq. 2.29, Chap. 2 are calculated to evaluate the statistics. In order to get the phonon probability distribution  $p_n$ , it is sufficient to calculate the higher order

phonon correlations  $N^{(n|n)}$ . The  $p_n$  then follow from a reverse recursion, starting from the smallest necessary higher order phonon number probability  $p_{n_\infty}$ . Within the Heisenberg operator formulation, applying the inductive method from Chap. 2 as in the case of the Jaynes-Cummings model, the equations for the phonon correlations are given by:

$$\frac{\dot{N}^{(n|n)}}{n} = -\kappa N^{(n|n)} - igC^{(n-1|n)} + igC^{(n|n-1)}. \quad (3.21)$$

In order to solve for the phonon-phonon-correlations, a complete set of equations, including the phonon assisted electronic quantities  $C^{(n|m)}$ ,  $P^{(n|m)}$  as well as the phonon coherences  $N^{(n|m)}$  are necessary. For  $n, m \geq 0$ , they fulfill the following EOMs:

$$\dot{N}^{(n|m)} = [i(n-m)\omega_{ph} - (n+m)\kappa]N^{(n|m)} - ig[nC^{(n-1|n)} - mC^{(n|m-1)}], \quad (3.22)$$

$$\begin{aligned} \dot{C}^{(n|m)} &= [i(n-m)\omega_{ph}C^{(n|m)} - (n+m)\kappa + 2\Gamma_r]C^{(n|m)} \\ &+ ig[nC^{(n-1|m)} - mC^{(n|m-1)}] - i\Omega(t)[P^{(n|m)} - (P^{(m|n)})^*], \end{aligned} \quad (3.23)$$

$$\begin{aligned} \dot{P}^{(n|m)} &= -i[\Delta - (n-m)\omega_{ph}]P^{(n|m)} - [(n+m)\kappa + \Gamma_r + \gamma_{pd}]P^{(n|m)} \\ &- ig[P^{(n|m+1)} + P^{(n+1|m)}] - imgP^{(n|m-1)} \\ &- i\Omega(t)(2C^{(n|m)} - N^{(n|m)}). \end{aligned} \quad (3.24)$$

### 3.2.3. Dynamics

For the investigation of the QD quantum acousto dynamics (QAD), Eqs. (3.22)-(3.24) are solved, where certain initial conditions have to be chosen. It is assumed, that the electronic and the phononic system is uncoupled at the initial time

$$\rho(0) = \rho_{QD}(0) \otimes \rho_{PH}(0), \quad (3.25)$$

so that expectation values of a combination of QD and phonon variables at  $t = 0$  are factorized. In the beginning, only the lower QD state is assumed to be populated, resulting in the initial condition:

$$N^{(0|0)} = V^{(0|0)} = 1, \quad (3.26)$$

$$\Rightarrow V^{(n|m)} \underset{3.25}{=} V^{(0|0)}N^{(n|m)} = N^{(n|m)}. \quad (3.27)$$

All other quantities are set to zero. Dependent on the assumed initial cavity phonon statistics,  $N^{(n|m)}$  can have the following values:

$$N^{(n|m)}(0) = \begin{cases} \text{(Fock)} & \delta_{nm} \frac{N!}{(N-n)!}, & \text{for } n \leq N \\ \text{(thermal)} & \delta_{nm} n! N^n, & N = \left[ \frac{1}{\exp(\frac{\hbar\omega_{ph}}{k_B T}) - 1} \right]. \end{cases} \quad (3.28)$$

In this chapter, the initial phonon numbers within the cavity are given rather low values (thermal statistics), corresponding to the low temperature regime. Starting from these values, the system dynamics can be calculated and for example timescales for the switch-on behavior of the phonon laser or phase transitions from and into different statistics can be analyzed within the temporal domain.

### 3.2.4. Stationary domain

Under the above described detuned optical excitation conditions ( $\omega_L = \omega_{cv} + \omega_{ph}$ ) and with losses ( $\kappa, \Gamma_r, \gamma_{pd}$ ) included, the system evolves into a steady state within a certain parameter range. All dynamic quantities become then time independent  $\dot{O}^{(n|m)} = 0$ , so that it is sufficient to solve Eqs. (3.22)-(3.23) in the stationary limit. Written in a rotating frame with the exciting laser field the system of linear equations reads:

$$\begin{pmatrix} \dots V^{(n|m)} & C^{(n|m)} & P^{(n|m)} & \bar{P}^{(n|m)} & V^{(n|m+1)} & C^{(n|m+1)} & P^{(n|m+1)} & \bar{P}^{(n|m+1)} \\ \chi_N^{(n|m)} & 0 & 0 & 0 & 0 & 0 & 0 & 0 \\ 2\Gamma_r & \chi_C^{(n|m)} & -i\Omega & i\Omega & 0 & 0 & 0 & 0 \\ i\Omega & -i\Omega & \chi_P^{(n|m)} & 0 & 0 & 0 & -ig & 0 \\ -i\Omega & i\Omega & 0 & \chi_{\bar{P}}^{(n|m)} & 0 & 0 & 0 & -ig \\ -i(m+1)g & 0 & 0 & 0 & \chi_N^{(n|m+1)} & 0 & i\Omega & -i\Omega \\ 0 & -i(m+1)g & 0 & 0 & 0 & \chi_C^{(n|m+1)} & -i\Omega & i\Omega \\ 0 & 0 & -i(m+1)g & 0 & i\Omega & -i\Omega & \chi_P^{(n|m+1)} & 0 \\ 0 & 0 & 0 & -i(m+1)g & -i\Omega & i\Omega & 0 & \chi_{\bar{P}}^{(n|m+1)} \dots \end{pmatrix} = \vec{0},$$

with  $\bar{P}^{(n|m)} \equiv (P^{(m|n)})^*$  being the complex conjugate of the phonon-assisted polarization. The diagonal free rotation and the damping terms of the linear system of equations are abbreviated as:

$$\chi_N^{(n|m)} \equiv [i(n-m)\omega_{ph} - (n+m)\kappa], \quad (3.29)$$

$$\chi_C^{(n|m)} \equiv [\chi_N^{(n|m)} - 2\Gamma_r], \quad (3.30)$$

$$\chi_P^{(n|m)} \equiv [\chi_N^{(n|m)} - i\omega_{cv} - \Gamma_r - \gamma_{pd}], \quad (3.31)$$

$$\chi_{\bar{P}}^{(n|m)} \equiv [\chi_N^{(n|m)} + i\omega_{cv} - \Gamma_r - \gamma_{pd}], \quad (3.32)$$

With focus on the input-output behavior in the stationary limit and parameter dependencies, for example  $\omega_L$ ,  $\kappa$  or  $\Gamma_r$ , which reveal the characteristics of the proposed device, the results are gained more easily as when solving the full dynamics with Eqs. (3.22)-(3.23).

## 3.3. QD-Cavity acousto dynamics

In this section, the QD-CAD is investigated for different sets of parameters. At first, the systems dynamics are calculated for vanishing loss and decay processes in subsection 3.3.1. For the chosen excitation frequency, this situation strongly resembles the usual cavity quantum electrodynamics for the Jaynes-Cummings Hamiltonian (2.30). This will in particular become apparent in Sec. 3.5.1, discussing the effective phonon laser. In the second part of this section 3.3.2, the dynamics are solved for finite inverse phonon lifetimes  $\kappa$ , radiative

decay of the electronic levels  $\Gamma_r$  and pure dephasing  $\gamma_{pd}$ , which results in phonon laser action. Within each temporal evolution, the electron-phonon coupling  $g$  and the Rabi-energy  $\Omega_R$  stay fixed.

### 3.3.1. Symmetric phonon assisted Rabi-oscillations by induced Raman in the lossless case

Within the proposed excitation scheme, the basic process, which causes the emission of phonons into the cavity, is an induced Raman process [Fig. 3.2]. Here, a laser, which couples the transition  $|v\rangle \rightarrow |c\rangle$  of the two level QD excites the system at the first order anti-Stokes resonance. This means, that the laser is blue detuned with respect to the electronic transition at  $\omega_L = \omega_{cv} + \omega_{ph}$ .

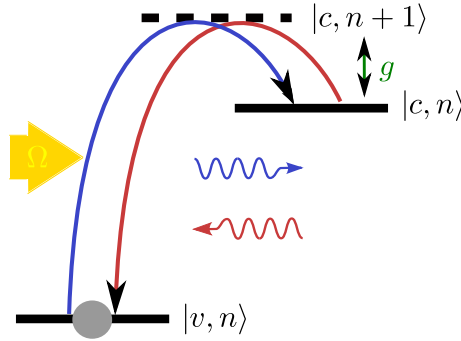


Figure 3.2.: Ideal case of a two level QD, coupled to an acoustic cavity ( $g$ ), which is driven by a single mode laser field ( $\Omega$ ) at the first order anti-Stokes resonance at  $\omega_L = \omega_{cv} + \omega_{ph}$ . The blue arrows denote the induced phonon emission process, while the red arrows denote the reverse process (reabsorption).

**Ideal case** .– If there are no losses included in the model ( $\kappa = \Gamma_r = \gamma_{pd} = 0$ ), this process just results in the induced emission and subsequent reabsorption of phonons. In the unrealistic case, where the upper state density is supposed to have an infinite lifetime, the system (schematically) undergoes symmetric phonon induced Rabi-oscillations, Fig. 3.2 with an effective Rabi-frequency  $g_{\text{eff}} \approx \frac{g\Omega_R}{\omega_{ph}}$  [See Sec. 3.5.1]. Starting in the lower state  $|v\rangle$ , the QD is excited into the upper state  $|c\rangle$ , while emitting phonons (blue arrows). The reabsorption of phonons is then involved in bringing the QD back into the lower state (red arrows).

This ideal case is presented in Fig. 3.3, illustrating the dynamics of the cavity phonon population  $N^{(1|1)}$  and the lower state density  $V^{(0|0)}$ . Before the optical laser switch-on, the system is initially assumed to be in the electronic ground state  $V^{(0,0)}(0) = 1$  with an empty acoustic phonon cavity  $N^{(1|1)}(0) = 0$ . Although this is a lossless system and similar dynamics compared with the JCM, there is a crucial difference visible in the behavior of the phonon number. One difference is obviously the number of interactions (electron-laser and electron-phonon). The second, however, is the form of the electron-phonon coupling Eq. 3.1, which is diagonal and non energy-conserving. Due to the diagonal electron-phonon

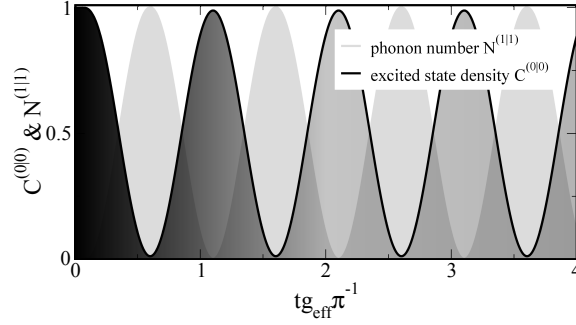


Figure 3.3.: The electronic ground state density  $V^{(0|0)}$  (black curve) and the average phonon number  $N^{(1|1)}$  (grey shaded area) performing phonon assisted Rabi-oscillations within an induced Raman process. The phonon number  $N^{(1|1)}$  exhibits values slightly larger than one (hardly visible).

coupling, even, when starting without any phonons in the system, it is possible to create more than one phonon while performing one cycle forth and back to the ground state. Due to higher order (non energy-conserving) phonon assisted processes, the cycle can be performed simultaneously within each of the phonon manifolds  $|v, n\rangle \rightarrow |c, n\rangle \rightarrow |v, n\rangle$ . Although, not deliberately addressed with the laser, higher order phonon processes occur within the cycle, so that visibly more than one phonon is created [See Fig. 3.3]. Further

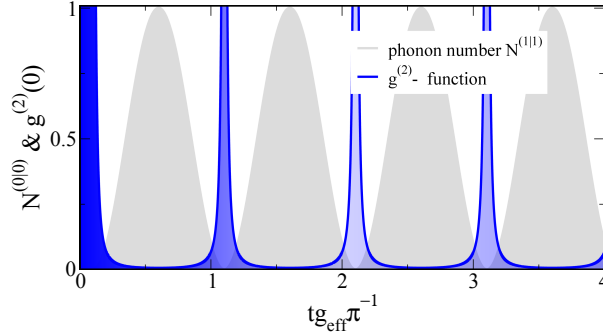


Figure 3.4.: Temporal evolution of the average phonon number  $N^{(1|1)}$  (grey shaded area) and the second order phonon correlation function  $g^{(2)}(0)$  (blue solid curve). With values larger than 1, the  $g^{(2)}$ -function illustrates bunching, i.e. there is an additional small fraction to the average phonon number, which is not in a Fock state.

Fig. 3.4 reveals, that this additional phonon population obviously does not result from the induced Raman process, as it is bunched ( $g^{(2)} > 1$ ). The phonon population, created within the induced Raman process is strictly in the Fock state, and would result in  $g^{(2)} = 0$ . The deviation of the phonon-phonon correlation function from zero is due to the higher order process related phonon density, which already occurs in this ideal, lossless case. Although mostly in the Fock state ( $g^{(2)}$  dropping almost to zero), part of the created

cavity phonon population is bunched. This excess population of the cavity results from fluctuations accompanying the optical excitation of the system, i.e., ordinary spontaneous emission of phonons within phonon assisted fluorescence emission  $\omega = \omega_{cv} - \omega_{ph}$  and Raman scattering (not induced)  $\omega = \omega_l - \omega_{ph}$ . For this reason, even without any pump processes included or initial thermal phonon populations assumed in the system, Eqs. (3.22)-(3.24) cannot be closed after the first or second order, as would be the case in the Jaynes-Cummings model. Strongly dependent on the external laser strength, many orders (up to 60) in the electron-phonon coupling have to be considered for the calculations. Since the phonon population, generated in that way, is a mixture of (mostly) Fock and thermal contributions, such a lossless laser driven QD-phonon cavity system is limited with respect to the regulation of the cavity statistics. However, in a more realistic treatment of such a system, losses have to be included, which reveal to have a great impact on the statistical properties of the phonon field [3.4.2].

### 3.3.2. Phonon lasing by a two level system

Of course, a finite phonon lifetime  $\kappa$  within the cavity will only cause a decay of the average cavity phonon number on a timescale given by the magnitude of the damping, not affecting the internal cavity statistics. The crucial parameter here is the radiative decay  $\Gamma_r$  of the excited QD state, as it serves as the cycling parameter [DRB<sup>+</sup>10, KCBK12] of the phonon laser. This parameter counteracts the excitation of the QD via the external laser field.  $\Gamma_r$  continuously recreates a population in the electronic ground state, but taking phonons from the cavity as in Figs. 3.2 and 3.3. Like this, a fresh cycle gets enabled [See also the discussion in Secs. 3.4.1 and 3.5.1].

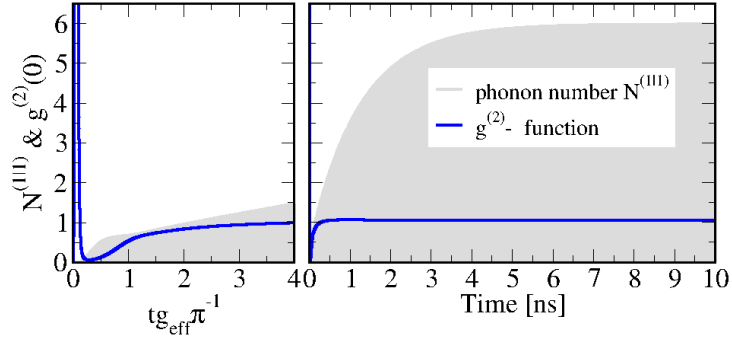


Figure 3.5.: Temporal evolution of the average phonon number  $N^{(1|1)}$  (grey shaded area) and second order phonon correlation function  $g^{(2)}(0)$  (blue solid curve). Phonon loss  $\kappa$ , radiative damping  $\Gamma_r$  and a pure dephasing  $\gamma_{pd}$  are included according to Eq. (3.3). (left) Timescales of the order of the effective coupling ( $\frac{g\Omega}{\omega_{ph}}$ ), (right) timescale of the order of the photon lifetime  $\kappa^{-1}$

For the case, where a phonon lifetime  $\kappa^{-1}$ , a pure dephasing  $\gamma_{pd}$  as well as a radiative damping  $\Gamma_r$  is introduced according to Eqs. (3.16)-(3.19), the temporal evolution of  $N \equiv N^{(1|1)}$  and  $g^{(2)}(0)$  are depicted in Fig. 3.5. In order to compare these results with the ideal case

of Fig. 3.4, the temporal evolution is split into two parts with different timescales. In Fig. 3.5a), the average phonon number and the  $g^{(2)}$ -function are depicted on a timescale in the range of  $g_{\text{eff}}^{-1}$ . Similar to Fig. 3.4, a large fraction of a Fock phonon ( $g^{(2)}(0) < 1$ ) is emitted into the cavity within one Rabi-period  $p_R = \frac{tg_{\text{eff}}}{\pi}$ . However, due to phonon loss and radiative decay, there are obviously no Rabi-oscillations occurring for the damped system. Instead, while  $N$  is increasing, also  $g^{(2)}$  increases, taking merely four periods  $p_R$  to approach the coherent value 1. However, it takes several nanoseconds (here  $p_R \gg 1$ ) [Fig. 3.5b)] for the system to reach a steady state, which is determined by the strength of the cavity loss  $\kappa$ . On long time scales, the phonon number grows with  $g^{(2)}$  converging to 1 from above. This behavior reveals the truly Poissonian characteristics of the phonon field within the cavity, as a Fock-state with a high number of phonons would always result in a convergence from below 1, as in this case  $g^{(2)}(0) = 1 - \frac{1}{N}$  [cf. Eq. (2.27)]. Further, the corresponding value of  $g^{(2)}$  for the steady state value of  $N = 6$  would be  $g^{(2)}(0) = 0.83$  for a Fock-state.

That it is indeed a Poissonian statistics and not a mixture of a Fock and a thermal statistics anymore is corroborated by Fig. 3.6. The temporal evolution of the phonon number probability distribution  $P(n)$ , as calculated with Eq. (2.29) confirms the indications for a coherent phonon cavity field. Starting from a Bose-Einstein distribution  $P(n) = n!(N)^p$

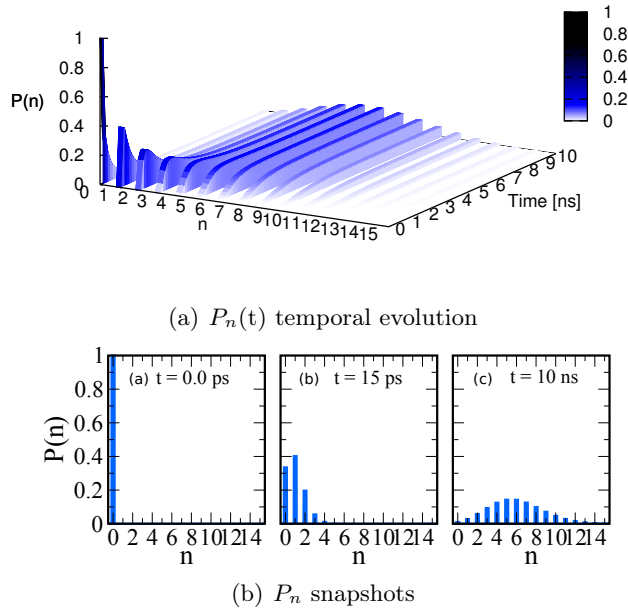


Figure 3.6.: (a) Temporal evolution of the phonon probability distribution  $P_n(t)$ . (b) Snapshots of  $P_n(t)$  at three different times:  $t = 0$ ,  $t = 15$  ps and  $t = 10$  ns.

with  $N = [\exp(\frac{\hbar\omega_{ph}}{k_B T}) - 1]^{-1}$  at  $t = 0$  in the low temperature regime  $T = 4$  K, the phonon system at first (within the timescale of  $g_{\text{eff}}^{-1}$ ) evolves into a mixture of a Fock and bunched

phonons ( $t = 15$  ps) and in the long time limit converges into a clear Poissonian statistics and steady state  $t \geq 10$  ns. This behavior can be explained as follows: Similar to the ideal case in Figs. 3.2 and 3.4, at first the system swings out of the thermal equilibrium by the laser excitation. In the presence of the laser, there is spontaneous emission of phonons, resulting in a large bunching  $g^{(2)}(0) \gg 1$  at the beginning. Reaching these high values is due to a super-Poissonian classical statistics of the cavity field at a vanishingly low phonon number. As in Fig. 3.4, the bunching results from spontaneous emission of phonons, always accompanying the laser excitation. In the equations, this behavior is reflected in the spontaneous emission terms to Eqs. (3.23) and (3.24), corresponding to anti-Stokes processes. Further, as already stated in the previous section, the occurrence of higher order phonon

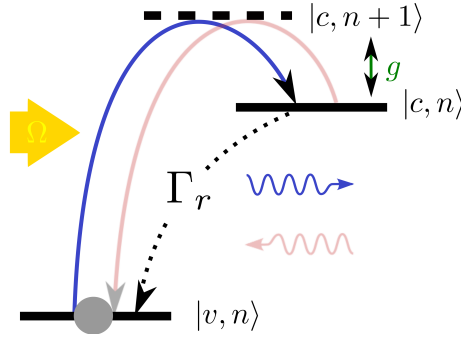


Figure 3.7.: Damped case of a two level QD. ( $g$ ) couples the laser transition, while ( $\Omega$ ) acts as the pump (induced Raman) at the first order anti-Stokes resonance. The blue arrows denote the induced phonon emission process, while the red arrows denote the reverse process. The dashed arrow represents the radiative decay of the lower laser level  $|c, n\rangle$  into the pump level  $|v, n\rangle$ .

processes originates from the non energy conserving character of the electron phonon coupling. Then, on the timescale of the induced Raman process  $g_{\text{eff}}^{-1}$ , a fraction of a Fock phonon is released into the cavity Fig. 3.2 (blue arrow). In contrast to the spontaneous emission of phonons, the Raman induced phonons are in a Fock-state. Yet, the statistics evolve into Poissonian statistics with time:

The fact, that now the phonon is not reabsorbed within the reverse process Fig. 3.2 (red arrow), as in the ideal case, states the important difference between those two cases. Instead, the cycling parameter  $\Gamma_r$  provides a recovery of the ground state density, but without destroying the before emitted phonons and thus allowing the phonons to remain in the cavity. The critical feature is, that the repetition of the induced Raman process is conditioned by the radiative decay of the upper state  $\Gamma_r$ . Subsequently, also the Raman process constitutes a random event in time and the resulting statistics is itself randomized. Thus, a process, that is individually generating Fock phonons, can create a coherent phonon field, if subordinate to a random event (here  $\Gamma_r$ ).

### 3.4. Classical to quantum regimes of a single quantum dot phonon laser

As demonstrated by the results of Sec. 3.3, the proposed system exhibits phonon laser action, i.e. the generation of a coherent cavity phonon field with  $g^{(2)}(0) = 1$ . As the realization of this effect requires a careful and optimal tuning of the relevant parameters, the introduced system is now investigated with respect to its steady state properties. Thus, the dependencies on the coherent pumping strength  $\Omega$ , the incoherent cycling parameter  $\Gamma_r$ , and the phonon loss  $\kappa^{-1}$  are examined in this section. It will become apparent, that the proposed device has a strong resemblance with certain types of single atom lasers. For instance, it exhibits typical effects in a one atom laser, such as threshold-less lasing, sub-Poissonian statistics, lasing without inversion (LWI) or self-quenching [MS92, MBW97, DRB<sup>+</sup>10]. However, there are also crucial and even beneficial differences to the photon case, owed to the diagonal electron-phonon coupling. For the phonon laser proposed in this work, there is no need to externally close the pump cycle by a cycling laser or an incoherent pump, as a closed cycle is already provided for by the radiative decay of the upper QD level.

Figure 3.7 shows a schematic representation of the pump cycle, realized by the coherent laser  $\Omega$  (yellow arrow), the electron phonon coupling  $g$  (green arrow) and  $\Gamma_r$  (dotted arrow). In contrast to Fig. 3.2, the reabsorption of cavity phonons is illustrated by more weakly drawn red arrows, in order to indicate, that this process is now much less sufficient, than in the undamped case. Here,  $\Omega$  acts as the coherent pump between the pump level  $|v, n\rangle$  and the upper laser level  $|c, n+1\rangle$ , which results in the induced emission of a phonon into the cavity  $|c, n+1\rangle \rightarrow |c, n\rangle$ . Before the next emission of a phonon can occur, it is necessary to repopulate the pump level again. This is realized by  $\Gamma_r = \Gamma_{c \rightarrow v}$ , constituting the decay of the lower laser level  $|c, n\rangle$  back into the pump level  $|v, n\rangle$ .

Depending on the (internal and external) parameter strengths, the phonon system can exhibit drastic changes in its statistical properties. Even if operating in the low phonon number regime, it is possible to tune the cavity statistics from classical (thermal and coherent) to quantum statistics. In the previous section, the dynamic transition from thermal via sub Poissonian into coherent phonon statistics was already presented for a fixed parameter set. In the following, the focus will be on the characterization of the system, i.e. the field properties in the steady state, corresponding to  $t \geq 10$  ns in Fig. 3.5 when changing the parameters. The calculations are carried out on the basis of Sec. (3.2.4).

#### 3.4.1. Steady-state properties

**Pump power dependence.** – In order to examine the systems threshold and input-output behavior, quantities, such as the average phonon number in the cavity and the phonon probabilities are calculated for varying excitation strength. Since this single QD phonon laser device is operated in the few phonon limit ( $N$  in the order of 10), spontaneous emission relevantly contributes to the build up of the cavity phonon population. This leads to a smooth transition from thermal emission to coherent laser action.

A quantity, that is frequently used for the identification of a laser transition in the quantum regime, is the Mandel-Q parameter [Hak79]. Defined as  $Q = N(g^{(2)}(0) - 1)$ , the smallest

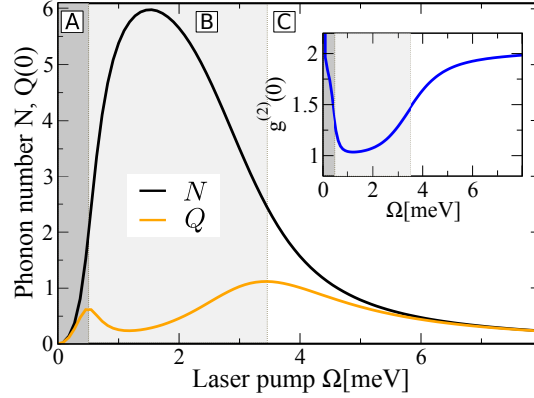


Figure 3.8.: Evolution of the average phonon number  $N$  (black curve), the Mandel- $Q$  parameter  $Q$  (yellow curve) and the phonon-phonon correlation function  $g^{(2)}(0)$  (inset: blue curve) against increasing laser pump power  $\Omega$ . In area A, the phonon laser is still operating below threshold. Within area B, there is coherent laser action. In area C, the phonon emission is in the non-lasing regime again.

deviation from a true coherent statistics is immediately reflected in the behavior of  $Q$ , thus giving a sensitive measure of the fluctuation strength relative to the field strength ( $N$ ). Vanishing for a fully coherent statistics, it is positive in the classical ( $Q > 0$ ) and negative ( $-1 < Q < 0$ ) in the quantum regime. Further,  $Q$  exhibits a qualitatively different behavior below and above threshold. Below threshold,  $Q$  is strictly monotonically in- or decreasing with a similar slope as  $N$ . In the limit of fully thermal statistics (only in the case of  $\tau = 0$ ), it even applies  $Q = N$  [Hak79]. Thus, the combined behavior of the average phonon number and the  $Q$ -parameter gives information about a possible threshold: A local maximum to  $Q$  identifies a change of the statistics, where the slope of the phonon number reveals the type of statistics the system has changed into.

Figure 3.8 shows the average phonon number  $N$  (black curve) as well as the Mandel- $Q$  parameter  $Q(0)$  (yellow curve) over varying laser pump strength  $\Omega$ . The two local maxima of  $Q$  allow for the identification of three regions (A,B,C) with qualitatively different emission properties: For small pump strengths in region A,  $N$  and  $Q$  are simultaneously increasing, meaning, that the system is operated below threshold and the emission is in the classical non-phonon-lasing regime. At the beginning of region B  $Q$  exhibits its first local maximum, while the phonon number is still increasing (characterizing the phonon laser *threshold*). Afterwards  $Q$  starts decreasing down to a minimum. This threshold denotes the onset of coherent phonon laser action. Within region B, at the minimum of  $Q$ ,  $N$  starts decreasing, but its slope is still opposing to  $Q$ . During this period, there is still a relevant fraction of coherent phonons generated within the cavity, as visible from Fig. 3.9(b) (mostly Poissonian phonon statistics). Finally, at the beginning of region C,  $Q$  exhibits a second *threshold*, from which on  $N$  and  $Q$  are now simultaneously decreasing. At higher optical laser pump powers, the system goes back the non-lasing regime and the emission is dominated by spontaneous emission (heating). The statistics is now completely thermal with  $g^{(2)}(0) = 2$  [inset to Fig.

3.8 blue curve], resulting in  $Q(0) = N(2 - 1) = N$  (Wick's theorem [Lou90]).

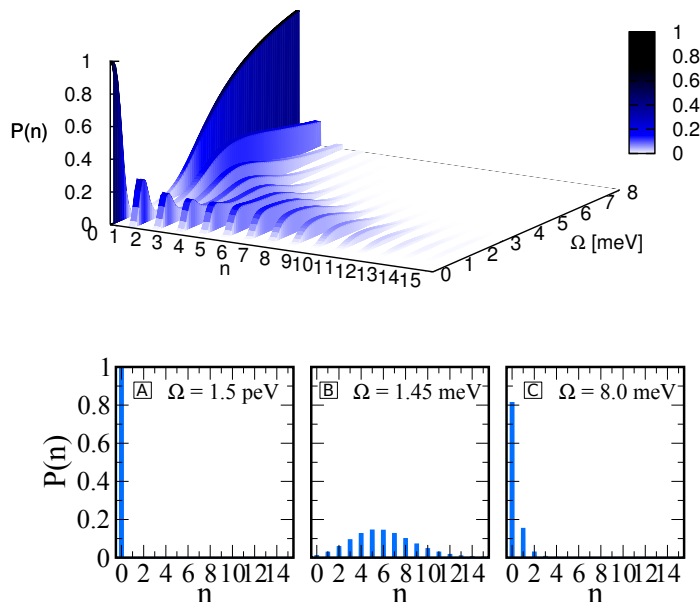


Figure 3.9.: (upper graph) Evolution of phonon number probabilities  $P_n$  over varying laser strength in the stationary regime. (lower graph)  $P_n$  at three different excitation strengths, corresponding to regions A, B and C in Fig. 3.8. Only in are B, the system exhibits a coherent statistics. Region C corresponds to a heating of the phonon system at the thermal value for  $g^{(2)}(0) = 2$ .

This behavior, typical also for a two level optical laser is called self-quenching. On the one hand, this effect is a result of the dynamical Stark shift, destroying the anti-Stokes resonance, i.e. the crucial induced Raman process is inhibited by the formation of new light-dressed states. On the other hand, the timescale of the Raman-process is now too slow, compared with the strength of the pump laser and the small phonon energy  $\hbar\omega_{ph}$ . Of course, a higher electron-phonon coupling strength  $g$  would suspend the formation of the dynamic Stark shift in favor of the induced Raman process and make phonon laser action realizable for higher pump strengths, too. For a better view on the statistics, the phonon probability distribution for three different excitation strengths, corresponding to the three operational regions ( $\Omega_A = 1.5$  peV,  $\Omega_B = 1.45$  meV and  $\Omega_C = 8.0$  meV) are additionally shown in Fig 3.9(lower graphs). A true Poissonian statistics is exhibited only within area B (snapshot at  $\Omega_B = 1.45$  meV). In area C, the statistics are back in the super-Poissonian regime (Bose-Einstein statistics), but at a higher phonon number (heating).

The key result, gained from Figs. 3.8 and 3.9 is the limited window for the generation of a coherent phonon field in this system. However, choosing  $\Omega$  in the range of  $0.7 - 3.4$  meV, lasing can be achieved for the particular parameter set (here:  $\kappa = 0.4 \frac{1}{\text{ns}}$ ,  $\Gamma_r = 10 \frac{1}{\text{ns}}$ ,

$\gamma_{pd} = 50 \frac{1}{\text{ns}}$ ). This region is of course conditioned by the specific system, which is used as a phonon source. Changing for example the phonon cavity- or the optical pump laser frequency, does considerably shift this window with the pump strength and also in its width. In a disadvantageous setting, when the onset of self-quenching turns up below the laser threshold, it can even vanish completely.

### 3.4.2. Damping and loss

Using now the knowledge from the previous paragraph about the ideal excitation regime for the chosen parameter set, the system will now be investigated according to its response towards modifying the radiative damping  $\Gamma_r$  and the phonon loss  $\kappa$ .

**Cycling parameter  $\Gamma_r$ .**— For a phonon energy  $\hbar\omega_{ph}$  sufficiently large, compared to the laser strength  $\Omega$  and the coherent linewidth  $\gamma_{pd}$  and if not deploying any other coherent or incoherent cycling mechanism, the parameter  $\Gamma_r$  closes the pump cycle for phonon lasing. In Fig. 3.10(a), the parameters are set to  $\kappa^{-1} = 500$  ps and  $\gamma_{pd} = 10$  ps, while the input-output curves are calculated for different values of the radiative damping  $\Gamma_r$ . Qualitatively, the average phonon number shows the same behavior for each value of the

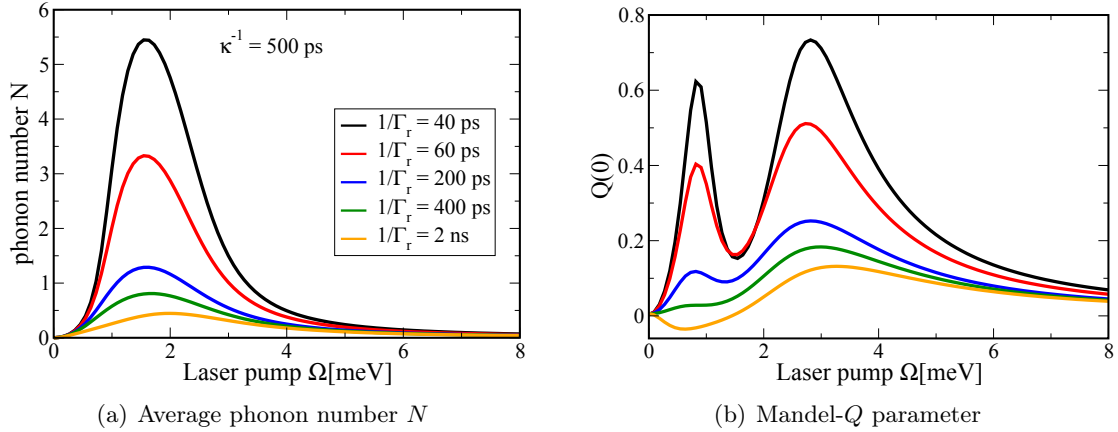


Figure 3.10.: Evolution of (a) the average phonon number  $N$  and (b) the Mandel-Q parameter  $Q$  for different strengths of  $\Gamma_r$  versus increasing laser strength  $\Omega$ . The maximum of  $N$  grows with increasing radiative decay  $\Gamma_r$ . The laser threshold (first maximum of  $Q$ ) is more pronounced at stronger  $\Gamma_r$ .

radiative constants  $\Gamma_r^{-1} = 40$  ps–2 ns. Apart from different maximum values, it increases up to  $\Omega = 1.5$  meV and decreases afterwards. However, a change in the operation is revealed by the behavior of  $Q$ , Fig. 3.10(b). For stronger radiative damping (black, red and blue curves), similar to Fig. 3.8(a),  $Q$  displays two well defined local thresholds, the first constituting the onset of the laser action and the second being the transition back into the non-lasing regime. For a damping, close to the phonon decay rate  $\kappa$ , the first threshold is close to becoming a plateau (green curve), while for a  $\Gamma_r$  significantly smaller than  $\kappa$ , the first maximum vanishes completely (yellow curve). In this case,  $Q$  becomes negative within region  $B$ , which means, that the phonon field in the cavity is mostly non-classical  $g^{(2)}(0) <$

1. This region constitutes a non-classical operational regime of the phonon laser, where the phonon system is externally pumped into a non-classical state. As the emission is stabilized, this regime is sometimes called *lasing in the quantum domain* [DRB<sup>+</sup>10]. As there is apparently no clearly visible threshold involved, this kind of lasing is thresholdless, which is a typical characteristic of a single atom (photon based) laser. In this region, the Raman induced phonon emission, emitting Fock phonons into the cavity works best. But, since the repopulation of the pump level  $|v\rangle$  through the random process  $\Gamma_r$  takes longer than the phonon loss, it plays only a minor role. The emitted phonons leave the cavity without again interacting with the QD. With higher excitation strengths, for the same reasons, as in Sec. 3.4.1, the quantum properties of the cavity phonon field are disabled, and the Raman induced emission is outpowered in favor of spontaneous emission.

**Phonon loss  $\kappa$ .** – A similar but contrary behavior is featured, when changing the phonon damping  $\kappa$  in Fig. 3.11. For a fixed radiative decay ( $\Gamma_r^{-1} = 200$  ps), the maximum phonon number decreases for increasing phonon lifetime  $\kappa^{-1}$  (from yellow to black). A noticeable difference is however, that the first threshold strongly shifts with increasing  $\kappa^{-1}$  towards smaller threshold pump powers  $\Omega_T \equiv \Omega_{Q_{max_1}}$  until it vanishes, Fig. 3.11(b) (yellow curve). In the case of the yellow curve, again, the phonon decay rate surpasses the repopulation rate of the lower QD state to such an extend, that higher phonon manifolds remain mostly unpopulated and coherent phonon generation via the induced Raman process cannot take place.

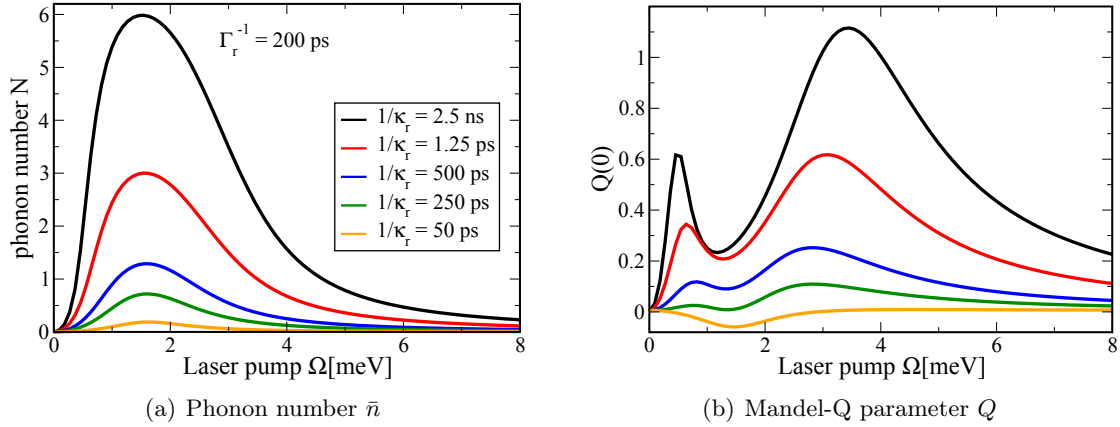


Figure 3.11.: Evolution of (a) the average phonon number  $\bar{n}$  and (b) the Mandel-Q parameter  $Q$  for different strengths of the phonon lifetime  $\kappa^{-1}$ . The maximum phonon number  $N$  is increased with growing phonon lifetime  $\kappa^{-1}$ . The threshold (first maximum of  $Q$ ) simultaneously shifts with  $\kappa^{-1}$  towards smaller pump powers  $\Omega$ . For small lifetimes  $\kappa^{-1}$ , the first threshold into lasing vanishes (orange curve).

This non-classical regime (yellow curve) of the emission is best reflected in the evolution of the inversion  $R \equiv C^{(0|0)} - V^{(0|0)}$ . It turns out, that within the phonon lasing regime (coherent) as well as the classical (thermal) regime, the inversion  $R$  has a value below zero [See also Sec. 3.5]. However, for sufficiently small cavity phonon lifetimes  $\kappa^{-1}$ , when entering

the non-classical regime, the inversion has values well above zero. Further, Fig. 3.12 shows,

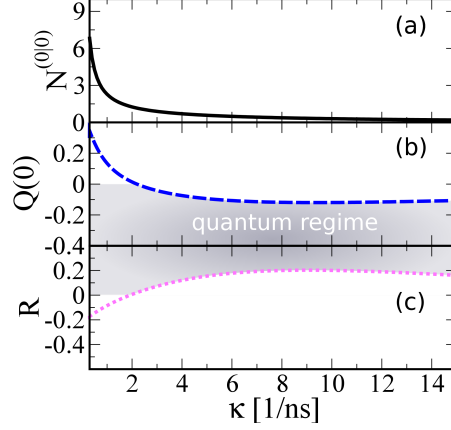


Figure 3.12.: Evolution of (a) the average phonon number (solid black curve), (b) the  $Q$ -parameter (blue dashed curve) and (c) inversion (magenta dotted curve) versus varying phonon loss rate  $\kappa$ .

that  $R$  crosses the zero simultaneously with the  $Q$ -parameter, i.e. at the point, when the phonon statistics performs the transition from the coherent into non-classical regime. The positive inversion results from exciting the QD via the induced Raman process. Recycling of phonons in the inverse process is not possible due to the high  $\kappa$ . Further,  $\Gamma_r$  is too slow in comparison to  $\kappa$ , so that the pump level (electronic ground state) does not efficiently gets populated and further interaction with the phonon field in the cavity is omitted. The coherent regime, however, requires a negative inversion  $R \leq 0$ , while a positive inversion corresponds to the quantum regime of the phonon laser.

### 3.5. Effective phonon laser

As it is now evident from the results of the previous sections, that phonon lasing is indeed possible for the proposed system, it is useful, developing a more feasible theoretical framework. Assuming the system to be operating above threshold, a factorizing approach including an effective Hamilton-operator leads to a set of equations, much easier to handle and thus fit for parameter studies and in general comparison with the full quantum mechanical case. The semiclassical (SC) approach serves as a convenient framework for a detailed analysis of the operational limits of phonon lasing. Giving access to simple analytic expressions for quantities such as the average phonon number, the threshold behavior or the maximum phonon number and their dependence on coupling constants and dissipative processes can conveniently be studied.

#### 3.5.1. Effective Hamiltonian approach

In this section, the system will be reduced only to the processes of interest, choosing a standard second order effective Hamiltonian approach. This way, certain physical processes can

be deliberately addressed, while others are neglected in a straightforward manner, already on the basis of the so derived Hamiltonian. The idea is, that the combination of the two interactions i.e, the non-diagonal electron-light plus the diagonal electron-phonon interaction, inherently involves several effective level structures, apart from just the electronic two-level system. Which one of these various effective structures is addressed, can be selected by choosing a certain excitation frequency of the external pump laser field. In order to realize a phonon laser, the system is here excited at the anti-Stokes resonance  $\Delta \approx -\omega_{ph}$ , exploiting the QD as three level  $\Lambda$ -type laser. For reducing the system to its function as a phonon laser, the effective Hamiltonian will be adjusted to this specific blue detuned excitation condition and be used for an analytic effective treatment. The effective subsystem will first serve as the basis of a semiclassical treatment and later on for an effective quantum mechanical (EQM) treatment as well.

The first step in deriving the new Hamiltonian is to write Eqs. (3.1) and (3.2) within a rotating frame  $|\psi\rangle \rightarrow U|\phi\rangle$  with the external laser field:

$$\mathcal{H}_{\text{RF}} \equiv U\mathcal{H}U^+ - i\hbar U\partial_t U^+, \quad (3.33)$$

$$U = e^{\frac{1}{\hbar}\hat{\Xi}t}|\phi\rangle, \quad \hat{\Xi} = \hbar\Omega_v|v\rangle\langle v| + \hbar\Omega_c|c\rangle\langle c| + \Omega_{ph}b^\dagger b, \quad (3.34)$$

where here,  $\Omega_v = -\Omega_c = -\frac{\omega_L}{2}$  and  $\Omega_{ph} = 0$ . Choosing this frame, the transformed Hamiltonian  $\mathcal{H}_{\text{RF}}$  is time independent apart from  $\Omega(t)$ , i.e. no rotation terms occur within the interactions.

$$\mathcal{H}_{0,\text{RF}} = -\frac{\hbar\Delta}{2}\sigma_z + \hbar\omega_{ph}b^\dagger b \equiv \frac{\hbar\Delta}{2} [|c\rangle\langle c| - |v\rangle\langle v|] + \hbar\omega_{ph}b^\dagger b, \quad (3.35)$$

$$\mathcal{H}_{I,\text{RF}} = \hbar\Omega(t)\sigma_x + \hbar g\sigma^\dagger\sigma(b^\dagger + b) \equiv \hbar\Omega(t)|v\rangle\langle c| + \hbar g|c\rangle\langle c|b^\dagger + H.c., \quad (3.36)$$

where  $\Delta = \omega_{cv} - \omega_L$  (here  $\approx -\omega_{ph}$ ) is the laser detuning from the electronic dipole transition. Now, choosing a unitary transformation  $e^{iS}\mathcal{H}e^{-iS}$  of the Hamiltonian Eqs. (3.1) and (3.2), a typical second order perturbative treatment [CT92], with

$$e^{iS}\mathcal{H}e^{-iS} \approx \mathcal{H}_{\text{eff}} = \mathcal{H}_{0,\text{RF}} + \mathcal{H}_{I,\text{RF}} + [iS, \mathcal{H}_{0,\text{RF}} + \mathcal{H}_{I,\text{RF}}] + \frac{1}{2}[iS, [iS, \mathcal{H}_{0,\text{RF}}]]. \quad (3.37)$$

is performed onto the Hamilton-Operator of Eqs. (3.35) and (3.36). The truncation to the second order of the series expansion (second order in the total combination of any coupling parameters) is justified with the coupling elements ( $\Omega/\hbar$  and  $g/\hbar$ ) being much smaller than the driving laser frequency  $\omega_L$  plus cavity phonon frequency  $\omega_{ph}$ . For eliminating any first order interaction terms, the operator  $S = S^+$  is chosen as:

$$S = \alpha|v\rangle\langle c| + \alpha^*|c\rangle\langle v| + \gamma|c\rangle\langle c|b^\dagger + \gamma^*|c\rangle\langle c|b. \quad (3.38)$$

With this, the first order term in the series expansion of Eq. (3.37) results in:

$$\begin{aligned} [iS, \mathcal{H}_0] &= i\alpha\hbar\Delta|v\rangle\langle c| - i\alpha^*\hbar\Delta|c\rangle\langle v| \\ &+ i\gamma\omega_{ph}|c\rangle\langle c|b^\dagger - i\gamma^*\omega_{ph}|c\rangle\langle c|b. \end{aligned} \quad (3.39)$$

If the prefactors in Eq. (3.38) are now chosen to be  $\alpha = \frac{i\Omega^*}{(\omega_{cv} - \omega_L)}$  and  $\gamma = \frac{ig}{\omega_{ph}}$ , the commutator  $[iS, H_0]$  can be achieved to exactly cancel with the interaction part of the Hamiltonian:

$$[iS, \mathcal{H}_0] = -\mathcal{H}_I, \quad (3.40)$$

$$\text{and thus } [iS, [iS, \mathcal{H}_0]] = -[iS, \mathcal{H}_I]. \quad (3.41)$$

The remaining terms of this second order expansion then only involve the free part  $\mathcal{H}_0$  and the commutator with the interaction part of the original Hamiltonian:

$$\begin{aligned} \mathcal{H}_{\text{eff}} &= \mathcal{H}_0 + \frac{1}{2}[iS, \mathcal{H}_I] \\ &= \hbar\left(\frac{\Delta}{2} + \frac{|\Omega|^2}{\Delta} - \frac{g^2}{\omega_{ph}}\right)|c\rangle\langle c| + \hbar\left(\frac{\Delta}{2} - \frac{|\Omega|^2}{\Delta}\right)|v\rangle\langle v| \\ &\quad - \hbar\left(\frac{1}{\Delta} - \frac{1}{\omega_{ph}}\right)\left[\frac{\Omega^*g}{2}|v\rangle\langle c|b + \frac{\Omega g}{2}|c\rangle\langle v|b^\dagger\right] \\ &\quad - \hbar\left(\frac{1}{\Delta} + \frac{1}{\omega_{ph}}\right)\left[\frac{\Omega^*g}{2}|v\rangle\langle c|b^\dagger + \frac{\Omega g}{2}|c\rangle\langle v|b\right]. \end{aligned} \quad (3.42)$$

Note, that at zero-detuning  $\Delta = 0$  of the laser, there does not arise an actual singularity. The terms leading to the denominators  $\frac{1}{\Delta}$  would already vanish within the original Hamiltonian in Eq. 3.35. In the next step the blue detuned excitation situation, as introduced in Sec. 3.2 with respect to phonon lasing, is used for further simplification of the effective Hamiltonian. Under the chosen excitation condition, where  $\Delta \approx -\omega_{ph}$  the prefactor of the last term in (3.42) gets really small. Further, it states a fast rotating term with frequency  $\omega_L - \omega_{cv} + \omega_{ph} \approx 2\omega_{ph}$  and is therefore neglected. In contrast, the second row, corresponding to an energy conserving process  $\omega_L - \omega_{cv} - \omega_{ph} \approx 0$  and the first row, which is diagonal with respect to the electronic system are kept, so that the new  $\mathcal{H}_{\text{eff}}$  reduces to:

$$\mathcal{H}_{0,\text{eff}} = \hbar\tilde{\omega}|c\rangle\langle c| + \hbar\omega_{ph}b^\dagger b \equiv \hbar\tilde{\omega}\sigma^\dagger\sigma + \hbar\omega_{ph}b^\dagger b, \quad (3.43)$$

$$\mathcal{H}_{I,\text{eff}} = \hbar g_{\text{eff}}\left(|c\rangle\langle v|b^\dagger + |v\rangle\langle c|b\right) \equiv \hbar g_{\text{eff}}\sigma^\dagger b^\dagger + H.c., \quad (3.44)$$

with the coupling strength of the effective subsystem  $g_{\text{eff}}$  and the detuning frequency  $\tilde{\omega}$ , renormalized with light- and phonon-related frequency-shifts (Stark- and Polaron shift):

$$g_{\text{eff}} = -\frac{\Omega g}{2}\left(\frac{1}{\Delta} - \frac{1}{\omega_{ph}}\right), \quad (3.45)$$

$$\tilde{\omega} = \Delta + \frac{2\Omega^2}{\Delta} - \frac{g^2}{\omega_{ph}}. \quad (3.46)$$

The effective system now rotates with  $\tilde{\omega}$ . Within the above approximations, disregarding the second row of Eq. (3.42), the new effective Hamiltonian in (3.44) is now restricted to the specific excitation condition. It is necessary to remember, that it can only adequately describe the systems behavior and dynamics, if optically driving the system at the anti-

Stokes resonance. The effective coupling element  $g_{\text{eff}}$  selects now only the induced phonon emission process. Processes, resonant with the band gap energy or Stokes processes are not included. If exciting the system at another frequency position, these processes would gain in relevance and either the full effective Hamiltonian Eq. (3.42) or an otherwise adjusted Hamiltonian is to be derived. Here, however, induced phonon emission is supposed to be dominant, so that  $\mathcal{H}_{\text{eff}}$  can be assumed to be valid within a certain range of parameters.

### 3.5.2. Effective spontaneous emission

At first sight, the right-hand side of Eq. (3.44) appears to describe a non-energy conserving process, in particular if comparing it with the interaction part of the Jaynes Cummings Hamiltonian, Eq. (2.30). However, in this effective subsystem (without dissipations included), the upper state  $|c\rangle$  plays the role of the ground state  $|v\rangle$  and vice versa, as illustrate by Fig. (3.13). Deriving the equations of motion for the case of an initially empty phonon cavity, results in a set of equations, similar to the JCM [See App. A.2]. The inversion (here

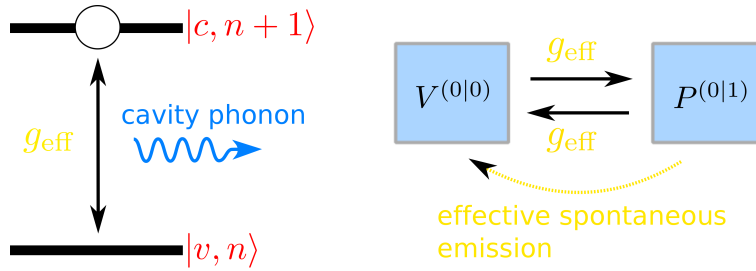


Figure 3.13.: Effective subsystem as described by the Hamiltonian in Eq. (3.44). The system emits a phonon via *effective spontaneous emission*, while passing into the upper state  $|c\rangle$ , i.e. it effectuates an inverse Jaynes-Cummings model, where  $|v\rangle$  represents the excited state and  $|c\rangle$  the ground state.

$R_{\text{eff}} = V^{(0|0)} - N^{(1|1)}$  is then simply given by the JCM-solution  $R_{\text{eff}}(t) = \cos(2g_{\text{eff}}t)$  according to App. A.2. However, here, the emission of a phonon takes place, while the electron is being transferred from the lower QD level into the upper state. This behavior was already presented in Sec. 3.3 in Fig. 3.3 on the basis of the full quantum (FQ) model, where the ground state density  $V^{(0|0)}$  and the phonon density  $N$  perform symmetric Rabi-oscillations. Due to the effective coupling, the ground state *spontaneously* decays into the upper state under the emission of a cavity phonon. However, here, the *effective spontaneous emission process* requires a higher order interaction path (second order in the effective coupling) involving the external laser field [See Fig. 3.13]. In total, this is a fourth order interaction process, including a second order interaction with each the phonon system as well as the external laser field.

### 3.5.3. Semiclassical limit of the effective phonon laser equations

In the following, the derived effective Hamiltonian Eq. (3.42), which is reduced to the induced Raman process will be used to derive the semiclassical limit of the phonon laser

equations. The aim is to gain simple analytic expressions for the input-output curves or estimates for the threshold behavior for this kind of phonon laser.

For the SC treatment, it is postulated, that phonon lasing is indeed possible and Poissonian phonon statistics are established within the acoustic cavity. Therefore, it can be assumed, that the expectation values of the phonon annihilation and creation operators  $N^{(0|1)} = \langle b \rangle$ ,  $N^{(1|0)} = \langle b^\dagger \rangle$  actually have nonzero values. These quantities will in the following be interpreted as the (classical) phonon field amplitudes. Using the same notations as in the previous sections and applying Heisenberg's EOM with the effective Hamiltonian in Eqs. (3.43),(3.44) and (3.3) results in

$$\dot{N}^{(0|1)} = -[i\omega_{ph} + \kappa]N^{(0|1)} - ig_{\text{eff}}P^{(0|0)*}, \quad (3.47)$$

$$\dot{P}^{(0|0)*} = [i\tilde{\omega} - \gamma]P^{(0|0)*} - ig_{\text{eff}}^*[C^{(0|1)} - V^{(0|1)}], \quad (3.48)$$

with  $\gamma := \Gamma_r + \gamma_{pd}$ . Due to the simple form of  $\mathcal{H}_{\text{eff}}$  the phonon field amplitude is driven solely by the polarization  $P^{(0|0)*} = \langle |c\rangle\langle v| \rangle$ . Just like Eqs. (3.22) - (3.24), the effective equations do not automatically close due to the quantum character of the effective interaction. Either a perturbative treatment, such as the inductive method, a recursive approach or further approximations have to be applied. Here, this problem will be addressed by presupposing a truly coherent phonon field and thus justifying the factorization of expectation values with respect to electronic and phononic operators [Hak94, CT92]. This procedure leads to a set of three phonon laser equations:

$$\dot{B} = [-i\omega_{ph} - \kappa]B - ig_{\text{eff}}P, \quad (3.49)$$

$$\dot{P} = [i\tilde{\omega} - \gamma]P - ig_{\text{eff}}RB, \quad (3.50)$$

$$\dot{R} = -2\Gamma_r(1 + R) + i2g_{\text{eff}}(P^*B - PB^*). \quad (3.51)$$

Since in this factorizing approach, higher order phonon correlations will not occur, the following abbreviations for the phonon amplitude, the polarization and the inversion have been introduced for convenience:

$$B \equiv N^{(0|1)}, \quad P \equiv P^{(0|0)*}, \quad R \equiv C^{(0|1)} - V^{(0|1)}. \quad (3.52)$$

In accordance with the functionality of the electronic polarization in this effective Jaynes-Cummings system, the conjugate of the polarization  $P^{(0|0)*}$  is chosen to be abbreviated as  $P$  in Eq. (3.52).

With this, Eqs. (3.49)-(3.51) formally strongly resemble the typical laser equations for an incoherently pumped two level laser [Hak94, MS92, ADG90, Gar11]. However, there are also crucial differences. As discussed before, the pump frequency, matching the phonon-frequency combined with the diagonal electron-phonon coupling is realizing a three-level  $\Lambda$ -type laser [Hak94, MBW97, DRB<sup>+</sup>10]. Within this pump- and electronic level structure, the lower state  $|v\rangle$  constitutes the pump level. From this state, the electronic density is coherently driven into the upper state  $|c\rangle$ , which here constitutes the lower laser level. Due to the laser pump being tuned in resonance with the anti-Stokes frequency  $\omega_{cv} + \omega_{ph}$ , the virtual intermediate phonon assisted excited state actualizes the upper laser level, cp

Fig. 3.7. As discussed before, the pump cycle is closed by the radiative decay  $\Gamma_r$ , which subsequently recreates the population in the pump level. Note, that compared to the single atom optical laser equations, in (3.49)-(3.51) the two electronic states play reversed roles. This means: Instead of being just a source of decoherence, that is destroying laser efficiency,  $\Gamma_r$  feeds the phonon field. Further, phonon lasing does not take place between the optical transition  $|v\rangle \rightarrow |c\rangle$ , so that  $\Gamma_r$  does not have the negative effect of decoherence. On the contrary, it leads to the refilling of the pump state and thus creates the basis of coherent phonon laser action.

### 3.5.4. Semiclassical Model in the Stationary Limit

In the following, the SC phonon laser equations will be treated and solved within the stationary limit. The goal is, to analyze the phonon laser with respect to its input-output-, the threshold behavior and the influence of losses and decoherence. Thus, the equations will be solved for the cavity-phonon number, which can be defined as

$$N \equiv B^*B = \langle b^\dagger \rangle \langle b \rangle. \quad (3.53)$$

for the classical coherent case. Due to the balance of pumping the system and the adverse effects of losses, the system is assumed to saturate within a steady state. The time derivatives in Eqs. (3.49)-(3.50) are set to zero. On the basis of Eq. (3.49) the phonon amplitude  $B \rightarrow Be^{-i\omega t}$  and the polarization  $P \rightarrow Pe^{i\omega t}$  are assumed to rotate with the same frequency  $\omega$ , where this output laser frequency  $\omega$  is still to be determined. With this, Eqs. (3.49)-(3.51) reduce to:

$$B = -\frac{ig_{\text{eff}}P}{[i(\omega_{ph} - \omega) + \kappa]}, \quad (3.54)$$

$$P = -\frac{ig_{\text{eff}}RB}{[-i(\tilde{\omega}(\Omega) + \omega) + \gamma]}, \quad (3.55)$$

$$2\Gamma_r(1 + R) = i2g_{\text{eff}}(P^*B - PB^*). \quad (3.56)$$

Due to their similarities, the same procedure of solution, known from the optical laser equations [Hak93] can be adopted here. Inserting first Eq. (3.55) into Eq. (3.56) results in:

$$2\Gamma_r(1 + R) = -2|B|^2 R \underbrace{\frac{2\gamma g_{\text{eff}}^2}{[(\tilde{\omega}(\Omega) + \omega)^2 + \gamma^2]}}_{\equiv W}, \quad (3.57)$$

$$\Rightarrow R = -\frac{\Gamma_r}{\Gamma_r + 2NW(\Omega)}. \quad (3.58)$$

From the expression in Eq. (3.58) it can be seen, that the inversion  $R$  is always negative and converges to  $R \rightarrow 0$  for the high phonon number limit  $N \rightarrow \infty$ . This prediction agrees

with the findings in Sec. 3.4.1 and the considerations within the previous paragraph. Inserting this expression for  $R$  back into Eq. (3.55) and subsequently into Eq. (3.54) gains

$$P = \frac{ig_{\text{eff}}\Gamma_r B}{[-i(\tilde{\omega} + \omega) + \gamma](\Gamma_r + 2NW(\Omega))}, \quad (3.59)$$

$$\Rightarrow B[i(\omega_{ph} - \omega) + \kappa] = \frac{g_{\text{eff}}^2 \Gamma_r B [i(\tilde{\omega} + \omega) + \gamma]}{[(\tilde{\omega} + \omega)^2 + \gamma^2](\Gamma_r + 2NW(\Omega))}. \quad (3.60)$$

Equation (3.60) can be divided by  $B$  assuming that the system is operating above threshold and therefore  $B$  has a non-zero value. This equation then gives on the one hand an expression for the phonon number  $N$ , as well as the resulting parameter dependent phonon laser frequency  $\omega$ .

### 3.5.4.1. Phonon number

Forming the real part of Eq. (3.60) results in

$$\kappa = \frac{\Gamma_r}{(\Gamma_r + 2NW(\Omega))} \frac{g_{\text{eff}}^2 \gamma}{[(\tilde{\omega} + \omega)^2 + \gamma^2]} = \frac{\Gamma_r}{(\Gamma_r + NW(\Omega))} \frac{W}{2}. \quad (3.61)$$

Rearranging this equation finally gives the explicit expression for the average phonon number:

$$N = \frac{\Gamma_r}{2\kappa_r W(\Omega)} (W(\Omega) - 2\kappa). \quad (3.62)$$

This formula is valid as long as  $N > 0$ , meaning that the system is operating within the phonon lasing regime. Obviously,  $N$  can formally get negative or zero. This is, when the expression in the brackets  $(W(\Omega) - 2\kappa) \leq 0$ , i.e. the phonon decay rate is sufficiently large, so that the function  $W \leq 2\kappa$ . Combining Eqs. (3.58) and (3.62), the maximum phonon number for a certain parameter set can be given by:

$$N = (R + 1) \frac{\Gamma_r}{2\kappa} \longrightarrow \frac{\Gamma_r}{2\kappa} \equiv N_{\text{max}}, \quad (3.63)$$

as according to Eq. (3.51), the maximum value of  $R$  is zero for higher phonon numbers.

### 3.5.4.2. Laser frequency

Before analyzing the threshold behavior of the system, the laser frequency  $\omega$  is determined by forming also the imaginary part of Eq. (3.60) and using Eq. (3.62) [Hak94]:

$$(\omega_{ph} - \omega) = \frac{\Gamma_r (\tilde{\omega} + \omega) W(\Omega)}{2\gamma (\Gamma_r + NW(\Omega))} \quad (3.64)$$

$$\stackrel{(3.62)}{=} \frac{\kappa}{\gamma} (\tilde{\omega} + \omega). \quad (3.65)$$

Rearranging this equation gives an explicit expression for the phonon laser frequency:

$$\omega = \frac{\omega_{ph} - \frac{\kappa}{\gamma} \tilde{\omega}}{1 + \frac{\kappa}{\gamma}} \approx \omega_{ph}, \quad (\kappa \ll \gamma). \quad (3.66)$$

Obviously, the phonon laser frequency  $\omega$  does not necessarily match the frequency of the acoustic cavity mode  $\omega_{ph}$ . Through  $\tilde{\omega}(\Omega)$ , it is even a function of the pump. Only in the case of small ratios  $\frac{\kappa}{\gamma}$ ,  $\omega$  can be assumed to approximately be  $\omega_{ph}$ . As will be discussed later, the laser condition  $(W(\Omega) - 2\kappa) > 0$  requires a sufficiently small ratio  $\frac{\kappa}{\gamma}$ , anyway. It is therefore safe to assume, that for a large range of pumping strengths, the acoustic cavity frequency approximately matches the output laser frequency. For the following considerations towards the threshold behavior of the phonon laser, setting  $\omega = \omega_{ph}$  is justified.

### 3.5.4.3. Threshold behavior

Starting from equation (3.62), the phonon lasing condition reads [Hak94]:

$$W(\Omega) - 2\kappa \stackrel{!}{\geq} 0. \quad (3.67)$$

Thus, the laser threshold can be determined by calculating the roots of Eq. (3.67). Due to the pump dependencies in Eqs. (3.45) and (3.46) in total,  $N$  has a quartic dependence on  $\Omega$ :

$$g_{\text{eff}}^2(\Omega) \stackrel{!}{=} \frac{\kappa}{\gamma} \left[ (\bar{\omega} + \frac{2\Omega^2}{\Delta})^2 + \gamma^2 \right] \quad \text{with} \quad \bar{\omega} \equiv \Delta - \frac{g^2}{\omega_{ph}} + \omega_{ph}. \quad (3.68)$$

Here, the frequency  $\bar{\omega}$  was introduced, giving the deviation of the optical pump laser frequency  $-\omega_L$  towards the polaron shifted resonance  $\omega_{cv} - \frac{g^2}{\omega_{ph}}$  from the actual phonon laser frequency  $\omega = \omega_{ph}$ . This detuning will turn out to have a great impact on the position of the threshold. It will be assumed to have a small yet finite value and be adjusted towards the best laser output.

Apart from  $\bar{\omega}$ , also the effective coupling strength  $g_{\text{eff}}$  is a function of the pump  $\Omega$  and Eq. (3.67) becomes negative also for higher pumping strengths. This root constitutes the second threshold back to the non-lasing regime. In total, Eq. (3.67) has four roots, while two of them are negative and therefore to be neglected for these considerations. The other two roots represent the two thresholds of this phonon laser:

$$T_{\mp} = \left[ \mathcal{G} \pm \sqrt{\mathcal{G}^2 - \Delta^2(\bar{\omega}^2 + \gamma^2)} \right]^{\frac{1}{2}}, \quad (3.69)$$

with

$$\mathcal{G} = \frac{g^2 \gamma \Delta^2}{8\kappa D^2} - 2\bar{\omega} \Delta \quad \text{and} \quad D = \left( \frac{1}{\omega_{ph}} - \frac{1}{\Delta} \right)^{-1}. \quad (3.70)$$

Thus, the position of the two thresholds, which together enclose the phonon lasing pump power interval  $[T_-, T_+]$ , depends on the various system parameters. The phonon lasing regime shifts, broadens or shrinks with the different damping  $\kappa$  and  $\Gamma_r$ , the decoherence

$\gamma_{pd}$  as well as the electron-phonon coupling strength  $g$ . Further, the thresholds strongly depend on the detuning of the exciting laser field  $\Delta$  (contained in  $\bar{\omega}$ ) and the phonon frequency  $\omega_{ph}$ . Of course, the detuning always has to be in the range of  $\Delta \approx -\omega_{ph}$ . However, the origin of the existence of a second threshold, and thus for the termination of phonon lasing, is the term  $\frac{2\Omega^2}{\Delta}$  in the effective Hamiltonian (3.43). As described before, this term results in a quartic dependence on  $\Omega$  in Eq. (3.67). Abandoning this term in Eqs. (3.54)-(3.55) would eliminate the second threshold  $T_+$  and results in a phonon number, given by the simple expression:

$$N = \frac{\Gamma_r}{2} \left( \frac{1}{\kappa} - \frac{\bar{\omega}^2 + \gamma^2}{\gamma g_{\text{eff}}^2} \right) \longrightarrow \frac{\Gamma_r}{2\kappa}, \quad (\Omega \rightarrow \infty). \quad (3.71)$$

For high pump strengths  $\Omega$ , the phonon number  $N$  just saturates at the maximum phonon number  $\frac{\Gamma_r}{4\kappa}$ . Note, that this scenario is only realistic, if the ratio  $\frac{\kappa}{\gamma}$  is sufficiently small due to long phonon lifetimes. In this case, the first threshold  $T_-$  occurs at lower pump strength  $\Omega \ll \Delta$ , the quenching is postponed and the term  $\frac{2\Omega^2}{\Delta}$  can be dismissed in Eq. (3.62). The laser threshold  $T_-$  then simplifies into:

$$T_- = \sqrt{\frac{4\kappa \omega_{ph}^2}{\gamma g^2} (\bar{\omega}^2 + \gamma^2)}. \quad (3.72)$$

Knowing, that the laser detuning is about  $\Delta \approx -\omega_{ph}$ , this formula can further be reduced and evaluated to

$$T_- = g \sqrt{\frac{4\kappa}{\gamma} \left( 1 + \frac{\omega_{ph}^2 \gamma^2}{g^4} \right)} \longrightarrow g \sqrt{\frac{4\kappa}{\gamma}}, \quad (g \gg \gamma \omega_{ph}). \quad (3.73)$$

Especially in the case of strong electron-acoustic cavity couplings, the laser threshold goes approximately linear with  $g$ . The system enters the phonon lasing regime the earlier, the smaller the ratio of  $\frac{\kappa}{\gamma}$ . Note, that Eqs. (3.71)-(3.73) are only valid in the many phonon regime, while Eqs. (3.62)-(3.69) also apply in the limit of few phonons. In order to prevent from the self-quenching behavior of the phonon laser, predicted by Eq. (3.69), one could try to eliminate the term  $\frac{2\Omega^2}{\Delta}$  by tuning parameters. Besides the optical laser pump strength  $\Omega$ , the only truly tunable parameter is the pump laser frequency  $\omega_L$ . For eliminating the self-quenching term from Eq. (3.55), the pump laser frequency has to be tuned together with the pump strength:

$$\omega_L \approx \frac{2\Omega^2}{\omega_{ph} + \frac{2\Omega^2}{\omega_{ph} + \dots}}. \quad (3.74)$$

Unfortunately, also  $g_{\text{eff}}$  is a function of  $\omega_L$  [see Eq. (3.45)], so that the laser turn-off cannot be suspended totally. Although, the behavior of formula Eq. (3.71) can be mimicked for a while, the beneficial effect is of minor impact, as the phonon number will still saturate [See Eqs. (3.63) and (3.71)]. The main advantage is probably the possibility of shifting the

first threshold (onset of phonon laser action) to lower pump powers by the simultaneous tuning of  $\Omega$  and  $\omega_L$  according to Eq. (3.74).

### 3.5.5. Comparison of the analytics with the full quantum model: – Input-output behavior

In order to estimate the validity of the effective SC model, it will first be benchmarked at the full quantum model (FQ) of the previous section. We focus on the stationary limit. For one, as the SC model can only describe coherent phonon populations, the two models can only be expected to agree within the phonon lasing regime. Nevertheless, the two models can for example be compared towards the predicted threshold behavior and dependencies on the different system parameters. They should exhibit a good coincidence within the lasing regime of the FQ model.

At first, in Fig. 3.14(a) the evolution of the phonon number  $N$  is plotted versus varying excitation strength (Rabi-Energy  $\Omega_R = 2\hbar\Omega$ ). The solid curve results from Eqs. (3.62)-(3.51) (SC model) and the dashed curve illustrates the results of Eqs. (3.22)-(3.24) (FQ model). Further, Fig. 3.14(a) shows the evolution of the Mandel-Q parameter  $Q = N(g^{(2)}(0) - 1)$ ,

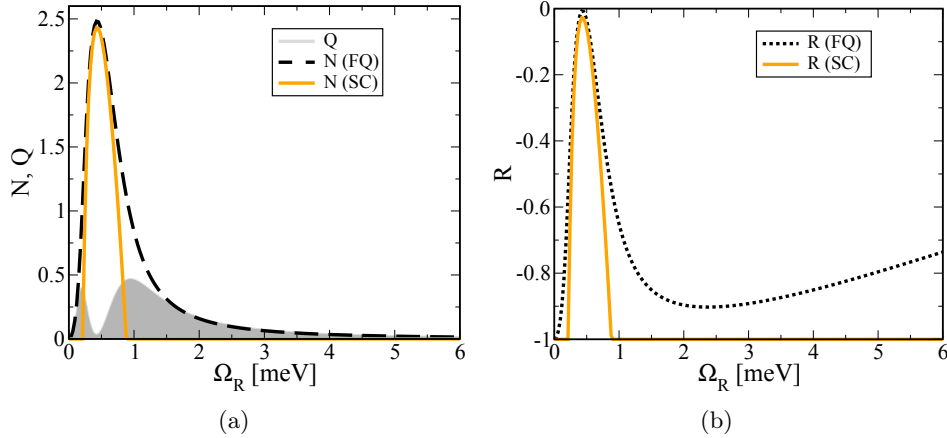


Figure 3.14.: Input-output behavior of the system: (a) The solid and the dashed curves show the phonon number  $N$  for the SC (orange solid) and the FQ model (black dashed curve), together with the Mandel- $Q$  parameter (shaded area). (b) Evolution of the inversion  $R$ . Here,  $\Gamma^{-1} = 200$  ps,  $\gamma_{pd} = 0.0 \frac{1}{\text{ns}}$  and  $\kappa^{-1} = 1$  ns. For both models,  $N$  exhibits self-quenching for larger  $\Omega$ . In (b), the inversion  $R$  illustrates an additional recovery only for the FQ model due to quasi resonant excitation  $\Omega_G \approx \omega_{ph}$ .

which indicates the thresholds by its local maxima for the FQ model. As presumed for the SC model,  $N$  (solid curve) stays zero until a critical pump value  $T_-$  [See Eq. (3.69)]. Within the pump interval  $T_- < \Omega_R < T_+$ , the phonon number grows almost up to the value of  $N_{\max}$  (here  $N_{\max} = 2.5$ ). Afterwards it begins to decrease and drops to zero again at  $\Omega_R = T_+$ . Within this regime, there is a very good agreement between the SC and the FQ model. However, in comparison to the SC model, the phonon number, calculated

with the FQ model (dashed curve) provides a more smooth transition from the non-lasing into the lasing regime and vice versa. Especially for strong excitation strengths  $\Omega_R > T_+$ , the dashed curve approaches zero only gradually. In this regime,  $N$  corresponds to a hot phonon population, indicated by the simultaneous slope of  $N$  and  $Q$ . A remarkably good agreement can be observed for the positions of the two thresholds. Both the laser threshold  $T_-$ , indicated by the first local maximum of  $Q$  and the laser switch-off  $T_+$  (indicated by the second local maximum of  $Q$ ) occur almost perfectly at the same pump powers. Also the maximum values of  $N$ , calculated by the different models are equally positioned.  $N_{\max}$  coincides with the local minimum of  $Q$ , introducing the self-quenching regime of the phonon laser. As discussed in the previous sections, this self-quenching behavior is due to the optical Stark shift. It is inflicted to the system by the strong laser pump powers and therefore inhibits the induced Raman process. For the SC model this means, that there is a loss of coherence between the two levels  $|v, n\rangle$  and  $|c, n+1\rangle$ .

According to formula Eq. (3.63), phonon lasing comes along with an inversion of  $R < 0$ . This inversion has to be created via the induced Raman process (FQ model). Inversions  $R < 0$  however, generated via resonant excitation (at band gap frequency  $\omega_{cv}$ ) do not indicate phonon lasing. In Fig. 3.14(b), the evolution of the inversion  $R$  is depicted as calculated with the two models. Same as the phonon number,  $R$  is quenched by the frequency shift  $\frac{2\Omega^2}{\Delta}$  for higher pump powers. In the case of the SC model, where any existing inversion  $R$  is due to the induced Raman process, (resonant processes were eliminated on the basis of the effective Hamiltonian Eq. (3.42)), the inversion simultaneously increases, then decreases and drops to zero with  $N$  [Fig. 3.14(a)]. The inversion, calculated with the FQ model shows a different behavior for larger  $\Omega_R$ . Fig. 3.14(b) nicely portrays the two different causes for a creation of an inversion  $R < 0$ . Within the phonon lasing regime,  $R$  clearly has to be created within the Raman process, so that coherent phonons can be generated. Beyond this regime, i.e. for higher excitation strengths ( $2\Omega \approx (\omega_{ph} - \frac{g^2}{\omega_{ph}})$ ), the external laser is strong enough to bridge the cavity phonon frequency  $\omega$ . Due to the finite radiative decay  $\Gamma_r$ , the electronic dipole resonance is broadened and the optical drive excites the system on resonance  $\omega_{cv}$ . Therefore, the inversion  $R$  is not just decreasing again, as in the SC case, but instead increases. Phonon lasing, however, still remains inhibited, as  $R < 0$  is not created by induced Raman (the effective coupling  $g_{\text{eff}}$ ) and does not involve coherent phonon generation according to Eq. (3.63).

### 3.5.6. Influence of pure dephasing

In the case of the optical two level laser, a pure dephasing of the optical laser resonance causes decoherence and termination of the laser activity. In this section, it will be investigated, what are the effects of a finite pure dephasing in the case of the phonon laser. It is obvious, from Eq. (3.62) and (3.69), that the phonon number and the positions of the two thresholds among others, also depends on the pure dephasing  $\gamma_{pd}$ .

Figure 3.15 shows the phonon number  $N$  (solid curves for the SC- and dashed curves for the FQ model) together with the  $Q$ -parameter (grey shaded area) versus varying laser strength for different values of the pure dephasing. According to the SC model, a finite pure dephasing has a beneficial effect towards phonon lasing as it prolongs the lasing interval

$T_- < \Omega_R < T_+$ . Up to an intermediate pure dephasing, as it is the case in typical semiconductor QDs (for example InGaAs) [BLS<sup>+</sup>01, KAK02], this feature of the phonon laser is also confirmed for the FQ-model. In both models it applies: The window for coherent

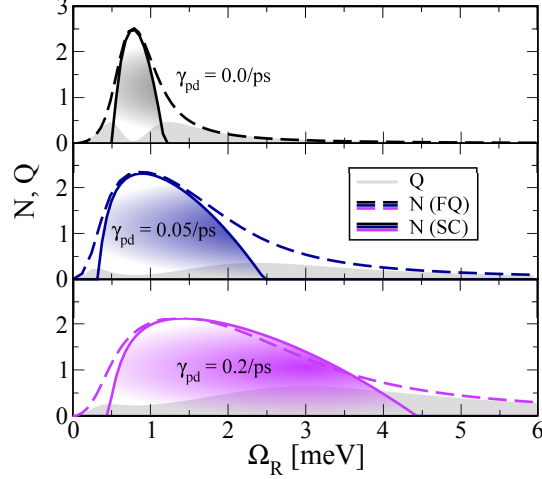


Figure 3.15.: Evolution of  $N$  and  $Q$  (grey shaded area) over varying laser pumping strength and different values of the pure dephasing.  $\gamma_{pd} =$  (a) 0/ps (black curves), (b) 0.1/ps (blue curves) and (c) 0.5/ps (violet curves) as calculated by the FQ (dashed curves) and the SC (solid curves).  $1/\Gamma_r = 200$  ps and  $1/\kappa = 1$  ns. The lasing window is predicted to grow with the pure dephasing.

phonon generation (phonon lasing regime) is the smallest for a vanishing pure dephasing  $\gamma_{pd} = 0$  with the kink in the evolution of the  $Q$ -parameter being the most pronounced. A finite pure dephasing enhances the phonon lasing regime, due to a broadening of the resonance. This broadening effect of the pure dephasing competes with the frequency shift  $\frac{2\Omega^2}{\Delta}$ , which brings the system out of resonance with the anti-Stokes process, being the foundation of this kind of phonon lasing. Due to  $\gamma_{pd}$ , the resonance with this process is preserved for a larger interval of the pumping strengths  $\Omega$ , thus extending the phonon lasing regime.

According to the FQ description, however, the beneficial effect of the pure dephasing has its limits, since it will eventually allow for the resonant excitation of the QDs bare electronic transition [Fig. 3.15(c), violet curve]. Although, the maximum phonon number is conserved for the high pure dephasing, there is a loss in coherence of the statistics. This is reflected in the behavior of the  $Q$ -parameter, now exhibiting only a small bump and weaker slope, instead of a decrease at the predicted phonon laser threshold  $T_-$ . Further, Fig. 3.16, nicely shows, that a too strong pure dephasing will result in a broadening of the phonon statistics. Obviously, the phonon probability distribution in Fig. 3.16(c) does not correspond to a truly Poissonian statistics anymore. Although, it exhibits typical coherent features, in parts it is broadened with respect to a Poissonian distribution (high phonon number  $N$  at a maximum phonon number probability  $P(n)$  at  $N = 0$  indicating a super-Poissonian distribution).

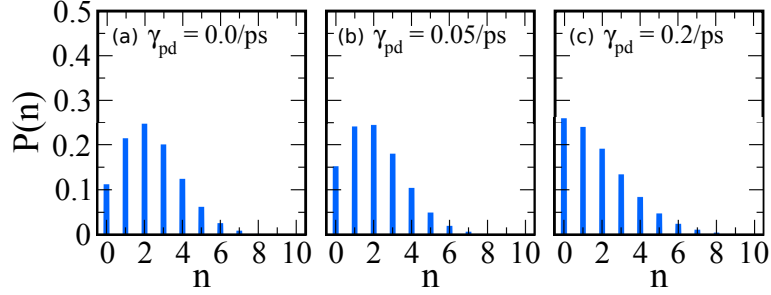


Figure 3.16.: Snapshots of the phonon probability distribution  $P(n)$  at different values  $\gamma_{pd} =$  (a)  $0.0/\text{ps}$ , and (b)  $0.05/\text{ps}$  and (c)  $0.2/\text{ps}$ . The radiative dephasing is set to  $1/\Gamma_r = 200\text{ps}$  and the photon loss is  $1/\kappa = 1\text{ns}$ . A pure dephasing leads to a broadening of the statistics (SuperPoissonian statistics).

The use of the effective model and Eqs. (3.50)-(3.62) is of course not always justified, but is reasonable in the case of an either intermediate pure dephasing or in exchange at a larger phonon frequency, i.e., if resonant excitation of the electronic transition can mainly be excluded.

### 3.5.7. Influence of phonon- and radiative decay

Naturally, the phonon laser activity strongly depends on the phonon lifetime  $\kappa$  and the cycling parameter  $\Gamma_r$ . The dependence of the phonon laser thresholds  $T_{\mp}$  is given by the prefactor  $W(\Omega) - 2\kappa = 0$ . As mentioned before, this equation has a quartic dependence on  $\Omega$ , resulting in a nonlinear behavior of the threshold versus the phonon decay rate. Furthermore, Eqs. (3.70) and (3.73) reveal, that the threshold into lasing occurs the earlier, the smaller the ratio  $\frac{\kappa}{\Gamma_r}$ . Besides the laser threshold, Eq. (3.70) can also map the width of the lasing regime.

In Fig. 3.17 the evolution of  $N$  (inset) and the thresholds  $T_{\mp}$  is depicted versus varying (a)  $\kappa$  and (b)  $\Gamma_r$ . In the case of the phonon number, the excitation strength is kept fixed at a value  $2\Omega = \frac{(T_- + T_+)}{2}$ , corresponding approximately at the pump position, where  $N_{\max}$  is realized. Obviously, the laser threshold  $T_-$  (solid curve) shifts with  $\kappa$  towards higher excitation strengths Fig. 3.17, while the laser switch-off  $T_+$  occurs at lower pump powers. This means, that the area for phonon lasing, which is enclosed by the two thresholds  $T_{\mp}$  decreases, and converges to zero with  $\kappa$ . Since  $\kappa$  is the inverse lifetime of the phonons inside the cavity, increasing its value results in a less efficient generation of coherent phonons. Phonons leave the cavity before having the possibility of again interacting with the system. The overall cavity phonon statistics can then be expected to be non-classical [See discussion to Fig. 3.12].

However, changing the value of the radiative decay  $\Gamma_r$  has a rather different effect, Fig. 3.17(b). In contrast to the dependence on  $\kappa$ , increasing  $\Gamma_r$  results also in an increase of the phonon number and delay of the self-quenching. As,  $\Gamma_r$  effectuates the repopulation of the electronic pump level  $|v\rangle$ , stronger values lead to a improved efficiency of the phonon laser. For strong radiative decay rates  $\Gamma_r$ , Eqs. (3.69) and (3.71) predict a regime, where the

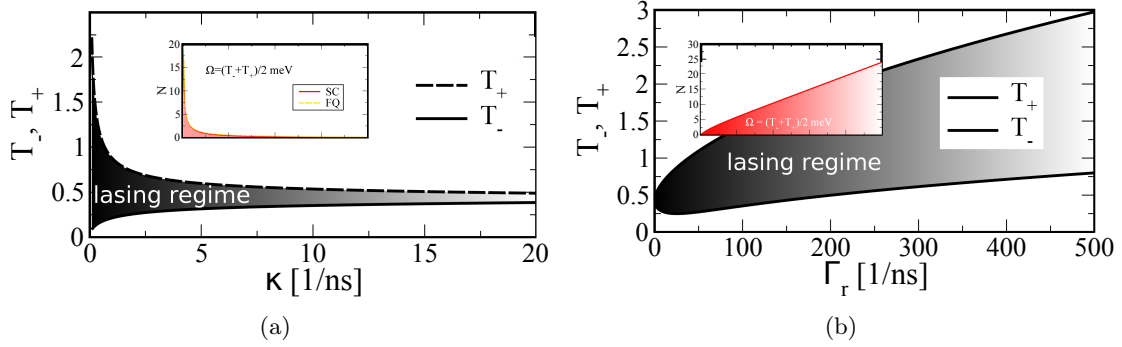


Figure 3.17.: Evolution of  $N$  (inset) and the two thresholds  $T_-$  and  $T_+$  over varying (a)  $\kappa$  and (b)  $\Gamma_r$ , respectively for vanishing  $\gamma_{pd} = 0.0/\text{ps}$ . For growing photon loss  $\kappa$ , the lasing regime collapses, while it is broadened with stronger radiative decay (cycling parameter  $\Gamma_r$ ). [See discussion to Fig. 3.15].

value of the phonon number  $N$  linearly follows  $\Gamma_r$ . The broadening of the phonon lasing window has the same cause, as discussed already for the pure dephasing. A broadening of the electronic resonance leads to a delayed self-quenching of the phonon number. The same restrictions as formulated for the pure dephasing for the validity of equations (3.58) and (3.62) apply here for the radiative decay. In the regime of either very high/small values of  $\kappa/\Gamma_r$ , the full QM-model is necessary for calculating the evolution of the thresholds  $T_-$  and  $T_+$  as well as the phonon number. When the area (phonon lasing regime) between  $T_-$  and  $T_+$  (shaded area) begins to collapse, which is equivalent with the absence of any threshold into the coherent regime, the FQ model predicts a transition into the non-classical regime [See Sec. 3.4.1].

### 3.5.8. High phonon number regime

Although this semiclassical theory was developed for the truly coherent case of only Poissonian statistics, the above discussions already show a remarkable agreement between the effective SC theory (3.62)-(3.69) even in the few phonon case. Assuming now the many phonon regime, caused by high a phonon lifetime (or stronger radiative decay), this theory can be simplified even more, according to Eqs. (3.71)-(3.73). In Fig. 3.18(a) the phonon number is depicted versus  $\Omega_R$  for a small phonon decay  $\kappa = 0.5 \mu\text{s}$ , where the thin black curve corresponds to the calculation with formula Eq. (3.62) and the bold grey curve to the simplified formula Eq. (3.71). In this many phonon regime, as predicted by Eq. (3.71), the self-quenching occurs with a strong delay, compared to the few phonon regime (even with finite pure dephasing). This simplified formula is however only valid for sufficiently small decay rates  $\kappa$ , as can be seen from Fig. 3.18(b). For larger values of  $\kappa$ , Eqs. (3.62) and (3.69) apply and for even higher values, as discussed in Sec. 3.4.1 even the FQ model has to be consulted. However, the results from Fig. 3.18 postulate a suspension of the self-quenching behavior.

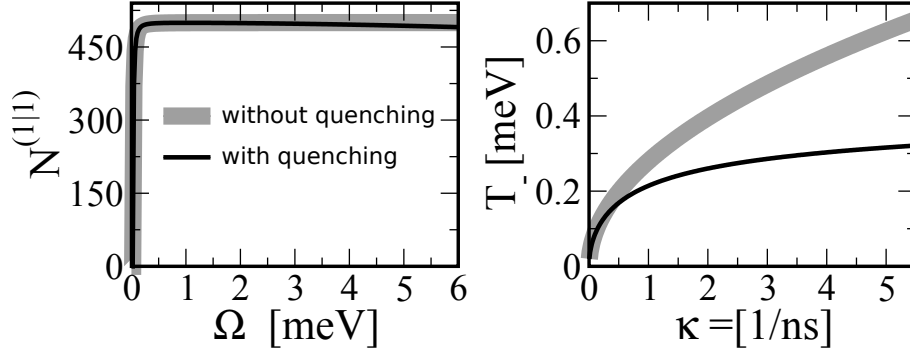


Figure 3.18.: Evolution of the (a) phonon number  $N$  versus varying  $\Omega_R$  ( $\kappa = 0.5 \mu\text{s}$ ) and (b) the laser threshold  $T_-$  versus varying  $\kappa$  ( $\Omega_R = (T_+ + T_-)/2$ ) at  $\gamma_{pd} = 0.0/\text{ps}$ . (a) For large photon lifetimes  $\kappa^{-1}$ , the self-quenching is inhibited, as given by the reduced formula in Eq. (3.71). (b) This formula becomes obsolete for larger  $\kappa$ .

### 3.6. Quantum theory of the effective phonon laser

In the previous section, the focus was on deriving a really simple semiclassical theory for the phonon laser, based on the effective Hamiltonian Eqs. (3.43) and (3.44). Within this approach, only coherent phonon populations can be described. Although already giving reliable results in the few phonon regime, it is best applied to the many-phonon regime. In this section, the effective Hamiltonian will be used to derive analytical expressions for the higher order phonon-phonon correlations. This effective quantum (EQ) theory bridges the gap between FQ and SC model and gives access to the full spectrum of phonon statistics as well as transitions between the different regimes (classical and quantum) in the few phonon limit.

Using again Heisenberg's EOM, and Eqs. (3.43) and (3.44), the equations for the  $n$ -th order phonon-assisted electronic densities  $V^{(n|n)} \equiv \langle |v\rangle \langle v| b^{\dagger n} b^n \rangle$ ,  $C^{(n|n)} \equiv \langle |c\rangle \langle c| b^{\dagger n} b^n \rangle$  and polarizations  $P^{(n-1|n)} \equiv \langle |v\rangle \langle c| b^{\dagger n-1} b^n \rangle$  read:

$$\dot{V}^{(n|n)} = -2n\kappa V^{(n|n)} + 2\Gamma_r C^{(n|n)} - ig_{\text{eff}} P^{(n|n+1)*} + ig_{\text{eff}} P^{(n|n+1)}, \quad (3.75)$$

$$\begin{aligned} \dot{C}^{(n|n)} &= -(2n\kappa + 2\Gamma_r) C^{(n|n)} + ig_{\text{eff}} P^{(n|n+1)*} - ig_{\text{eff}} P^{(n|n+1)} \\ &\quad + ing_{\text{eff}} P^{(n-1|n)*} - ing_{\text{eff}} P^{(n-1|n)}, \end{aligned} \quad (3.76)$$

$$\begin{aligned} \dot{P}^{(n-1|n)} &= -[(2n-1)\kappa + \gamma - i(\tilde{\omega} + \omega)] P^{(n-1|n)} \\ &\quad + ig_{\text{eff}} C^{(n|n)} - ig_{\text{eff}} V^{(n|n)} - ing_{\text{eff}} C^{(n|n)}. \end{aligned} \quad (3.77)$$

For the dynamics, this set of equations can be treated the same way as Eqs (3.22)-(3.24), related to a similar numerical effort. In this section, however, the focus is on an analytical expression for the higher order phonon correlations in the stationary domain.

### 3.6.1. Stationary limit of the effective quantum model

For the stationary regime, the derivatives in Eqs. (3.75)-(3.77) are again set to zero. Since the densities only couple to the imaginary part of the phonon-assisted polarization (here abbreviated as  $\bar{P}^{(n-1,n)} \equiv \Im P^{(n-1,n)}$ ), the equations can further be simplified to the real manifold:

$$0 = -2n\kappa V^{(n|n)} + 2\Gamma_r C^{(n|n)} + g_{\text{eff}} \bar{P}^{(n|n+1)}, \quad (3.78)$$

$$0 = -(2n\kappa + 2\Gamma_r) C^{(n|n)} - g_{\text{eff}} \bar{P}^{(n|n+1)} - ng_{\text{eff}} \bar{P}^{(n-1|n)}, \quad (3.79)$$

$$0 = \frac{[((2n-1)\kappa + \gamma)^2 + (\tilde{\omega} + \omega)^2]}{[(2n-1)\kappa + \gamma]} \bar{P}^{(n-1|n)} + g_{\text{eff}} C^{(n|n)} - g_{\text{eff}} V^{(n|n)} - ng_{\text{eff}} V^{(n-1|n-1)}. \quad (3.80)$$

Here, the imaginary part of the original equation for  $P^{(n-1|n)}$  was formed.  $P^{(n-1|n)}$  has a real- as well as an imaginary part due to the free energy rotation with  $(\tilde{\omega} + \omega)$  in Eq. (3.80), resulting in the prefactor in front of  $\bar{P}$ . Due to the similarity of this set of equations with a two level optical laser, the same treatment is applicable as for example in Refs. [ADG90, Gar11].

Adding Eqs. (3.77) and (3.79) results in a simple relationship for the imaginary part of the polarization and the higher order phonon-phonon correlation:

$$2n\kappa \underbrace{(V^{(n|n)} + C^{(n|n)})}_{N^{(n|n)}} = 2n\bar{P}^{(n-1|n)}, \quad (3.81)$$

$$\Rightarrow \bar{P}^{(n-1|n)} = \frac{\kappa}{g_{\text{eff}}} N^{(n|n)}. \quad (3.82)$$

The condition Eq. (3.82) is used for eliminating the densities  $C$  and  $V$  from Eq. (3.80) in favor of the polarization  $\bar{P}$ ,

$$0 = -2n\kappa V^{(n|n)} + 2\Gamma_r C^{(n|n)} + g_{\text{eff}} \bar{P}^{(n|n+1)} \quad (3.83)$$

$$= -2ng_{\text{eff}} \bar{P}^{(n-1|n)} + 2(n\kappa + \Gamma_r) C^{(n|n)} + 2g_{\text{eff}} \bar{P}^{(n|n+1)}, \quad (3.84)$$

so that the electronic densities can be expressed as:

$$C^{(n|n)} = \frac{ng_{\text{eff}}}{(n\kappa + \Gamma_r)} \bar{P}^{(n-1|n)} + \frac{g_{\text{eff}}}{(n\kappa + \Gamma_r)} \bar{P}^{(n|n+1)}, \quad (3.85)$$

$$V^{(n|n)} = \frac{\Gamma_r}{2\kappa} \frac{g_{\text{eff}}}{(n\kappa + \Gamma_r)} \bar{P}^{(n-1|n)} - \frac{g_{\text{eff}}}{(n\kappa + \Gamma_r)} \bar{P}^{(n|n+1)}. \quad (3.86)$$

Inserting these equations into (3.80) and using again Eq. (3.82), results in a three-term recursion relation, [ADG90, Gar11] for the phonon-phonon correlations:

$$a_n N^{(n+1|n+1)} + b_n N^{(n|n)} - c_n N^{(n-1|n-1)} = 0, \quad (3.87)$$

with the prefactors defined as

$$a_n = \frac{2\kappa}{(n\kappa + \Gamma_r)}, \quad (3.88)$$

$$b_n = \frac{(n\kappa - \Gamma_r)}{(n\kappa + \Gamma_r)} + \frac{n\kappa}{((n-1)\kappa + \Gamma_r)} + \frac{\kappa}{g_{\text{eff}}^2} \frac{[((2n-1)\kappa + \gamma)^2 + (\tilde{\omega} + \omega)^2]}{((2n-1)\kappa + \gamma)}, \quad (3.89)$$

$$c_n = \frac{n\Gamma_r}{((n-1)\kappa + \Gamma_r)}. \quad (3.90)$$

Further, multiplying Eq. (3.87) with  $N^{(n-1|n-1)}$  and rearranging it for  $B^n \equiv \frac{N^{(n|n)}}{N^{(n-1|n-1)}}$  gives a simple recursion formula for the (higher order) phonon correlation ratios:

$$B^n = \frac{c_n}{[b_n + a_n B^{n+1}]}. \quad (3.91)$$

In order to calculate the  $n$ -th order phonon correlation with this recursive formula, a starting  $n = 0$  and a breaking point  $n = n_{\text{krit}}$  is necessary. Note, that in general the phonon correlations and thus the ratios  $B^n$  do not necessarily converge to zero. This is only true for a Fock statistics, where correlations of higher orders than the number of phonons in the system are strictly zero. The expectation value operator correlations (or ratios) are not to be confused with the correlated part of the expectation value  $\delta\langle b^{\dagger n} b^n \rangle$ , occurring for example in a typical correlation cluster expansion [KK08]. These would indeed converge to zero for higher occupation numbers, while the here calculated correlation ratios increase with the average phonon number  $N$ . For the ratios  $B^n$  this means, that in the case of a thermal or a coherent statistics, it applies [Lou90, Gla63]:

$$B^n = \frac{n!N^n}{(n-1)!N^{n-1}} = nN, \quad \text{thermal}, \quad (3.92)$$

$$B^n = \frac{N^n}{N^{n-1}} = N, \quad \text{Poissonian}. \quad (3.93)$$

However, using equation Eq. (3.91) and the fact, that  $B^n > 0, \forall n$ , an upper bound for the correlation ratios can be deduced:

$$B^n \leq \frac{c_n}{b_n} \longrightarrow \frac{2\Gamma_r}{\kappa}, \quad (3.94)$$

which corresponds to four times the maximum coherent phonon number (3.63) resulting from the SC model. With that, the combination of  $a_n B^{n+1}$  actually converges to zero. Dependent on how broad the statistics is, the phonon correlation ratios can strongly deviate from this value even for large  $n$ . Therefore, the starting point  $n_{\text{krit}}$  has to be chosen according to the present statistics and average phonon number, i.e. dependent on the pa-

parameter set. With the repeated use of Eq. (3.91) the phonon number and any higher order correlation ratios are given by continuous fractions:

$$N^{(1|1)} = \frac{N^{(1|1)}}{N^{(0|0)}} = B^1 = \frac{c_1}{b_1 + a_1 \frac{c_2}{b_2 + a_2 \frac{c_3}{b_3 + \dots}}}, \quad (3.95)$$

$$B^n = \frac{c_n}{b_n + a_n \frac{c_{n+1}}{b_{n+1} + a_{n+1} \frac{c_{n+2}}{b_{n+2} + \dots}}}. \quad (3.96)$$

The start value is  $N^{(0|0)} = V^{(0|0)} + C^{(0|0)} = 1$  and the cut-off value is  $B^{n_{\text{krit}}} = \frac{c_n}{b_n}$ . The higher order phonon correlations, for calculating for example the  $g^{(2)}(0)$ -function or the phonon-probability distribution, can be calculated from the ratios:

$$N^{(n|n)} = B^1 B^2 \dots B^{n-1} B^n. \quad (3.97)$$

### 3.6.2. Verification of the effective phonon laser Hamiltonian

This EQ approach can now serve as an additional tool for verifying the adequacy of the effective Hamiltonian Eqs. (3.43) and (3.44) with respect to the description of a phonon laser. Figure 3.19(a) shows the input-output curves  $N(\Omega_R)$ , calculated with the SC model (shaded blue area), the FQ model (bold grey curve) and the EQ model (thin black curve). For a vanishing pure dephasing, the results from the FQ and the EQ are an exact match. This corroborates the validity of the effective Hamiltonian for this regime. There is no visible deviation for the phonon number or the  $Q$ -parameter. The higher order correlations calculated with FQ (blue filling) and EQ (black curve) coincide as well, which is demonstrated by the phonon number probability distribution in Fig. 3.19(b). This means, that the full phonon population within the cavity is generated by the effective subsystem only, and there are truly no other processes involved. Thus, in the regime of a pure-dephasing, small compared to the cavity phonon frequency,  $\gamma_{pd} \ll \omega_{ph}$ , the anti-Stokes excitation condition [3.7] automatically selects the phonon laser, described by the effective Hamiltonian Eqs. (3.43) and (3.44).

### 3.6.3. Conclusion

In conclusion, a theory for a QD-phonon laser was presented, where an analytical semiclassical approach was benchmarked with a full quantum theoretical treatment and verified by an effective quantum model. Coupled to a single mode acoustic cavity, the QD can be operated as a phonon laser. Making use of an induced Raman process, an effective subsystem can be addressed by an external pump laser field. The different emission regimes of the system were analyzed, predicting among others, beneficial effects of an intermediate pure dephasing with respect to the QD dipole transition on the width of the coherent laser

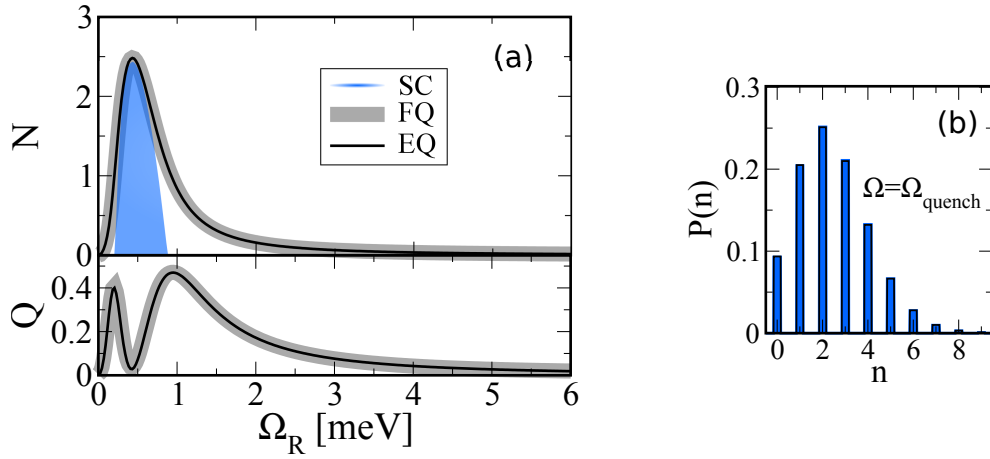


Figure 3.19.: Evolution of the (a)  $N$  and  $Q$  versus varying  $\Omega_R$  ( $\kappa = 0.5 \mu\text{s}$ ), calculated with the three different models: FQ (bold grey curve), EQ (thin black curve) and SC (blue area). (b)  $P(n)$  at  $\Omega_{\text{quench}}$ .  $\gamma_{pd} = 0.0/\text{ps}$  as calculated with the FQ (blue filling) and the EQ (black curve). The coincidence between the FQ- and the EQ models is perfect (at a vanishing pure dephasing).

regime. Further, low phonon life times or strong weak radiative decay rates can also result in a stable non-classical emission statistics.

# 4

## Phonon-assisted Mollow triplet

In recent years, non-equilibrium phonons [SDR<sup>+</sup>10, WRZI04], cavity phonons and coherent phonons have been predicted and reported to have great impact on the emission properties of quantum light emitters [TBF<sup>+</sup>02, FLKJP13, TBF<sup>+</sup>02]. The variety of newly developed phonon devices (phonon lasers, phonon cavities and combined optical devices [VHK<sup>+</sup>09, GLPV10, FLKJP13]) therefore strongly motivate the study of phonon coupling- and multi-phonon-features [CFC<sup>+</sup>10, MKH08] in optical emitters [VAK02, MVTG06, BJS<sup>+</sup>07], i.e. atoms, molecules or semiconductor nanostructures [e.g. quantum dots (QDs), nano layers, nanotubes, etc]. In linear or non-linear optical spectroscopy experiments, these processes can be revealed and allow further study of the coupled dynamics of phonons, electrons and light. Stationary or time dependent laser fields, applied to the quantum light and phonon emitters, serve as external control to the phonon statistics [KCBK12] and therefore the emission properties of the device.

In this chapter, different excitation scenarios are distinguished, involving the weak and the strong excitation regime as well as the continuous wave (CW) and the pulsed optical excitation. In the limit of weak external laser fields, i.e. below the regime, where Rabi-oscillations can occur, the electronic system is only weakly perturbed by the electron-light interaction. In this limit, the spectrum can be divided into elastic and inelastic scattering of the input laser field, as well as resonance and phonon-assisted fluorescence, originating from direct excitation of electronic transitions [KWH<sup>+</sup>10, MVA12]. However, in the high driving field limit, the spectrum is transformed into the Mollow-triplet: The emission will consist of three emission lines [Mol69, VLT09, GTVC<sup>+</sup>10], centered at the incident driving frequency  $\omega_l$ , with the so-called Mollow sidebands equally distanced from the triplet center ( $\omega = \omega_l \mp \omega_G$ ) by the generalized Rabi-frequency  $\omega_G$ .

In contrast to this previous work, this chapter is focused on higher order LO-phonon signatures in the resonance fluorescence emission spectrum of the lowest bound transition of a semiconductor QD, externally driven by a strong laser pulse. Next to the ordinary emission-triplet about the exciting laser frequency, the coupling to LO-phonons results

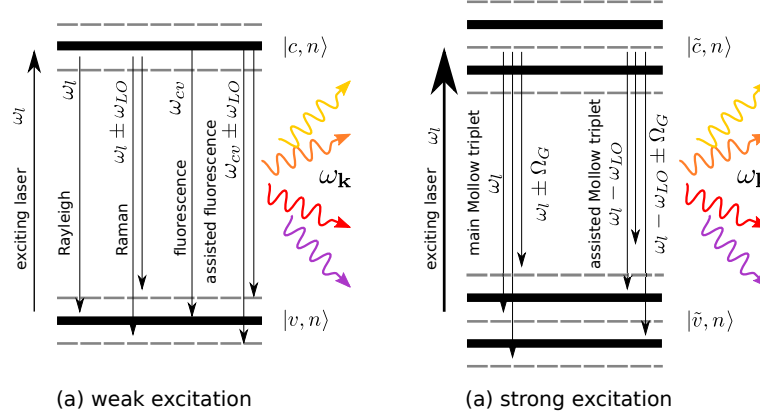


Figure 4.1.: Scheme of two-level system interacting with a (a) weak external laser field: the electronic levels and the light field are separated. There is emission from the (phonon-assisted) transitions (fluorescence) and (phonon-assisted) scattering (Rayleigh and Raman). (b) strong external laser field: The electronic levels are dressed with the laser field. The emission consists of triplets centered at the initial laser frequency  $\omega_l$  (Mollow triplet) and at the Raman frequencies  $\omega_l \mp \omega_{LO}$  (phonon-assisted Mollow triplet: only Stokes depicted).

in additional phonon-assisted triplets centered at the (higher order) Raman-frequencies ( $\omega = \omega_l \mp p\omega_{LO}$ ). The different expected contributions to the signal are visualized for weak optical excitation in Fig. 4.1(a) and the Mollow regime in Fig. 4.1(b). The corresponding frequencies additionally collected in Tab. 4.1.

Contribution	Detected signal	Excitation regime
0-th order Fluorescence	$\omega_s = \omega_{cv}$	Weak
$n$ -th order Phonon-assisted fluorescence	$\omega_s = \omega_{cv} \pm n\omega_{LO}$	Weak
0-th order Rayleigh	$\omega_s = \omega_l$	Weak
$n$ -th order Raman	$\omega_s = \omega_l \pm n\omega_{LO}$	Weak
Mollow triplet	$\omega_s = \omega_l \pm \Omega_G$	Strong
$n$ -th order phonon-assisted Mollow triplet	$\omega_s = \omega_l \pm n\omega_{LO} \pm \Omega_G$	Strong

Table 4.1.: Spectral positions of the different emission structures at weak and strong optical excitation  $\Omega_R \ll \omega_{LO}$ .

Beyond this, we find a third regime of strong optical excitation, where the spectrum is again drastically altered, compared with both the weak and the typical Mollow regime. That is, when the laser strength, i.e. the Rabi-frequency  $\Omega_R$  coincides with the LO-phonon frequency  $\omega_{LO}$  (or  $n\omega_{LO}$ , with  $n \in \mathbb{N}$ ). Within this scenario, new non-perturbative features are predicted in the spectrum, that are directly related to the electron-phonon coupling strength. In fact, these extra features will be seen to serve as a possible measure for the

Huang-Rhys factor [HR50, KCRK11]. A strong optical excitation tuned to this condition results in the furthermore formation of quasi-particles, involving the QD-transition, the external laser field and the phonon system. Similar to the coherent phonon generation of the last chapter, the strong optical drive induces a change of the LO-phonon system. Dependent on the driving regime and the spectral position of the laser field, higher order phonon-correlations are excited, demanding a full implementation of the quantum correlations. This excludes a description, based of a second-order Born approximation, which is limited to a thermal equilibrium und bath assumption for the phonons. Therefore, we again make use of the inductive equation of motion (EOM) method of Chap. 2, [KCR<sup>+</sup>11, CRCK10, AHK99] and derive a closed set of EOMs, which can be extended up to an arbitrary accuracy in a collective electron-LO-phonon interaction. Choosing this approach, strong coupling phonon features and multi-phonon processes involving non-equilibrium and higher temperature effects, which will certainly occur during strong optical excitation, can adequately be described and featured in the spectrum. The findings presented in the current chapter are in parts published in Refs. [KCRK11, KCR<sup>+</sup>11, KR10].

For calculating the emission signals of the QD in the strong and the weak excitation regime and later on, also in the time domain, different methods will be applied. In the steady state, the spectrum is calculated applying the quantum regression theorem, while for the temporal behavior of the emission, a multi-mode field description is used. As an introduction of this method, however, this multi-mode method is first applied to the usual Mollow-triplet in the stationary limit.

## 4.1. Input-laser field and emitted light field

Since in this chapter, there is no phonon cavity involved for the LO-phonons and the light emission is supposed to be into free space, a multi-mode description will be used for the LO-phonons, as well as the emitted photons. Such as in the previous chapter Chap. 3 the QD is optically driven with an external laser field. However, the spectral position of the laser is variable. This incoming laser field can be described classically [Muk95]. However, for the temporal evolution of the emission, the emitted light field (generated via spontaneous emission) is treated fully quantum mechanically, with modes  $k_j$ :

$$\begin{aligned}
 E(r, t) &= E_l^*(t)e^{(i\omega_l t - ik \cdot r)} + E_l(t)e^{(-i\omega_l t + ik \cdot r)} \\
 &+ \sum_{j=1}^f E_j c_{k_j}^\dagger(t)e^{-ik_j \cdot r} + E_j c_{k_j}(t)e^{ik_j \cdot r}.
 \end{aligned} \tag{4.1}$$

The temporal evolution of the input laser field is contained in the envelope function  $E_l(t)$ , while the temporal behavior of the output field modes is given by the evolution of the photon operators  $c_{k_j}^{(\dagger)}(t)$ . This treatment of the emission already reveals the non-linear character of the light emission. Obviously, the emission modes are considered to be unpopulated at the beginning. This means, that the emitter first has to interact with the classical input field. This interaction with the incoming intensity therefore already corresponds to

an intensity  $|E|^2$ , i.e. requires a second order interaction at least. The output intensity, i.e. the emission into the quantized mode continuum also corresponds to a second order process (emitted intensity), together resulting at least in a fourth order interaction for the description of the light emission at optical excitation [Muk95].

#### 4.1.1. Hamilton-operator and equations of motion

According to Chap. 2, Sec. 2.2, the free parts of the quantized fields are described by Eq. (4.4), where  $a$  ( $a^\dagger$ ),  $c_{k_j}$  ( $c_{k_j}^\dagger$ ) and  $b_q$  ( $b_q^\dagger$ ) are the electron, photon and phonon annihilation (creation) operators. The electron-phonon coupling is described by the Fröhlich Hamiltonian (coupling element  $g^{\mathbf{q}} = g_c^{\mathbf{q}} - g_v^{\mathbf{q}}$ ) [MZ07]. Further, the quantized multi-mode electromagnetic field Hamiltonian describes the quantum light emission of the QD into free space. The total Hamiltonian of the coupled system reads in the RWA [KK08, Hau04, AHK99]:

$$\mathcal{H}_I^{e-l} = \hbar\Omega(t)a_v^\dagger a_c + \hbar \sum_k M^k a_v^\dagger a_c c_k^\dagger + H.c., \quad (4.2)$$

$$\mathcal{H}_I^{e-ph} = \hbar \sum_q a_c^\dagger a_c (g_q^* b_q^\dagger + g_q b_q), \quad (4.3)$$

$$\mathcal{H}_0 = \sum_{i=v,c} \hbar\omega_i a_i^\dagger a_i + \sum_k \hbar\omega_k c_k^\dagger c_k + \hbar\omega_{LO} \sum_q b_q^\dagger b_q + H.c.. \quad (4.4)$$

Here,  $\omega_{\mathbf{k}}$ ,  $\omega_l$  and  $\omega_{LO}$  denote the corresponding photon frequency of mode  $k$ , the laser frequency and the LO-phonon frequency. For the numerical calculations, the parameters are chosen of an InGaAs/GaAs-QD cf. [KWH<sup>+</sup>10] and App. A.1.

#### 4.1.2. Treatment of the multi-mode phonon system

For the free phonon part in Eq. (4.4), the Einstein-approximation of a constant dispersion relation for the LO-phonons is applied [Mad78]. This assumption significantly simplifies the treatment of the phonon system, as it is possible to introduce collective phonon operators and electron-phonon coupling elements:

$$B^\dagger \equiv \frac{1}{g} \sum_q g_q^* b_q^\dagger, \quad B \equiv \frac{1}{g} \sum_q g_q b_q, \quad (4.5)$$

$$\text{with } g \equiv \sqrt{\sum_q |g_q|^2}. \quad (4.6)$$

The factor  $\frac{1}{g}$  is introduced in order to normalize the commutator relation for the effective phonon operators:

$$[B, B^\dagger] = 1, \quad (4.7)$$

and thus realize a more symmetric appearance of the new collective electron-phonon coupling strength  $g$  in the equations of motion. With this, the electron-phonon interaction can directly be expressed by the new operators:

$$\mathcal{H}_I^{e-ph} = \hbar g a_c^\dagger a_c (B^\dagger + B), \quad (4.8)$$

which is formally identical to the electron-acoustic cavity coupling in Eq. (3.2). Although, the free phonon Hamiltonian Eq. (4.4) cannot be rewritten in terms of  $B^{(\dagger)}$ , such as (4.3), the following commutator however conveniently results in:

$$\begin{aligned} [\hbar\omega_{LO} \sum_q b_q^\dagger b_q, B^{\dagger n} B^m] &= \hbar\omega_{LO} \frac{1}{g} (n \sum_q g_q^* b_q^\dagger B^{\dagger n-1} B^m - B^{\dagger n} m \sum_q g_q^* b_q B^{m-1}) \\ &= (n - m) \hbar\omega_{LO} B^{\dagger n} B^m, \end{aligned} \quad (4.9)$$

due to the Einstein approximation. Therefore, with Eqs. (4.8) and (4.9) the multi-mode phonon system can be treated the same way as a single phonon mode. Instead of solving equations for each combination  $\{q_j\}$  of relevant phonon modes, only one effective mode  $B$  has to be considered.

### 4.1.3. Treatment of the multi-mode photon system

In the case of the electron-photon interaction in (second term in Eq. (4.2)) and the free photon Hamiltonian (Eq. (3.1), second term) with a varying dispersion relation, this treatment cannot be applied and equations for the full free photon mode continuum have to be solved. For the further description, it is therefore useful introducing multi-indices for the photon operators, as the photon operators can occur to any order within each of the different modes  $k_1 \dots k_f$ .

$$\begin{aligned} c^{\dagger p} &:= c_{k_1}^{\dagger p_1} c_{k_2}^{\dagger p_2} \dots c_{k_{f-1}}^{\dagger p_{f-1}} c_{k_f}^{\dagger p_f}, & c^s &= c_{k_1}^{s_1} c_{k_2}^{s_2} \dots c_{k_{f-1}}^{s_{f-1}} c_{k_f}^{s_f} \\ c^{\dagger(p \pm 1, j)} &\equiv c_{k_1}^{\dagger p_1} \dots c_j^{\dagger p_j \pm 1} \dots c_f^{\dagger p_f}, & c^{(s \pm 1, j)} &\equiv c_{k_1}^{s_1} \dots c_j^{s_j \pm 1} \dots c_f^{s_f} \\ p &\equiv (p_1 + p_2 + \dots + p_f), & s &\equiv (s_1 + s_2 + \dots + s_f). \end{aligned} \quad (4.8)$$

Further, abbreviations are introduced for the photon- and phonon assisted electronic operator correlations similar to Eqs. (3.12)-(3.15). However, here, additional indices for the photon operators from Eq. (4.8) occur.

$$\begin{aligned} V_{(n|m)}^{(p|s)} &\equiv \langle |v\rangle \langle v| c^{\dagger p} c^s B^{\dagger n} B^m \rangle, \\ C_{(n|m)}^{(p|s)} &\equiv \langle |c\rangle \langle c| c^{\dagger p} c^s B^{\dagger n} B^m \rangle, \\ P_{(n|m)}^{(p|s)} &\equiv \langle |v\rangle \langle c| c^{\dagger p} c^s B^{\dagger n} B^m \rangle, \\ N_{(n|m)}^{(p|s)} &\equiv \langle c^{\dagger p} c^s B^{\dagger n} B^m \rangle, \end{aligned} \quad (4.9)$$

Choosing a rotating frame with the external laser frequency  $\omega_l$  (such as in Eq. (3.34)) and applying Heisenberg's equation of motion to Eqs. (4.2)-(4.8), results in the following general set of EOMs:

$$\begin{aligned}
 \frac{d}{dt}V_{(n|m)}^{(p|s)} &= [i \sum_{j=1}^f (p_j - s_j)(\omega_{k_j} - \omega_l) + i(n - m)\omega_{LO} - (n - m)\kappa]V_{(n|m)}^{(p|s)} \\
 &- i \sum_{j=1}^f (p_j M^{k_j} P_{(m|n)}^{(s|p-1,j)})^* + i \sum_{i=1}^f s_j M^{k_j} P_{(n|m)}^{(p|s-1,j)} \\
 &+ i \sum_{j=1}^f M^{k_j} P_{(n|m)}^{(p+1,j|s)} - i \left( \sum_{j=1}^f M^{k_j} P_{(m|n)}^{(s+1,j|p)} \right)^* \\
 &+ i\Omega(t)P_{(n|m)}^{(p|s)} - i \left( \Omega(t)P_{(m|n)}^{(s|p)} \right)^* \tag{4.10}
 \end{aligned}$$

$$\begin{aligned}
 \frac{d}{dt}C_{(n|m)}^{(p|s)} &= [i \sum_{j=1}^f (p_j - s_j)\omega_{k_j} + i(n - m)\omega_{LO} - (n - m)\kappa]C_{(n|m)}^{(p|s)} \\
 &- i \sum_{j=1}^f M^{k_j} P_{(n|m)}^{(p+1,j|s)} + i \left( \sum_{j=1}^f M^{k_j} P_{(m|n)}^{(s+1,j|p)} \right)^* \\
 &- i\Omega(t)P_{(n|m)}^{(p|s)} + i \left( \Omega(t)P_{(m|n)}^{(s|p)} \right)^* \\
 &+ i n g C_{(n-1|m)}^{(p|s)} - i m g C_{(n|m-1)}^{(p|s)}, \tag{4.11}
 \end{aligned}$$

$$\begin{aligned}
 \frac{d}{dt}P_{(n|m)}^{(p|s)} &= [i \sum_{j=1}^f (p_j - s_j)(\omega_{k_j} - \omega_l) + i(n - m)\omega_{LO} - i\Delta - (n - m)\kappa - \gamma_{pd}]P_{(n|m)}^{(p|s)} \\
 &- i \sum_{j=1}^f p_j (M^{k_j} C_{(m|n)}^{(p-1,j|s)})^* - i \sum_{j=1}^f M^{k_j} (C_{(n|m)}^{(p|s+1,j)} - V_{(n|m)}^{(p|s+1,j)}) \\
 &- i\Omega(t) \left( C_{(n|m)}^{(p|s)} - V_{(n|m)}^{(p|s)} \right) \\
 &- i g P_{(n|m+1)}^{(p|s)} - i g P_{(n+1|m)}^{(p|s)} - i m g P_{(n|m-1)}^{(p|s)}, \tag{4.12}
 \end{aligned}$$

Here, subscript-indices correspond to the order of phonon creation- ( $n$  or left slot, respectively), and annihilation ( $m$  or right slot, respectively) operators. The superscript indices correspond to the photonic multi indices, denoting the total order of photon- creation ( $p$ ) and annihilation ( $s$ ) operators. As introduced above in Eq. (4.8), a superscript  $x - 1, j$  indicates a reduction in the order of photon operators by 1 in the mode  $k_j$ .  $\Delta = \omega_{cv} - \omega_l$  is the frequency detuning of the laser towards the optical transition frequency of the QD. As both the electron light couplings are non-diagonal, crossings of the interaction paths leads to free rotation parts with the laser frequency, also for the electronic densities in Eqs. (4.11) and (4.12). All three equations exhibit potential nonlinear interaction with the light fields, best reflected by the photon-assisted polarization  $P_{(n|m+1)}^{(p|s)}$ . For an odd number of

photon operators  $n + m$ , and  $n < m$ , this quantity rotates with a higher order combination of photon and laser frequencies:

$$\begin{aligned}\chi_{P(0|0)}^{(p|s)} &= -\sum_{j=1}^f d_j \omega_{k_j} + (d_j + 1)\omega_l - \omega_{cv}, \quad n < m, \\ &= -\omega_k + 2\omega_l - \omega_{cv}, \quad (m = 1),\end{aligned}\tag{4.13}$$

$$\begin{aligned}\chi_{P(0|0)}^{(p|s)} &= \sum_{j=1}^f d_j \omega_{k_j} - (d_j - 1)\omega_l - \omega_{cv}, \quad n < m, \\ &= \omega_k - \omega_{cv} \quad (n = 1),\end{aligned}\tag{4.14}$$

where  $d_j = |p_j - s_j|$ . While rotation terms, such as Eq. (4.14) can also occur for interacting with only the scattering modes  $k_1 \dots k_f$ , the rotation terms of Eq. (4.13) needs the combined interaction with the scattering modes and the external laser field. In the case of  $m = 1$ , two negative frequencies are canceled with a double of the laser frequency. Thus, a quantity, which is non-energy conserving on the basis of the electron- and photon operators gets to be energy-conserving again through a higher order laser assistance. As will become apparent in the following paragraph, these quantities are the ones responsible for typical non-linear emission features, such as the Mollow-triplet.

## 4.2. Stationary spectrum:–Mollow triplet

In order to calculate the emission spectrum, making use of Eqs. (4.11)-(4.12) the interaction with the quantized field modes is only regarded up to the second order. Further, second order photon-assisted driving terms are disregarded as well.

$$O_{(n|m)}^{(p|s)} \stackrel{!}{=} 0, \quad (p + 1 \geq 2).\tag{4.15}$$

This perturbative approach is well justified, even in the strong excitation regime, since the light emission is into free space. Therefore, once emitted, the photons will no further interact or be reabsorbed by the system and any back-action terms (Eq. (4.15)) can be omitted. In the steady state, the emission spectrum can be calculated by the steady state photon emission rate [Muk95, KJHK99], represented by:

$$S(\omega_k) \equiv \frac{d}{dt} \langle c_k^\dagger c_k \rangle = \frac{i}{\hbar} [H, c_k^\dagger c_k].\tag{4.16}$$

Calculating the right hand side of Eq. (4.16) simply results in:

$$S(\omega_k) = 2 \text{Im}(MP_{(0|0)}^{(1|0)}).\tag{4.17}$$

This equations states the first order interaction, which is with the electron-photon coupling  $M$ .

### 4.2.1. Without phonon interaction

*Second order:*– Applying the above discussed perturbative treatment (Eq. (4.15)) for the photon system and disregarding the interaction with the LO-phonons, a recursively closed system of equations can be derived for the stationary limit. Omitting the subscript indices for the phonon-operators, the steady state photon-assisted polarization reads:

$$P^{(1|0)}\chi_P^{(1|0)} = -iM^{k*}C^{(0|0)} - i\Omega\underbrace{(2C^{(1|0)} - N^{(1|0)})}_{\equiv R^{(1|0)}}, \quad (4.18)$$

where  $\chi_P^{(1|0)}$  is defines as in Eqs. (3.29)-(3.32) from Chap. 3 and contains the free rotation and damping prefactors of Eq. (4.12).

*Third order:*– The conduction band density  $C^{(0|0)}$  in Eq. (4.18) is already proportional to the second order in the electron-photon coupling  $M^k$  and in the stationary limit simply saturates at a steady state value dependent on pumping strength, losses and detuning frequency.

$$C^{(0|0)} = \frac{2|\Omega|^2\gamma}{2\Gamma_r(\Delta^2 + \gamma^2) + 4|\Omega|^2\gamma} \rightarrow \frac{1}{2}, \quad (4|\Omega|^2 \gg \frac{2\Gamma_r(\Delta^2 + \gamma^2)}{\gamma}), \quad (4.19)$$

Note, that for the analytic solution in the steady state, a radiative dephasing  $\Gamma_r$  and  $\gamma = \Gamma_r + \gamma_{pd}$  had to be introduced according to Eq. 2.38 due to the second order perturbative treatment of the emitted photon field. The photon-assisted inversion (expression within the brackets of Eq. (4.18)) is just proportional to the first order in  $M$ , so that the equation reads:

$$R^{(1|0)}\Gamma_r = \Gamma_r N^{(1|0)} - iM^k(P^{(0|0)})^* - 2i\Omega P^{(1|0)} + 2i\Omega(P^{(0|1)})^* \quad (4.20)$$

*Fourth order:*– Here, already a higher order interaction term, as mentioned in Eq. (4.13) appears, with rotation terms  $\chi_P^{(0|1)}$  containing a double of the laser frequency  $\omega_l$ . The other two terms are already closed in the hierarchy, as  $P^{(0|0)}$ , such as  $C^{(0|0)}$  in Eq. (4.19), is already second order in  $M$  and is just a number:

$$P^{(0|0)} = -\frac{i\Omega(2C^{(0|0)} - 1)}{\chi_P^{(0|0)}} \rightarrow 0, \quad (4|\Omega|^2 \gg \frac{2\Gamma_r(\Delta^2 + \gamma^2)}{\gamma}). \quad (4.21)$$

The second term in Eq. (4.20) is the same as in Eq. (4.16) and recursively be inserted. The only remaining equations are for the higher order polarization and the single photon-operator:

$$P^{(0|1)}\chi_P^{(0|1)} = -i\Omega R^{(0|1)}, \quad (4.22)$$

$$\frac{d}{dt}N^{(1|0)} = N^{(1|0)}\epsilon + iM^k(P^{(0|0)}). \quad (4.23)$$

At this point the equations are closed, since the complex conjugate of Eq. (4.22) just reproduced Eq. (4.20) and the polarization  $P^{(0|0)}$  again ist just a number. The prefactor

$\epsilon = i(\omega_l - \omega_k) + \delta$  in (4.23) contains next to the rotating frame also the width  $\delta$  of the scattered laser field. For the strong excitation case (Mollow regime), Eqs. (4.18)-(4.23) can be combined into an analytic expression for the photon assisted polarization using Eqs. (4.19) and (4.18), it results into:

$$P^{(1|0)} = \frac{-iM\frac{1}{2}}{\chi_P^{(1|0)} + \frac{2|\Omega|^2}{\left(\chi_R^{(1|0)} + \frac{2|\Omega|^2}{\chi_P^{(0|1)*}}\right)}}, \quad (4.24)$$

Note, that this formula Eq. (4.24) is only valid in the truly strong excitation regime, when

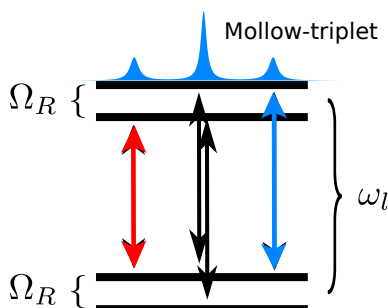


Figure 4.2.: Scheme of two-level system interacting with a strong external laser field: The electronic levels are dressed with the laser field and the spectrum consists of the Mollow-triplet (blue emission structure). It exhibits a central emission peak at the incident laser frequency  $\omega_l$ , a red detuned sideband at  $\omega_l - \Omega_R$  and a blue detuned sideband at  $\omega_l + \Omega_R$ .

coherent contributions to the spectrum in Eq. (4.23) can be omitted. In the weak excitation regime, coherent scattering will be present in the spectrum and the equation for  $N^{(1|0)}$  has to be integrated for consistence with the definition of the signal in Eq. (4.16).

Without the electron-phonon interaction, the spectrum exhibits the typical three peak structure [as depicted in Figs. 4.2 (schematically) and 4.3(a)]. The Mollow triplet center is spectrally positioned at an emission frequency  $\omega_k = \omega_l$  and the triplet sidebands at  $\omega_k = \omega_l \mp \Omega_R$  [CT92]. For resonant excitation, the ratio of both the triplet sidebands towards the triplet center line is 1 : 3. In the detuned case, these ratios change drastically, with different ratios for the lower energy and the higher energy sideband, because of resonance effects between the sidebands and the bare electronic transition.

In the semiconductor case, a non vanishing electron-LO-phonon interaction is often of importance and will deliberately change the emission spectrum, especially in the Mollow triplet regime. As the diagonal electron-phonon interaction inhibits a recursion, such as for Eqs. (4.19)-(4.22), the spectrum will be calculated using the quantum regression theorem for two-time operator correlations.

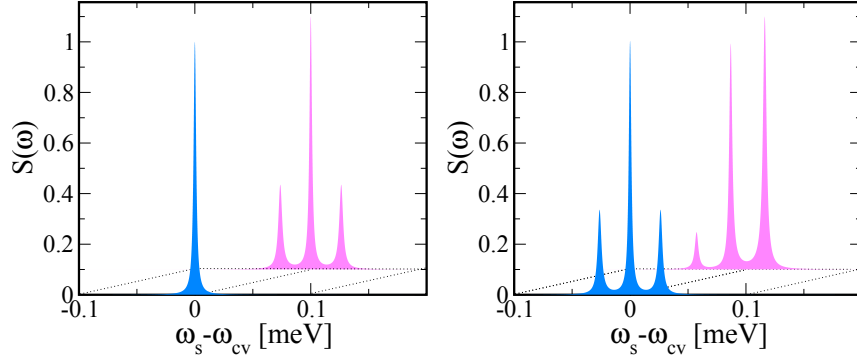


Figure 4.3.: Emission spectrum of a two level system (a) in the weak (blue curve in the front) and in the strong (pink curve in the back) excitation regime. (b) Mollow triplet for resonant (blue curve in the front) and slightly detuned excitation (pink curve in the back).

#### 4.2.2. The power spectrum and the quantum regression theorem

In the stationary regime, the spectrum can be calculated via the Fourier-transformation of the first order correlation function [MW95, Lou90]:

$$S(\omega_s) = \text{Re} \int_0^\infty d\tau \langle E^{(-)}(t) E^{(+)}(t + \tau) \rangle e^{i\omega_s \tau} \quad (4.25)$$

In the far field, using the Weisskopf-Wigner approximation, the negative  $E^{(-)}$  and the positive  $E^{(+)}$  frequency parts of the light field can be associated with the Pauli-operators  $\sigma^\dagger = |c\rangle\langle v|$  and  $\sigma = |v\rangle\langle c|$  [SZ97], respectively and the two time correlation results in:

$$\langle E^{(-)}(t) E^{(+)}(t + \tau) \rangle = I \langle \sigma^\dagger(t) \sigma(t + \tau) \rangle. \quad (4.26)$$

This means, that in the stationary case, the interaction with the emission modes  $\{k\}$  in the Hamiltonian Eq. (4.2)-(3.1) can be omitted and Eqs. (4.12)-(4.12) formally coincide with the equations Eqs. (3.23)-(3.24) of the last chapter. The only difference is, that here,  $g$  and  $B^{(\dagger)}$  correspond to the collective electron-phonon coupling and phonon operators of Eq. (4.6).

Two-time correlations, such as in Eq. (4.26) can be calculated using the *quantum regression formula* [BP02, Car99]. If for a system of operators  $\{O_\alpha\}$  it applies:

$$\frac{d}{dt} \langle O_\alpha(t) \rangle = \sum_\beta G_{\alpha\beta} \langle O_\beta(t) \rangle, \quad (4.27)$$

i.e. it is a system of linear differential equations, the same set of equations apply for the two time correlators:

$$\frac{d}{d\tau}\langle O_\mu(t)O_\alpha(t+\tau)\rangle = \sum_{\beta} G_{\alpha\beta}\langle O_\mu(t)O_\beta(t+\tau)\rangle, \quad (4.28)$$

With the same *regression matrix*  $G_{\alpha\beta}$  as in Eq. (4.27) [See App. A.4]. Here, we are interested in the two-time correlation  $\langle\sigma^\dagger(t)\sigma(t+\tau)\rangle$  and therefore in a set of equations, such as:

$$\frac{d}{d\tau}\langle\sigma^\dagger(t)O_{ij}^{nm}(t+\tau)\rangle = \sum_{ls,rp} G_{ij,ls}^{nm,rp}\langle\sigma^\dagger(t)O_{ls}^{rp}(t+\tau)\rangle. \quad (4.29)$$

The subscript indices correspond to the electronic levels  $|v\rangle$  and  $|c\rangle$ , while the superscripts indicate the order of phonon operators. In the previously introduced used notation, the operators  $O_{ij}^{nm}$  are given as:

$$O_{vv}^{nm} = |v\rangle\langle v|B^{\dagger n}B^m, \quad (4.30)$$

$$O_{cc}^{nm} = |c\rangle\langle c|B^{\dagger n}B^m, \quad (4.31)$$

$$O_{vc}^{nm} = |v\rangle\langle c|B^{\dagger n}B^m, \quad (4.32)$$

$$O_{cv}^{nm} = |c\rangle\langle v|B^{\dagger n}B^m. \quad (4.33)$$

Before solving the set of equations Eqs. (4.33) with Eq. (A.12), the initial values  $\langle\sigma^\dagger O_{ij}^{nm}\rangle(t)$  have to be calculated, which are given by the single time correlations:

$$\langle\sigma^\dagger(t)O_{vv}^{nm}(t)\rangle = \langle O_{cv}^{nm}\rangle(t) \equiv \bar{P}_{(n|m)}^{(0|0)}(t), \quad (4.34)$$

$$\langle\sigma^\dagger(t)O_{cc}^{nm}(t)\rangle = 0, \quad (4.35)$$

$$\langle\sigma^\dagger(t)O_{vc}^{nm}(t)\rangle = \langle O_{cc}^{nm}\rangle(t) \equiv \bar{C}_{(n|m)}^{(0|0)}(t), \quad (4.36)$$

$$\langle\sigma^\dagger(t)O_{cv}^{nm}(t)\rangle = 0. \quad (4.37)$$

Since here, the spectrum is calculated in the stationary regime ( $t \rightarrow \infty$ ), the initial values are given by Eq. (4.27) and setting the derivatives to zero. The resulting set of linear equations for the initial values Eqs. (4.37) is then simply given by the linear system of equations of Sec. (3.2.4).

### 4.3. Phonon-assisted Mollow triplet

In the case of an electron-phonon interaction and typical semiconductor features, such as a pure dephasing  $\gamma_{pd}$ , the emission spectrum in the weak excitation regime, as well as in the Mollow-triplet regime [See Figs. 4.4 and 4.9] is changed considerably. All peak positions, that can be expected in the weak excitation and the usual Mollow-regime are collected in Tab. 4.1.

As calculated with Eq. (A.12), Figure. 4.5 shows the emission spectrum of a semiconductor QD, interacting with LO-phonons over the Raman-shift, i.e. emission-energy minus the

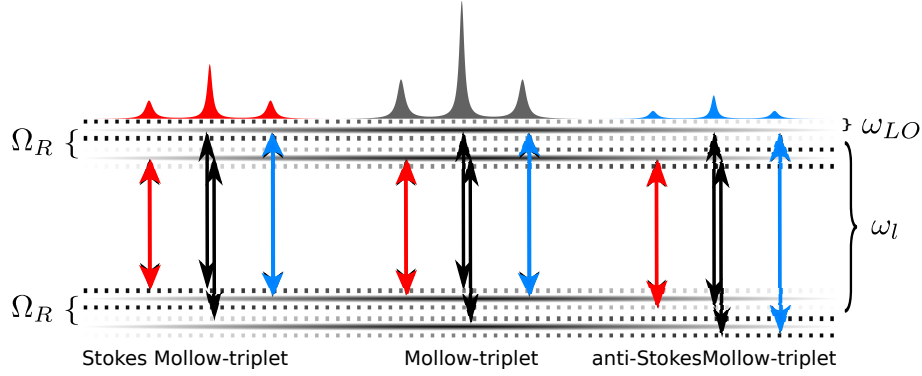


Figure 4.4.: Scheme of a QD interacting with a strong laser field (resonant excitation). The dotted lines indicate the (first order) interaction with the LO-phonons. In the strong excitation regime, additional triplets appear at the positions of the phonon satellites  $\omega_l \mp \omega_{LO}$  ( $\mp \Omega_R$ ) (positions of the Raman scattering lines).

bare system energy  $\epsilon_s - \epsilon_{cv} = \hbar(\omega_s - \omega_{cv})$ . The spectrum is broadened due to a pure dephasing of  $\gamma_{pd} = 0.05/ps$  and a radiative decay of  $\Gamma_r = 0.005/ps$ . The QD is assumed to be excited at its bare electronic resonance, which leads to a slightly detuned excitation frequency of the laser with respect to the new phonon induced polaron shifted QD resonance  $\omega_{cv}^p = \omega_{cv} - \frac{g^2}{\omega_{LO}}$ . In the weak excitation regime (blue plot), this results in a spectral separation of the Rayleigh (Raman) and the fluorescence (phonon-assisted fluorescence) lines and peaks. In the Mollow-triplet regime (pink curve), same as in Fig. 4.3, the frequency

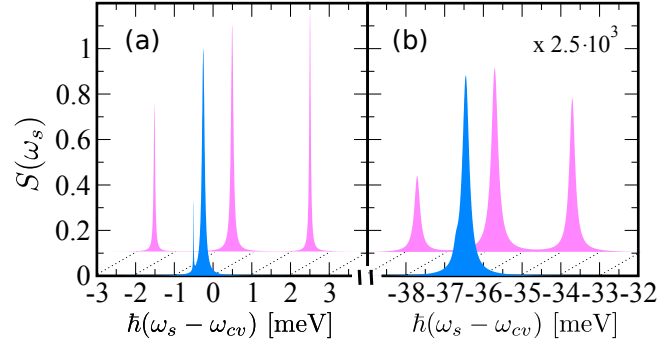


Figure 4.5.: Emission spectrum of a QD interacting with LO-phonons (a) in the range of the bare QD resonance  $\hbar\omega_{cv}$  in the weak- (blue curve in the front) and in the strong excitation regime (pink curve in the back). (b) Spectrum in the spectral range of the first order Stokes Raman energy  $\hbar\omega_l - \hbar\omega_{LO}$ . The phonon assisted triplet is additionally broadened by the background and the short LO-phonon lifetime  $\kappa^{-1}$ .

detuning leads to an asymmetry of the Mollow triplet [Fig. 4.5(a)] and changed ratios between the heights of the triplet center and the Mollow sidebands. Due to the interaction

with the LO-phonons, at a multiple of a phonon frequency, phonon-assisted Mollow-triplet satellites appear, centered around the Raman resonances, cp. Fig. 4.4. Figure. 4.5(b) shows the spectral area around the first order Stokes Raman resonance  $\epsilon_s = \epsilon_l - \epsilon_{LO}$ . In the weak excitation regime (blue curve), it exhibits the first order phonon assisted fluorescence peak and the Raman Stokes satellite (only indicated as a kink), while in the strong excitation regime, there is a formation of a phonon assisted Mollow triplet, centered at the Stokes Raman frequency  $\omega_l - \omega_{LO}$ . The phonon structures appear to be strongly broadened in comparison to the peaks at the bare systems resonance. The reason is, that phonon-related structures are relatively weak, so that they are additionally broadened by the background (radiative and pure dephasing) of the much more intense features close the band gap energy. Further, the LO-phonons are assumed to have a finite (and relatively short) lifetime, as compared with the rest of the dissipative timescales. This is however in the regime, where the Rabi-frequency of the exciting laser field is still much smaller than a phonon frequency  $\Omega_R \leq \omega_{ph}$ . For sufficiently strong external laser strengths, the spectrum exhibits a variety of spectral features, which are due to the formation of additional quasi-particles of electron, light-field and phonons.

#### 4.3.1. Anti-crossings of the Mollow-sidebands and the Mollow-triplet centers

The Mollow triplet sidebands are usually spectrally positioned in the distance of the Rabi-frequency  $\Omega_R$  (at resonant excitation) with respect to the laser frequency  $\omega_l$ . Therefore, for a Rabi-frequency  $\Omega_R \approx \omega_{LO}$  the sidebands of the bare Mollow triplet would cross the central peaks of the phonon assisted triplets at  $\omega_l \mp \omega_{LO}$  and vice versa.

Figure 4.6 shows the spectrum in the spectral area about the main triplet resonance 4.6(a) at  $\omega_l$  and the area around the 1st order Stokes triplet 4.6(b) at  $\omega_l - \omega_{LO}$  for the case of matching phonon- and Rabi-frequency  $\Omega_R = \omega_{LO}$ . Apparently, instead of melting triplet sidebands and centers, additional spectral features appear. In the case of the Stokes triplet, the central peak has obviously disappeared in favor of a variety of peaks in its proximity. As it is hard to analyze those features in the spectrum for only one snapshot of the Rabi-frequency  $\Omega_R$ , the spectrum is now plotted over the varying Rabi-frequency, normalized with an LO-phonon frequency  $\frac{\Omega_R}{\omega_{LO}}$ . The spectrum is calculated for resonant  $\omega_l = \omega_{cv}$  [Fig. 4.7(a)] and detuned  $\omega_l = \omega_{cv} - \Delta$  [Fig. 4.7(a)] optical excitation. The  $x$ -axis is the deviation of the emitted frequency minus the band-gap frequency  $\omega_s - \omega_{cv}$ , also divided by  $\omega_{LO}$ . Thus, for resonant excitation, the main-triplet is centered at 0 and the phonon satellite triplets are centered at  $\mp 1$ .

In the case of resonance between the laser frequency with the bare electronic transition frequency  $\omega_l = \omega_{cv}$  [Fig. 4.7(a)], the evolution of the Mollow sidebands goes linear with the laser strength. However, when the Rabi-frequency enters the regime  $\Omega \approx \omega_{LO}$  ( $x = y = 1$ ), the 3D-plot nicely illustrates an anticrossing of the triplet sidebands with the triplet centers. Instead of mixing with the  $(n + 1)$ th order phonon satellite triplet center, the  $n$ th order phonon assisted lower energy triplet sideband blends into the higher energy sideband of the  $(n + 2)$ th order (and vice versa). This higher order triplet center itself performs an anticrossing with the  $(n + 1)$ th order triplet center etc. In Fig. 4.7(a) this behavior is

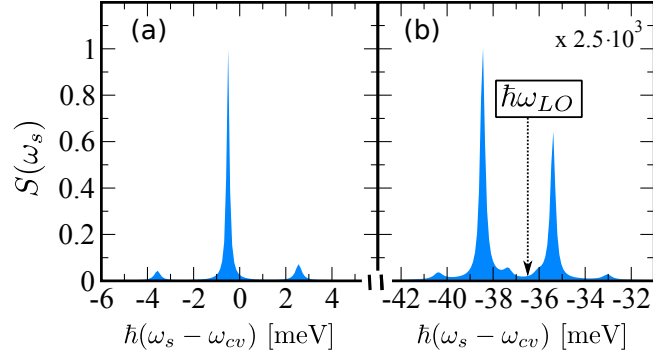


Figure 4.6.: Emission spectrum of a QD interacting with LO-phonons in the strong excitation regime with  $\hbar\Omega_R \approx \hbar\omega_{LO}$ . (a) shows the spectral area about the QD resonance  $\omega_{cv}$  [here  $\hbar(\omega_{cv} - \omega_l) = \hbar\frac{g^2}{\omega_{LO}}$  corresponds to the polaronshift]. In this spectral area, the spectrum does consist of a strongly modified, but still triplet-like structure (not Mollow-triplet). (b) shows the area about the Stokes position  $\hbar(\omega_l \mp \omega_{LO})$ . The dashed line in (b) indicates the usual position of the anti-Stokes Raman line, at which the spectrum now exhibits a minimum (anticrossing) with several spectral features in its proximity.

most strikingly demonstrated at the frequency position of the 1st Stokes Raman frequency at  $(x = -1, y = 1)$ . At this frequency position several spectral structures coincide: The three most pronounced features at this position are (i) the lower energy Mollow sideband originating from the main triplet emerging from the right, (ii) the 1st order Stokes triplet center that is positioned at  $\omega_l - \omega_{LO}$  and (iii) the higher energy sideband of the 2nd order Stokes triplet emerging from the left. As is clearly visible, these three peaks do not cross, but exhibit an anticrossing. This behavior can be observed at all triplet centers for that particular excitation strength. The sidebands seem to get averted at some point, and then blend in together with the lower/higher energy sideband of the higher/lower order triplet. Further, especially the phonon assisted triplet centers additionally collapse during the anticrossing  $(x = -1, y = 1)$ , as already depicted in Fig. 4.6(b). While in the regime  $\Omega_R \leq \omega_{LO}$  a considerable proportion of the emission intensity was collected at the Raman-frequencies  $\omega_s = \omega_l \mp n\omega_{LO}$ , there is almost no emission originating at these frequencies for  $\Omega_R \approx \omega_{LO}$  anymore (at the anticrossings). Obviously, the phonon satellites experience an additional frequency splitting. A small decrease of the 0th order triplet center i.e. at the bare laser frequency  $\omega_l = \omega_{cv}$  (here 0) is visible as well. In total, the emission strength of the triplet centers is diminished in favor of an enhanced emission at the sidebands, which constructively interfere with the central peaks. Note, that the splittings of the triplet centers also occur at the anti-Stokes positions  $\omega_l + \omega_{LO}$ . In fact, the anti-Stokes features are only revealed via the anti-crossings at  $\Omega_G = \omega_{LO}$ , as they are dependent on a here vanishing LO-phonon number for the weak excitation regime.

A similar behavior is illustrated for a detuned optical excitation in Fig. 4.7. Since here, the Rabi-frequency is modified with the frequency detuning  $\Delta$  of the laser with respect to the QD transition frequency, the Mollow triplet sidebands evolve nonlinearly with the

laser strength, i.e. with the generalized Rabi-frequency  $\Omega_G = \sqrt{\Omega_R^2 + \Delta^2}$  [AE75]. Note, that due to the stronger generalized Rabi-frequency  $\Omega_G > \Omega_R$ , the anticrossings occur at lower actual laser powers. In Fig. 4.7(b) the laser is spectrally positioned at one half of a

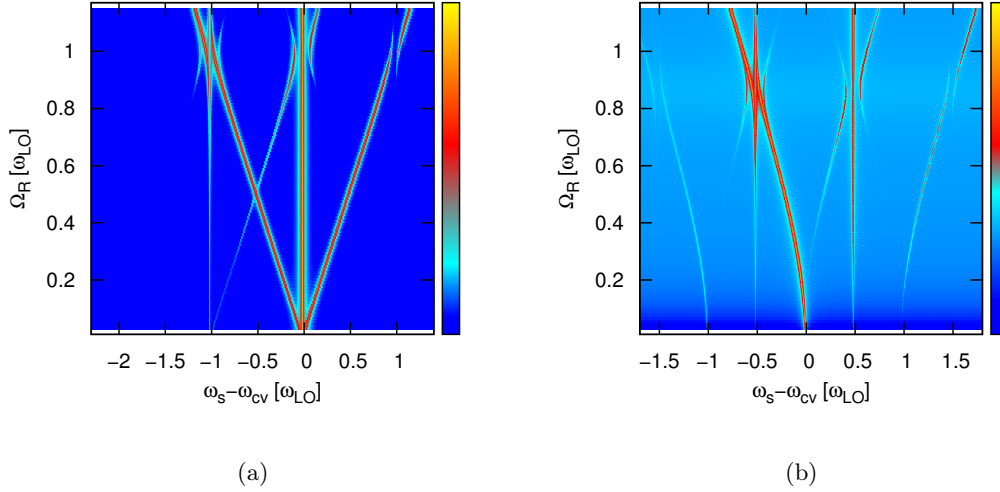


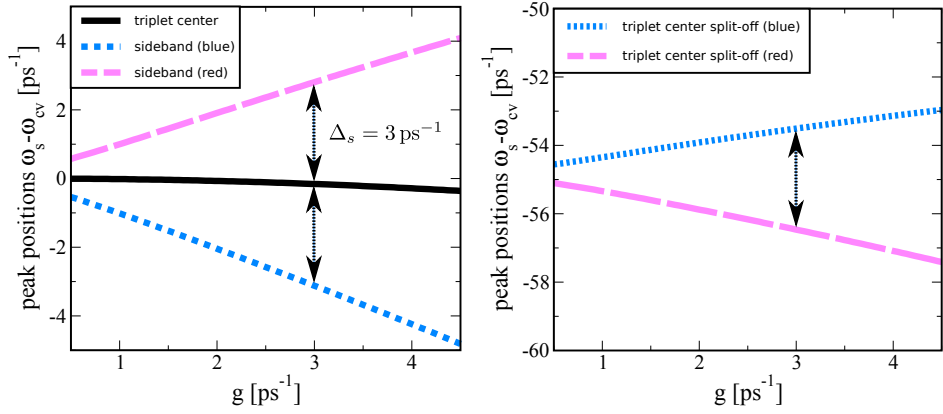
Figure 4.7.: Emission spectrum of a QD over varying laser strength. (a) For resonant optical excitation  $\omega_l = \omega_{cv}$ , the spectrum exhibits the Mollow triplet and additional phonon-assisted Mollow triplets centered about  $\omega_s = \omega_l \mp n\omega_{LO}$ . At  $(x = \mp n, y = 1)$  further anticrossings between the sidebands and the centers (also split) occur. (b) For spectrally detuned optical excitation  $\omega_l = \omega_{cv} + \Delta$  (at  $\Delta = \frac{\omega_{LO}}{2}$ ) the anticrossings and splittings appear earlier due to  $\Omega_G = \sqrt{\Omega_R + \Delta^2}$ . At low powers  $\Omega_R \approx 0$ , the triplet sidebands emerge at a spectral distance of  $\Omega_G \approx \Delta \hat{=} 0.5$  from the respective central peak.

phonon frequency ( $\omega_l = \omega_{cv} + \Delta$ , and  $\Delta = \frac{\omega_{LO}}{2}$ ) with respect to  $\omega_{cv}$ , so that the main Mollow triplet center appears at  $x = 0.5$ . The spectral distance of the triplet sidebands from the center frequencies are significantly larger, than in the resonant case and the anticrossings and center-splittings appear below  $x = 1$ . Since at comparably small  $\Omega_R \rightarrow \Omega_G = \sqrt{\Omega_R^2 + \Delta^2} \approx \Delta$ , the lower/higher energy triplet sidebands of the main Mollow triplet start in Fig. 4.7(b) at  $x = 0/x = 1$ . The phonon-assisted features are, as before, spectrally distanced with  $n\omega_{LO} \hat{=} nj$ , ( $j \in \mathbb{Z}$ ). However, the behavior of the peaks (triplet sidebands and -centers) remains qualitatively the same as in the resonant case [Fig. 4.7(a)]. This means, that it may be of advantage, changing to a spectrally detuned excitation, in order to observe the anticrossings at reduced laser strengths, given, that the anticrossings still appear for large laser frequency detunings  $\Delta$ .

### 4.3.2. Strength of the anticrossings of the sidebands and the splittings of the phonon satellites

At resonant excitation, the anticrossings of the phonon satellites and the splittings of the phonon assisted triplet centers occur at an excitation strength of  $\Omega_R \approx \omega_{LO}$ . The strength of these splittings, however, can be expected to depend on the collective electron-phonon coupling strength  $g$  of Eq. (4.6) [See Tab. 4.2].

In order to determine the functional dependence of the anticrossing- and splitting frequen-



(a) Anticrossings at the main Mollow triplet center

(b) Splitting of the Stokes Mollow triplet center

Figure 4.8.: (a) Spectral positions of the phonon assisted triplet sidebands  $\omega_s = \omega_l + \omega_{LO} - \Omega_R$  (pink dashed curve) and  $\omega_s = \omega_l - \omega_{LO} + \Omega_R$  (dotted blue curve) that perform anticrossings (arrows) with the main Mollow triplet center at  $\omega_s = \omega_l$  (solid black curve). The anticrossing strength grows with increasing  $g$ . (b) Splitting of the Stokes-triplet central peak at  $\omega_s = \omega_l - \omega_{LO}$  into two peaks. The excitation strength is held at  $\Omega_R = \omega_{LO}$ . The laser frequency is adjusted to the polaron shifted QD resonance at  $\omega_l = \omega_{cv} - \frac{g^2}{\omega_{LO}}$ .

cies, the spectral positions  $\omega_s - \omega_{cv}$  of those features are plotted over varying collective electron phonon coupling  $g$ . The optical excitation strength is kept at  $\Omega_R = \omega_{LO}$ , i.e. at the laser strength, where the anticrossings and splittings occur. Figure 4.8(a) shows the evolution of the peak positions of the features about the excitation frequency. These are the main triplet center at  $\omega_s = \omega_l = \omega_{cv}$  (black curve) and the two phonon assisted triplet sidebands: (pink dashed curve) the lower energy triplet sideband at about  $\omega_s = \omega_{cv} + \omega_{LO} - \Omega_R$  originating from the anti-Stokes triplet and (blue dashed curve) the higher energy triplet sideband at about  $\omega_s = \omega_{cv} + \omega_{LO} - \Omega_R$  originating from the Stokes triplet. At a Rabi-frequency of  $\Omega_R = \omega_{LO}$ , the three lines would coincide in their spectral positions  $\omega_s$ :

$$\omega_s = \begin{cases} \omega_l, & \text{main triplet center} \\ \omega_l + \omega_{LO} - \Omega_R, & \text{Anti-Stokes sideband (red)} \\ \omega_l - \omega_{LO} + \Omega_R, & \text{Stokes sideband (blue),} \end{cases} \quad (4.38)$$

But instead they are spectrally separated due to the anticrossing/splitting. As can be seen from Fig. 4.8(a), the anticrossing strengths  $\Delta_s$  (spectral separation of the sidebands with respect to the main peak indicated by the arrows) increases with the  $g$ .

A similar behavior is visible for the frequency splitting of the phonon-assisted triplet center into to separate peaks. Figure 4.8(b) shows the spectral area about the Stokes Mollow triplet center  $\omega_s = \omega_l - \omega_{LO}$ . As already discussed at Fig. 4.7, the phonon assisted Mollow centers split into two peaks for a laser strengths with  $\Omega_R = \omega_{LO}$ . Apparently, the strength of these splitting is increasing with  $g$  as well. As indicated with the arrows, the sidebands-anticrossings and the splitting of the phonon-assisted triplet center is apparently of the same order of magnitude.

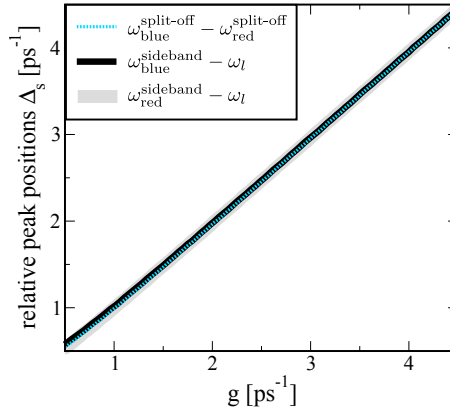


Figure 4.9.: Spectral separation  $\Delta_s$  of the neighboring peaks of Fig. 4.8(a) and (b) over varying  $g$ . Dashed turquoise curve: splitting strength of the Stokes-triplet center into two peaks. Black/grey curves: anticrossing strength of the Stokes- and the anti-Stokes sidebands with the main triplet central peak. ( $\Omega_R = \omega_{LO}$ ).

Since all the spectral features (for excitation at the polaron shifted QD resonance  $\omega_{cv} = \omega_{cv}^p(g)$ ) are additionally moving with  $g$  (polaronshift  $\frac{g^2}{\omega_{LO}}$ ) it is hard to tell from Fig. 4.8, if the anticrossing- and splitting strengths are indeed linear in  $g$ . However, plotting the spectral separations  $\Delta_s$  between the vicinal peaks of Fig. 4.8 against varying  $g$  actually confirms the linear dependence of the sideband anticrossings, as well as the center splittings with the collective electron-phonon-coupling  $g$ , Fig. 4.9: Hence, the anticrossings and splittings are a direct result of the formation of new quasi particles, occurring at sufficiently high laser strengths. The various peak positions, that the spectrum exhibits at Rabi-frequency  $\Omega_R = \omega_{LO}$  are listed in Tab. 4.2. With that knowledge, the strong driving regime introduces a possibility of measuring the electron-phonon coupling strength via the Huang-Rhys factor ( $F = \frac{g^2}{\omega_{LO}^2}$ ) in an optical spectroscopy experiment. As here,  $g$  is determined by the spectral position of particular features in the spectrum, the delicate measurement [SDW<sup>+</sup>11, HMS<sup>+</sup>99, HBG<sup>+</sup>01] of the relative peak height  $\mathcal{E}_{\text{satellite}} = e^{-F} F$  (first order phonon satellite peak height) of the phonon satellite with respect to the main fluorescence peak can be avoided.

The anticrossings also occur for a detuned optical excitation [c.f. Fig. 4.7], and at much

Contribution	Detected signal	Color shift
Main triplet center	$\omega_s = \omega_{cv}$	non
$n$ -th order Anti-/Stokes triplet center	$\omega_s = \omega_{cv} \mp \omega_{LO} - \Omega_R - \frac{g}{2}$	red
$n$ -th order Anti-/Stokes triplet center	$\omega_s = \omega_{cv} \mp \omega_{LO} - \Omega_R + \frac{g}{2}$	blue
Main anticrossing	$\omega_s = \omega_{cv} - g$	red
Main anticrossing	$\omega_s = \omega_{cv} + g$	blue
$n$ -th order Anti-/Stokes anticrossing	$\omega_s = \omega_{cv} \pm n\omega_{LO} - \Omega_R + g$	red
$n$ -th order Anti-/Stokes anticrossing	$\omega_s = \omega_{cv} \mp n\omega_{LO} + \Omega_R - g$	blue

Table 4.2.: Spectral positions of the sidebands anticrossings and center splittings at an excitation frequency of  $\Omega_R = \omega_{LO}$ . (resonant excitation).

smaller Rabi-frequencies, namely  $\Omega_R = \sqrt{\omega_{LO}^2 - \Delta^2}$ . However, as visible from Fig. 4.10, the quasi-particle features at  $\Omega_G = \omega_{LO}$  are getting less pronounced with increasing detuning  $\Delta$ .

The key finding of the previous discussion is, that the emission spectrum in the strong excitation regime exhibits phonon-assisted Mollow triplets at  $\Omega_G \leq \omega_{LO}$  and additional polaron features such as anticrossings and frequency splittings for  $\Omega_G \approx \omega_{LO}$ . Since these features are directly proportional to the collective electron-phonon coupling strength, the peak positions and energy splitting allow an alternative measure of  $g$  or the Huang-Rhys-factor, if exciting the QD in this regime. These features occur for any given temperature and independent of the intensity of phonon-assisted peaks.

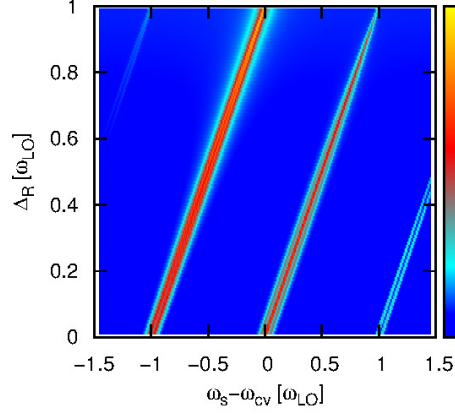


Figure 4.10.: Spectrum of a QD for varying laser frequency detuning  $\Delta$  at a Rabi-frequency shifted with the excitation strength position, where the anticrossings occur

$$\Omega_R(\Delta) = \sqrt{\omega_{LO}^2 - \Delta^2}.$$

## 4.4. Time-resolved light emission from semiconductor quantum dots

While in the stationary regime, the different contributions to the spectrum can be discriminated via their spectral position or linewidth, the time dependent spectrum also gives information about their different temporal behavior. In the following, the dynamics of the emission lines and peaks will be investigated for weak to strong pulsed optical excitation. The time-resolved spectrum allows to analyze build-up and decay dynamics of the above discussed strong electron-phonon coupling features in the spectrum. Since the assumption of a steady state, i.e. the calculation of the emissions spectrum via the power spectrum formula (4.25) is not valid for a pulsed optical excitation, the full multi-mode field expansion of the emitted light field is now incorporated according to Eq. (4.12)-(4.12).

### 4.4.1. Time-resolved signal

The time resolved Spectrum is given by the intensity

$$S(r_s, \omega_s, t) = \langle E_s^-(r_s, t) E_s^+(r_s, t) \rangle, \quad (4.39)$$

measured at a time-resolving spectrometer and detector [EW77] [See Fig. 4.11]. Here  $E_s^{(-)}$  and  $E_s^{(+)}$  denote the positive and the negative rotating frequency part of the detected electromagnetic light field. Corresponding to Fig. 4.11, the detected field is temporally, and spectrally filtered before being detected. The filtering process is described via a convolution of the incoming field  $E^{(\pm)}(r, t)$  with a filtering function (here chosen as Gaussian

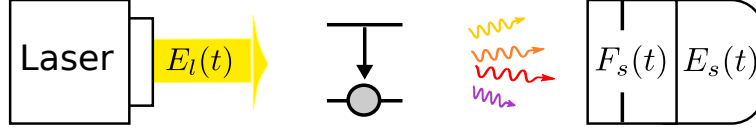


Figure 4.11.: Scheme of the experimental setup for measuring the time-resolved spectrum  $S(r_s, \omega_s, t)$ . The sample is excited with a pulsed laser field  $E_l(t)$  and emits photons into a continuum of optical modes. The emission is spectrally filtered (filtering function  $F_s(t)$ ) and measured as  $E_s(t)$  with a time-resolving detector.

$F_s(t) = e^{-\frac{t}{\sqrt{2}\Delta t}} e^{-i\omega_s t}$ , which simulates the time- and frequency resolution of the supposed experimental setup [Sto94]:

$$E_s^{(\pm)}(r_s, t) = \int_{-\infty}^{\infty} dt' F_s^{(*)}(t - t') E^{(\pm)}(r_s, t'). \quad (4.40)$$

Inserting this definition of the detected light field into the expression for the intensity Eq. (4.39) at the detector results in the "physical spectrum" as introduced in Ref. [EW77]

$$S(r_s, \omega_s, t) = \int_{-\infty}^{\infty} dt'_1 \int_{-\infty}^{\infty} dt'_2 F_s(t - t'_1) F_s^*(t - t'_2) \langle E^{(-)}(r_s, t'_1) E^{(+)}(r_s, t'_2) \rangle. \quad (4.41)$$

Reviewing this formula reveals, that the formula for the Power spectrum corresponds to a filter with an infinitely sharp spectral resolution, i.e.  $F_s(t) = e^{-i\omega_s t}$ . According to Ref. [KJHK99], the integrals are eliminated in favor of a multi-mode electromagnetic field expansion and applying a far field approximation for  $E(z, t)$ . Following this procedure, the time-resolved signal is evaluated, calculating the photon-coherences  $\langle c_{\mathbf{k}_1}^\dagger c_{\mathbf{k}_2} \rangle$  for any pair of  $\mathbf{k}_1$  and  $\mathbf{k}_2$ , using [EW77, KJHK99, KWH<sup>+</sup>10]

$$\begin{aligned} S(z\mathbf{e}_z, \omega_s, t) &= \sum_{k_1, k_2} \frac{\hbar \sqrt{\omega_{k_1} \omega_{k_2}}}{2\epsilon_0 c^2 V} \langle c_{k_1}^\dagger c_{k_2} \rangle e^{-i(k_1 - k_2)z} \\ &\times e^{-\left\{ \frac{[(k_1 - k_D)c\Delta t]}{\sqrt{2}} \right\}^2} e^{-\left\{ \frac{[(k_2 - k_D)c\Delta t]}{\sqrt{2}} \right\}^2} \end{aligned} \quad (4.12)$$

for the propagation of the emission in  $z$ -direction. The two frequency mode photon coherences  $\langle c_{k_1}^\dagger c_{k_2} \rangle$ , which determine the spectrum  $S(z\mathbf{e}_z, \omega_s, t)$  couple to the photon-assisted polarizations [KWH<sup>+</sup>10, KK06]

$$\begin{aligned} \frac{d}{dt} \langle c_{k_1}^\dagger c_{k_2} \rangle &= -i(\omega_{k_1} - \omega_{k_2}) \langle c_{k_1}^\dagger c_{k_2} \rangle \\ &-i \{ M_{k_1} P_{(0|0)}^{(k_2|0)} - (M_{k_2} P_{(0|0)}^{(k_1|0)})^* \}. \end{aligned} \quad (4.13)$$

and therefore to the set of equations given by Eqs. (4.11)-(4.12). Neglecting again any backaction terms of the emission modes, according to Eq. (4.15) the set can be simplified

to a set of equations as given in Appendix (A.6)-eqA.8. As initial condition, the QD is assumed to start in the ground state  $|v\rangle$ . Further, the emission modes  $\{k\}$  are assumed to be unoccupied at the beginning, so that photon-assisted quantities are set to zero at  $t = 0$ . The phonons are assumed to be in an initial thermal equilibrium at the beginning, so that the phonon correlations can be calculated using Wick's theorem [Lou73], modified with the collective coupling strength:

$$N_{(n|n)}^{(0|0)} \equiv \langle B^{\dagger n} B^n \rangle(0) = n! N_{\text{ph}}^n g^n. \quad (4.14)$$

Further, combined phononic and electronic operator correlation expectation values are factorized before the arrival of the external light pulse:

$$\begin{aligned} \langle V_{(n|n)}^{(0|0)} \rangle(t=0) &= \langle a_v^\dagger a_v^\dagger B^{\dagger n} B^n \rangle(0) = \langle a_v^\dagger a_v \rangle \langle B^{\dagger n} B^n \rangle(0) \\ &= \langle V^{(0|0)} \rangle \langle B^{\dagger n} B^n \rangle(0). \end{aligned} \quad (4.15)$$

#### 4.4.2. Temporal emission dynamics

In the weak excitation regime, the fluorescence- and scattering (Rayleigh and Raman) contributions can be spectrally resolved [See Tab 4.1]. For pulsed excitation, the different contributions can further be discriminated via their different temporal behavior. While the elastic and inelastic scattering contributions are present in the spectrum only during the excitation with the pulse, the lifetime of the fluorescence contributions usually surpass the timescale of a short laser pulse. In the fluorescence processes, the emitter is excited into a higher state, which subsequently decays back into the ground state via spontaneous emission of photons. Therefore, the lifetime of the fluorescence peaks is given by the lifetime of the excited state density (for the two-level case), i.e, the radiative decay  $\Gamma_r$ . However, the Rayleigh and Raman-scattering is characterized by the excitation into a virtual intermediate state [See Fig. 4.1], given by the laser frequency. Effectively, the electron remains in the groundstate, while the laser light is scattered with frequency  $\omega_s = \omega_l$  (elastic  $\rightarrow$  Rayleigh) or  $\omega_s = \omega_l \mp n\omega_{LO}$  (inelastic  $\rightarrow$  Raman).

##### 4.4.2.1. Time-resolved spectrum in the weak excitation regime

Figure 4.12 shows the temporal evolution of the full emission- and scattering spectrum of the QD at excitation with a short Gaussian laser pulse (FWHM=4 ps), that is centered at time  $\tau_0 = 12$  ps. The laser has a frequency detuning of  $\Delta = \frac{\omega_{LO}}{2}$  from the polaron shifted electronic resonance  $\omega_{cv}$  and a maximum pulse strength of  $\Omega_{\text{max}} = \Omega_R(\tau_0) = 0.1$  meV. Note, that at this excitation strength, the spectrum is already exhibiting the Mollow triplet in the power spectrum. The short temporal width of the excitation pulse with  $\Delta\tau = 4$  ps necessarily results in a large spectral width of the total spectrum, so that all emission lines and peaks are spectrally broadened beyond the radiative or pure dephasing ( $\Gamma_r, \gamma_{pd}$ ). The effect of this time-dependent spectral broadening is, that dressed state signatures (such as a Mollow triplet in the stationary regime) are suppressed in the spectrum up to excitation strengths, comparable to the inverse pulse length  $\Delta\omega = \frac{1}{\Delta t}$ . Although the maximum pulse strength  $\Omega_{\text{max}}$  well surpasses the radiative lifetime of the excited state, the spectrum

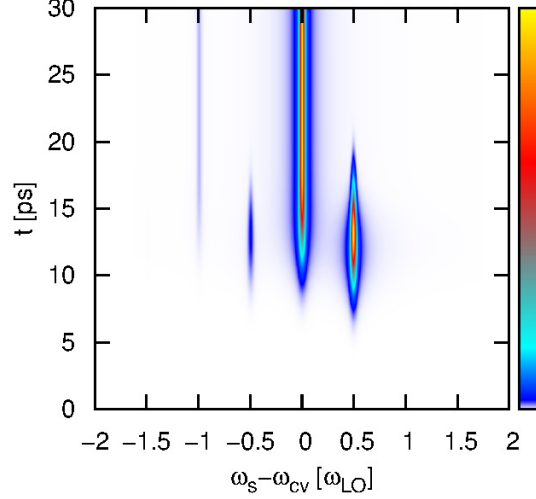


Figure 4.12.: Time-resolved spectrum of the QD for weak pulsed optical excitation (Gaussian pulse shape with FWHM=4 ps). The QD is excited between the main resonance and the anti-Stokes position at  $\omega_l = (\omega_{cv} + \omega_{LO}/2)$ . The main spectral contributions are (i) the Rayleigh scattering *line* at  $\omega_s = \omega_l$  ( $x = 0.5 \hat{=} \frac{\omega_{LO}}{2}$ ), (ii) the Stokes-Raman scattering at  $\omega_s = \omega_l - \omega_{LO}$  ( $x = -0.5 \hat{=} -\frac{\omega_{LO}}{2}$ ), (iii) the main fluorescence contribution at  $\omega_s = \omega_{cv}$  ( $x = 0$ ) and (iv) the phonon-assisted fluorescence (Stokes) at  $\omega_s = \omega_{cv} - \omega_{LO}$  ( $x = -1 \hat{=} \omega_{LO}$ ). The initial temperature is  $T = 4$  K.

exhibits no signs of a Mollow-triplet formation. Instead, the different contributions (fluorescence and scattering) can clearly be distinguished by their spectral positions and their evolution in the time domain. These are here the fluorescence peaks, originating from direct emission at the electronic bandgap energy  $\omega_s - \omega_{cv} = 0$  and the phonon assisted emission in the spectral distance of an LO-phonon frequency  $\omega_s - \omega_{cv} = \mp\omega_{LO}$  and the scattering contributions Rayleigh  $\omega_s - \omega_{cv} = \Delta$  and Raman  $\omega_s - \omega_{cv} = \Delta - \omega_{LO}$ . For the sake of clarity all simulations are done at an initial temperature of 4 K. Therefore, the higher frequency phonon satellites (anti-Stokes) are hardly visible neither for the fluorescence nor the scattering contributions due to the small average phonon number  $\bar{N}_{LO}$ . Since the pulse is still relatively weak, compared with the excitation duration, the initial phonon number obviously remains low after the pulse. Heating or induced phonon emission, that could be caused by the optical excitation is here negligible. In contrast, the lower energy phonon satellites are clearly visible, as it comes along with the spontaneous emission of phonons.

***Dynamics of the Fluorescence emission:***– However, all the fluorescence contributions, visible in Fig. 4.12 build up while the pulse is present and still gain in strength

during the negative slope of the pulse. Further, they remain visible well after the pulse has been switched off. In this simple two-level case, the lifetime of the excited state density coincides with the lifetime of the fluorescence contributions. There is no in- or out-scattering via additional radiative- or non-radiative processes between further electronic levels. This could drastically change the fluorescence emission dynamics [WRW<sup>+</sup>11, KR10] of a nanostructure, as will be discussed in Sec. 4.5.

**Dynamics of the scattering contributions:**– In contrast to that, the temporal evolution of the scattering contributions at the spectral position of the laser  $\omega_s = \omega_l$  and in the distance of an LO-phonon energy  $\omega_s = \omega_l \mp \omega_{LO}$  just mimic the slope of the pulse. With the same explanation as for the fluorescence peaks, only the Stokes-Raman scattering at  $\omega_s = \omega_l - \omega_{LO}$  is strong enough in comparison to the main peaks, in order to be visible in the spectrum.

#### 4.4.2.2. Time-resolved spectrum in the strong excitation regime

Figure 4.13 shows the time-resolved spectrum under the same excitation conditions as in Fig. 4.12, but for a strong laser pulse (compared with the spectral width of the pulse). Such as in the stationary case, in the regime of strong pulsed optical excitation, the emission spectrum of the QD exhibits a variety of additional features, while on the other hand it is lacking the typical (perturbative) spectral separation of the scattering and fluorescence contributions during the pulse. Due to the formation of dressed states (which evolve in time due to the  $\Omega_G(t)$ ), scattering and fluorescence cannot be discriminated anymore, neither in the spectral nor the temporal domain. Further, there is a multiple of additional sidebands emerging from the the central peaks. These emission structures can be attributed to the fact, that for pulsed excitation the laser pulse has a spectral and temporal width, causing interference of emission contributions at different times and frequencies [FRZ85, MKLM12]. Note, that in the positive slope of the pulse, these extra sideband peaks are occurring below the snapshot Mollow-frequency ( $\omega_s < \Omega_G$ ), while in the negative slope of the pulse they have a blue color shift ( $\omega_s > \Omega_G$ ). Without considering an explicit electron-phonon interaction, the occurrence of the red shifted sideband peaks is discussed for example in Ref. [MKLM12], linking the appearance of these multiple peaks to the pulse area.

This work however is focused on the extra phonon features in the spectrum and their temporal behavior. Most of the sideband emission is still collected about the usual Mollow-triplet frequencies at  $\omega_l(\mp \hbar\omega_{LO}) \mp \hbar\Omega_G(t)$ . As the Rabi-frequency  $\Omega_R(t)$  is now time-dependent, the sidebands occurring at about  $\omega_l(\mp \hbar\omega_{LO}) \mp \Omega_G(t)$  follow the temporal evolution of the now time-dependent generalized Rabi-energy  $\hbar\Omega_G(t)$ . Due to the detuned optical excitation, the sidebands again show an asymmetry with respect to the emission strength and therefore also with respect to the raising and the trailing edge of the pulse shape. In particular, this can be recognized in the lower energy Mollow sidebands, exhibiting much higher intensities in the down-slope, compared to the up-slope of the excitation pulse. The Gaussian laser pulse however is symmetric in time. This temporal asymmetry of the sidebands intensity can be explained as follows: In contrast to the higher energy Mollow sidebands, the lower energy Mollow sidebands (main and phonon assisted) start at the undressed electronic- ( $\omega_D - \omega_{cv} = 0$ ) and phonon assisted systems resonances ( $\omega_D - \omega_{cv} = \mp \omega_{LO}$ ).

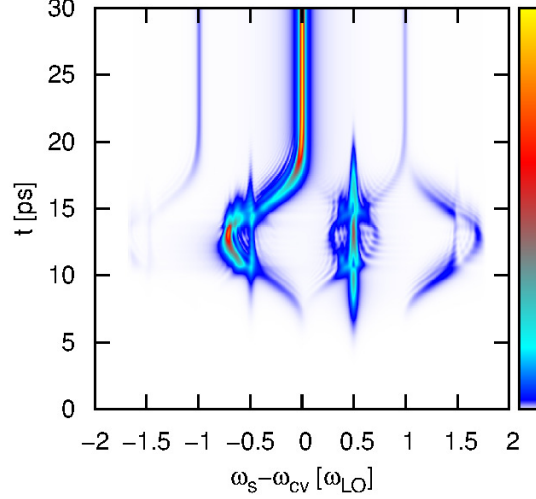


Figure 4.13.: Time-resolved spectrum of the QD for strong pulsed optical excitation (Gaussian FWHM=4 ps). The QD is excited between the main resonance and the anti-Stokes positions  $\omega_l = (\omega_{cv} + \omega_{LO}/2)$ . The main features are central peaks at the former scattering frequencies (i) (Rayleigh position)  $\omega_s = \omega_l$  ( $x = 0.5 \hat{=} \frac{\omega_{LO}}{2}$ ), (ii) (Stokes-Raman position)  $\omega_s = \omega_l - \omega_{LO}$  ( $x = -0.5 \hat{=} -\frac{\omega_{LO}}{2}$ ) and Mollow-like sidebands evolving at about (iii)  $\omega_s = \omega_l \mp \Omega_G(t)$  and (iv)  $\omega_s = \omega_l - \omega_{LO} \mp \Omega_G(t)$ .

Such as in the stationary spectrum, this results in enhancement effects between the lower energy Mollow sidebands and the undressed systems resonances, at which the sidebands at first appear. In the down-slope of the pulse, the enhancements are stronger than during the rise time of the pulse. This is due to the fact, that the incoherent fluorescence contributions gets most intense, when the pulse and therefore the light dressed system states are decaying into the undressed system.

After the pulse at about 20 ps, the spectrum consists only of the usual fluorescence peaks at the systems transition frequencies  $\omega_{cv}(\mp\omega_{LO})$ , showing slow emission dynamics compared to the pulse following dynamics of the strong-coupling features. The central features at  $\omega_l \mp \omega_{LO}$  first increase rather smoothly together with the excitation pulse. However, at Rabi-frequencies comparable to the LO-phonon frequency  $\Omega_G(t) \approx \omega_{LO}$ , i.e. the anticrossing positions [See 4.2], this smooth pulse following behavior is interrupted by the additional strong-electron-light-phonon coupling features, discussed in the previous section. The Mollow-centers collapse, while the emission intensity is distributed to the Mollow (multiple) sidebands. Further, the phonon related splittings, which go proportional with the coupling strength  $g$  [See Fig. 4.9] also occurs in the pulsed case. It is of course less

resolved due to the large spectral width of the laser pulse and the multiple peak character of the Mollow sidebands. Due to the frequency detuning of the laser in Fig. 4.13, the lower frequency Mollow sidebands (main and phonon assisted) blend into the resonances at  $\omega_{cv} = 0$  and  $\omega_{cv} \mp \omega_{LO}$  [BCFM88], when the excitation pulse decays. The generalized Rabi-frequency is  $\Omega_G = \sqrt{\Omega_R^2 + \Delta^2} \approx \Delta$  in the case of comparably low pulse strengths.

#### 4.4.2.3. Evolution of the different spectral contributions

In Fig. 4.14(a), the temporal evolution of the most prominent features in the dynamic spectrum are compared for weak and strong pulsed excitation. In the weak excitation regime Fig. 4.14(a), it can nicely be seen, that the Rayleigh contribution (black curve) at  $\omega_s - \omega_{cv} = \omega_l$  is shaped just like the Gaussian pulse. A similar behavior is displayed for the anti-Stokes Raman scattering (grey curve) at  $\omega_s - \omega_{cv} = \omega_l - \omega_{LO}$ , also following the excitation pulse in its temporal dynamics. The fluorescence peak (red curve) at the electronic bandgap (red curve)  $\omega_s - \omega_{cv} = 0$ , and the lower energy phonon sideband (blue curve) at  $\omega_s - \omega_{cv} = -\omega_{LO}$  build up with a short temporal offset towards the Rayleigh and Raman scattering lines. At first the preceding polarization has to decay into the upper QD state

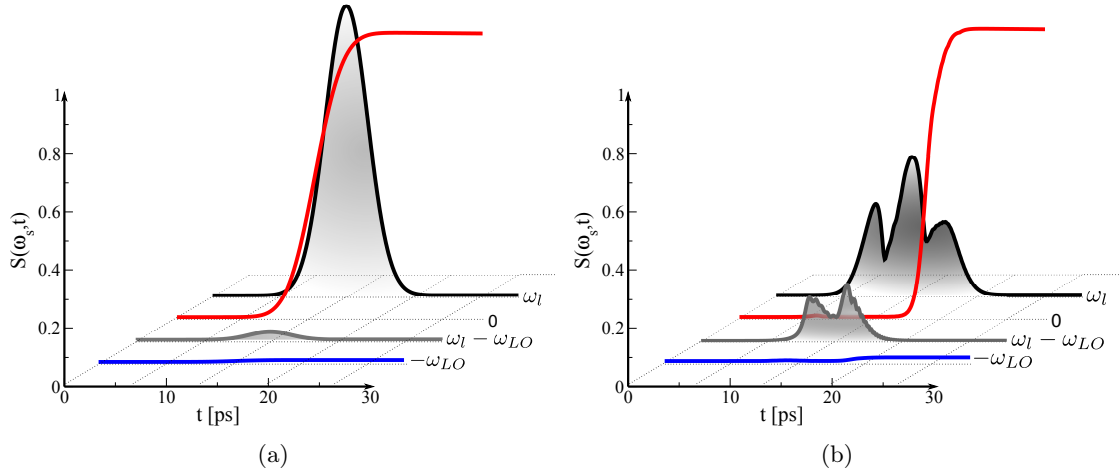


Figure 4.14.: Temporal evolution of the spectrum at different frequency positions for (a) weak and (b) strong pulsed excitation: Position of the laser (black curve)  $\omega_s - \omega_{cv} = \omega_l$ , the electronic bandgap (red curve)  $\omega_s - \omega_{cv} = 0$ , the anti-Stokes Raman frequency (grey curve)  $\omega_s - \omega_{cv} = \omega_l - \omega_{LO}$  and the lower energy phonon sideband (blue curve)  $\omega_s - \omega_{cv} = \omega_{cv} - \omega_{LO}$ .

density, before any fluorescence emission is possible.

In the strong excitation regime Fig. 4.14(b) the dynamics of the spectrum at the selected frequency positions are strongly changed. On the one hand due to time dependent dressed state formation and on the other hand because of light induced polaron features. During the up-slope of the pulse, the spectral feature positioned at the Rayleigh frequency (black curve), which now corresponds to the Mollow center exhibits a similar behavior, such as

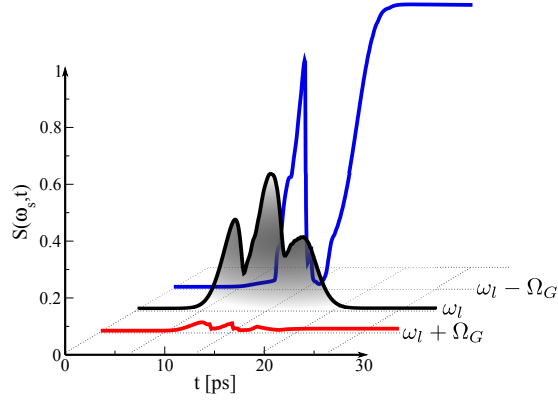


Figure 4.15.: Temporal evolution of the main central peak and the Rabi-sidebands: Position of the laser (black curve)  $\omega_s - \omega_{cv} = \omega_l$ , the lower energy Rabi-sideband (red curve)  $\omega_s - \omega_{cv} = \Delta - \Omega_G$  and the higher energy Rabi-sideband (blue curve)  $\omega_s - \omega_{cv} = \Delta + \Omega_G$ .

the Rayleigh scattering line in the left plot. At the beginning and the end of the pulse, the generalized Rabi-frequency is still well below an LO-phonon frequency  $\Omega_G(t) < \omega_{LO}$ . But instead of rising to the shape of the pulse, such as in Fig. 4.14(a) the central peak collapses two times. At those time-points, where the black curve exhibits its local minima, the Rabi-frequency just matches the phonon frequency  $\Omega_G \approx \omega_{LO}$ , leading to the anticrossings and frequency splittings, discussed in Sec. 4.3. Therefore, there are two collapses of the central peak, one in the positive slope- and one in the negative slope of the pulse 4.3.2. In direct comparison with the Raman line in the weak excitation regime, the central peak of the phonon related triplet (grey curve) is strongly enhanced. This is due to the proximity to the lower energy Rabi-sideband and a mutual amplification of neighboring structures. Apparently the phonon assisted center peak exhibits two maxima, which just occur at the two temporal minima of the main central peak. Obviously, in the strong excitation regime (in the range of an LO-phonon frequency), the emission structures at the Rayleigh and the Raman position do not have matching envelopes anymore. From Fig. 4.6, it was visible, that additionally to the anticrossing, there is a splitting of the phonon-assisted Mollow center. The strong enhancement of the emission intensity at the Raman position is due to a the broadened split-off peaks at  $\omega_s - \omega_{cv} = -\omega_{LO} \mp g$ . Further, due to the multiple peak structure of the time-resolved spectrum in the strong driving regime [FRZ85, MKLM12], there are several peak positions for the Rabi-sidebands due to time-frequency uncertainty of the actual instantaneous Rabi-frequency of the pulse at a certain point in time. Therefore the anticrossing- and splitting positions, in the stationary case sharply located at  $\omega_s - \omega_{cv} = \mp\omega_{LO}$  and  $\omega_s - \omega_{cv} = \mp\omega_{LO} \mp g$  [See Tab. 4.2], now also occur at a multiple of frequency-time-points. This results in the temporal oscillations of the envelope of the Raman peak (grey curve), as at different time points (corresponding to a multiple of Rabi-frequencies), the multiple peaks cross (or anticross) the Raman peak. In Figure 4.15, the temporal evolution of the spectrum at the Mollow-triplet positions, i.e.,

the Mollow-center frequency  $\omega_s - \omega_{cv} = \Delta$  and the lower and higher frequency Mollow-sideband positions  $\omega_s - \omega_{cv} = \mp\Omega_G$  are depicted. Due to the detuned excitation and the enhancement effects, discussed before, the lower energy sideband (red curve) is much more intense, than the higher energy sideband (blue curve). Same, as the central peak (black curve), the sidebands exhibit a rather bumpy temporal envelope, caused by anticrossings and splittings. The lower energy Rabi-sideband further exhibits a strongly asymmetric envelope, with most of the emission occurring in the down-slope of the pulse, as blending into the fluorescence peak that begins to build up while the pulse decays.

In conclusion to this section, the emission spectrum of a QD interacting with LO-phonons exhibits distinctive temporal dynamics of the quasi-particle features discussed in the previous section. As directly conditioned to the presence of an optical laser field, these features share their dynamics with the temporal evolution of the laser pulse. The temporal envelope of the spectrum is however strongly modified in the regime of matching phonon- and Rabi-frequency. In contrast to the weak excitation case, bare and phonon assisted features do not exhibit the same shape. The time-resolved calculations further prove, that the strong excitation polaron features do also occur at an extremely strong spectral broadening of all peaks, here inflicted by the short temporal width of the laser.

## 4.5. Excitation frequency dependence of the emission dynamics of semiconductor quantum dots

In the previous sections, the focus was explicitly on the non-equilibrium phonon features in the emission spectrum. In contrast to that, the emission dynamics after weak optical excitation of the different emission structures from a quantum dot (QD) will be investigated, based on a modified model. In order to properly describe the emission dynamics of a certain type of system, different levels have to be taken into account dependent on the size and the shape of the QD [SWL<sup>+</sup>09, SWB07]. This is the case especially for higher laser frequency detunings with respect to the first electronic transition frequency. In- and out-scattering mechanisms between the several QD states leads to an altered emission dynamics compared to the simple two-level case. Therefore, the time evolution of the different spectral contributions can strongly depend on the spectral position of the exciting laser pulse. The presence of phonons leads to extra emission features in the spectrum, causing resonance effects, also altered when changing the optical excitation frequency. As applying weak optical excitation, the level of description with respect to the phonon system can be reduced to a simple second order Born factorization method [Fri96, KWH<sup>+</sup>10]. At the end of this section, the results will be compared with experimental observations.

### 4.5.1. Quantum dot modeled as a three level system

For a better modeling of the actual emission dynamics of the QD at different frequency detuned excitation conditions, it is described by a multi-level structure [HSM<sup>+</sup>00, SGB99, HGL<sup>+</sup>95]. Our model involves two valence band states  $|v_1\rangle$  and  $|v_2\rangle$  and a conduction

band state  $|c\rangle$ . Starting from a Hamilton operator similar to Eqs. (4.2)-(4.4) [KWH<sup>+</sup>10, KCR<sup>+</sup>11], here written in the electron-hole picture:

$$\mathcal{H}_0 = -\hbar \sum_{i=1,2} \omega_{v_i} d_{v_i}^\dagger d_{v_i} + \hbar \omega_c a_c^\dagger a_c + \hbar \sum_k \omega_k c_k^\dagger c_k + \hbar \omega_{LO} \sum_q b_q^\dagger b_q, \quad (4.16)$$

$$\mathcal{H}_I^{e-l} = \hbar \sum_{i=1,2} \Omega_i(t) d_{v_i} a_c e^{i\omega_L t} + \hbar \sum_{i,k} M_k^{v_i} d_{v_i} a_c c_k^\dagger + H.c., \quad (4.17)$$

$$\mathcal{H}_I^{e-ph} = -\hbar \sum_{i,q} d_{v_i}^\dagger d_{v_i} (g_q^{v_i*} b_q^\dagger + g_q^{v_i} b_q) + \hbar \sum_q a_c^\dagger a_c (g_q^{c*} b_q^\dagger + g_q^c b_q), \quad (4.18)$$

with  $d_{v_i} \equiv a_{v_i}^\dagger$  and  $d_{v_i}^\dagger \equiv a_{v_i}$  denoting the hole destruction and creation operators of the valence bands  $i \in 1, 2$ . As usual, Eq. (4.16) describes the free motion of the particles and quasi particles. The coupling to the light fields is modeled in the same way, as in Sec. 4.1.1, with a coupling of the emitter to the external laser field (first term in Eq. (4.17)) and the quantized emission field modes (second term in Eq. (4.17)). Here, however, there are two valence band states  $v_1$  and  $v_2$  supposed to be relevant for the dynamics. Accordingly, the electron-phonon coupling  $\mathcal{H}_I^{e-ph}$ , given by the Fröhlich interaction [Hak93, HR50] in Eq. (4.18) is adjusted to the three-level case. Due to the weak excitation regime considered in this section, multiple excitations within the QD are neglected, so that the fermionic system can be modeled by the states [See Fig. 4.16(a)]:

$$|g\rangle = |0_{v_1}, 0_{v_2}, 0_c\rangle, \quad |e_1\rangle \equiv |1_{v_1}, 0_{v_2}, 1_c\rangle, \quad |e_2\rangle \equiv |0_{v_1}, 1_{v_2}, 1_c\rangle, \quad (4.19)$$

with

$$\begin{aligned} X_i |g\rangle &\equiv a_c^\dagger d_{v_i}^\dagger |0_{v_1}, 0_{v_2}, 0_c\rangle = |\delta_{i1v_1}, \delta_{i2v_2}, 1_c\rangle = |e_i\rangle, \\ X_i^\dagger |e_i\rangle &= |g\rangle, \quad X_i |e_i\rangle = X_i^\dagger |g\rangle = 0. \end{aligned} \quad (4.20)$$

According to this,  $|g\rangle$  denotes the fermionic ground state without any excitation. The excited states  $|e_1\rangle$  as well as  $|e_2\rangle$  denote system states with a single excitation each, with either a hole produced in the valence band states  $|v_1\rangle$  or  $|v_2\rangle$ , respectively. Utilizing the condition  $\mathbb{1} = |g\rangle\langle g| + |e_1\rangle\langle e_1| + |e_2\rangle\langle e_2|$ , the Hamilton-operator can be cast in the more convenient form:

$$\mathcal{H}_0 = \hbar \sum_i \omega_{c v_i} |e_i\rangle\langle e_i| + \hbar \sum_k \omega_k c_k^\dagger c_k + \hbar \omega_{LO} \sum_q b_q^\dagger b_q, \quad (4.21)$$

$$\mathcal{H}_I^{e-l} = \hbar \sum_{i=1,2} \Omega_i(t) |g\rangle\langle e_i| e^{i\omega_L t} + \hbar \sum_{i,k} M_k^{v_i} |g\rangle\langle e_i| c_k^\dagger + H.c., \quad (4.22)$$

$$\mathcal{H}_I^{e-ph} = \hbar \sum_{i,q} |e_i\rangle\langle e_i| \left\{ \underbrace{(g_q^{c*} - g_q^{v_i*})}_{g_q^{i*}} b_q^\dagger + \underbrace{(g_q^c - g_q^{v_i})}_{g_q^i} b_q \right\}. \quad (4.23)$$

Especially, the representation of the exciton-phonon interaction in Eq. (4.23) is more adequate, than Eq. (4.18) since it naturally eliminates the phonon-coupling to the ground state. Similar to Sec. 4.1.2, collective couplings  $g_i$  and operators  $B_i$  are introduced:

$$B_i \equiv \sum_q \frac{g_q^i}{g_i} b_q, \quad \text{with} \quad g_i = \sqrt{\sum_{q'} |g_{q'}^i|^2}, \quad (4.24)$$

$$[B_i, B_j^\dagger] = \frac{\sum_q g_q^{i*} g_q^j}{g_i g_j} \equiv G^{ij} \quad \Rightarrow \quad G^{ii} = 1. \quad (4.25)$$

Note, that the commutation relations in Eq. (4.25) are only unity for operators, that correspond to the same valence-band state  $i$ . With this, the exciton-phonon interaction finally simplifies to:

$$\mathcal{H}_I^{e-ph} = \hbar \sum_{i=1,2} g_i |e_i\rangle \langle e_i| (B_i^\dagger + B_i), \quad (4.26)$$

with an effective coupling element  $g_i$  defined in Eq. (4.24).

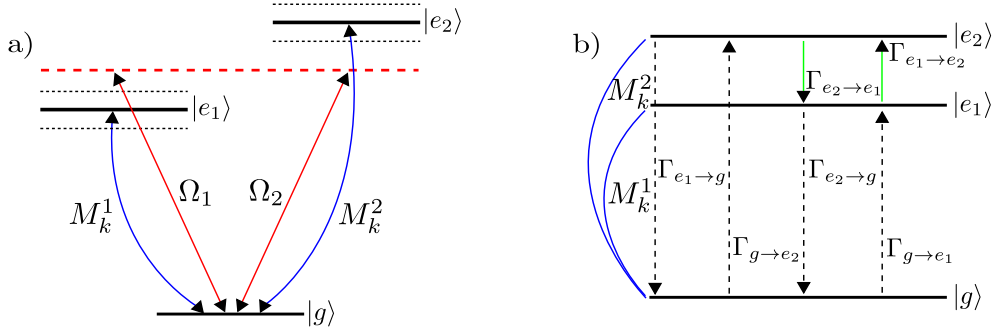


Figure 4.16.: (a) shows the V-type level scheme of the QD: The blue arrows denote the coupling to the quantized radiation modes and the red arrows illustrate the coupling to the external laser field. The coupling to the LO-phonon system is indicated by the dashed lines, with a constant LO-phonon dispersion, according to the Einstein model  $\hbar\omega = 36,4 \text{ meV}$ . The Huang-Rhys factor, defining the effective electron-phonon coupling strengths  $g_i = \sqrt{\sum_q |g_q^i|^2}$  is chosen as  $F = 0.01$ . [HBG<sup>+</sup>01, KAK02] (b) Relaxation scheme: The radiative lifetimes  $\Gamma_{e_i \rightarrow g}$  and  $\Gamma_{g \rightarrow e_i}$  are dependent on the exciton-photon coupling strengths  $M_k^i$ , indicated by the dashed arrows. The dipole moment is assumed to be  $d_{e_i} = 0.6 e_0 \text{ nm}$ . The in- and out scattering between the two excited states  $|e_1\rangle$  and  $|e_2\rangle$ , with an energy spacing of  $83 \text{ meV}$ , are incorporated phenomenologically  $\Gamma_{e_2 \rightarrow e_1} = 0.0045 \text{ meV}$  and using the detailed balance condition.

Conclusively, the QD level scheme and the Hamilton-operator of Eqs. (4.21)-(4.26) is illustratively summarized in Fig. 4.16(a). Due to the simple exciton picture, chosen for the calculations [Eq. (4.19)], the QD exhibits a V-type level structure, i.e. there are two

transitions  $|g\rangle \rightarrow |e_i\rangle$  to be coupled by the laser field (red arrows) and the emission field modes (blue curved arrows). Note, that in Eq. (4.22) it was assumed, that the energy spacing between the two excitonic states  $|e_1\rangle$  and  $|e_2\rangle$  is strongly non-resonant with the driving laser field. Laser induced transitions between those states  $|e_i\rangle \rightarrow |e_j\rangle$  are therefore neglected. The dotted curves denote the extra phonon assisted levels according to Eq. (4.26). The red dashed line features the frequency position of the laser. In the following, the laser frequency will be placed at different positions in the proximity of at least one of the excitonic resonances.

Crucial for the emission dynamics, as depicted in Fig. 4.16(b), are decay processes between the different levels. Due to the fully quantized exciton-photon coupling with the quasi-continuous multi-mode emission field in Eq. (4.22), radiative lifetimes between the states  $|e_{i/j}\rangle$  and  $|g\rangle$  ( $\Gamma_{e_{i/j} \rightarrow g}$  and  $\Gamma_{g \rightarrow e_{i/j}}$ , indicated by dashed arrows) are automatically incorporated on the base of the Hamilton-operator. The relaxation mechanisms, involving a decay between the excited states  $|e_1\rangle$  and  $|e_2\rangle$  are phenomenologically introduced via Lindblad formalism [Car02] (See also Eq. 3.3) and using the detailed balance condition  $\frac{\Gamma_{n' \rightarrow n}}{\Gamma_{n \rightarrow n'}} = \exp\left[-\frac{\hbar(\omega_n - \omega_{n'})}{k_B T}\right]$  [Muk95] (indicated by green arrows). Such in- and out scattering rates can be calculated on a microscopic footing, using an effective exciton-phonon Hamilton operator approach. Describing second order LO-phonon processes, a higher order Markovian perturbation theory delivers scattering rates  $\Gamma_{e_i \rightarrow e_j}$  between the two exciton states [DMR<sup>+</sup>10].

#### 4.5.2. Dynamics: Factorizing approach to the equations of motion

Throughout this section, the QD is assumed to be driven by the external laser in the weak excitation regime. It is therefore an appropriate approximation, that the state of the LO-phonon system will be unaffected by the optical excitation. The phonon system will be assumed to remain in a thermal equilibrium at all times, i.e. in contrast to the previous sections, there are no Fock- or coherent phonons present in the system. Thus, a typical second order Born factorization with respect to the phonon system and using Eq. (4.24) will result in [Fri96]:

$$\begin{aligned} \langle |m\rangle \langle n | B_i^\dagger B_j \rangle &= \frac{\sum_{q,q'} g_q^{i*} g_q^j}{g_i g_j} \langle |m\rangle \langle n | b_q^\dagger b_{q'} \rangle \approx \frac{\sum_{q,q'} g_q^{i*} g_q^j}{g_i g_j} \langle |m\rangle \langle n | \rangle \langle b_q^\dagger b_{q'} \rangle \delta_{qq'} \\ &= G^{ji} n_{LO} \equiv n_{LO}^{ji}, \quad \longrightarrow \quad n_{LO}^{ii} = n_{LO}, \end{aligned} \quad (4.27)$$

where  $n_{LO} = 1/[\exp\frac{\hbar\omega_{LO}}{k_B T} - 1]$  is the temperature dependent equilibrium phonon number and  $n_{LO}^{ji}$  the effective phonon number, that will occur in the equations of motion for the dynamics. The multi-mode emission will be treated in the same manner, as in the previous section Sec. 4.2.

Due to the third energy level, leading to a higher number of equations and the here used truncation scheme, altered compared with Eqs. (3.12)-(3.15) is more suitable. The excitonic quantities will be represented by:

$$\sigma_{ij}^{00} \equiv \langle |i\rangle \langle j| \rangle \quad \text{with} \quad i, j \in \{g, e_1, e_2\}, \quad (4.29)$$

denoting the three excitonic densities, and the corresponding polarizations between the three states. Using the second order Born-factorization of Eq. (4.27) and neglecting photon backaction Eq. (4.15), operator correlations can only occur up to the first order in the phonon and the photon system.

The assistance with a single phonon or photon operator will be denoted via Greek subscript indices, corresponding to either a missing  $\gamma = 0$ , an annihilation  $\gamma = 1$  or a creation operator  $\gamma = \dagger$ .

$$\sigma_{ij}^{k\alpha l\beta} \equiv \langle |i\rangle \langle j| c_k^\alpha B_l^\beta \rangle \quad \text{with} \quad \alpha, \beta \in \{0, 1, \dagger\}, \quad l \in \{1, 2\}, \quad (4.29)$$

and further  $\omega^0 \equiv 0$ ,  $\omega^1 \equiv \omega$ ,  $\omega^\dagger \equiv -\omega$ . Here, the index  $l$  indicates, that the particular phonon operator belongs to the effective phonon mode  $B_l^{(\dagger)}$  defined in (4.24). The subscript index  $k$  denotes the respective photon operator  $c_k^{(\dagger)}$ . With this, the equations of motion can be given in the compact form:

$$\begin{aligned} \dot{\sigma}_{ij}^{k\alpha l\beta} &= i(\bar{\delta}_{ig}\omega_{cv_i} - \bar{\delta}_{jg}\omega_{cv_j} + \omega_k^\alpha + \omega_{LO}^\beta + \frac{i}{2}[\bar{\delta}_{ig}\Gamma_{i \rightarrow j} + \bar{\delta}_{jg}\Gamma_{j \rightarrow i}] - \bar{\delta}_{ij}\gamma_{ij})\sigma_{ij}^{k\alpha l\beta} \\ &+ \bar{\delta}_{jg}\frac{1}{2}\Gamma_{j \rightarrow i}\dot{\sigma}_{ii}^{k\alpha l\beta} + \bar{\delta}_{ig}\frac{1}{2}\Gamma_{i \rightarrow j}\dot{\sigma}_{jj}^{k\alpha l\beta} \\ &+ i\delta_{gi} \sum_{n=e_1, e_2} \Omega^n \sigma_{nj}^{k\alpha l\beta} e^{-i\omega_L t} - i\bar{\delta}_{jg}\Omega^j \sigma_{ig}^{k\alpha l\beta} e^{-i\omega_L t} \\ &+ i\bar{\delta}_{ig}\Omega^i \sigma_{gj}^{k\alpha l\beta} e^{i\omega_L t} - i\delta_{jg} \sum_{n=e_1, e_2} \Omega^{n*} \sigma_{in}^{k\alpha l\beta} e^{i\omega_L t} \\ &+ i\delta_{\alpha 1}\delta_{gi} \sum_{n=e_1, e_2} M_k^n \sigma_{nj}^{0l\beta} + i\delta_{\alpha 0}\delta_{gi} \sum_{k'} \sum_{n=e_1, e_2} M_{k'}^n \sigma_{nj}^{k'l\beta} - i\delta_{\alpha 0}\bar{\delta}_{jg} \sum_{k'} M_{k'}^j \sigma_{ig}^{k'l\beta} \\ &+ i\delta_{\alpha 0}\bar{\delta}_{ig} \sum_{k'} M_{k'}^i \sigma_{gj}^{k'l\beta} - i\delta_{\alpha \dagger}\delta_{jg} \sum_{n=e_1, e_2} M_k^n \sigma_{in}^{0l\beta} - i\delta_{\alpha 0}\delta_{jg} \sum_{k'} \sum_{n=e_1, e_2} M_{k'}^n \sigma_{in}^{k'l\beta} \\ &+ i\bar{\delta}_{ig} \left( \delta_{\beta 0} \sum_{\gamma=1, 2} g_i \sigma_{ij}^{k\alpha i\gamma} + \delta_{\beta 1} g_i \sigma_{ij}^{k\alpha 0} [n_{LO}^{li} + G^{li}] + \delta_{\beta \dagger} g_i \sigma_{ij}^{k\alpha 0} n_{LO}^{il} \right) \\ &+ i\bar{\delta}_{jg} \left( \delta_{\beta 0} \sum_{\gamma=1, 2} g_j \sigma_{ij}^{k\alpha j\gamma} + \delta_{\beta 1} g_j \sigma_{ij}^{k\alpha 0} n_{LO}^{lj} + \delta_{\beta \dagger} g_j \sigma_{ij}^{k\alpha 0} [n_{LO}^{jl} + G^{jl}] \right). \end{aligned} \quad (4.30)$$

To have a better understanding of these equations, it is useful keeping in mind, that a Kronecker delta with Greek indices  $\delta_{\gamma 1}$  or  $\delta_{\gamma 2}$  indicates a spontaneous emission term, present due to the quantization of the phonon- and the photon system. Accordingly, the Kronecker symbols with  $\delta_{\gamma 0}$  only occur for solely excitonic expectation values with respect to the particular interaction. This is due to the second order truncation and factorization scheme of Eqs. (4.15) and (4.27).

For calculating the time resolved spectrum  $S(\omega_s, t)$  according to formula Eq. (4.12), again the photon coherences  $\langle c_k^\dagger c_{k'} \rangle$  have to be determined solving Eq. (4.30).

$$\partial_t \langle c_k^\dagger c_{k'} \rangle = i(\omega_k - \omega_{k'}) \langle c_k^\dagger c_{k'} \rangle + i \sum_{n=e_1, e_2} \left\{ M_k^n \sigma_{g,n}^{k'l0} - M_{k'}^n \sigma_{n,g}^{k'l0} \right\} \quad (4.31)$$

The set of equations is solved numerically with the system initially prepared in its ground state with  $\sigma_{gg}^{00} \equiv \langle |g\rangle\langle g| \rangle = 1$ .

## 4.6. Excitation dependent emission dynamics

In this section the time-resolved light emission of a semiconductor QD calculated in frequency- and time domain. Since the model includes the interaction of the excitonic system with LO-phonons, this will lead to phonon assisted features in the spectrum. Besides the phonon-assisted fluorescence, there will be inelastic scattering contributions, which are red- and blue shifted with an LO-phonon frequency ( $\omega \mp \omega_{LO}$ ) with respect to the bare excitonic features. It turns out, that the presence of LO-phonons in the system has a crucial influence on the emission dynamics, when exciting at certain frequency positions. As this effect is introduced via the equilibrium phonon number, it is strongly temperature dependent.

### 4.6.1. Time-resolved spectrum of a quantum dot

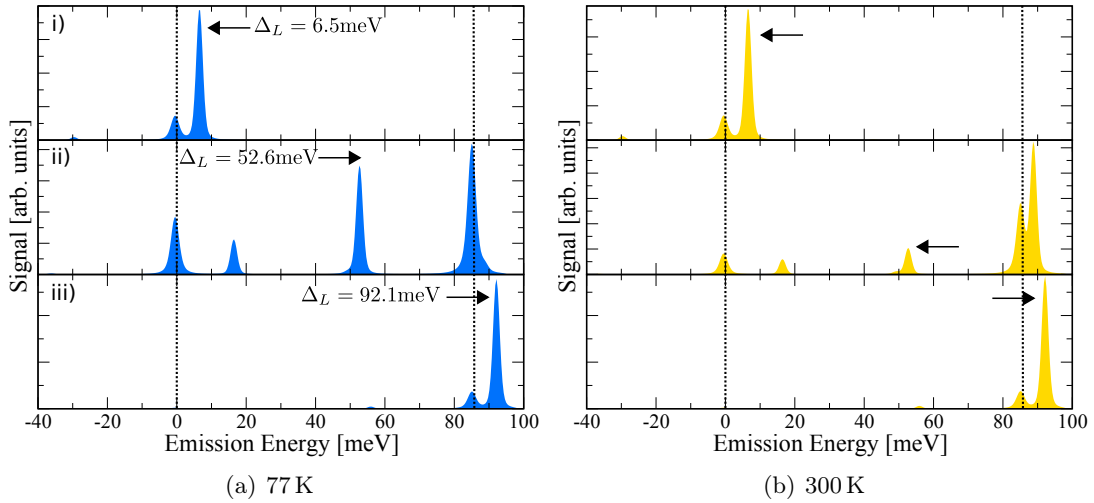


Figure 4.17.: Dynamic emission and scattering spectrum of a QD at three different laser detunings  $\Delta_L = \omega_{cv_1} - \omega_L$  with respect to the first optical transition i), ii) and iii): The dotted lines mark the energies of the excitonic transitions  $\hbar\omega_{cv_1}$  and  $\hbar\omega_{cv_2}$ . The arrows point at the current frequency position of the external laser pulse (FWHM= 2 ps), temporally centered at  $t = 8$  ps. The time resolved spectrum is depicted for a temperature of (a) 77 K and (b) 300 K. In both cases,  $S(\omega_s, t)$  is taken at time  $t = 9$  ps. At that time, also the incoherent fluorescence contributions are already visible in the spectrum.

Figure. 4.17, shows the full time-resolved spectrum  $S(\omega_s, t = 9 \text{ ps})$  of the QD at three different excitation frequencies of the external laser: i)  $\Delta_L = 6.5 \text{ meV}$ , ii)  $\Delta_L = 52.6 \text{ meV}$  and

iii)  $\Delta_L = 92.1$  meV. The laser pulse has a FWHM of 2 ps and is centered at 8 ps. The temporal resolution of the set up is set to  $\Delta_t = 600$  fs so that the fast coherent contributions to the spectrum can be properly resolved [See Sec. 4.4.1]. For all three frequency positions of the laser, the spectrum is calculated at (a) 77 K as well as (b) 300 K. In the upper i) and lower graphs iii) of Fig. 4.17, respectively, the laser frequency position (pointed at with the black arrows) is close to either the first-  $\omega_{cv_1}$  or the second  $\omega_{cv_2}$  QD transition frequency (indicated by the dotted lines). Although the exciting laser pulse is rather short, the transition, which is distant to the laser does barely contribute to the spectrum at that short time scales. The temperature difference seems to have a negligible influence. For the middle graph ii), with the laser frequency positioned well in between the two resonances, however, both transitions are immediately visibly excited. Further, the spectrum strongly changes with temperature due to the proximity of the Raman frequencies  $\omega_s = \omega_L \mp \omega_{LO}$  [See also Tab. 4.1] to the QD transitions frequencies. This is a result of the resonance Raman effect, amplifying the respective Raman scattering contribution and the fluorescence contributions, close to each other. Here, most prominently, the Raman anti-Stokes contribution on the right of the second transition frequency, almost not visible at 77 K, strongly gets enhanced at 300 K. Simultaneously, also the here located fluorescence emission peak gets magnified. As will be illustrated in the following, this enhancement of the scattering and emission peaks (resonance Raman effect) leads to a temperature dependence on the emission dynamics of the QD.

#### 4.6.2. Emission dynamics

In Fig. 4.18, the evolution of the different scattering and emission contributions are depicted over time (on time scales of the 2 ps-pulse) for the first laser detuning  $\Delta_L = 6.5$  meV. Figure 4.18(a) shows the main contributions of the spectrum, Rayleigh scattering at the position of the laser  $\omega_s = \omega_l$  (red curve), fluorescence from the first transition at  $\omega_s = \omega_{cv_1}$  (black curve) and fluorescence from the second transition at  $\omega_s = \omega_{cv_2}$  (purple curve). If exciting close above the first QD band gap, obviously only the first transition plays a role in the emission dynamics of the QD and the spectrum simulates the behavior of the spectrum of a two-level system [Compare Fig. 4.14]. The Rayleigh contribution follows the dynamics of the pulse, while the fluorescence contribution builds up subsequently and later on decays on the time scale of the radiative lifetime of the first excited state density  $\sigma_{e_1 e_1}^{00} = \langle |e_1\rangle \langle e_2| \rangle$ . The same behavior is shown by the phonon assisted contributions in Fig. 4.18(b), i.e. the Stokes Raman contribution at  $\omega_s = \omega_l - \omega_{LO}$  (blue curve), the phonon assisted fluorescence related to the first excited state  $\omega_s = \omega_{cv_1} - \omega_{LO}$  and the phonon assisted fluorescence related to the second transition at  $\omega_s = \omega_{cv_2} - \omega_{LO}$ .

However, positioning the laser differently, leads to altered emission dynamics for the fluorescence contributions. This can be seen already on relatively small timescales, comparable with the temporal pulse width= 2 ps in Fig. 4.19. Here, the QD is excited in between the two transition frequencies according to Fig. 4.17 ii) resulting in fluorescence signatures at both, the first- and the second excitonic transition. As Fig. 4.17 ii) exhibits a temperature dependence for this excitation frequency, the temporal evolution of the structures is shown at 77 K as well as 300 K. The temporal behavior of the Rayleigh- (red curves) and Raman

(pink curves) contributions remain unaffected either by the laser detuning, as well as by the change of temperature. They just exhibit an enhancement due to resonance effects with phonon assisted processes, which are stronger due to the increased phonon number  $n_{LO}$ . The long-lived part to the Raman contributions is just due to the fluorescence underground related to the second excited state close by. In contrast to Fig. 4.18, where the fluorescence peaks (purple curves) were not visible at all, these contributions now constitute the main incoherent features in the spectrum. However, after being build up during the action of the laser pulse, they also decay on the time scale of the radiative lifetime and due to out-scattering into  $|e_1\rangle$ . Due to the resonance Raman effect between the anti-Stokes Raman line and the fluorescence at  $\omega_s = \omega_{cv_2}$ , these peaks are strongly enhanced in the case of  $T = 300$  K. The fluorescence at  $\omega_s = \omega_{cv_1}$ , however, shows a much smaller deviation on pulse-width timescales, as Raman frequencies more distant. Nevertheless, due to in-scattering from the excited state  $|e_2\rangle$ , their temperature dependence is assigned to the fluorescence contributions at  $\omega_{cv_1} (\mp \omega_{LO})$ , leading mainly to a change in their build up time and their emission intensity. Therefore, due to the electron-phonon interaction, the emission intensity non monotonously evolves with the laser detuning  $\Delta_L$ . This behavior

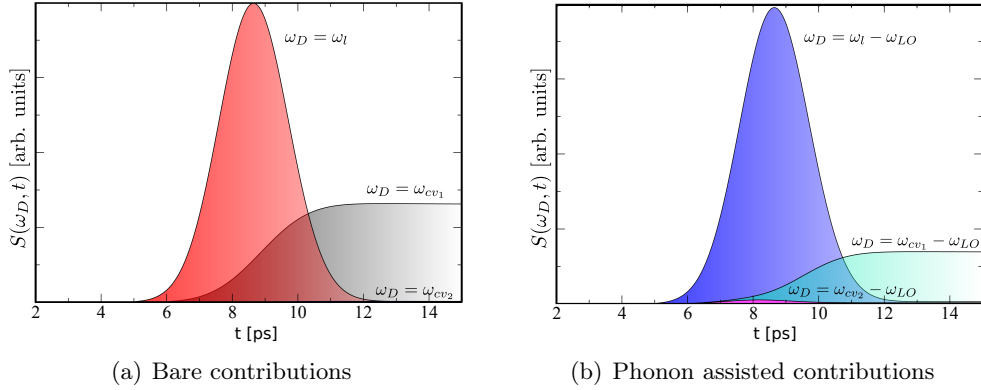


Figure 4.18.: Temporal evolution of the different emission and scattering structures for excitation near the first excitonic resonance  $\Delta_L = 6.5$  meV. (a) Bare contributions: The Rayleigh scattering (red curve) evolves together with the excitation pulse. The fluorescence emission from the first excitonic resonance (black curve) and the second excitonic resonance (green curve, hardly visible) exhibit slow dynamics, dependent on the creation of an excited state density and its radiative lifetime. There is almost no emission from the second transition frequency, as the higher state remains almost unpopulated at this optical excitation frequency. (b) (Stokes) Raman scattering (blue curve), phonon-assisted fluorescence emission from the first excitonic resonance (green curve) second excitonic resonance (purple curve). The phonon-assisted exhibit the same dynamic characteristics as the bare features. The phonon-assisted fluorescence from the second transitions (purple curve) is relatively strong due to its proximity to other spectral features (resonance effect).

is pronounced at higher temperatures, especially if involving resonance effects with anti-Stokes contributions.

In Fig. 4.20, the temporal behavior of the fluorescence emission peaks are collected for three different positions of the laser pulse at longer time scales. Obviously, the build up time of the fluorescence is strongly dependent on the initial population of the second excited state. Since the rate  $\Gamma_{e_1 \rightarrow e_2}$  is much smaller than the reverse process, the decay of

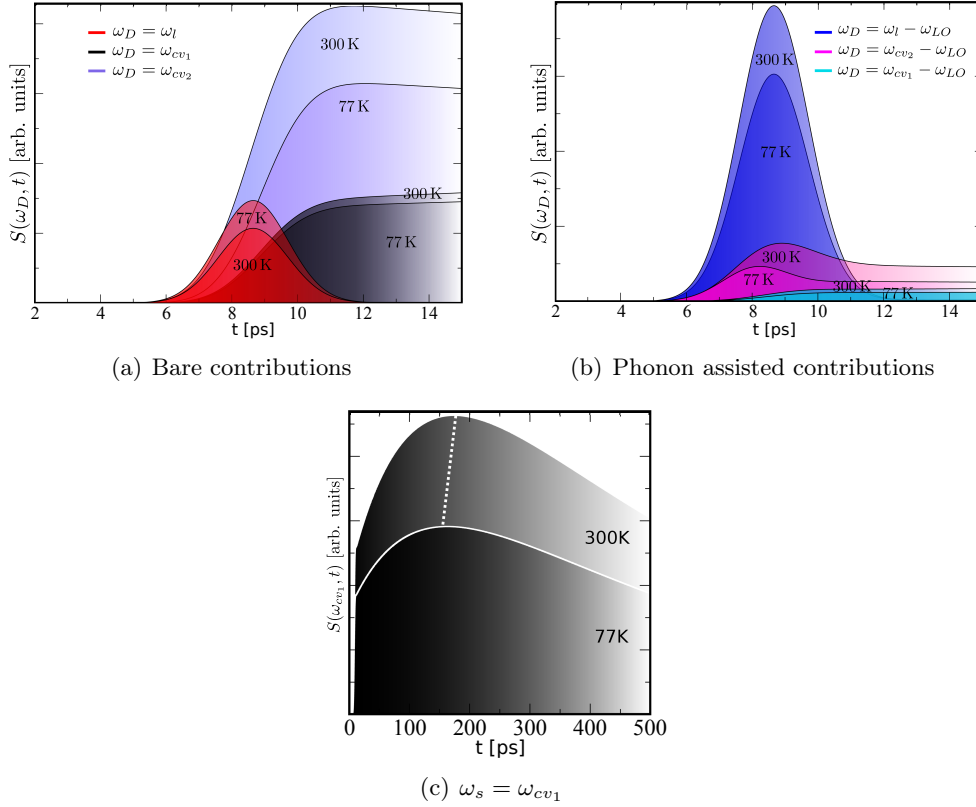


Figure 4.19.: Temporal evolution of the different emission and scattering structures for excitation between the first and the second excitonic resonance  $\Delta_L = 52.6$  meV at  $T = 77$  K and  $T = 300$  K. Short time scales: (a) Bare contributions: Rayleigh scattering (red curve), fluorescence emission from the first excitonic resonance (black curve) and the second excitonic resonance (green curve). (b) (Stokes) Raman scattering (blue curve), phonon-assisted fluorescence emission from the first excitonic resonance (green curve) second excitonic resonance (purple curve). Long time scales: (c) Evolution of the fluorescence from the first resonance at  $T = 77$  K and  $T = 300$  K. The temperature induced enhancement of the resonant Raman effect effectuates a change of the emission dynamics and intensity.

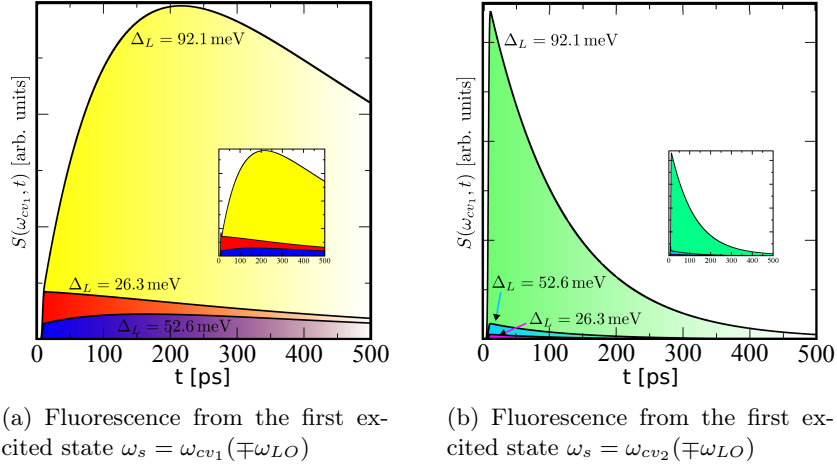


Figure 4.20.: Temporal evolution of the fluorescence contributions related to (a) the first excited state and (b) the second excited state at different excitation frequencies.

the first (phonon assisted) fluorescence peak is less steep, see for example the red curve in Fig. 4.20(a).

Finally, the QD model is compared to experimental results [WRW<sup>+</sup>11], where the QD is excited in proximity to the second order phonon assisted fluorescence peak of the first resonance at  $\Delta \approx \omega_{cv_1} + 2\omega_{LO}$ . Therefore, the frequencies of the Stokes Raman coincides with the frequency of the first order phonon assisted fluorescence peak. Thus, the temporal evolution shows three different timescales. On the one hand, there is the fast Raman component, which directly follows the excitation pulse. Further, such in Fig. 4.20, there is the rise time of the peak, on a timescale of about 250 ps and the long timescale given by the strength of the radiative decay, which here is theoretically incorporated via the multi-mode quantized radiation field coupling.

## 4.7. Conclusion

A microscopic model for the steady state and time-resolved resonance fluorescence spectrum of a semiconductor QD transition in the strong excitation regime was presented in this chapter. In the high driving regime, the spectrum exhibits a variety of different strong-coupling features: In difference to atomic systems, additional phonon assisted LO-phonon sidebands appear in the fluorescence and the scattering contribution of the spectrum in the weak driving regime. For stationary pulses in the Mollow-regime, the spectrum exhibits additional phonon-assisted (also higher order) Mollow triplets. For Rabi-frequencies in the range of an LO-phonon frequency, there are anti-crossing between the Mollow-sidebands and the Mollow centers, which go with the effective electron-phonon coupling strength. Further, the phonon assisted Mollow-centers split into two lines, also with a splitting strength proportional to the electron-phonon coupling. These polaron features and also the light

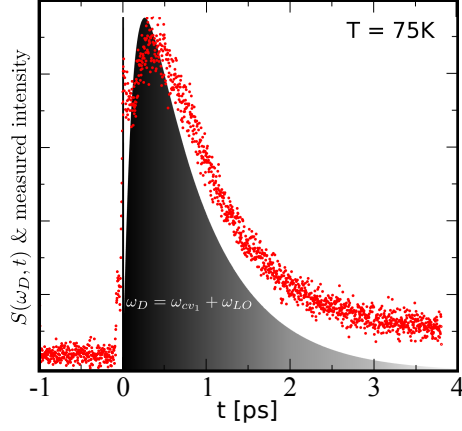


Figure 4.21.: Comparison between measured emission intensity and calculated time resolved spectrum at  $\omega_s = \omega_{cv_1} + \omega_{LO}$ . The position of the laser is approximately  $\hbar\Delta_L \approx 72$  meV, so that at the detection frequency  $\omega_s = \omega_{cv_1} + \omega_{LO}$  the frequency for the Stokes Raman process and the anti-Stokes phonon assisted fluorescence coincide.

induced multi-phonon processes demand a theoretical treatment of the phonon system, which is beyond the usual bath assumptions. The time resolved spectrum shows a similar behavior, there are however additional interference effects due to the spectral and temporal width of the laser pulse, as well as temporal asymmetries of the emission intensities of the Rabi-sidebands. Also for short excitation pulses, phonon-related anti-crossings and splittings occur, strongly changing the time-resolved spectrum in the high driving regime, towards the situation without electron-phonon interaction. Further, the strong optical excitation induces the emission of phonons, resulting in time-dependent and non-equilibrium phonon statistics.

Further, it was found, that the emission dynamics of a multi-level QD, here modeled as a V-type semiconductor QD clearly depends on the spectral position of the exciting laser. We considered LO-phonon interaction, which results in LO-phonon assisted emission and scattering features. These structures show similar temporal evolutions as the main fluorescence or scattering processes, respectively. The electron-LO-phonon interaction introduced a further temperature dependence to the spectrum and the temporal behavior of the emission components, mainly caused by the resonance Raman effect.



# 5

## Quantum control: Single photon delayed feedback

Towards the aim of quantum information processing and quantum networks, the stabilization of particular quantum states can be realized via extrinsic means of quantum control, i.e. in form of the repeated action of a sensor-controller-actuator loop. Within such a continuous measurement feedback setup the respective external control parameter is adjusted accordingly, in order to force the system into the desired quantum state [ZDP<sup>+</sup>12, VMS<sup>+</sup>12, WM10].

In contrast to that, there is also the possibility for an intrinsic quantum feedback, where the feedback is generated via designing the environment. Among others, this can be the placement of a mirror in front of a quantum emitter system [AHR<sup>+</sup>11].

In this chapter, a quantum feedback control scheme in cavity quantum electrodynamics (cQED) is proposed, involving a Jaynes-Cummings model (JCM), subject to photon loss placed in front of a half-cavity [CKS<sup>+</sup>13]. For the cQED operated in the weak coupling regime, Rabi-oscillations at the time scale of the electron-photon coupling strength can be recovered via the intrinsic feedback. Deliberately studying feedback in the quantum limit, i.e. single photon delayed feedback, a fully quantized model of delayed feedback beyond the classical Lang - Kobayashi model [LK80, HDY<sup>+</sup>11, MMT90] is used here [DZ02]. For properly describing the quantum feedback, the model involves the coupling to a quasi continuum of quantized (outside of the cavity) photon modes.

### 5.1. Model for the cQED with quantum feedback

The model system, considered in this chapter is a two-level emitter, coupled to a single microcavity photon mode. This cavity-emitter system is subject to photon loss, introduced through a coupling to an external continuum of photon modes, Fig. 5.1. The coupling to this external photon reservoir is structured via the external mirror in front of the cav-

ity: The distance  $L$ , the external mirror is placed at is regarded sufficiently large, that the assumption of a pure mode continuum is still valid and an altering in the local field strength in the single-mode microcavity can be ruled out. However, the mirror installs an additional boundary condition to the quasi continuous modes, creating a feedback of photons, previously emitted by the cavity. The timescale of the feedback is determined by the round trip time, i.e. the time the photons need to travel forth to the mirror and back to the cavity. Therefore, the feedback is dependent on the mirror distance  $L$  and the speed of light outside the cavity. As known from the classical theory [LK80, OLS10], the feedback time (delay) is thus given by  $\tau = 2L/c_0$ . As the efficiency of the photon feedback is determined by the amount of photons, to be reflected back to the cavity-emitter system, it is at first necessary to ensure, that the total photon population actually meets the mirror to be reflected. It is therefore assumed, that the out-coupled photon is focused onto the external mirror by a lens, placed in between the cavity and the mirror [DZ02].

### 5.1.1. Quantum approach to the external optical feedback

For the description of the system, a fully quantized Hamiltonian states the basis for the calculations. In an RWA [WM08], the Hamilton-operator reads:

$$H_0 = \hbar \sum_{i=v,c} \omega_i a_i^\dagger a_i + \hbar \omega_0 c^\dagger c + \hbar \int dq \omega_q d_q^\dagger d_q \quad (5.1)$$

$$H_I = -\hbar M \left( a_v^\dagger a_c c^\dagger + a_c^\dagger a_v c \right) - \hbar \int dq \left( G_q c^\dagger d_q + G_q^* d_q^\dagger c \right). \quad (5.2)$$

Here,  $H_0$  in Eq. (5.1) constitutes the free motion of the electronic two-level system, described by the fermionic annihilation (creation) operators  $a_i^{(\dagger)}$  of the ground  $i = v$  and the excited state  $i = c$ , the free energy parts of the cavity photon mode and the outside continuum photon modes with bosonic ladder operators  $c^{(\dagger)}$  and  $d_q^{(\dagger)}$ , respectively. In the following, the frequency of the cavity photon mode  $\omega_0$  is assumed to be in resonance with the emitters gap frequency  $\omega_c - \omega_v \equiv \omega_{cv} = \omega_0$ .  $H_I$  describes the interactions of the system. Here,  $M$  is the coupling parameter for the interaction between the cavity photon mode

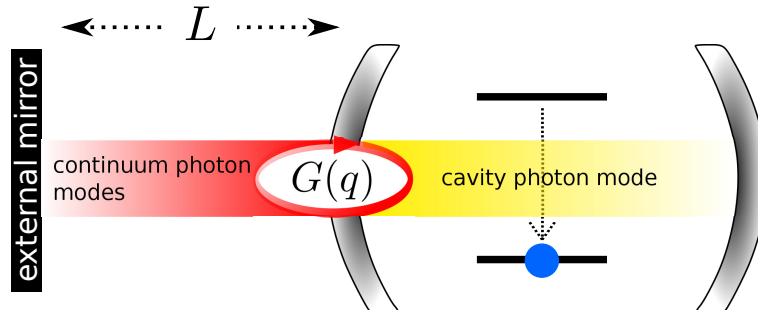


Figure 5.1.: Interaction scheme of a strongly coupled electron-photon dynamics in a microcavity with input-output coupling to a photon continuum in front of a mirror.

and the emitter, entering in the usual Jaynes-Cummings Hamiltonian. The second term in Eq. (5.2) introduces the interaction between the single cavity mode, with the external photon modes. The coupling element  $G_q$  of the tunnel Hamiltonian is derived via the extra boundary condition introduced through the external mirror and has the following form [YTC00, WM08]:

$$G_q = G \sin(q L), \quad (5.3)$$

Hereby, the energy dispersion for the external continuum modes is taken as the free dispersion of light:  $\omega_q = c_0 q$ , according to the preliminary assumptions. By its sinusoidal dependence of  $q$ , it describes an interaction of the cavity mode with standing wave modes between cavity and emitter.  $L$  is the distance between the cavity and the external mirror. For the calculations, the cavity coupling strength is assumed in the order of magnitude of  $M = 50 \mu\text{eV}$  [LHVB<sup>+</sup>09]. For the cavity-reservoir coupling  $G$  a value is chosen according to a typical cavity loss  $\kappa \propto G$ .

### 5.1.2. Equations of motion

With regard to the possible implementation of dissipative processes, the dynamics of the observables, such as the electronic-, and the photon densities, are calculated using Heisenberg's equation of motion [KK11, KCR<sup>+</sup>11]. Within the one-electron assumption  $a_v^\dagger a_v + a_c^\dagger a_c = 1$  and the single photon limit, a closed set of equations exactly describes the dynamics of the system:

$$\partial_t \langle E \rangle = iM \langle T^\dagger c \rangle - iM \langle T c^\dagger \rangle, \quad (5.4)$$

$$\partial_t \langle T c^\dagger \rangle = -iM \langle E \rangle + iM \langle c^\dagger c \rangle - i \int dq G_q^* \langle T d_q^\dagger \rangle e^{-i(\omega_0 - \omega_q)t}, \quad (5.5)$$

$$\partial_t \langle T d_q^\dagger \rangle = iM \langle d_q^\dagger c \rangle - iG_q \langle T c^\dagger \rangle e^{-i(\omega_0 - \omega_q)t}, \quad (5.6)$$

$$\partial_t \langle c^\dagger d_q \rangle = iG_q^* \langle c^\dagger c \rangle - iM \langle T^\dagger d_q \rangle - i \int dq' G_{q'}^* e^{-i(\omega_0 - \omega_q)t} \langle d_{q'}^\dagger d_q \rangle, \quad (5.7)$$

$$\partial_t \langle d_{q'}^\dagger d_q \rangle = +iG_q^* \langle d_{q'}^\dagger c \rangle e^{-i(\omega_0 - \omega_q)t} - iG_{q'} \langle c^\dagger d_q \rangle e^{i(\omega_0 - \omega_q)t}, \quad (5.8)$$

where  $T := a_v^\dagger a_c$  states the operator observable for the electronic transition and  $E := a_c^\dagger a_c$  for the excited state density. For simplicity, the equations are written within a rotating frame according to  $T \rightarrow T e^{-\omega_{cv}t}$ ,  $c \rightarrow c e^{-i\omega_0 t}$  and  $d_q \rightarrow d_q e^{-\omega_q t}$ .

Starting from the usual cavity emitter dynamics, described by the typical Jaynes-Cummings terms in Eq. (5.4), the excited state density couples to the photon assisted polarization  $\langle T^\dagger c \rangle$ . Then again, this quantity couples back to the densities  $\langle E \rangle$  and  $\langle c^\dagger c \rangle$  via the electron photon coupling. Further, the tunnel coupling between the cavity mode and the outside continuum modes leads to external photon assisted polarization  $\langle T d_q^\dagger \rangle$  in Eq. (5.5). These correlations are the consequence of quantized treatment of the photons, describing the correlated motion of the systems emitter and outside photon reservoir. As both those systems are coupled to the cavity photon mode, this results in a cavity mediated effective coupling

between the two systems, i.e. an interaction via a virtual cavity photon. Following all the interaction paths, one gets from the dynamics of the emitter in Eq. (5.4) to the dynamics of the photon reservoir in Eq. (5.8).

For the derivation of these equations, it was used, that the number of excitations in the system  $N$ , described with the Hamiltonian in Eq. (5.1) and (5.2), is composed of the number of excitations inside the cavity  $N_c = \langle E \rangle + \langle c^\dagger c \rangle$  and outside the cavity  $N_{\text{ex}} = \sum_q \langle d_q^\dagger d_q \rangle$ . As the total number of excitations is assumed to be conserved in the system  $N = N_c + N_{\text{ex}}$ , so that the equation of motion for the cavity photons is given by:  $\partial_t \langle c^\dagger c \rangle = -\partial_t (\langle E \rangle + N_{\text{ex}})$ . As in this work, the focus is on the revelation of single photon event in quantum feedback, the total number of excitations is summed up to  $N = 1$ . In this true quantum limit, the above equations Eqs. (5.4)-(5.8) fully characterize the system and a factorization of correlation is neither applicable nor necessary. Higher order photon (cavity- as well as reservoir) assisted excited state densities are zero at all times. In this single excitation (single photon) limit, quantum processes can be observed, recently successfully performed in experiments [HBW<sup>+</sup>07, PGR<sup>+</sup>07].

For the calculations, parameters typical for a self-organized InAs quantum dot microcavity system are consulted [AHR<sup>+</sup>11, UAR<sup>+</sup>11, LHV<sup>+</sup>09, WVT<sup>+</sup>09, NKI<sup>+</sup>10], the approach, however, is not restricted to this kind of semiconductor system, but can be deployed to atomic or molecular systems as well.

## 5.2. Single photon feedback

In this section, the quantum feedback for the emitter-cavity-reservoir system will be investigated according to Fig. 5.1 and Eqs. (5.4)-(5.8). In order to better discriminate the influence and the interplay between the different subsystems, at first, three limiting cases of the total system will be discussed before. These cases are defined on the one hand on the presence or the from of the tunnel coupling element  $G_q$  in Eq. (5.3), where (A) a vanishing out-coupling  $G_q = 0$  reproduces the Jaynes-Cummings model of Eqs. (2.30). (B) A constant coupling to the reservoir  $G_q = \text{const.} \neq 0$  establishes the weak coupling situations, without the boundary condition of the external mirror. On the other hand, (C) a vanishing emitter cavity coupling  $M = 0$  with  $G_q = G \sin(qL)$  is assumed, with an emitter in front of the mirror. Subsequently, the full system (D), with cavity coupling and mirror is discussed. As the quantity of interest, the average photon number in the cavity or the excited state density of the emitter are consulted for the comparison of the different limits (A)-(D). As initial condition, the emitter starts in the excited state  $\langle E \rangle = 1$  with no photons in the cavity nor the reservoir. In Fig. 5.2 these cases are presented from top to bottom. Fig. 5.2(A) shows the well known solution of the Jaynes-Cummings model. As a lossless system shows Rabi-oscillations of the photon density, corresponding to a strong coupling limit. For this one-photon case, the Rabi-oscillations between 0 and 1 occur at the time scale of the bare Rabi-frequency  $2M$ . The solution of the Jaynes-Cummings model is given by [WM08]:  $\langle c^\dagger c \rangle(t) = \frac{N_c}{2} [1 - \cos(2Mt)]$ . The reason for this symmetric behavior is the conservation of the number of excitations inside the cavity  $N_c(t) = 1$ .

One figure below in Fig. 5.2(B), the Jaynes Cummings model is extended to a tunnel coupling with an external photon reservoir  $G_q = \text{const.}$  In the case shown here, the photon

loss due to this out coupling well surpasses the cavity coupling strength. As a consequence, the Rabi-oscillations cannot take place anymore. As the emitter decays, injecting a photon into the cavity, this photon leaves the cavity before being reabsorbed by the emitter. In this limit, the dynamics are given by an exponential rate for the cavity loss. The excitation is lost to an unstructured photon continuum, i.e. the tunnel coupling element  $G_q$  is not or only weakly dependent on the wave number  $q$ . In contrast to case (A), the cavity coupling strength  $M$  is not accessible. In this limit of a weak coupling situation ( $G \gg M$ ) and emitter starting in its excited state, the solution for the photon population in the cavity can be approximated to:  $\langle c^\dagger c \rangle(t) \approx \sin^2(Mt) \exp(-\kappa t)$ , cf. Fig. 5.2(B).

In Fig. 5.2(C) there are at first signatures of quantum feedback. The distance of the emitter to the mirror is set in the range of cm. As the emitter decays into its ground state, it directly emits a photon into the photon reservoir. For times smaller than the delay time  $t < \tau = 2L/c_0$  (here 75 ps) the dynamics resemble those of case (B). This means, that before reaching the round trip time, the structured character of the photon reservoir is not yet resolved in time. However, for time larger than the delay time  $t > \tau$ , the structure of the external continuum, modeled with  $G_q = G \sin(qL)$ , finally is resolved and a delayed

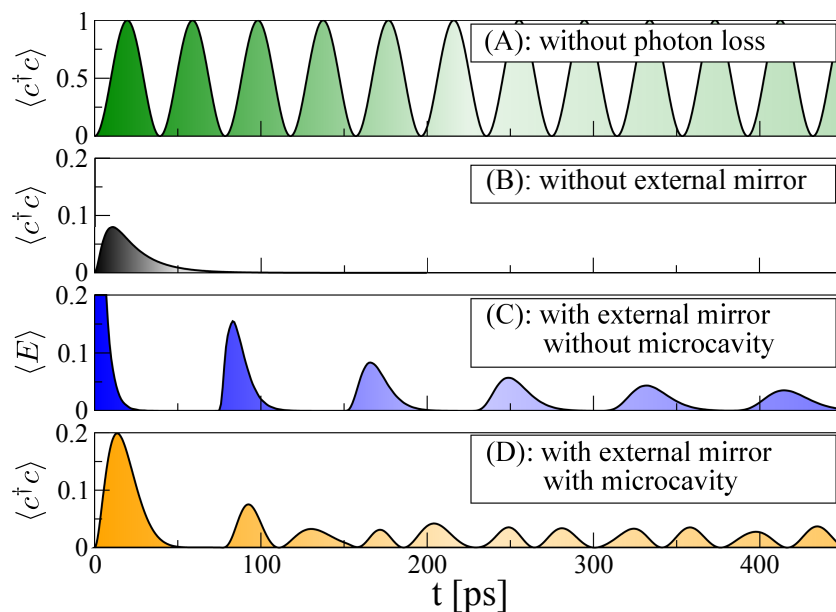


Figure 5.2.: Dynamics in the single-excitation limit. Case (A): Without outcoupling, regular Rabi oscillations occur. In the weak coupling limit without external mirror (B) or with feedback in a bigger cavity (C), no Rabi oscillations occur and excited state density just decays or the dynamics just involve the round trip time  $\tau$ . (D): Although the ratio of tunnel coupling strength  $G_0$  to cavity coupling strength  $M$  indicates the weak coupling limit, with an external mirror and a microcavity, the delayed feedback effect leads to Rabi oscillations again. Note, that in case (C) the occupation of the upper level  $\langle E \rangle$  is depicted, while in cases (A,B,D) the evolution of the cavity photon density  $\langle c^\dagger c \rangle$  is shown.

feedback to the density is induced at multiples of  $\tau$ . Due to the presence of the mirror in the distance  $L$ , the photon returns after one round trip (forth to the mirror and then back to the emitter)  $\tau$ . This process is repeated, leading to oscillations of the emitter density  $\langle E \rangle$  at the time scale of  $\tau$ . This behavior of the excited state density can analytically be modeled for an initial condition  $\langle E \rangle(0) = 1$  for the time interval  $[m\tau, (m+1)\tau]$  [DZ02]:

$$\langle E \rangle(t) = (m!2^m)^{-1}[\kappa(t - \tau m)]^{2m} \exp[-\kappa(t - m\tau)], \quad (5.9)$$

where  $\kappa = \pi G^2/c_0$ . Performing a minimum-maximum analysis of Eq. (5.9) yields, that the maximum value for the excited state density after one round trip is reached at  $t_{\max} = \tau + 2/\kappa$  with a value of  $\langle E \rangle(t_{\max}) = \exp(-2)$ , cf. Fig. 5.2(C), constituting an upper bound for delayed feedback effects. It can be concluded, with the noticeable finding, that an emitter in front of a mirror does not exhibit any Rabi oscillations, although there are no additional losses included. Here, a continuous energy exchange between emitter and cavity is taking place [DZ02, CM87].

This is changed, if considering now the full system [Eqs. (5.4)-(5.8)]. In difference to case (C), now there are strong coupling features visible. On the one hand, situation (C) is reproduced within  $t < \tau$ . As before, the emitted photon is totally lost into the mode continuum as in the weak coupling limit, cf. Fig. 5.2(B), since ( $M \ll G$ ) and Rabi-oscillations do not occur. According to the chosen mirror distance, the delayed feedback reintroduces the photon back into the cavity after 75 ps. From this time on, there is an onset of irregular oscillations, which are not on the time scale of the delay time, as in case (C), but occur with frequency of approximately  $2M$ . With time duration, these feedback induced Rabi-oscillations even become highly regular at 225 ps, i.e. they can now be clearly identified with Rabi-oscillations with frequency  $2M$ , as in the strong coupling regime. Surprisingly, the time scale of the oscillations depend on the cavity coupling strength only, rather than the tunnel coupling parameter. However, in comparison to the ideal Jaynes-Cummings case (A), the oscillations amplitude is much smaller than 1. The amplitude is reduced according to the upper bound, as discussed for case (C) and depends on the tunnel coupling strength  $G_q$ . With the here chosen parameter set of ( $\tau = 75$  ps,  $M = 55$   $\mu$ eV,  $\kappa = 160$   $\frac{1}{\text{ns}}$ ) maximum amplitude after a first round trip in the range of about 5% of the initial excitation.

In the following subsection, the restoration of the strong coupling situation as depicted in Fig. 5.2(D) through delayed feedback will be discussed in more detail.

### 5.2.1. Feedback induced restoration of strong coupling signatures

A key characteristic of the Jaynes-Cummings model, i.e. the strong coupling situation (requiring  $M \gg G$ ) is the conservation of the total excitation within the cavity, in the single excitation case discussed here:  $N_c(t) = \langle c^\dagger c \rangle + \langle E \rangle = 1$ . Both oscillators, the emitter and the cavity, periodically exchange this excitation.

To investigate the strong coupling signatures visible in the weak coupling ( $M \ll G$ ) case Fig. 5.2(D), the effect of the feedback on the total excitation number within the cavity  $N_c$  is investigated. In Fig. 5.3 the temporal evolution of  $N_c$  (black, dashed curve) is plotted together with dynamics of the cavity photon number. At first  $t < \tau$ , while the excited state density is decaying and the photon (orange curve) is leaving the cavity, the total

number of excitations  $N_c$  is just dropping to zero. After one  $\tau$ -interval, when photon population is reentering the cavity, also  $N_c$  is build up again, until it decreases anew at  $Mt = 2$ . However, at  $t > \frac{3}{M}$ , the external feedback mechanism establishes a permanent excitation within the cavity  $N_c(t) > 0$ , cf. Fig. 5.3(left). Over time, the delayed feedback results in an almost stationary number of excitations  $N_c$ , caused by the ongoing back coupling of lost cavity photon from the photon reservoir. Although  $N_c < 1$ , its constant value allows for a periodic exchange of excitation between emitter and cavity mode, as in the ideal Jaynes Cummings case. This excitation transfer occurs at a rate given by the electron-photon coupling element  $M$ , as known from typical Rabi-oscillations. As at longer times, Fig. 5.3(right) the fluctuations of  $N_c$  are small compared with its value, the oscillations in fact occur with the bare Rabi-frequency of the emitter-cavity system. In contrast to Fig. 5.2(C), the presence of the emitter, which is itself unaffected by the out coupling mechanism, inside the cavity leads to a storage of excitation. The emitter is able to keep a necessary amount of excitation on the timescale of the electron-photon coupling element from decaying into the reservoir. After several round trip times, the feedback signal is almost equally distributed over time, leading to a constant flow of excitation into the cavity, cf. in Fig. 5.3(left). As a consequence of two mechanisms jointly obtaining a constant amount of total excitation in the cavity, these feedback induced Rabi-oscillations state a very robust feature. On larger timescales Fig. 5.3(right), the behavior of the photon population is approximately given by formula  $\langle c^\dagger c \rangle(t) = \frac{N_c}{2} [1 - \cos(2Mt)]$ .

In the current example, the mirror distance and the electron-photon coupling element where chosen to fulfill the condition  $\tau M = 1$ . In order to demonstrate the robustness of the feedback induced Rabi-oscillations towards the delay time  $\tau$ , the quantities of Fig. 5.3 are now calculated for a different set of parameters. In Fig. 5.4, again the evolution of the photon number (solid curve) and the excitation number (dashed curve) is depicted, but for a delay time of  $\tau = \frac{11}{5} M^{-1}$ . Obviously, the increase of the round trip time with

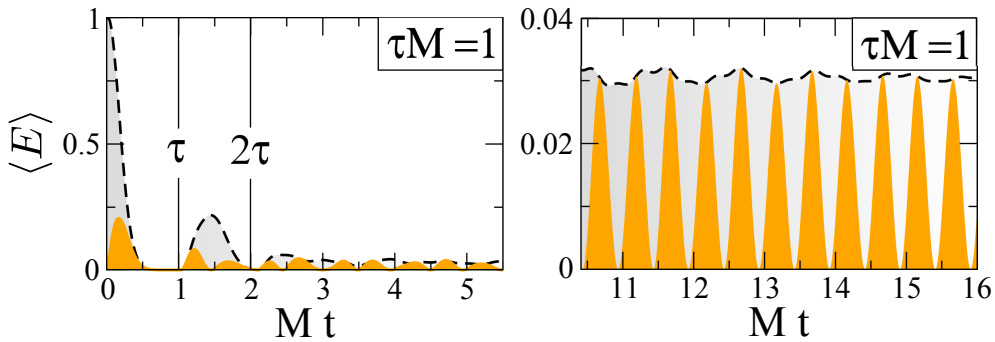


Figure 5.3.: Temporal evolution of the photon density in the cavity (orange area) and total amount of excitation  $N_c$  (dashed line) inside the cavity. The parameters are chosen as in Fig. 5.2(D). After several round trip times  $\tau$ , there is a finite and almost constant amount of excitation inside the cavity, that leads to regular Rabi oscillations. The oscillation period reveals the electron-photon coupling strength  $M$ .

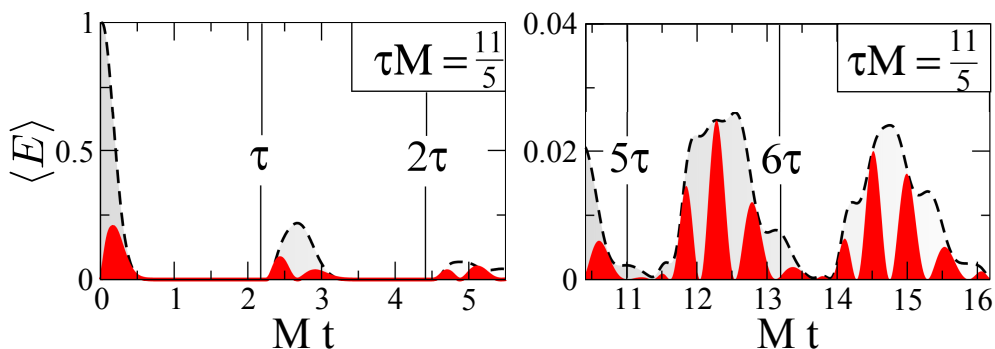


Figure 5.4.: Robustness discussion: Temporal evolution of the photon density (red area) and the total amount of excitation energy  $N_c$  inside the cavity (dashed line) for  $\tau = \frac{11}{5}M^{-1}$ . The Rabi-oscillations still occur for a fluctuating excitation number  $N_c$ , with an oscillation period proportional to  $M$  occur. The round trip time  $\tau$  inflicts an envelope onto the sinusoidal oscillation behavior (at this timescale).

respect to the cavity coupling strength leads to additional and more pronounced drops in  $N_c$  in comparison with Fig. 5.3. However, at longer times  $Mt > 20$  (not shown),  $N_c$  again saturates at a constant nonzero value. What is noticeable from Fig. 5.4(right), that even within the regime of only temporary excitation within the cavity, the Rabi-oscillations occurring during these periods are already fairly regular, thus revealing the electron-photon coupling strength  $M$ .

### 5.2.2. Conclusion

In this chapter, a fully quantized approach was applied for the description of a time delayed feedback in the quantum limit. The inclusion of photon-photon delay effects into the Jaynes-Cummings model restores Rabi oscillations in the weak coupling regime. Here, the photonic tunnel exchange rate  $G_q$  together with the action of the emitter serving as an excitation storage on  $M^{-1}$  generally realizes a constant number of cavity excitation, even for an arbitrary parameter set. The consequence are regular Rabi oscillations with frequency  $2M$  in the long time limes.

# 6

## Coherent control and entanglement of radiatively coupled $\Lambda$ -systems

### 6.1. Introduction

Quantum electrodynamics (QED) addresses the quantized emission and dynamic properties of light emitters, such as atoms or nanostructures, often coupled to single mode cavities. [Hoh10, MIM<sup>+</sup>00, TS10, RGGJ10, LVT08, PMOaU<sup>+</sup>]. On the basis of such cavity emitter systems, coherence phenomena, superradiance, nonlinear optics, lasing or entanglement can be achieved and studied. Compared to atoms or molecules, forming cQED systems, solid state based systems [MKB<sup>+</sup>00, KGK<sup>+</sup>06, BSL<sup>+</sup>09]) are promising candidates for technological use of these effects. On the one hand, these structures, such as for example semiconductor quantum dots (QDs) or nitrogen vacancy centers (NV-centers) show atom-like emission properties, based on spatial confinement. Typical cQED phenomena like vacuum Rabi-splitting and oscillations [LVT08, GTVC<sup>+</sup>10, CKR09] have already been realized for such systems. On the other hand, their emission properties and localization are scalable by design. On the downside, many of these solid nanostructures are also subject to several decoherence phenomena (excited state lifetimes, pure dephasing), due to the strong coupling to the solid state environment, they are embedded in and consist of. With rather long decoherence times, negatively charged NV-centers in diamond promise to be a good option for studying coherence phenomena or entanglement [HA08, WSSB13, SRX<sup>+</sup>10]. This chapter is focused on the principle possibility of a long range interaction between two cavity-coupled  $\Lambda$ -systems, subject to decoherence and photon loss. Based on a microscopic theory, phenomena such as cavity assisted coherent population transfer between the two radiatively coupled  $\Lambda$ -systems and deterministic entanglement are studied. The calculations will however focus on parameters, typical for NV-centers, which can be addressed as  $\Lambda$ -type level systems [STN<sup>+</sup>06, TCT<sup>+</sup>10, MGT<sup>+</sup>11]. Such as in the previous chapters, the calculations are based on an equation of motion approach [CRCK10, KCR<sup>+</sup>11], treating

the electron-photon coupling up to an arbitrary accuracy. With this method, both, the material quantities, such as the electronic densities, polarization or the combined lower states four-level subsystem of the coupled emitters, as well as the field quantities, such as the photon-number and probability distribution are accessible. Here, in order to focus on the methodological description and principle investigation, only electron-photon and electron-laser coupling is regarded. At first, the calculations are reduced to only one emitter in the cavity, discussing the basic processes in such a system and then extended the considerations to the description of two cavity coupled  $\Lambda$ -type emitters.

## 6.2. Cavity-QED of an optically driven $\Lambda$ -system

In this section the system consists of a  $\Lambda$ -system [See Fig. 6.1] with an upper state  $|a\rangle$  and two lower states  $|b\rangle$  and  $|c\rangle$ . The transition  $|b\rangle \rightarrow |a\rangle$  is driven by an external laser field, while the other transition  $|c\rangle \rightarrow |a\rangle$  is coupled to a single cavity mode. This interaction scheme is similar to the usual scheme used for stimulated Raman adiabatic passage (STIRAP) [BTS98]. Usually, this scheme includes two coherent laser fields, each driving one transition in the  $\Lambda$ -system. In such a system, coherent population transfer between the two lower states  $|b\rangle$  and  $|c\rangle$  can be induced by the two laser fields. Although there is no direct interaction between the two lower states, a coherence between the lower states  $P_{cb} \equiv \langle |c\rangle\langle b| \rangle$  is created due to the combined interactions [SZ97]. In consequence, the electron can be transferred between those states, but without passing the upper state. The usual pulse sequence is as follows: The electron starts in the state  $|b\rangle$ , with the laser (control laser) coupling the transition  $|b\rangle \rightarrow |a\rangle$  still switched off. The first laser pulse (Stokes laser) to arrive is driving the empty transition  $|c\rangle \rightarrow |a\rangle$ , therefore not yet affecting the systems dynamics. With an offset, a second pulse (control laser), that is temporally overlapping with the first pulse (Stokes laser) arrives. The resulting coherence transfers the electron between the lower states. In order to prevent any excitation into the upper state  $|a\rangle$ , it is best to choose a frequency detuning of the laser and the cavity with respect to the transitions, which is in the range of the respective Rabi-frequency.

Here, a cavity coupling replaces the action of the Stokes laser [JH11, IAB<sup>+</sup>99] in the typical STIRAP setting [as illustrated in Fig. 6.1]. To control the transfer, the second transition is still driven by a coherent laser field. In difference to the usual setup, the cavity is always on. The interaction with the classical laser field, however, also allows for a controlled time dependent transfer envelope.

The free  $H_0$  and the interaction part  $H_I$  for the cavity coupled and optically driven  $\Lambda$ -system reads in RWA:

$$H_0 = \sum_{i \in \{a,b,c\}} \hbar\omega_i |i\rangle\langle i| + \hbar\omega_0 c^\dagger c, \quad (6.1)$$

$$H_I = \hbar[\Omega(t)|b\rangle\langle a|e^{i\omega_L t} + g_{\text{cav}}|c\rangle\langle a|c^\dagger] + H.c., \quad (6.2)$$

Here,  $\Omega_L(t)$  is the time dependent coupling to the external laser field, driving the transition  $|b\rangle \rightarrow |a\rangle$ , and  $g_{\text{cav}}$  denotes the cavity coupling for the transition  $|c\rangle \rightarrow |a\rangle$ .  $c^\dagger/c$  are the usual photonic creation- and annihilation operators of the quantized electromagnetic field.

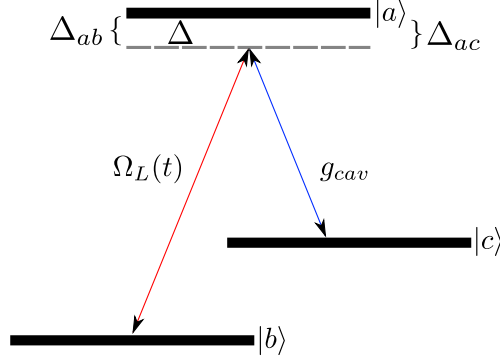


Figure 6.1.: Scheme of a  $\Lambda$ -system, placed within a single mode cavity, with cavity mode 0. The lower levels  $|b\rangle$  and  $|c\rangle$  each are coupled to the excited state  $|a\rangle$ . The transition  $|c\rangle \rightarrow |a\rangle$  is coupled by the cavity  $g_{cav}$ . The transition  $|b\rangle \rightarrow |a\rangle$  is driven by the exciting laser  $\Omega(t)$ , with frequency  $\omega_L$ . For the stimulated Raman process, the frequency detunings of the laser  $\Delta_L$  and the cavity  $\Delta_{cav}$  from the respective transitions are usually a match.

As also depicted in Fig. 6.1, laser and cavity are often frequency detuned with respect to the electronic transitions by  $\Delta_L = \omega_{ab} - \omega_L$  and  $\Delta_{cav} = \omega_{ac} - \omega_0$ . These detunings prevent from exciting the  $\Lambda$ -system into the upper state  $|a\rangle$ .

### 6.2.1. Equations of motion for the single $\Lambda$ -system

In the following, the same form of abbreviation for the three photon assisted electronic densities and polarizations is used:

$$C^{(p|s)} = \langle |c\rangle \langle c| c^{\dagger p} c^s \rangle, \quad B^{(p|s)} = \langle |b\rangle \langle b| c^{\dagger p} c^s \rangle, \quad A^{(p|s)} = \langle |a\rangle \langle a| c^{\dagger p} c^s \rangle, \quad (6.3)$$

$$P_{ca}^{(p|s)} = \langle |c\rangle \langle a| c^{\dagger p} c^s \rangle, \quad P_{ba}^{(p|s)} = \langle |b\rangle \langle a| c^{\dagger p} c^s \rangle, \quad P_{bc}^{(p|s)} = \langle |b\rangle \langle c| c^{\dagger p} c^s \rangle. \quad (6.4)$$

Starting with the equation for the polarization  $P_{bc}^{(p|s)}$ , as this is the coherence, relevant for the STIRAP-process its EOM reads according to Sec. 2.6:

$$\begin{aligned} \dot{P}_{bc}^{(p|s)} = & i[(p-s)\omega_0 - \omega_{cb}]P_{bc}^{(p|s)} + i\Omega_L P_{ca}^{(s|p)*} e^{-i\omega_L t} \\ & - ig_{cav} s P_{ba}^{(p|s-1)} - ig_{cav} P_{ba}^{(p+1|s)}. \end{aligned} \quad (6.5)$$

The photon assisted lower states polarization  $P_{bc}^{(p|s)}$  is driven by the two other coherences only, agreeing with the corresponding equation in the usual STIRAP setup [SZ97] [See

Appendix A.5]. The only difference is, that the coherences here are  $p$  times photon creation- and  $s$  times annihilation operator assisted.

$$\begin{aligned}\dot{P}_{ba}^{(p|s)} &= i[(p-s)\omega_0 - \omega_{ab}]P_{ba}^{(p|s)} - i\Omega_L(A^{(p|s)} - B^{(p|s)})e^{-i\omega_L t} - ig_{\text{cav}}P_{bc}^{(p|s+1)}, \quad (6.6) \\ \dot{P}_{ca}^{(p|s)} &= i[(p-s)\omega_0 - \omega_{ac}]P_{ca}^{(p|s)} + ig_{\text{cav}}(A^{(p|s+1)} - C^{(p|s+1)}) + ig_{\text{cav}}pA^{(p-1|s)} \\ &\quad - \Omega_L P_{bc}^{(s|p)*} e^{-i\omega_L t}.\end{aligned}\quad (6.7)$$

In the equations for the polarizations, corresponding to the two transitions of the  $\Lambda$ -system, finally there appear the three photon-assisted densities:

$$\begin{aligned}\dot{A}^{(p|s)} &= [(p-s)\omega_0]A^{(p|s)} + i\Omega_L P_{ba}^{(p|s)} e^{i\Omega_L t} - i\Omega_L P_{ba}^{(s|p)*} e^{-i\omega_L t} \\ &\quad + ig_{\text{cav}}P_{ca}^{(p+1|s)} - ig_{\text{cav}}P_{ca}^{(s+1|p)*},\end{aligned}\quad (6.8)$$

$$\dot{B}^{(p|s)} = [(p-s)\omega_0]B^{(p|s)} - i\Omega_L P_{ba}^{(p|s)} e^{i\omega_L t} + i\Omega_L P_{ba}^{(s|p)*} e^{-i\omega_L t} \quad (6.9)$$

$$\begin{aligned}\dot{C}^{(p|s)} &= [(p-s)\omega_0]C^{(p|s)} - ig_{\text{cav}}P_{ca}^{(p+1|s)} + ig_{\text{cav}}P_{ca}^{(s+1|p)*} \\ &\quad + ig_{\text{cav}}pP_{ca}^{(s|p-1)*} - ig_{\text{cav}}sP_{ca}^{(p|s-1)}.\end{aligned}\quad (6.10)$$

Note, that in the case of  $p \neq s$ , ( $p + s > 0$ ) for the photon-assisted densities in Eqs. (6.7) and (6.6) it applies:

$$\{|A^{(p|s)}|, |C^{(p|s)}|, |B^{(p|s)}|\} = \begin{cases} 0, & \text{Fock, thermal statistics,} \\ \geq 0 & \text{coherent statistics.} \end{cases} \quad (6.11)$$

From this, the same condition follows for  $P_{ba}^{(p|s)}$ , while the opposite is true for  $P_{ca}^{(p|s)}$  and  $P_{bc}^{(p|s)}$ . For an initial Fock or a thermal statistics in the cavity, the latter two quantities can only exist for  $p \neq s$ . In particular, the lower states polarization  $P_{bc}^{(p|s)}$  is driven by polarizations, that have either a photon operator more or less with respect to the densities. This means, that a control laser and cavity induced transition  $|b\rangle \rightarrow |c\rangle$  ( $|c\rangle \rightarrow |b\rangle$ ) between the lower states, can only occur under the emission (absorption) of a cavity photon. In the following sections, the case which will be of particular interest for an initially empty cavity. Therefore, the quantity  $P^{(0|0)}$ , relevant in the classical STIRAP-scheme, does not exist for the here considered cavity-assisted STIRAP analog. However, writing the equation for  $P_{bc}^{(0|1)}$  Eq. (6.5) in a rotating frame with the exciting laser field  $P_{bc}^{(0|1)+} \rightarrow P_{bc}^{(0|1)} e^{i\omega_L t}$ , the similarity to the Raman process becomes apparent [See Tab. 4.1]:

$$\dot{P}_{bc}^{(0|1)+} = -i[\omega_0 + \omega_{cb} - \omega_L]P_{bc}^{(0|1)+} + i\Omega_L P_{ca}^{(1|0)*} - ig_{\text{cav}}sP_{ba}^{(0|0)+}, \quad (6.12)$$

This quantity exhibits a free rotation part, that is creating a resonance, if the cavity frequency matches the frequency of the drive plus the frequency gap between the lower levels  $\omega_0 - \omega_L = (\omega_{ac} + \Delta_{\text{cav}}) - (\omega_{ab} + \Delta_L) = \omega_{cb}$ . Thus, the resonance condition is met for equal detunings  $\Delta_{\text{cav}} \approx \Delta_L$  from the respective transition frequencies. In favor of a laser quanta with frequency  $\omega_L$ , a frequency detuned photon (detuned by  $\omega_{cb}$  from  $\omega_{ac}$ ) is created or destroyed, similar to an inelastic scattering process. The difference is of course,

that there is a transition between two electronic states, but since they are not coupled through any of the light fields or modes, this transition works as an inelastic process, where the system gains or loses a certain amount of energy from or into the cavity field.

### 6.2.2. Effective two level system

A form of interaction, described by  $H_I$  is known to result in a time-dependent eigenstate of the form  $|\phi\rangle(t) = \alpha(t)|b, n\rangle + \beta(t)|c, n'\rangle$  [SZ97, FL02], not including the excited state  $|a, n\rangle$  in the superposition of the unperturbed system states. Choosing the right systems parameter and initial conditions, it is possible to permanently keep the system within this state. The dynamics is reduced to the two lower electronic states  $|b, n\rangle$  and  $|c, n'\rangle$  only. Sometimes, it can be advantageous to use this knowledge for an effective Hamiltonian-

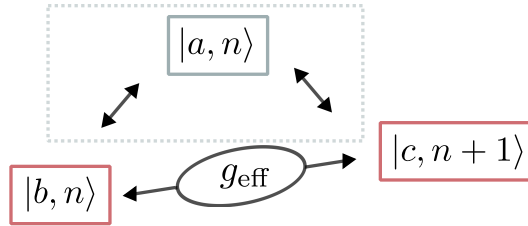


Figure 6.2.: Scheme of the interaction sequence of a  $\Lambda$ -system. Under the condition  $\Delta_{ab} = \omega_{ab} - \omega_L = \omega_{ac} - \omega_0 = \Delta_{ac}$  this sequence can be reduced into an effectively coupled two level subsystem (red boxes). The excited state  $|a, n\rangle$  within the dotted box is eliminated as does not take part in the dynamics.

approach, eliminating the excited state  $|c\rangle$  [CT92, BPM07, IAB<sup>+</sup>99] from the interaction [See Fig. 6.2]. For this purpose, the Hamiltonian is written in a rotating frame according to  $|\psi\rangle \rightarrow |\phi\rangle = e^{i\frac{\hat{\Xi}}{\hbar}t}|\psi\rangle$ :

$$\hat{\Xi} = \hbar\Omega_c|c\rangle\langle c| + \hbar\Omega_b|b\rangle\langle b| + \hbar\Omega_a|a\rangle\langle a| + \hbar\Omega_0c^\dagger c. \quad (6.13)$$

Subsequently, the Hamilton-operator of Eqs. (6.1) and (6.2) is transformed according to  $\mathcal{H}_{\text{eff}} = e^{iS}\mathcal{H}e^{-iS}$ , with

$$S = S^\dagger = \alpha|b\rangle\langle a| + \alpha^*|a\rangle\langle b| + \gamma|c\rangle\langle a|c^\dagger + \gamma^*|a\rangle\langle c|c. \quad (6.14)$$

The quantities  $\alpha$  and  $\gamma$  are determined:

$$\text{with } \alpha \equiv \frac{i\Omega(t)e^{i(\omega_l - (\Omega_a - \Omega_b))t}}{[\omega_{ab} - (\Omega_a - \Omega_b)]}, \quad \gamma \equiv \frac{ig_{\text{cav}}e^{i(\Omega_0 - (\Omega_a - \Omega_c))t}}{[\omega_{ac} - (\Omega_a - \Omega_c) - (\omega_0 - \Omega_0)]} \quad (6.15)$$

Applying a second order perturbation calculation [See also Chap. 3, Sec. 3.5.1] with respect to the series expansion of the unitary transformation, the effective Hamiltonian is given by:

$$\begin{aligned}
 \mathcal{H}_{\text{eff}} &= \hbar \left( \omega_c - \Omega_c - \frac{g_{\text{cav}}^2}{\hbar[\omega_{ac} - (\Omega_a - \Omega_c) - (\omega_0 - \Omega_0)]} c^\dagger c \right) |c\rangle\langle c| \\
 &- \hbar \left( \omega_b - \Omega_b + \frac{\Omega^2(t)}{\hbar[\omega_{ab} - (\Omega_a - \Omega_b)]} \right) |b\rangle\langle b| + \hbar(\omega_0 - \Omega_0) c^\dagger c \\
 &- \frac{\hbar|g_{\text{cav}}||\Omega|}{2} \left[ \frac{1}{[\omega_{ab} - (\Omega_a - \Omega_b)]} + \frac{1}{[\omega_{ac} - (\Omega_a - \Omega_c) - (\omega_0 - \Omega_0)]} \right] \times \left\{ \right. \\
 &\quad \left. |b\rangle\langle c| c e^{i(\omega_l - (\Omega_a - \Omega_b))t} e^{-i(\Omega_0 - (\Omega_a - \Omega_c))t} + H.c. \right\}. \tag{6.16}
 \end{aligned}$$

Choosing the rotating frame as  $\Omega_b = 0$ ,  $\Omega_a = \omega_l$ ,  $\Omega_c = \omega_{cb}$  and  $\Omega_0 = \omega_l - \omega_{cb}$ , according to energy-conservation with respect to the stimulated Raman process, Eq. (6.16), finally results in the following effective Hamiltonian (in a similar form previously derived in Ref. [IAB<sup>+</sup>99]):

$$\begin{aligned}
 \mathcal{H}_{\text{eff}} &= \hbar(\omega_0 - \omega_L + \omega_{cb}) c^\dagger c + \hbar \frac{g_{\text{cav}}^2}{\Delta_{ac}} |c\rangle\langle c| c^\dagger c - \hbar \frac{\Omega(t)^2}{\Delta_{ab}} |b\rangle\langle b| \\
 &+ \hbar g_{\text{eff}} \left( |b\rangle\langle c| c + |c\rangle\langle b| c^\dagger \right). \tag{6.17}
 \end{aligned}$$

Here, the energy of the system was additionally shifted towards towards  $\omega_i - \omega_b$ . Expressed within the  $n$ -th photon manifold  $n = \{|c, n+1\rangle, |b, n\rangle\}$ , the effective Hamiltonian can be given by

$$\mathcal{H}_{\text{eff}}^{(n)} \hat{=} \begin{pmatrix} \hbar \left( (\omega_0 - \omega_L + \omega_{cb})n - \frac{\Omega(t)^2}{\Delta_{ab}} \right) & g_{\text{eff}} \sqrt{n+1} \\ g_{\text{eff}}^* \sqrt{n+1} & \hbar \left( \omega_0 - \omega_L + \omega_{cb} - \frac{g_{\text{cav}}^2}{\Delta_{ac}} \right) (n+1) \end{pmatrix}, \tag{6.18}$$

with the effective coupling element given as

$$g_{\text{eff}} = -\frac{\Omega(t)g_{\text{cav}}}{2} \left( \frac{1}{\Delta_{ab}} + \frac{1}{\Delta_{ac}} \right). \tag{6.19}$$

This effective Hamiltonian obviously strongly resembles the Jaynes-Cummings Hamiltonian [SZ97] with a direct coupling between the states  $|b, n\rangle$  and  $|c, n+1\rangle$  under the emission/absorption of a photon and the condition of a non vanishing electron-photon-  $g_{\text{cav}}$  and electron-laser coupling  $\Omega(t)$ . In this effective Jaynes-Cummings model (JCM),  $|c\rangle$  corresponds to the ground- and  $|b\rangle$  to the excited state of the effective two-level system. Assuming a temporal evolution of the systems state as  $|\psi(t)\rangle = \sum_n [\alpha_{c,n}(t)|c, n\rangle + \alpha_{b,n}(t)|b, n\rangle]$  and a CW excitation  $\Omega(t) = \Omega$ , this model can straightforward be solved for the amplitudes  $c_{i,n}$  ( $i \in \{c, b\}$ ) in Schrödinger's picture [For the derivation see [SZ97] and Chap. 2 Sec.

2.6.1]. Accordingly, the inversion of the effective two-level system  $R(t) = \sum_n [\alpha_{c,n}(t)|c, n\rangle - \alpha_{b,n}(t)|b, n\rangle]$  is then given by:

$$R(t) = \sum_n P_n(t=0) \left[ \left( \frac{\Delta_n}{\Omega_{G,n}} \right)^2 + \frac{4g_{\text{eff}}^2(n+1)}{\Omega_{R,n}^2} \cos(\Omega_{G,n}t) \right]. \quad (6.20)$$

The difference to the JCM is, that not only the generalized Rabi-frequency  $\Omega_{G,n}$ , but also the frequency detuning  $\Delta_n$  inherits an additional dependence on the photon manifold  $n$ :

$$\Delta_n = -(\omega_{cb} + (\omega_0 - \omega_L) - \frac{g_{\text{cav}}^2}{\Delta_{ac}}(n+1) + \frac{\Omega^2}{\Delta_{ab}}), \quad (6.21)$$

$$\Omega_{G,n} = \sqrt{\Delta_n^2 + 4g_{\text{eff}}^2(n+1)}. \quad (6.22)$$

The system is operated at resonance (fulfilling the Raman resonance condition in Eq. (6.12)), if the cavity frequency  $\omega_0$  minus the laser frequency  $\omega_L$  match the lower frequency gap  $\omega_{cb}$ , i.e., laser and cavity are equally detuned from their respective transition.

Of course, this effective description is only valid for specific initial conditions, i.e., the electron has to be in one of the lower states. Further, the interaction timescales with respect to the two transitions  $|b\rangle \rightarrow |a\rangle$  and  $|c\rangle \rightarrow |a\rangle$  cannot deviate from each other in orders of magnitude, in order to justify the application of  $\mathcal{H}_{\text{eff}}$ . Although the form of  $g_{\text{eff}}$  suggests a coupling of the lower states regardless of the interaction strengths, detunings, pulse width or transition frequencies. An asymmetric coupling of the two transitions, however, or an insufficient detuning will result in the population of the excited state, meaning, that  $\mathcal{H}_{\text{eff}}$  is restricted to a well to be chosen parameter set. Therefore, the following calculations of the systems dynamics (compared with the effective predictions) will be based on the full Hamilton-operator of the system, giving therefore reliable information about the completeness and the timescale of the executed population transfer.

Later on, in Sec. 6.3, a population switch between two  $\Lambda$ -systems in rather bad optical cavities (with strong decay constants of the cavity mode) will be investigated. The question will be, if under such weak coupling conditions, the population switch is still manageable up to a sufficient percentage and within reasonable transfer times. This section, however, is supposed to give a basic understanding of the single cavity-coupled  $\Lambda$ -system and should serve as a measure to discriminate it from the case of the two radiatively coupled  $\Lambda$ -systems. As it turns out, there are crucial differences in their sensitivity towards several parameters, which is among others a counterintuitive asymmetry in the dependence on the cavity- and the laser detuning.

### 6.2.3. Coherent population transfer in a cavity-coupled $\Lambda$ -system – Ideal case

As a preliminary examination, the  $\Lambda$ -system be considered as lossless. In the following paragraphs, limitations arising from the inclusion of dissipative processes will be benchmarked on the now presented *ideal* case. Although, the case of a closed system is here referred to as ideal, the population transfer will always deviate by a small percentage from a total

transfer. Even under a frequency detuning of the laser and the cavity towards their respective transition, it is possible to excite the upper state  $|a\rangle$ , making the coherent population transfer incomplete. Further, a finite width of the laser pulse can lead to a resonant excitation, introducing an asymmetry to the coupling situation. This can lead to quite strong deviations from the effective model, which breaks down in just these cases. In general, the choice of parameters influences the achievable completeness of the transfer.

In Fig. 6.3 the inversion between the two lower states is depicted over time at CW excitation by the laser ( $\Omega(t) = \Omega$ ), driving the transition  $|b\rangle \rightarrow |a\rangle$ . Figure 6.3 compares the solutions as calculated with the full model (FM)  $R(t) = B^{(0|0)} - C^{(0|0)}$ , using Eqs. (6.5)-(6.10) with the analytic results  $R(t) = \sum_n [|\alpha_{c,n}(t)|^2 - |\alpha_{b,n}(t)|^2]$  of the effective JCM of Eqs. (6.18)-(6.20). The system starts in the lower electronic state  $|b\rangle$  ( $B^{(0|0)} = 1$ ), which (under CW excitation) corresponds to the excited state of the effective JCM. The cavity is assumed to be initially unpopulated, with  $N \equiv N^{(1|1)} = 0$ . For a coherent population transfer, i.e. the realization of the effective subsystem of Eq. (6.18), the electronic population is supposed to be transferred between the states  $|b\rangle$  and  $|c\rangle$ , without passing the upper state  $|a\rangle$ . The population of the upper density  $A^{(0|0)}$  during the transfer process has to be negligible. For better comparison with the effective model, the time is given in units of  $g_{\text{eff}}$ . For a symmetric coupling of the two transitions, the coupling parameters  $g_{\text{cav}} = \Omega$ , as well as the frequency detunings with respect to the two transitions  $\Delta_{ab} = \Delta_{ac} = \Delta$  are chosen to be equal. In Fig. 6.3(a) the detuning strength is given a value, large enough compared with the coupling elements  $\Delta = 150\Omega$ , in order to prevent the excitation of the system. Apparently, the effective JCM and the FM are in perfect agreement, for these excitation conditions. The  $\Lambda$ -system relaxes from the effective excited state  $|b\rangle$  into the ground state  $|c\rangle$ , so that the inversion  $R$  (in both the effective JCM and the FM) is performing symmetric Rabi-oscillations between 1 and  $-1$  with a period of  $t = g_{\text{eff}}^{-1}$ . However, in Fig. 6.3(b),

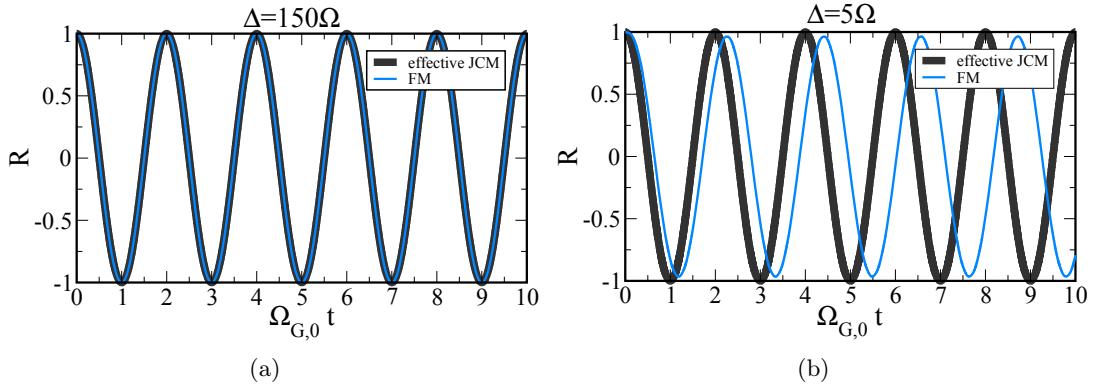


Figure 6.3.: Temporal evolution of the inversion  $R$ , calculated with the effective JCM (black curve) and the FM (blue curve) at a frequency detuning (a)  $\Delta_{ab} = \Delta_{ac} = 150\Omega$  and (b)  $\Delta_{ab} = \Delta_{ac} = 5\Omega$  under CW optical excitation and matching coupling parameters  $\Omega = \text{const} = g_{\text{cav}}$ .

the frequency detuning of only five times the coupling strengths  $\Delta = 5\Omega$  is obviously not sufficient anymore to effectuate a total transfer between the lower state in the case of the

FM. This is due to a population of the upper state  $|a\rangle$ . The stimulated Raman transition is superimposed by the a resonant excitation of the optical transitions. How much population actually will be built up in the upper state, also strongly depends on the pulse width and shape. In any case, the transfer will not reach 100%, if the frequency detunings, eliminating the involvement of the upper state, are too small compared with the coupling parameters. Further, the Rabi-frequency is no longer given by the effective coupling strength  $g_{\text{eff}}$ . In contrast to the FM, according to the effective JCM [See Eq. (6.19)] the detuning strength  $\Delta$  only influences the timescale of the population transfer, not the efficiency.

Another reason for spoiling a total coherent population transfer can be either unequal coupling strengths  $g \neq \Omega$  or frequency detunings  $\Delta_{ab} \neq \Delta_{ac}$  of the two optical transitions. In Figure 6.4(a), the temporal evolution of  $R$  is calculated for the detuning of Fig. 6.3(a) but different coupling parameters  $\Omega = \text{const} = 2g_{\text{cav}}$ . As can be deduced from Eqs. (6.21) and (6.21), a non symmetric coupling of the optical transitions leads to a detuning from the effective two-level transition. This causes an incomplete oscillation amplitude of  $R$ , i.e. the population is not totally transferred from the initial state  $B^{(0|0)}$  into the target state  $C^{(0|0)}$ . This behavior is demonstrated for both models, even at detuning strengths much larger than the coupling constants  $\Delta \gg \Omega$ . The same behavior is illustrated for unequal detuning strengths in 6.4(b). Note, that this stimulated Raman process is symmetric with respect to the detunings, i.e. changing the laser detuning  $\Delta_{ab}$  has exactly the same effect as changing the cavity detuning  $\Delta_{ac}$ . In order to achieve an as complete population transfer as possible

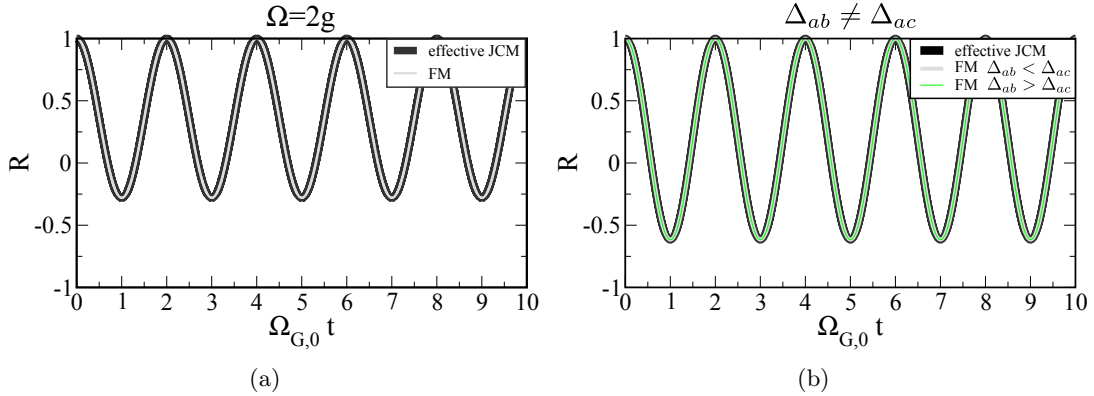


Figure 6.4.: Temporal evolution of the inversion  $R$ , calculated with the effective JCM (black curve) and the FM (colored curves). (a) at different values for the two coupling parameters  $\Omega = \text{const} = 2g_{\text{cav}}$ . The frequency detuning is set to  $\Delta_{ab} = \Delta_{ac} = 150\Omega$ . (b) at diverging values for the frequency detunings  $\Delta_{ab} \neq \Delta_{ac}$ . Here, the coupling strengths are equal  $g_{\text{cav}} = \Omega$ .

for a single  $\Lambda$ -system, it is usually preferable, to adjust an as symmetric coupling situation as possible.

### 6.2.4. Influence of photon loss

Since within this coherent population transfer, a photon is emitted into the cavity, a photon loss can inhibit the possibility of reestablishing the population of the initial state or even inhibit the transfer in the first place. In Fig. 6.5, the evolution of the inversion  $R$  is depicted in the case of a finite photon loss with  $10\kappa = g_{\text{cav}} = \Omega$ . In the case of the JCM Hamiltonian, such a coupling strength would still result in damped oscillations of the inversion. Here,

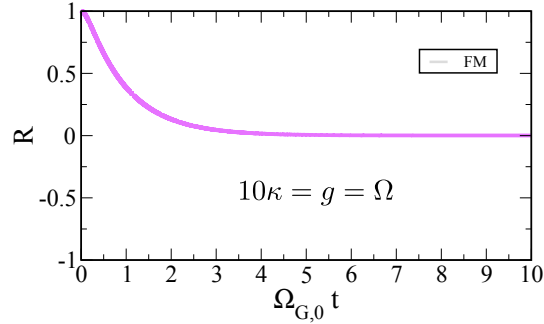


Figure 6.5.: Temporal evolution of the inversion  $R$ , calculated according to the FM under the influence of a photon loss  $10\kappa = g = \Omega$ . The systems does not exhibit Rabi-oscillations anymore, but saturates at the value  $R = 0.5$ .

however, instead of demonstrating effective Rabi-oscillations, as in the lossless cases, the inversion just decreases to zero, i.e. the population is never fully transferred to the target state  $|b\rangle \rightarrow |c\rangle$ . As the transfer process demands a second order interaction with  $g_{\text{eff}} \propto g_{\text{cav}}\Omega$ , there are no Rabi-oscillations occurring, although both the coupling parameters are stronger than the loss alone. The consequence of this higher order effective coupling is, that the transfer process requires a particularly strong emitter-cavity coupling, i.e. a strong coupling with respect to the transition  $|c\rangle \rightarrow |a\rangle$  with  $\kappa \ll g$  can still be insufficient. Since the stimulated Raman process produces a photon, that eventually leaves the cavity, this process will be eliminated for the population switch between two  $\Lambda$ -systems in Sec. 6.3.

### 6.2.5. Influence of the cavity statistics on the population transfer efficiency

So far, the cavity was assumed to be initially unpopulated  $N(0) \equiv \langle c^\dagger c \rangle(0) = 0$ , corresponding to a Fock state with  $P_0(t=0) = 1$ . However, if the statistics is initially in thermal state, the Rabi-oscillations will be altered. Therefore, in Fig. 6.6 the population transfer is depicted for a cavity, initially containing a thermal statistics with an average photon number of  $N \equiv N^{(1|1)} = 0.1$  and  $P_n(t=0) = \frac{1}{N+1} \left( \frac{N}{N+1} \right)^n$ . As also apparent from Eq. (6.20), the Rabi-frequency of the inversion is hardly influenced by the state of the system, since the 0th order photon probability  $P_0(t=0)$  is still the most prominent at the beginning. However, there are higher order probabilities  $P_n(0)$  with  $n > 0$  changing the oscillation amplitude of  $R$ . However, compared to the Fock case in 6.3, in the case of the initial thermal state, the oscillation amplitude is reduced. As visible form the perfect

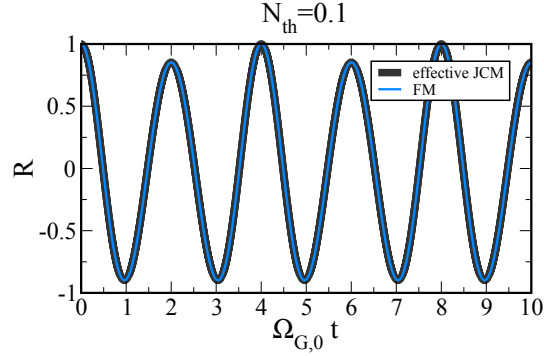


Figure 6.6.: Temporal evolution of the inversion  $R$  for an initial thermal state of the cavity statistics  $N_{th}(t=0) = 0.1$ . Coupling and detuning parameters as in Fig. 6.3.

agreement between the two models (JCM and FM), the cause of the amplitude loss is not due to a leakage out of the effective subsystem Eq. 6.18. In difference to the situation in Fig. 6.3(b) the decreased amplitude is here due to the thermal cavity statistics, causing a detuning situation more comparable to the non symmetric coupling in Fig. 6.4. This can be explained with the behavior of the photon probabilities  $P_n(t) = |\alpha_{b,n}(t)|^2 + |\alpha_{c,n}(t)|^2$ , which can be derived for the effective JCM, using Eq. (6.18):

$$\begin{aligned}
 P_n(t) &= P_n(t=0) \left\{ \cos^2\left(\frac{\Omega_{G,n}t}{2}\right) + \left(\frac{\Delta_n}{\Omega_{G,n}}\right) \sin^2\left(\frac{\Omega_{G,n}t}{2}\right) \right\} \\
 &+ P_{n+1}(t=0) \left(\frac{4g_{\text{eff}}^2 n}{\Omega_{G,n-1}^2}\right) \sin^2\left(\frac{\Omega_{G,n-1}t}{2}\right). \quad (6.23)
 \end{aligned}$$

Considering this formula, the photon probabilities can rotate with different generalized Rabi-frequencies  $\Omega_{G,n}$  and amplitudes, dependent on the initial cavity statistics  $P_n(t=0)$ . This is the reason, why the population is not fully transferred from  $|b\rangle$  to  $|c\rangle$ . Figure 6.7 shows the temporal behavior of the photon probabilities (as calculated with the FM) for an initially empty and an initially thermal populated cavity. In 6.7(a) the photon probabilities just follow the dynamics of the inversion (or densities respectively). During the transfer process from the state  $|b, 0\rangle$  ( $P_0 = 1$ ) containing no photons, the systems evolves into the state  $|c, 1\rangle$  ( $P_1 = 1$ ) containing exactly one photon. Higher order photon probabilities remain unpopulated, as the relaxing effective two level system can only result in the emission of a Fock-photon. The condition for the transfer between the zero- and the one-photon state is, that there is only one Rabi-frequency present at the beginning. Otherwise, the resonance condition dependent on a symmetric coupling of the two transitions cannot be met. This is not the case for the thermal statistics in Fig. 6.7(b). Initially, many of the  $P_n$  have relevantly high values. But most importantly, the probability  $P_1(t=0)$  of finding  $n = 1$  photons in the cavity at the beginning is unequal one. Therefore, the oscillation amplitude is reduced with respect to the Fock case. The  $P_n$  corresponding to the different photon manifolds each rotate with their individual Rabi-frequencies.

However, as during the transfer process, a photon gets injected into the cavity, the former

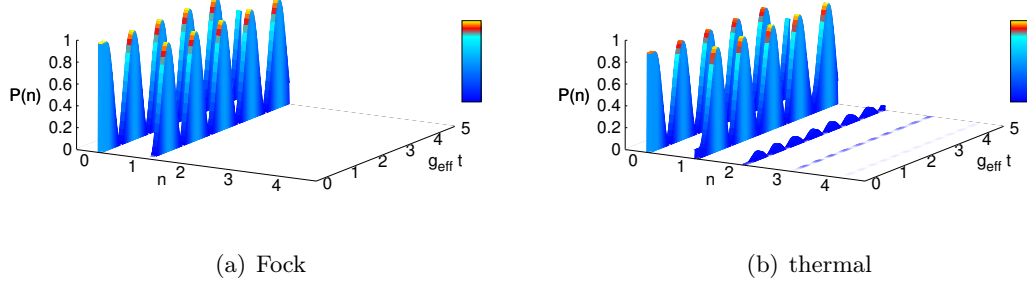


Figure 6.7.: Temporal evolution of the photon probability distribution  $P(n)$  for a cavity statistics initially in (a) a Fock state ( $N^{(1|1)} = 0$ ) and (b) a thermal state  $N^{(1|1)} = 0.1$ . The photon, that is introduced into the cavity via the stimulated Raman process is in the Fock state.

thermal statistics  $N_{th} = 0.1$  is now heavily doped with a Fock-photon  $N_{\text{Fock}} = 1$  [KCR<sup>+</sup>11]. Since this Fock-photon is now dominating the cavity statistics, the different initial conditions are compensated. Therefore, after half a Rabi-period, the cavity field is similar in the two cases, resulting in a similar dynamics of the transfer process. However, the amount of thermal cavity photons still results in chaotic and incomplete oscillation amplitudes, as known from the JCM in the limit of a thermal cavity statistics [SZ97].

Figure 6.7 shows the temporal evolution of the photon probability distribution  $P_n(t)$  for the initially empty (a) and the thermally (b) prepared cavity, corresponding to Fig. 6.6. Since in the case of  $N^{(0|0)}(t=0) = 0$  (Fock), i.e.  $P_0 = 1$  the system oscillates between the states  $|b, 0\rangle \rightarrow |c, 1\rangle$ , the photon probability distributions just reproduces these Rabi-oscillations. With the same Rabi-frequency as the densities, the probabilities oscillate between the probability of finding no photons and a single Fock photon in the cavity  $P_0(t) \rightarrow P_1(t)$ . All other probabilities  $P_n$  with  $n \geq 2$  remain exactly zero. In the thermal case with  $N^{(0|0)}(0) = B^{(1|1)} = 0.1$ , the photon probabilities at  $t = 0$  display a Bose-Einstein distribution with probabilities  $P_n$  for  $n \geq 2$  clearly nonzero. When the excitation pulse starts, a photon is injected into the cavity. Although, the Rabi-oscillations performed by  $P_0(t)$  and  $P_1(t)$  (as well as  $R$  in Fig. 6.6) resemble the behavior in the Fock case, there is again a difference in amplitude. Obviously, the probability  $P_0$  of finding zero photons in the cavity is initially lower, than in the the Fock case, so that the amplitude of  $P_0$  cannot be reduced by 1 in favor of  $P_1$ . Instead, the higher order probabilities are participating in the amplitude exchange [See also Fig. 6.8]. As given by formula Eq. (6.23), the higher order probabilities  $n \geq 2$  oscillate with larger effective Rabi-frequencies of approximately  $\Omega_{G,n} = \sqrt{\Delta_n^2 + 4g_{\text{eff}}^2(n+1)}$ , while  $P_0$  and  $P_1$  oscillate with the effective coupling element, given by Eq. (6.19) (same as the population inversion). As the amplitudes of the densities, depicted in Fig. 6.3(a) and 6.6 depend on the initial amplitudes of all the  $P_n(0)$  combined with their respective Rabi-frequencies  $g_{\text{eff}}^n$ , in the thermal case, the coherent population transfer cannot be complete. This is, although the system is perfectly within the effective

subsystem. Thus, in order to achieve a maximum transfer rate, the statistics in the cavity should best not involve thermal contributions.

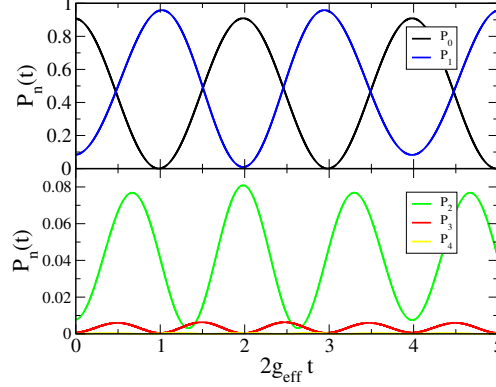


Figure 6.8.: Temporal evolution of the photon probabilities  $P_n(t)$  for  $n \in \{0, 1, 2, 3, 4\}$  for a cavity statistics initially in a thermal state  $N^{(1|1)} = 0.1$

### 6.3. Cavity QED of two radiatively coupled $\Lambda$ -systems

Dealing with a single laser driven  $\Lambda$ -system coupled to an optical cavity as in the previous sections, the population transfer between the lower state can only occur under the emission or the absorption of a photon, i.e. within a stimulated Raman process. However, assuming more than one of such emitters in the cavity, the population switch can also occur under the exchange of a "virtual photon" [IAB<sup>+</sup>99, YXFD10].

This section will focus on the theoretical investigation of two radiatively coupled  $\Lambda$ -systems as depicted in Fig. 6.9. The distance between the two systems is supposed to be large enough, that any Coulomb interaction between system 1 ( $S_1$ ) and system 2 ( $S_2$ ) can be disregarded. However, both  $\Lambda$ -systems being coupled to a single radiation mode, the two emitters experience a Coulomb-like coupling nonetheless. Such a radiation induced coupling can enforce transitions between the states  $|b_1, c_2, 0\rangle \rightarrow |c_1, b_2, 0\rangle$ , without involving the rest of the system states. Similar to the previous section, an effective two-level system, serving as a benchmark will be derived. As such a model is of limited applicability [See for Sec. 6.2] within a certain parameter range, it can only be used for giving rough information about timescales or efficiency at optimum for the processes of interest. More accurate theoretical predictions, especially in the presence of dissipative processes, will be gained solving the FM in Sec. 6.4. In fact, the findings of the following sections demonstrate, that the creation of a deterministic entanglement between two radiatively coupled NV-centers (described as  $\Lambda$ -systems) is achievable even in the case of a weak coupling situation.

#### 6.3.1. Equations of motion for the coupled $\Lambda$ -systems: Full model

The Hamiltonian of the system is basically the same as in Eqs. (6.1) and (6.2), with both systems coupled to the same cavity mode but different lasers with frequencies  $\omega_L^1$  and  $\omega_L^2$

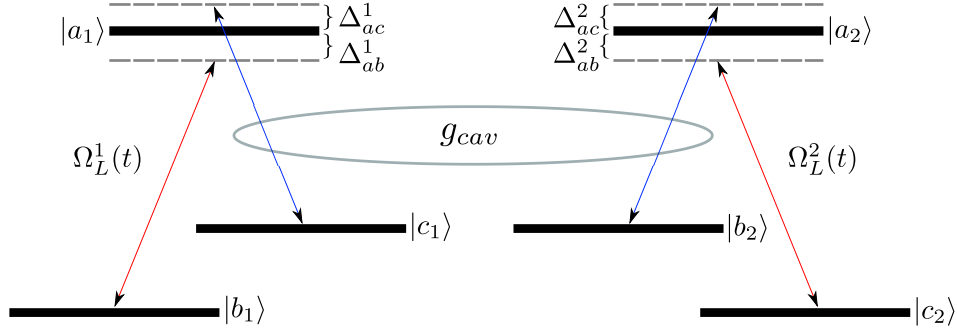


Figure 6.9.: Scheme of two radiatively coupled ( $g_{cav}$ )  $\Lambda$ -systems 1 and 2, each one driven by an external laser field  $\Omega_L^1$  and  $\Omega_L^2$ , respectively. The laser frequencies and the cavity frequency are detuned from the respective transitions by  $\Delta_{ab}^j = \omega_{ab}^j - \omega_l^j$  and  $\Delta_{ac}^j = \omega_{ac}^j - \omega_0$ .

[See Fig. 6.9]. In order to study the influence of photon loss and radiative decay, a coupling to a Markovian bath is assumed. Thus, the damping of the cavity mode  $\kappa$  as well as the excited state electronic densities  $\gamma_{ij}$ ,  $i, j \in \{a, b, c\}$  are given in the usual Lindblad form [Car99, BP02]:

$$\mathcal{L}(\rho) = \sum_{x=[ab],[ac]} \hat{\gamma}_x \rho \hat{\gamma}_x^\dagger - \frac{1}{2} \{ \hat{\gamma}_x^\dagger \hat{\gamma}_x, \rho \} + \hat{\kappa} \rho \hat{\kappa}^\dagger - \frac{1}{2} \{ \hat{\kappa}^\dagger \hat{\kappa}, \rho \} \quad (6.24)$$

with  $\hat{\gamma}_x = \sqrt{\gamma_x} |x\rangle\langle a|$  and  $\hat{\kappa} = \sqrt{\kappa} c$ . These dampings, as source of potential excitation loss will lead to further deviations from the rough effective model. Using Eqs. (6.1), (6.2) and (6.24), the equations for the densities and polarizations are given by:

$$\begin{aligned} \dot{\sigma}_{ij,\alpha}^{(p|s)} &= i[\omega_{ij,\alpha} + \tilde{\gamma}_{ij,\alpha}(1 - \delta_{ij}) + \omega_0(p - s) - (p + s)\kappa] \sigma_{ij,\alpha}^{(p|s)} + \tilde{\gamma}_{ij,\alpha} \delta_{ij} \sigma_{aa,\alpha}^{(p|s)} \\ &+ i\Omega_\alpha^* (\delta_{ia} \sigma_{bj,\alpha}^{(p|s)} - \delta_{jb} \sigma_{ia,\alpha}^{(p|s)}) + i\Omega_\alpha (\delta_{ib} \sigma_{aj,\alpha}^{(p|s)} - \delta_{ja} \sigma_{ib,\alpha}^{(p|s)}) \\ &+ ig_{cav,\alpha}^* (\delta_{ia} \sigma_{cj,\alpha}^{(p+1|s)} - \delta_{jc} [\sigma_{ia,\alpha}^{(p+1|s)} + s \sigma_{ia,\alpha}^{(p|s-1)}]) \\ &+ ig_{cav,\alpha} (\delta_{ic} [\sigma_{aj,\alpha}^{(p|s+1)} + p \sigma_{aj,\alpha}^{(p-1|s)}] - \delta_{ja} \sigma_{ic,\alpha}^{(p|s+1)}) \\ &- is g_{cav,\beta}^* \sigma_{ij,\alpha|ca,\beta}^{(p|s-1)} + ip g_{cav,\beta} \sigma_{ij,\alpha|ac,\beta}^{(p-1|s)}, \end{aligned} \quad (6.25)$$

with

$$\sigma_{ij,\alpha}^{(p|s)} \equiv \langle |i_\alpha\rangle \langle j_\alpha | c^\dagger{}^p c^s \rangle, \quad (6.26)$$

$$\sigma_{ij,\alpha|mn,\beta}^{(p|s)} \equiv \langle |i_\alpha, m_\beta\rangle \langle j_\alpha, n_\beta | c^\dagger{}^p c^s \rangle \quad (6.27)$$

For more clarity, the laser rotation is here included within  $\Omega_\alpha = \Omega_{L,\alpha}^{-i\omega_{l,\alpha}t}$ . Here, the Greek indices denote, if the electronic quantities belong to system  $S_1$  or  $S_2$ , with  $\alpha \neq \beta \in \{1, 2\}$ . The dampings  $\tilde{\gamma}$  in the first row are given by Eq. (6.24):

$$\tilde{\gamma}_{aa} = 2\tilde{\gamma}_{ab} = 2\tilde{\gamma}_{ac} = -(\gamma_{ab} + \gamma_{ac}), \quad (6.28)$$

$$\tilde{\gamma}_{bb} = \gamma_{ab}, \quad \tilde{\gamma}_{cc} = \gamma_{ac}, \quad \tilde{\gamma}_{cb} = 0. \quad (6.29)$$

The first four rows of (6.25) just describe the interaction of the  $\Lambda$ -system  $S_\alpha$  with the cavity mode and the respective laser field. The last row, however, describes the indirect interaction of  $S_\alpha$  with  $S_\beta$ , a coupling mediated by the cavity mode, that leads to the appearance of the two-particle quantities in Eq. (6.27).

$$\begin{aligned} \dot{\sigma}_{ij,\alpha|mn,\beta}^{(p|s)} &= i[\omega_{ij,\alpha} + \omega_{mn,\beta} + \tilde{\gamma}_{ij,\alpha}(1 - \delta_{ij}) + \tilde{\gamma}_{mn,\beta}(1 - \delta_{mn}) - (p + s)\kappa] \sigma_{ij,\alpha|mn,\beta}^{(p|s)} \\ &+ \tilde{\gamma}_{ij,\alpha} \delta_{ij} \sigma_{aa,\alpha|mn,\beta}^{(p|s)} + \tilde{\gamma}_{mn,\beta} \delta_{mn} \sigma_{ij,\alpha|aa,\beta}^{(p|s)} + i\omega_0(p - s) \sigma_{ij,\alpha|mn,\beta}^{(p|s)} \\ &+ i\Omega_\alpha^* (\delta_{ia} \sigma_{bj,\alpha|mn,\beta}^{(p|s)} - \delta_{jb} \sigma_{ia,\alpha|mn,\beta}^{(p|s)}) + i\Omega_\alpha (\delta_{ib} \sigma_{aj,\alpha|mn,\beta}^{(p|s)} - \delta_{ja} \sigma_{ib,\alpha|mn,\beta}^{(p|s)}) \\ &+ i\Omega_\beta^* (\delta_{ma} \sigma_{ij,\alpha|bn,\beta}^{(p|s)} - \delta_{nb} \sigma_{ij,\alpha|ma,\beta}^{(p|s)}) + i\Omega_\beta (\delta_{nb} \sigma_{ij,\alpha|an,\beta}^{(p|s)} - \delta_{ma} \sigma_{ij,\alpha|nb,\beta}^{(p|s)}) \\ &+ ig_{cav,\alpha}^* (\delta_{ia} \sigma_{cj,\alpha|mn,\beta}^{(p+1|s)} - \delta_{jc} [\sigma_{ia,\alpha|mn,\beta}^{(p+1|s)} + s \sigma_{ia,\alpha|mn,\beta}^{(p|s-1)}]) \\ &+ ig_{cav,\beta}^* (\delta_{ma} \sigma_{ij,\alpha|cn,\beta}^{(p+1|s)} - \delta_{nc} [\sigma_{ij,\alpha|ma,\beta}^{(p+1|s)} + s \sigma_{ij,\alpha|ma,\beta}^{(p|s-1)}]) \\ &+ ig_{cav,\alpha} (\delta_{ic} [\sigma_{aj,\alpha|mn,\beta}^{(p|s+1)} + p \sigma_{aj,\alpha|mn,\beta}^{(p-1|s)}] - \delta_{ja} \sigma_{ic,\alpha|mn,\beta}^{(p|s+1)}) \\ &+ ig_{cav,\beta} (\delta_{nc} [\sigma_{ij,\alpha|an,\beta}^{(p|s+1)} + p \sigma_{ij,\alpha|an,\beta}^{(p-1|s)}] - \delta_{na} \sigma_{ij,\alpha|mc,\beta}^{(p|s+1)}). \end{aligned} \quad (6.30)$$

These photon assisted two-particle quantities have their own dynamics, determined by the initial conditions. They strongly influences the evolution of the one-particle quantities of Eq. (6.25). The equation for the photon correlations of the cavity mode  $N^{(p|s)} \equiv \langle c^{\dagger p} c^s \rangle$ , whose population for  $p + s > 1$  is aimed at circumventing in the following, is given by:

$$\dot{N}^{(p|s)} = i[(p - s)\omega_0 + i(p + s)\kappa]N^{(p|s)} + i \sum_{\alpha=1,2} (p g_{cav,\alpha} \sigma_{ac,\alpha}^{(p-1|s)} - s g_{cav,\alpha}^* \sigma_{ca,\alpha}^{(p|s-1)}) \quad (6.31)$$

To solve this set of equations Eqs. (6.25) and (6.30), initial conditions with respect to the photon mode are chosen according to Eq. (3.28). However, the following sections will focus on the case of an initially empty cavity, starting in state  $|b_1, c_2, n = 0\rangle$ , therefore:

$$\sigma_{bb,1}^{(0|0)} = \sigma_{cc,2}^{(0|0)} = \sigma_{bb,1|cc,1}^{(0|0)} = 1. \quad (6.32)$$

In this case, all other quantities are zero at the beginning.

### 6.3.2. Effective two-level system

To have a more intuitive view on the system, a rough effective model for the favored adiabatic population transfer process is derived in this subsection, as the FM involves a

quite large and therefore hard to analyze set of equations. For this purpose, the system will be strongly reduced with respect to its degrees of freedom, eliminating most of the various interaction paths of the FM. However, already on the basis of this so derived Hamiltonian, the predicted timescales for a population switch between the  $\Lambda$ -systems state a complement to previous predictions [IAB<sup>+</sup>99]. The calculations, employing the FM of Eqs. (6.25) and (6.30) will further confirm these results in Sec. 6.4.

If starting in state  $|b_1\rangle$  in system  $S_1$  and  $|c_2\rangle$  in system  $S_2$  with an empty cavity  $N = 0$ , the state of the system can be given as:

$$\begin{aligned} |\psi(t)\rangle &= \alpha_{b_1,c_2,0}|b_1, c_2, 0\rangle + \alpha_{c_1,b_2,0}|c_1, b_2, 0\rangle \\ &+ \alpha_{a_1,c_2,0}|a_1, c_2, 0\rangle + \alpha_{c_1,a_2,0}|c_1, a_2, 0\rangle + \alpha_{c_1,c_2,1}|c_1, c_2, 1\rangle, \end{aligned} \quad (6.33)$$

As depicted in Fig. 6.10, a transition from  $|b_1, c_2, 0\rangle \rightarrow |c_1, b_2, 0\rangle$  (red boxes) would involve the states within the grey boxes, i.e also the emission of a photon by  $S_1$  and subsequent reabsorption of the photon by  $S_2$ . In some cases, however, if aiming at the generation of ground state entanglement or under intermediate or even weak coupling situations, it can be of advantage to suppress the emission of a cavity photon. In order to realize such a transition, the excited states  $|a_1, c_2, 0\rangle$  and  $|c_1, a_2, 0\rangle$  have again to be eliminated from the interaction paths. In difference to the single emitter case of the previous section, the intermediate state  $|c_1, c_2, 1\rangle$ , involving the cavity degree of freedom will be eliminated from the system. In principle of operation and as usual, this is done by choosing particular excitation conditions. Unlike from the previous considerations within Sec. 6.2, the excitation now has to deviate from the stimulated Raman resonance, the process which was exploited before. Thus, the cavity detunings and the laser detunings are requested to have unequal values  $\Delta_{ab}^i - \Delta_{ac}^i \neq 0$ ,  $i \in \{1, 2\}$  and the system can adiabatically pass between initial and target state, within the subsystem depicted in Fig. 6.10. Therefore, also the state  $|c_1, c_2, 1\rangle$  will be negligibly populated and can be eliminated from the effective dynamics as well.

In order to adiabatically eliminate the three states in the second row of Eq. (6.33), Schrödinger's equation is applied to state Eq. 6.33  $i\hbar \partial_t \langle i_1, m_2, n | \psi(t) \rangle = \langle i_1, m_2, n | H | \psi(t) \rangle$ :

$$i\hbar \dot{\alpha}_{b_1,c_2,0} = \hbar\Delta_{b_1,c_2,0} \alpha_{b_1,c_2,0} + \hbar\Omega_1^+ \alpha_{a_1,c_2,0}, \quad (6.34)$$

$$i\hbar \dot{\alpha}_{c_1,b_2,0} = \hbar\Delta_{c_1,b_2,0} \alpha_{c_1,b_2,0} + \hbar\Omega_2^+ \alpha_{c_1,a_2,0}, \quad (6.35)$$

$$i\hbar \dot{\alpha}_{c_1,c_2,1} = \hbar\Delta_{c_1,c_2,1} \alpha_{c_1,c_2,1} + \hbar g_{\text{cav},1}^+ \alpha_{a_1,c_2,0} + \hbar g_{\text{cav},2}^+ \alpha_{c_1,a_2,0}, \quad (6.36)$$

$$i\hbar \dot{\alpha}_{a_1,c_2,0} = \hbar\Delta_{a_1,c_2,0} \alpha_{a_1,c_2,0} + \hbar\Omega_1^- \alpha_{b_1,c_2,0} + \hbar g_{\text{cav},1}^- \alpha_{c_1,c_2,1}, \quad (6.37)$$

$$i\hbar \dot{\alpha}_{c_1,a_2,0} = \hbar\Delta_{c_1,a_2,0} \alpha_{c_1,a_2,0} + \hbar\Omega_2^- \alpha_{c_1,b_2,0} + \hbar g_{\text{cav},2}^- \alpha_{c_1,c_2,1}, \quad (6.38)$$

where the free rotation parts and the  $\pm$  superscripts at the coupling elements containing the rotating frames from Eq. (6.13) are defined as:

$$\Delta_{i_1,j_2,n} \equiv [\omega_{i_1} - \Omega_{i_1} + \omega_{j_2} - \Omega_{j_2} + n(\omega_0 - \Omega_0)], \quad (6.39)$$

$$\Omega_\alpha^\pm \equiv \Omega e^{\pm i(\omega_{L,\alpha} - \Omega_\alpha + \Omega_b)t}, \quad (6.40)$$

$$g_{\text{cav},\alpha}^\pm \equiv g_{\text{cav},\alpha} e^{\pm i(\Omega_0 - \Omega_\alpha + \Omega_c)t}, \quad (6.41)$$

In order to restrict the dynamics to the states  $|b_1, c_2, 0\rangle$  and  $|c_1, b_2, 0\rangle$ , the dispensable subspace is consequently assumed not to take part in the dynamics. Therefore, the derivatives of the respective coefficients vanish  $\dot{\alpha}_{c_1, c_2, 1} = \dot{\alpha}_{a_1, c_2, 0} = \dot{\alpha}_{c_1, a_2, 0} = 0$  [BPM07].

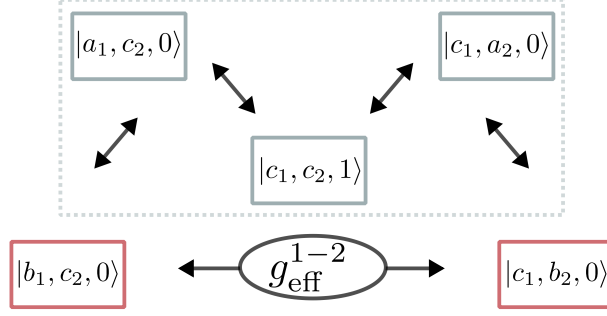


Figure 6.10.: Scheme of the effectively coupled two level subsystem (red boxes). The eliminated subspace is indicated by the states within the grey dotted box. The irrelevant subspace within the dotted box is not taking part in the dynamics, if starting in the relevant subsystem (red boxes) and avoid not only resonance with the transitions  $\Delta_l \gg \Omega$ , but also inhibit the induced Raman process  $\Delta_{ab} \neq \Delta_{ac}$ .

$$\alpha_{c_1, c_2, 1} = -\frac{g_{cav,1}^+}{\Delta_{c_1, c_2, 1}} \alpha_{a_1, c_2, 0} - \frac{g_{cav,2}^+}{\Delta_{c_1, c_2, 1}} \alpha_{c_1, a_2, 0}, \quad (6.42)$$

$$\alpha_{a_1, c_2, 0} = -\frac{\Omega_1^-}{\Delta_{a_1, c_2, 0}} \alpha_{b_1, c_2, 0} - \frac{g_{cav,1}^-}{\Delta_{a_1, c_2, 0}} \alpha_{c_1, c_2, 1}, \quad (6.43)$$

$$\alpha_{c_1, a_2, 0} = -\frac{\Omega_2^-}{\Delta_{c_1, a_2, 0}} \alpha_{c_1, b_2, 0} - \frac{g_{cav,2}^-}{\Delta_{c_1, a_2, 0}} \alpha_{c_1, c_2, 1}, \quad (6.44)$$

Inserting Eqs. (6.43), (6.44) and Eq. (6.42) into each other, and finally into Eqs. (6.34), (6.35), this results in two coupled equations of motion for:

$$\begin{aligned} i\hbar \dot{\alpha}_{b_1, c_2, 0} &= \hbar \left[ \Delta_{b_1, c_2, 0} - \frac{\hbar |\Omega_1|^2}{\Delta_{a_1, c_2, 0}} \left( 1 + \frac{|g_{cav,1}|^2}{\Delta_{a_1, c_2, 0} \bar{\Delta}_{c_1, c_2, 1}} \right) \right] \alpha_{b_1, c_2, 0} \\ &\quad - \frac{\hbar g_1^- g_2^+ \Omega_1^+ \Omega_2^-}{\Delta_{a_1, c_2, 0} \Delta_{c_1, a_2, 0} \bar{\Delta}_{c_1, c_2, 1}} \alpha_{c_1, b_2, 0} \end{aligned} \quad (6.45)$$

$$\begin{aligned} i\hbar \dot{\alpha}_{c_1, b_2, 0} &= \hbar \left[ \Delta_{c_1, b_2, 0} - \frac{\hbar |\Omega_2|^2}{\Delta_{c_1, a_2, 0}} \left( 1 + \frac{|g_{cav,2}|^2}{\Delta_{c_1, a_2, 0} \bar{\Delta}_{c_1, c_2, 1}} \right) \right] \alpha_{c_1, b_2, 0} \\ &\quad - \frac{\hbar g_2^- g_1^+ \Omega_2^+ \Omega_1^-}{\Delta_{a_1, c_2, 0} \Delta_{c_1, a_2, 0} \bar{\Delta}_{c_1, c_2, 1}} \alpha_{b_1, c_2, 0}, \end{aligned} \quad (6.46)$$

With  $\bar{\Delta}_{c_1, c_2, 1} \equiv \Delta_{c_1, c_2, 1} - \frac{\hbar^2 |g_1|^2}{\Delta_{a_1, c_2, 0}} - \frac{\hbar^2 |g_2|^2}{\Delta_{c_1, a_2, 0}}$ . Choosing the rotating frame as in Sec. 6.2 and assuming, that the two  $\Lambda$ -systems are identical with  $g_1 = g_2$ ,  $\Omega_1 = \Omega_2$  and  $\omega_{i,1} = \omega_{i,1}$ ,  $\mathcal{H}_{\text{eff}}^{1-2}$  finally reduces to:

$$\mathcal{H}_{\text{eff}}^{1-2} = -\hbar g_{\text{eff}}^{1-2} \left[ |b_1, c_2, 0\rangle \langle c_1, b_2, 0| + |c_1, b_2, 0\rangle \langle b_1, c_2, 0| \right], \quad (6.47)$$

$$\text{with } g_{\text{eff}}^{1-2} = \frac{|\Omega|^2 |g|^2}{\Delta_{ab}^2 (\Delta_{ac} - \Delta_{ab} - \frac{2|g|^2}{\Delta_{ab}})}. \quad (6.48)$$

In contrast to the effective coupling element for the STIRAP process of Eq. (6.19),  $g_{\text{eff}}^{1-2}$

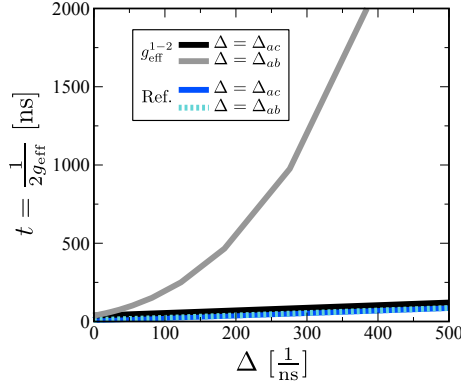


Figure 6.11.: Timescale of the effective interaction between the two  $\Lambda$ -systems as given by  $g_{\text{eff}}^{1-2}$  (Eq. (6.48)) and  $g_{\text{eff}}$  as given in Ref. [IAB<sup>+</sup>99] versus the laser frequency detuning  $\Delta = \Delta_{ab}$  (solid grey curve and dashed turquoise curve) and the cavity detuning  $\Delta = \Delta_{ac}$  (black and blue curves). The transfer time exhibits a linear dependence on  $\Delta_{ac}$  in both models, but a quadratic dependence on  $\Delta_{ab}$  in the here calculated Hamiltonian only.

holds an imbalance in the laser- and the cavity detuning. According to Eq. (6.48), the absolute value of the cavity detuning  $\Delta_{ac}$  is unimportant to the process, while the laser detuning  $\Delta_{ab}$  has to be nonzero. However, not surprisingly, the relative deviation from the STIRAP resonance condition  $\Delta_{ac} - \Delta_{ab} \approx 0$  enters the effective coupling parameter. For keeping the system in the effective two-level subspace, this condition must not be met. The population transfer would involve the emission of an actual, but a virtual photon, which must be circumvented for the adiabatic population switch. In Fig. 6.11 the interaction timescale, as given via the effective coupling is depicted over varying cavity detuning  $\Delta_{ac}$  as well as laser detuning  $\Delta_{ab}$ . It exhibits a linear dependence on  $\Delta_{ac}$ , but a quadratic dependence on  $\Delta_{ab}$ . The transfer time is further compared with the predictions given in

Ref. [IAB<sup>+</sup>99], which finds an identical linear dependence for both detunings [See Appendix A.6]. This deviation will further be discussed in Sec. 6.4.

$$\begin{aligned}\tilde{\alpha}_{b_1, c_2, 0} &= \frac{1}{2} \left\{ (\tilde{\alpha}_{b_1, c_2, 0}(0) + \tilde{\alpha}_{c_1, b_2, 0}(0)) e^{i|g_{\text{eff}}^{1-2}|t} + (\tilde{\alpha}_{b_1, c_2, 0}(0) - \tilde{\alpha}_{c_1, b_2, 0}(0)) e^{-i|g_{\text{eff}}^{1-2}|t} \right\}, \\ \tilde{\alpha}_{c_1, b_2, 0} &= \frac{1}{2} \left\{ (\tilde{\alpha}_{c_1, b_2, 0}(0) + \tilde{\alpha}_{b_1, c_2, 0}(0)) e^{i|g_{\text{eff}}^{1-2}|t} + (\tilde{\alpha}_{c_1, b_2, 0}(0) - \tilde{\alpha}_{b_1, c_2, 0}(0)) e^{-i|g_{\text{eff}}^{1-2}|t} \right\},\end{aligned}$$

Starting in level  $|b_1, c_2, 0\rangle$ , the probabilities are given by [YXFD10]:

$$|\alpha_{b_1, c_2, 0}|^2 = \frac{1}{2} [1 + \cos(2|g_{\text{eff}}^{1-2}|t)], \quad (6.49)$$

$$|\alpha_{c_1, b_2, 0}|^2 = \frac{1}{2} [1 - \cos(2|g_{\text{eff}}^{1-2}|t)]. \quad (6.50)$$

According to Eqs. (6.49) and (6.50), the system exhibits Rabi-oscillations between the state  $|b_1, c_2, 0\rangle$  and  $|c_1, b_2, 0\rangle$  under adiabatic excitation conditions. Without passing the excited states and under the exchange of a virtual photon, Eqs. (6.49) and (6.50) describes a periodic population switch between the two  $\Lambda$ -systems.

While operating within the reduced subspace  $\{|b_1, c_2\rangle, |c_1, b_2\rangle\}$  (the photon degree of freedom is skipped), the system obviously exhibits ground state entanglement between the two  $\Lambda$ -systems, i.e. the system will be in the inseparable state  $|\psi_{\text{eff}}\rangle = \alpha_{b_1, c_2}(t)|b_1, c_2\rangle + \alpha_{c_1, b_2}(t)|c_1, b_2\rangle$ , with  $\alpha_{b_1, c_2}(t) \neq 0$  and  $\alpha_{c_1, b_2}(t) \neq 0$  during the transfer. In order to theoretically demonstrate entanglement within the coherent transfer process of the subsystem, the concurrence  $C$  will be calculated according to Ref. [Woo98].

## 6.4. Deterministic entanglement of distant NV-centers at weak coupling conditions

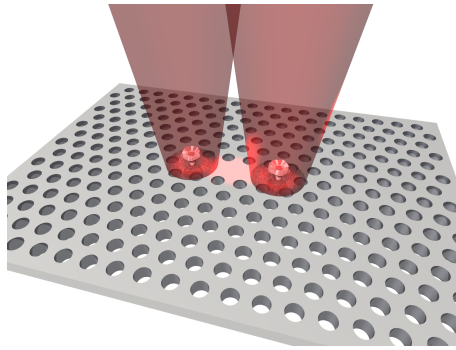


Figure 6.12.: Illustration of two NV centers in nanodiamonds, which are indirectly coupled through a photonic crystal cavity.

In the following the results calculated with Eqs. (6.25), (6.30) compared with (6.49) and (6.50) are presented in this section. At first, the system will be studied for the ideal and

lossless case. Afterwards, the influence of dissipative processes on the entanglement is investigated. As an application, the model is in detail discussed regarding NV-centers placed in photonic crystal cavities Fig. 6.12. Using experimentally achievable parameters, it is shown, that under weak coupling conditions usually found for these systems, a deterministic long range entanglement between two NV-centers (described as  $\Lambda$ -systems) is possible.

#### 6.4.1. NV centers

In this subsection, the material system is briefly introduced. Due to its comparably long radiative lifetime and as a scalable solid state nanostructure, the negatively charged NV center in diamond offers the possibility of generating single photons or entanglement [BCR<sup>+</sup>12, HA08, WSSB13, SRX<sup>+</sup>10]. It exhibits an optical transition at  $2.94 \frac{1}{f_s}$  with a triplet ground state  $|m_s = 0\rangle$  and  $|m_s = \pm 1\rangle$  [WSSB13]. Applying magnetic fields and strain, the excited state  $|e\rangle$  together with the ground states  $|m_s = 0\rangle$  and  $|m_s = 1\rangle$  constitutes a  $\Lambda$ -system [STN<sup>+</sup>06, TCT<sup>+</sup>10, MGT<sup>+</sup>11], as introduced in the previous sections. Placed into a photonic crystal cavity, and exchanging  $\{|a\rangle, |b\rangle, |c\rangle\}$  with  $\{|e\rangle, |0\rangle, |1\rangle\}$ , the NV center(s) can be described by the models illustrated in Figs. 6.1 and 6.9. For the generation of entanglement between the two NV centers, i.e. the reduction to the effective subsystem of Eq. (6.49) and Fig. 6.10, two NV centers are placed in two anti-nodes of the cavity mode of a photonic crystal cavity. Since it is still technically demanding designing a strong coupling situation for such systems, the generation of entanglement can be intermitted via the negative influence of a cavity loss. The following calculations will prove, that these conditions can be counteracted, leading to entanglement compatible with the results achieved in other typical systems [AGR<sup>+</sup>82, BR12].

#### 6.4.2. Entanglement at strong coupling conditions:– Ideal case

In this subsection, the influence of coupling parameters and detunings on the population exchange for an ideal lossless system will be discussed on the basis of the effective model (EM) Eq. (6.49) and the full model (FM) Eqs.(6.25) and (6.30).

The system is assumed to be prepared in the systems state  $|b_1, c_2, 0\rangle$ , i.e., with initial conditions according to Eq. 6.32. The two identical NV-centers are supposed to be excited with CW lasers  $\Omega_1 = \Omega_2$  of the same laser frequencies  $\omega_{L,1} = \omega_{L,2}$ . In order to keep the system within the reduced subspace of Fig. 6.10, the lasers and the cavity are supposed to be detuned from the respective optical transitions as depicted by Fig. 6.9. With a laser detuning of the opposite sign of the cavity detuning (here:  $\Delta \equiv \Delta_{ab} = -\Delta_{ac}$ ) it is ensured, that the system is far enough detuned from the Raman resonance  $\omega_L - \omega_0 = \omega_{cb}$ .

As for the population switch, the system has to evolve from  $|0_1, 1_2, 0\rangle$  into the state  $|c_1, b_2, 0\rangle$  in the EM or in the case of the FM  $\sigma_{bb,1} = \sigma_{cc,2} = 1 \rightarrow \sigma_{cc,1} = \sigma_{bb,2} = 1$ , in Fig. 6.13(a), the temporal evolution of the probability amplitudes as calculated by Eqs. (6.49) (bold blue curve) and 6.50 (bold grey curve) are depicted together with the initial densities of system  $S_1$  ( $\sigma_{bb,1}$  thin turquoise curve) and the target density of system  $S_2$  ( $\sigma_{bb,2}$  thin black curve). Despite of the rough assumption, carried out for the derivation of the EM, there is very good agreement between the models. At CW laser excitation, the system is caught almost perfectly within the lower states, performing a periodic total population switch between  $S_1$

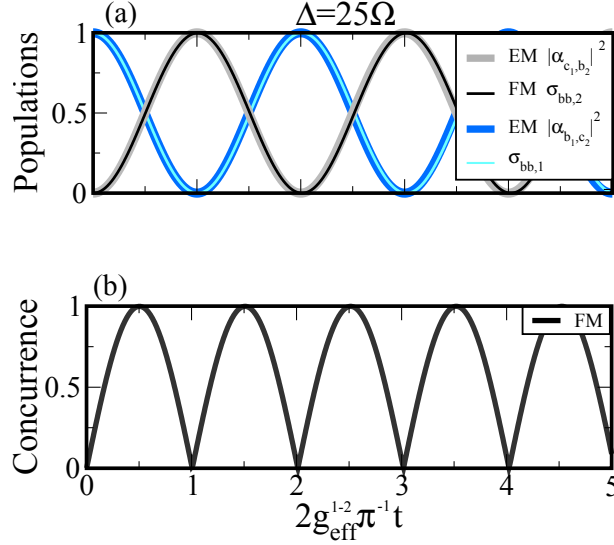


Figure 6.13.: Temporal evolution of the (a) probability amplitudes of the target state  $|\alpha_{c_1,b_2}|^2$  (bold grey curve) and the initial state  $|\alpha_{b_1,c_2}|^2$  (bold blue curve) and the corresponding population densities  $\sigma_{bb,2}$  (thin black curve) and  $\sigma_{bb,1}$  (thin turquoise curve). At a detuning strength  $\Delta = \Delta_{ab} = \Delta_{ac}$ , the results from the EM and FM are already in very good agreement. (b) Evolution of the the concurrence  $C$  (black curve). The time is given in units of the effective coupling element  $g_{\text{eff}}^{1-2}$  (FM).

and  $S_2$ . As a measure of the entanglement, the concurrence  $C$  as calculated with the FM is plotted in Fig. 6.13(b). Same as the population densities it performs Rabi-oscillations between 0 and 1, with the maximum value reached at the time point of the maximum entangled ground state  $\frac{1}{\sqrt{2}}(|b_1, c_2, 0\rangle + i|c_1, b_2, 0\rangle)$ . For the ideal case, this state is reached at time  $t = \frac{\pi}{g_{\text{eff}}^{1-2}}$ .

However, choosing a detuning  $\Delta = 5\Omega$ , that is of the order of the coupling strengths as depicted in Fig. 6.14, the system is not detuned enough neither from the respective transition frequencies, nor the Raman resonance. Even at small timescales within a few Rabi-periods, the deviation between the EM and the FM are clearly visible. The transfer between the initial and target state is not complete anymore, with a significantly altered Rabi-frequency. This behavior is comparable to the detuning sensitivity of the STIRAP process in Fig. 6.3. There is, however, a qualitative difference between the two effective models, when it comes to the particular influence of the two detunings  $\Delta_{ab}$  and  $\Delta_{ac}$  or the relationship between the coupling strengths.

This deviation is demonstrated in Fig. 6.15. According to formula Eq. (6.48) the subsystem breaks down for a too small or vanishing laser detuning  $\Delta_{ab} \approx \Omega$ . As shortly discussed before [See Fig. 6.11], this does not apply for the cavity detuning  $\Delta_{ac}$ . In principle, the effective two level system is supposed to hold even for a vanishing detuning  $\Delta_{ac} \rightarrow 0$ . Further, according to Eqs. (6.45), (6.46), (6.49) and (6.50), a deviation between cavity-

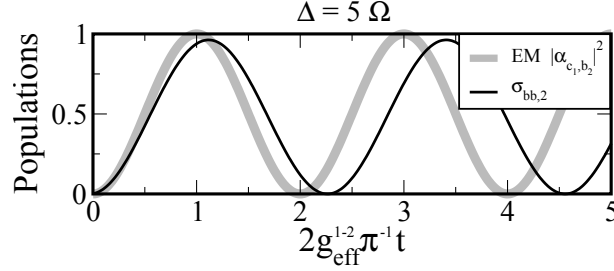


Figure 6.14.: Temporal evolution of the target probability amplitudes  $|\alpha_{c_1,b_2}|^2$  (bold grey curve) and population density  $\sigma_{bb,2}$  (thin black curve) for a detuning of the order of the coupling parameters  $\Delta = 5\Omega = 5g$ . In the case of the FM, the population transfer is not complete, with an altered Rabi-frequency with respect to the EM.

$g_{\text{cav}}$  and laser coupling strength  $\Omega$  is predicted to be insignificant to the completeness of the transfer process. Note, that in the case of the STIRAP-subsystem of the previous section, unequal strengths for the cavity- and the laser coupling led to an incomplete population transfer [See Eq. (6.21) and Fig. 6.4]. In order to verify these features of the EM in this section, the evolution of the densities and probability amplitudes are calculated both for a vanishing cavity detuning  $\Delta_{ac} \rightarrow 0$  and  $\Delta_{ab} = 50\Omega$  in Fig. 6.15(a) and (b) and a vanishing laser detuning  $\Delta_{ab} \rightarrow 0$  and  $\Delta_{ac} = 50\Omega$ , as well as deviating values for the cavity- and the laser coupling strength, using the FM. For better comparison with the EM, the time is again given in units of the effective coupling strength  $g_{\text{eff}}^{1-2}$ . Obviously and as predicted by the EM, in the cases of an asymmetric detuning situation with  $\Delta_{ab} \gg \Omega$  or in the case of a difference between electron-laser and electron-cavity coupling strengths in 6.15(a), the dynamics of the system remain unchanged, compared with the EM. The crucial deviation from the STIRAP resonance  $\Delta_{ac} - \Delta_{ab}$  stays the same, while the duration of the process scaling with Eq. (6.48) is strongly enhanced by the reciprocally quadratic dependence of  $g_{\text{eff}}^{1-2} \propto \frac{1}{\Delta_{ab}^2}$  and the quadratic dependence on the coupling strengths. The reason for this asymmetry is, that the cavity degree of freedom is eliminated from the dynamics. Via spontaneous emission, the  $\Lambda$ -systems experiences an effective coupling. As this coupling is realized via the exchange of a virtual photon and therefore by definition independent of resonance (or detuning), the effective system does not need a finite cavity detuning. In contrast to this, the effective subsystem cannot be realized without a finite laser detuning for both laser driven transitions. This is nicely demonstrated in Fig. 6.15(b), where all three densities of the second subsystem are depicted. The system obviously does not stay within  $\{|b_1, c_2, 0\rangle, |c_1, b_2, 0\rangle\}$  but loses excitation into the excited states, at time scales strongly deviating from the inverse effective coupling strength  $1/g_{\text{eff}}^{1-2}$ .

This short comparison between the EM and the FM under ideal conditions should provide a better judgment of the results, that will be presented in the following section. As the achievement of a preferably strong entanglement between the NV centers demands a fine tuning of counteracting parameters, it is sometimes necessary finding a compromise with a good entanglement yet acceptable transfer time. For tuning parameters to the optimum,

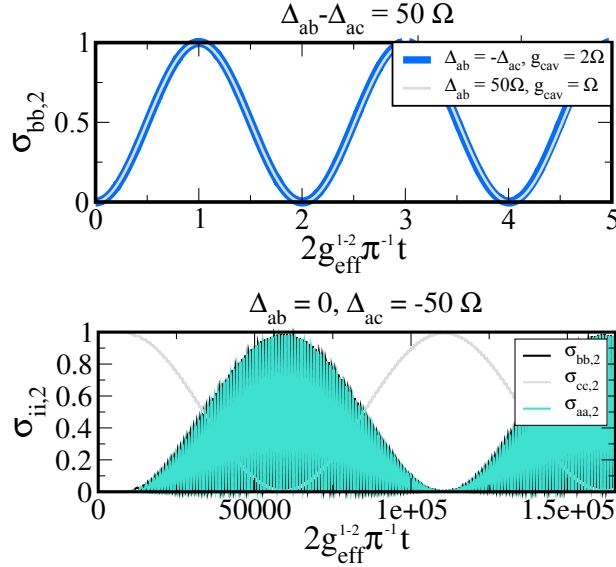


Figure 6.15.: (a) Temporal evolution of target state population densities  $\sigma_{bb,2}$  for a equal detunings, but different coupling strengths (fat blue curve) and different detunings ( $\Delta_{ab} = 50\Omega$ ,  $\Delta_{ac} = 0$ ) but equal couplings  $g_{\text{cav}} = \Omega$ . As long as the Raman process remains disabled, the transfer remains of total efficiency. (b) Evolution of the three densities of system  $S_2$  at a vanishing laser detuning  $\Delta_{ab} = 0$ . At a vanishing laser detuning, the effective subsystem is destroyed. The upper states  $\sigma_{aa}$  get involved in the dynamics. The frequency mismatch with the Raman resonance is the same in all three cases  $\Delta_{ab} - \Delta_{ac} = -50\Omega$ .

it is required to know, if an entanglement loss is due to dissipation or just a violation of the effective subsystems.

## 6.5. Influence of dissipation on the entanglement between the NV centers

The two dominating dissipative processes, occurring for the here discussed NV center-photonic crystal devices, is on the one hand a considerably strong photon decay, compared with the cavity coupling strength as well as a radiative dephasing. Although the latter is weak compared to  $\kappa$ , it begins to matter at some point at larger time scales. For the cavity coupling, a value for an NV center, sitting at a field maximum of a photonic crystal cavity [See Appendix A.6.1]. The used value of the cavity emitter coupling  $g_{\text{cav}} = 19.1 \text{ ns}^{-1}$  is currently in the range of experimental accessibility [ML08, WSK<sup>+</sup>10, STN<sup>+</sup>06, FSH<sup>+</sup>12] and will be used for most of the following calculations. The laser coupling strength will be set to the same value as the cavity coupling  $\Omega = g_{\text{cav}}$ . In Fig. 6.16, the target state density (a)  $\sigma_{bb,2}$  as a measure of the transfer and (b) the concurrence  $C$  as a measure of the entanglement during the transfer is depicted for three different sets of parameters, as

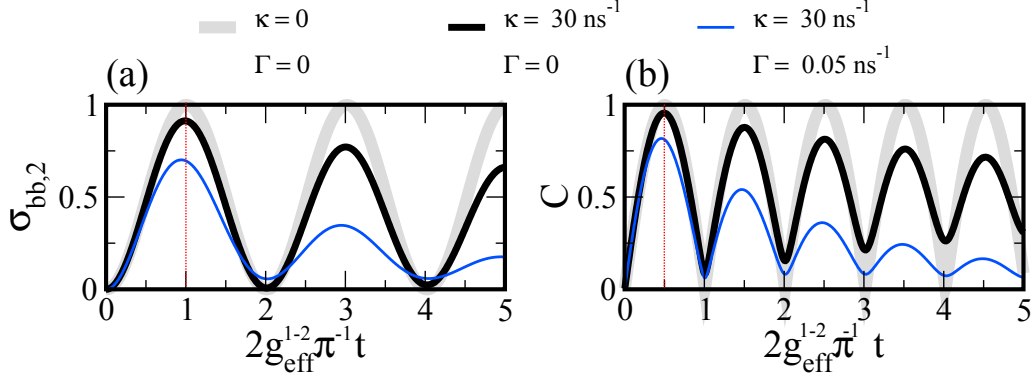


Figure 6.16.: Temporal evolution of the (a) target density  $\sigma_{bb,2}$  and the (b) concurrence  $C$  without dissipative processes (bold grey curve), with a finite photon loss rate  $\kappa = 30 \text{ ns}^{-1}$  (black curve) and with photon loss as well as radiative decay  $\Gamma_r = 0.05 \text{ ns}^{-1}$  (thin blue curve). For all calculations, the laser detuning is set to  $\Delta_{ab} = \Delta = 25g_{cav}$  and the cavity detuning is additionally scaled with the photon decay rate  $\Delta_{ac} = \Delta + 2\kappa$ .

calculated with the FM. For all cases, the laser detuning is chosen as  $\Delta_{ab} = \Delta = 25g_{cav}$  and a cavity detuning is accordingly set to  $\Delta_{ac} = \Delta + 2\kappa$ . The grey curves represent the ideal case, without photon- and excited state decay  $\kappa = \Gamma_r = 0$ . The black curves are the results for a finite photon lifetime in the cavity  $\kappa = 30 \text{ ns}^{-1}$  but still without radiative decay. Compared with the ideal case, the degree of transfer and entanglement is slightly reduced for the chosen detunings, reducing at each oscillation period. The first transfer, (the occurrence for the ideal case is marked by the red line), however, is almost complete, with a concurrence close to  $C \approx 1$ . A even larger detuning will even improve the transfer efficiency, but on the other hand also strongly increase the transfer time. Besides the fact, that small transfer times are feasible, a slow population switch promotes the impact of other decay processes. This effect is visible for the blue curves, where a radiative decay  $\Gamma_r$  of the upper state is added. Although the radiative decay is small compared with the photon loss rate  $\Gamma_r \ll \kappa$ , it has a strong effect on the efficiency of the transfer and therefore the degree of entanglement. Since the influence of the radiative decay will become stronger, the longer the transfer is taking, it can be of advantage, choosing a smaller detuning for aiming at a shorter transfer time.

Note, that in contrast to the population transfer process for the single  $\Lambda$ -system, there are still Rabi-oscillations occurring for the case with strong radiative decay. This is astonishing, as the population switch here even requires a fourth order interaction process, and the photon loss is even stronger compared with  $g_{cav}$ . The reason is, as predicted by [IAB<sup>+</sup>99], that there is no actual photon produced within the cavity, that could be exposed to this cavity loss  $\kappa$ .

Further, as visible from the red lines, marking the transfer time point of maximum transfer  $t_{max}$  in Fig. 6.16(a) or maximum concurrence  $C_{max}$  6.16(b), the transfer time is affected by the dissipative processes. Therefore, the following considerations will focus on a balanced

relationship of maximum transfer efficiency (concurrence) and maximum transfer time under the influence of photon- and radiative decay. The tool to regulate these two values are the laser-  $\Delta_{ab}$  and the cavity detuning  $\Delta_{ac}$  strengths.

### 6.5.1. Influence of photon decay and coupling strength on the concurrence

In order to particularly investigate the influence of the photon life time  $\kappa^{-1}$  (quality factor  $Q$ ) and the cavity coupling strength  $g_{cav}$  on the entanglement, the concurrence  $C$  and the transfer time  $t_{max}$  are calculated for varying cavity loss in Fig. 6.17(a) and (b). In order to restrict  $t_{max}$ , the laser detuning is chosen to be  $\Delta_{ab} = \Delta = 9g_{cav}$ . In order to counteract the growing cavity loss, the cavity detuning is additionally varied simultaneously  $\Delta_{ac} = -(\Delta + 2\kappa)$ . The cavity couplings are given values between  $g_{cav} = 12.57 \frac{1}{ns}$  and  $g_{cav} = 1.257 \frac{1}{ns}$ , both experimentally achievable values. As to be expected, the transfer

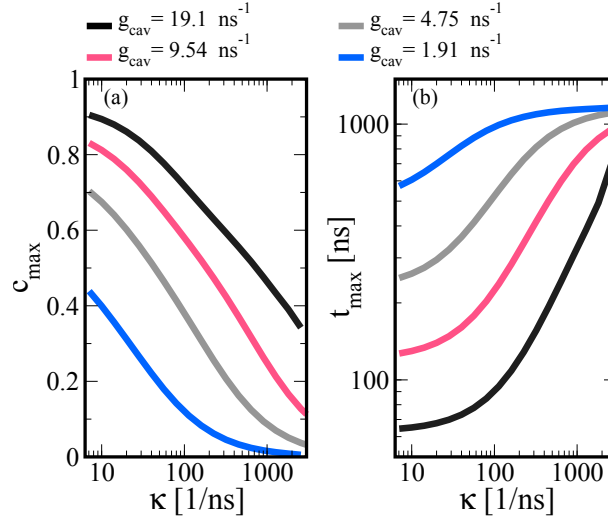


Figure 6.17.: (a) Concurrence  $C_{max}$  and (b) transfer time  $t_{max}$  as a function of the inverse cavity photon lifetime  $\kappa$ . The evolution is calculated for four different cavity coupling strengths between  $g_{cav} = 19.1 \frac{1}{ns}$  and  $g_{cav} = 1.91 \frac{1}{ns}$ . For all calculations, the laser detuning is set to  $\Delta_{ab} = \Delta = 9g_{cav}$  and the cavity detuning to  $\Delta_{ac} = -(\Delta + 2\kappa)$ . The coupling strengths are set to be equal  $\Omega = g_{cav}$ .

efficiency and therefore the concurrence  $C$  obtained, decreases with decreasing photon lifetime  $\kappa^{-1}$ . Simultaneously, the transfer time  $t_{max}$  grows. Further, there is also a strong dependence on the cavity coupling strength  $g_{cav}$ . For smaller  $g_{cav}$ , the transfer time is increased, leading to a higher impact of both, the photon decay, as well as the radiative lifetime  $\Gamma^{-1}$ . Further, the simultaneous tuning of  $\Delta_{cav}$  leads to higher entanglement times. Such a variation of the cavity detuning with  $\kappa$  can be of advantage if aiming at inhibiting the STIRAP resonance [cf. Eq. (6.48)]. However, as illustrated in Fig. 6.18 this simultaneous tuning of  $\kappa$  can also be a disadvantage for smaller coupling parameters. For the stronger cavity coupling (solid curves), the tuning of  $\Delta_{ac}$  together with  $\kappa$  is clearly of advantage

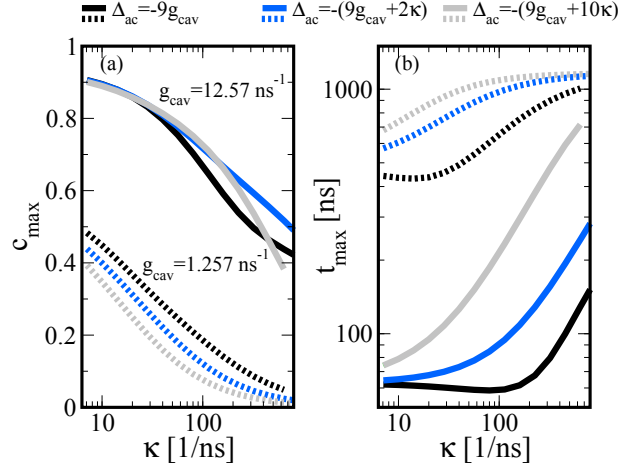


Figure 6.18.: (a) Concurrence  $C_{\max}$  and (b) transfer time  $t_{\max}$  as a function of the inverse cavity photon lifetime  $\kappa$ . The evolution is calculated for two different cavity coupling strengths  $g_{\text{cav}} = 19.1 \frac{1}{\text{ns}}$  (solid curves) and  $g_{\text{cav}} = 1.91 \frac{1}{\text{ns}}$  (dotted curves). The laser detuning is again set to  $\Delta_{ab} = \Delta = 9g_{\text{cav}}$  with  $\Omega = g_{\text{cav}}$ . For each of the cavity couplings, the entanglement generation is calculated for cavity detunings, scaling with  $\Delta_{ac} = -(\Delta + \{0\kappa, 2\kappa, 10\kappa\})$ .

within a limited area between large and short photon life times  $\kappa^{-1}$ . However, in the regime of small  $\kappa$ , the tuning has a negative influence. The reason for that is, that the process is still fast compared to  $\kappa$ . An increase of  $\Delta_{ac}$  only results in a longer entanglement time, supporting the impact of the radiative decay. In the limit of large  $\kappa$ , the transfer time is prolonged to such an extent, that the radiative dephasing starts to be dominating in all three cases. For the smaller cavity coupling (dotted), this is the case from the beginning, so that there is no advantage in proportionally tuning  $\Delta_{ac}$  with  $\kappa$ , Fig. 6.18(b). Here, it is of most importance, that the process occurs as fast as possible in order to prevent the action of  $\Gamma$ . This is of course only the case, as the initial detuning  $\Delta = 9g_{\text{cav}}$  is already chosen to be in a regime, where the entanglement process is still fast compared with the radiative decay, yet already of a high degree.

### 6.5.2. The dependence of the entanglement generation on the detuning strengths: - - The interplay between detuning and dissipative processes

As already visible from the analytical model Eq. (6.48) and depicted in Fig. 6.14, the cavity- and the laser detuning affect the entanglement generation in different ways. In Fig. 6.19, the concurrence  $C_{\max}$  and the entanglement time  $t_{\max}$  are depicted as a function of the frequency detuning. The black curves correspond to the variation of the laser detuning  $\Delta = \Delta_{ab}$  and the grey curves correspond to the variation of the cavity detuning  $\Delta = \Delta_{ac}$ . The detuning, that is not varied in the respective case, is set to  $\Delta_{ab/ac} = 9g_{\text{cav}}$ . The calculations are executed for two different photon decays  $30 \frac{1}{\text{ns}}$  (solid curves) and  $\kappa = 300 \frac{1}{\text{ns}}$ .

Both currently accessible values for the proposed NV center photonic crystal cavity system [ML08, WSK<sup>+</sup>10]. In agreement with the EM, the generation of entanglement requires

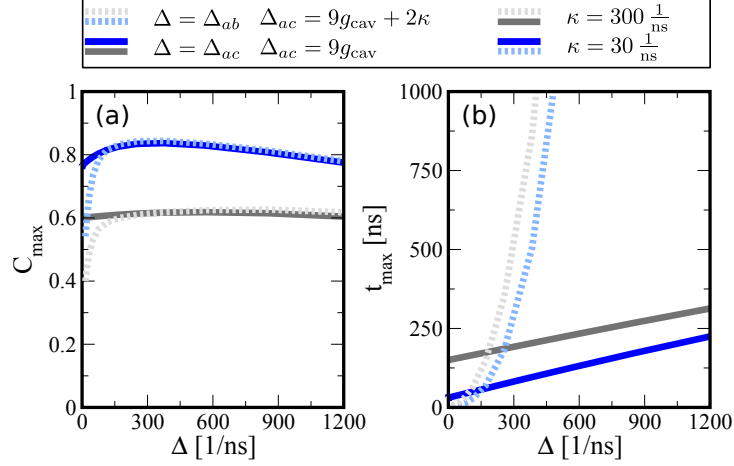


Figure 6.19.: (a) Concurrence  $C_{\max}$  and (b) entanglement time  $t_{\max}$  as a function of the laser detuning  $\Delta = \Delta_{ac}$  (solid curves) and the cavity detuning  $\Delta = \Delta_{ab}$  (dashed curves), each for two different photon decay rates  $\kappa = 30 \frac{1}{ns}$  (grey curves) and  $\kappa = 300 \frac{1}{ns}$  (blue curves). In all cases, the cavity coupling strength is  $g_{cav} = 19.1 \frac{1}{ns}$ . While one detuning is varied, the other one is held at  $\Delta_{ac} = 9g_{cav} + 2\kappa$  or  $\Delta_{ab} = 9g_{cav}$ , respectively. For large enough detuning strengths, the evolution of  $C$  is similar for both detunings. The transfer time  $t_{\max}$  shows a linear dependence on  $\Delta = \Delta_{ac}$  and a quadratic dependence on  $\Delta = \Delta_{ab}$  [See also Fid. 6.11].

a sufficiently large laser detuning, while the adiabatic population switch still works for a vanishing cavity detunings. Although in both cases, the entanglement time grows with increasing detuning strength  $\Delta$ , it shows different functional dependencies. As predicted by Eq. (6.48), the  $t_{\max}$  shows a more parabolic behavior for the variation of  $\Delta_{ab}$  (black curves), while the evolution of  $t_{\max}$  with  $\Delta_{ac}$  exhibits a linear-like slope (grey curves) [See also Fig. 6.11]. In both detuning cases and for both  $\kappa$ -strengths, the concurrence shows a maximum at a certain detuning strength, which is due to the radiative decay  $\Gamma$ , becoming important at higher transfer times  $t_{\max}$ . For the two different  $\kappa$ , this maximum occurs at different detunings, comparable with the value of the respective  $\kappa$ . For higher radiative decay, the beneficial effect of a detuning stays dominant compared to the diminishing effect of the radiative decay as the realization of the effective subsystem is only given for a sufficiently small overlap with the STIRAP resonance. Fig. 6.19 proves, that it is possible to achieve a considerate entanglement between the NV centers, even in the case of the low  $Q$  cavity. According to the photon life time and the excited states lifetime, the detunings can be adjusted to a significant value of  $C_{\max}$  and a reasonable entanglement time  $t_{\max}$ . In order to study the robustness of the used entanglement scheme towards transition frequency fluctuations, the entanglement generation is now investigated for a constant value of  $|\Delta_{ab} - \Delta_{ac}|$ , i.e. at a fixed overall detuning strength in Fig. 6.20. In order to simulate

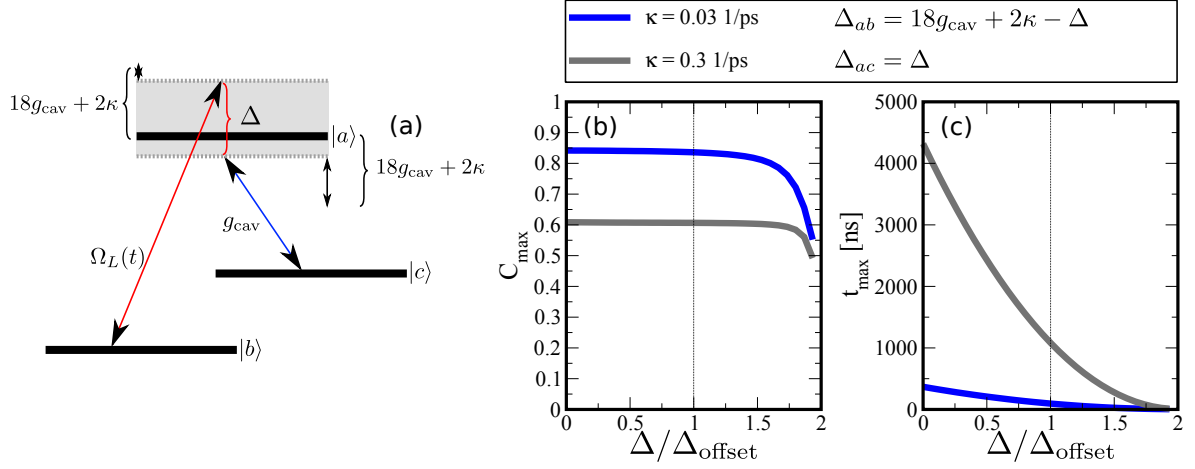


Figure 6.20.: (a) Scheme of a  $\Lambda$ -system at detuned excitation conditions. A detuning interval (grey area) is moved around the transitions. The laser frequency (red arrow) is adjusted at the upper bound of the interval and the cavity frequency (blue arrow) is adjusted at the lower bound of the detuning interval. (b) Concurrence achieved for two different  $\kappa = 30 \frac{1}{\text{ns}}$  (blue curve) and  $\kappa = 300 \frac{1}{\text{ns}}$  (grey curve) at transfer times depicted in (c) as a function of the moving delta interval  $\Delta \in [0, 18g_{cav} + 4\kappa]$ . For better comparison of the results for the different cavity losses,  $\Delta$  is normalized with the corresponding  $\Delta_{offset} = 9g_{cav} + 2\kappa$ .

such fluctuations, a detuning interval of  $\Delta = [0, 18g_{cav} + 2\kappa]$  is varied around the transition frequencies according to  $\Delta_{ab} = 18g_{cav} + 2\kappa - \Delta$  and  $\Delta_{ac} = -\Delta$  as illustrated in Fig. 6.20(a). As apparent from Fig. 6.20(b), the entanglement generation is almost invariant against a movement of the total delta interval, as long as the total detuning  $|\Delta_{ab} - \Delta_{ac}|$  is held constant, i.e., the scheme is robust against fluctuations in the detuning strengths. As previously pointed out, the concurrence is only affected, if the laser detuning becomes small compared with the coupling strength  $\Delta < 5g_{cav} = \Omega$ . However, for the sake of small transfer times it is of advantage, choosing a quite small laser detuning at the kink of the curves [Fig. 6.19].

### 6.5.3. Conclusion

In conclusion, photonic crystal cavities and NV centers can be considered to be promising candidates for a deterministic entanglement generation between spatially distant NV centers. Even at intermediate and weak coupling conditions, it is possible to achieve a considerable entanglement at reasonable transfer times, overcoming short photon life times. Further, the simple effective model serves as a reliable estimate for the interaction time scales, that can be expected. This timescale, however must not be large compared with the radiative lifetime of the excited state manifold. In contrast to previous models, an asymmetric dependence on the laser and the cavity detuning is found. This prediction is further confirmed by the results, that were gained using the full model.

# 7

## Conclusion and outlook

This thesis focuses on the theoretical solid state quantum optics and quantum control in photonic and phononic structured environments.

For a phonon laser with a semiconductor QD to serve as the active medium, which is coupled to an acoustic phonon cavity and driven by an optical laser field, the phonon emission dynamics is investigated on the basis of the higher order phonon-phonon correlations. Employing an equation of motion approach, transition of the phonon system state can be accessed via the higher order phonon coherences. Within a detuned optical excitation scheme, the internal cavity-phonon statistics are controlled from thermal and coherent to non-classical statistics. For more convenient considerations, an effective Hamiltonian approach of the stationary phonon laser yields simple analytical formulas for the input-output relations and the threshold behavior. An analysis of the different emission regimes predicts among others beneficial effects on phonon lasing for intermediate dephasing of the QD dipole transition. As the induced Raman process addressed with the frequency detuned external laser selects an effective inverse Jaynes-Cummings model, the radiative decay serves therefore as a natural pump of the effective upper laser level and establishes a beneficial process. Further, low phonon life times or weak radiative decay rates can also result in a stable non-classical emission statistics. Future studies could involve the inclusion of dissipative processes already on the basis of an effective Hamiltonian, as could be performed within a projection operator approach in Liouville-space or using an equation of motion approach to investigate other beneficial dissipative regimes for phonon lasing. Interesting could also be the consideration of feedback from the surroundings, implemented either on the basis of additional Lindblad-terms containing the phonon number of the external reservoir, or even a full multi-mode description with a time-delayed feedback of phonon-population. Furthermore, a detailed derivation of possible experimental signatures need to be employed to provide a proposal for experimental set-ups to investigate phonon laser dynamics as e.g. in the spectrum or in a detection of the phonon phase space.

Regarding the time-resolved emission spectrum in the high driving regime, a variety of accompanying LO-phonon features is investigated. In difference to atomic systems, the microscopic model reveals additional phonon assisted LO-phonon sidebands that appear in the fluorescence and the scattering contribution of the spectrum. These polaron features and the light induced multi-phonon processes demand a theoretical treatment of the phonon system, which is beyond the usual bath assumptions. For stationary pulses in the Mollow-regime, the spectrum exhibits additional phonon-assisted (also higher order) Mollow triplets. For Rabi-frequencies in the range of an LO-phonon frequency, anti-crossing between the Mollow-sidebands and the Mollow centers appear, which go with the effective electron-phonon coupling strength. Further, the phonon assisted Mollow-centers split into two lines, also with a splitting strength proportional to the electron-phonon coupling. The time resolved spectrum shows additional interference effects due to the spectral and temporal width of the laser pulse, as well as temporal asymmetries of the emission intensities of the Rabi-sidebands. Also for short excitation pulses, phonon-related anti-crossings and splittings occur, strongly changing the time-resolved spectrum in the high driving regime, towards the situation without electron-phonon interaction.

As an application of this time-resolved microscopic model and in collaboration with Stefan Werner et al., it was theoretically and experimentally found, that the emission dynamics of a multi-level QD, here modeled as a V-type semiconductor QD, clearly depends on the spectral position of the exciting laser. A future project in this direction would involve also the acoustical phonon contributions and the derivation of an effective theoretical model to treat the many-mode phonon field in non-equilibrium conditions.

In the final part of the thesis, a fully quantized approach is applied to describe a time delayed feedback mechanism in the quantum limit. The inclusion of photon-photon delay effects into the Jaynes-Cummings model restores Rabi oscillations even in the weak coupling regime. Here, the photonic tunnel exchange rate together with the action of the emitter serves as an excitation storage and realizes a constant number of cavity excitation. This allows feedback enhanced Rabi oscillations, that reveal in the very weak coupling limit the microscopic coupling element in the long time limes.

Further, as an example of coherent quantum control in the solid state, the generation of entanglement between radiatively coupled nitrogen-vacancy (NV) centers is proven to be possible, even at strong cavity loss rates. The calculations are based on an effective analytical treatment and are complemented with a full quantum mechanical description of two coupled three-level systems, that involves the cavity mediated interaction between the NV-centers. It is shown that photonic crystal cavities and NV centers can be considered to be promising candidates for a deterministic entanglement generation between spatially distant NV centers. This is true, even at intermediate and weak coupling conditions, since it is possible to achieve a considerate entanglement at reasonable transfer times, overcoming short photon life times. In contrast to previous models, a counterintuitive asymmetry towards the detuning of frequencies is predicted. This prediction is further confirmed by the results, that were gained using the full model.

---

# A

## Appendix

### A.1. Parameters of an InGaAs/GaAs-QD

Aus [Web02] und [LWWK07]

Parameter	Character	Value	Unit
Mass density	$\rho$	5370	kg/m <sup>3</sup>
Sound velocity	$v$	5110	m/s
Deformation potential (CB)	$D_c$	-14.6	eV
Deformation potential (VB)	$D_v$	-4.8	eV
Effektive Mass (CB)	$m_c^*$	0.067	$m_0$
Effektive Mass (VB)	$m_v^*$	0.45	$m_0$
LO-phonon energy	$\hbar\omega_{LO}$	36.4	meV
Width of wavefunction (CB)	$a_c$	3.19	nm
Width of wavefunction (VB)	$a_v$	5.8	nm

### A.2. Jaynes-Cummings-model

The equations of motion for the JCM Eq. (2.30) according to Eq. (2.38) read for resonance between cavity and emitter:

$$\dot{C}^{(0|0)} = 2\text{Im}(gP^{(0|0)}) = -\dot{N}^{(1|1)}, \quad (\text{A.1})$$

$$\dot{P}^{(0|0)} = -igC^{(0|0)} - ig(2C^{(1|1)} - N^{(1|1)}), \quad (\text{A.2})$$

Assuming an initially empty cavity, the equations can be simplified to:

$$\dot{R}^{(0|0)} = -4\text{Im}(gP^{(0|0)}), \quad (\text{A.3})$$

$$\dot{P}^{(0|0)} = igR^{(0|0)}, \quad (\text{A.4})$$

where  $R^{(0|0)} \equiv N^{(0|0)} - C^{(0|0)}$  is the negative inversion. This results just in a simple second order differential equation for  $R$ , that is (for  $R(t=0) = -1$ ) solved via:

$$R(t) = -\cos(2gt). \quad (\text{A.5})$$

### A.3. Equations for the emission spectrum of a quantum dot

$$\begin{aligned} \frac{d}{dt} \langle V_{(n|m)}^{(k|0)} \rangle &= i[(n-m)\omega_{LO} + (1-\delta_{k|0})(\omega_k - \omega_l) + i(n+m)\kappa] \langle V_{(n|m)}^{(k|0)} \rangle \\ &- (1-\delta_{k|0})i(M \langle P_{m|n}^{(0|0)} \rangle)^* \\ &+ \delta_{k|0} \| i \sum_{\bar{k}} M \langle P_{(n|m)}^{(\bar{k}|0)} \rangle - \delta_{k|0} i \sum_{\bar{k}} (M \langle P_{(m|n)}^{(\bar{k}|0)} \rangle)^* \\ &+ i\tilde{\Omega}(t) \langle P_{(n|m)}^{(k|0)} \rangle - i(\tilde{\Omega}(t) \langle P_{(m|n)}^{(0|k)} \rangle)^*, \end{aligned} \quad (\text{A.6})$$

$$\begin{aligned} \frac{d}{dt} \langle C_{(n|m)}^{(k|0)} \rangle &= i[(n-m)\omega_{LO} + (1-\delta_{k|0})(\omega_k - \omega_l) + i(n+m)\kappa] \langle C_{(n|m)}^{(k|0)} \rangle \\ &- \delta_{k|0} \| i \sum_{\bar{k}} M \langle P_{(n|m)}^{(\bar{k}|0)} \rangle + \delta_{k|0} i \sum_{\bar{k}} (M \langle P_{(m|n)}^{(\bar{k}|0)} \rangle)^* \\ &- i\tilde{\Omega}(t) \langle P_{(n|m)}^{(k|0)} \rangle + i(\tilde{\Omega}(t) \langle P_{(m|n)}^{(0|k)} \rangle)^* \\ &+ (1-\delta_{n|0})n ig^2 \langle C_{(n-1|m)}^{(k|0)} \rangle \\ &- (1-\delta_{m|0})m ig^2 \langle C_{(n|m-1)}^{(k|0)} \rangle, \end{aligned} \quad (\text{A.7})$$

$$\begin{aligned} \frac{d}{dt} \langle P_{(n|m)}^{(k|0)} \rangle &= -i[\omega_{cv} - (n-m)\omega_{LO} + i(n+m)\kappa] \langle P_{(n|m)}^{(k|0)} \rangle \\ &+ i[(1-\delta_{k|0})(\omega_k + \omega_l) - i\gamma] \langle P_{(n|m)}^{(k|0)} \rangle \\ &- (1-\delta_{k|0})iM^* \langle C_{n|m}^{(0|0)} \rangle \\ &- \delta_{k|0} \| i \sum_{\bar{k}} M^* (\langle C_{(n|m)}^{(0|\bar{k})} \rangle - \langle V_{(n|m)}^{(0|\bar{k})} \rangle) \\ &- i\tilde{\Omega}(t) (\langle C_{(n|m)}^{(k|0)} \rangle - \langle V_{(n|m)}^{(k|0)} \rangle)_- \\ &- i \langle P_{(n|m+1)}^{(k|0)} \rangle_+ - i \langle P_{(n+1|m)}^{(k|0)} \rangle \\ &- (1-\delta_{m|0})m ig^2 \langle P_{(n|m-1)}^{(k|0)} \rangle. \end{aligned} \quad (\text{A.8})$$

## A.4. Quantum regression theorem

Two-time correlations, such as in Eq. (4.26) can be calculated using the *quantum regression formula* [BP02, Car99]. If for a system of operators  $\{O_\alpha\}$  it applies:

$$\frac{d}{dt}\langle O_\alpha(t) \rangle = \text{Tr}[O_\alpha(\mathcal{L}\rho(t))] \equiv \text{Tr}[(\mathcal{L}^\dagger O_\alpha)\rho(t)] = \sum_{\beta} G_{\alpha\beta}\langle O_\beta(t) \rangle, \quad (\text{A.9})$$

i.e. it is a system of linear differential equations, the same set of equations apply for the two time correlators:

$$\begin{aligned} \frac{d}{d\tau}\langle O_\mu(t)O_\alpha(t+\tau) \rangle &= \text{Tr}[(\mathcal{L}^\dagger O_\alpha)U(t+\tau, t)O_\mu\rho(t)] \\ &= \sum_{\beta} G_{\alpha\beta}\langle O_\mu(t)O_\beta(t+\tau) \rangle, \end{aligned} \quad (\text{A.10})$$

With  $\sigma \equiv |v\rangle\langle c|$ , Eq. (4.29) becomes:

$$\begin{aligned} \frac{d}{d\tau}\langle \sigma^\dagger(t)O_{ij}^{nm}(t+\tau) \rangle &= \sum_{rp} G_{ijcc}^{nm,rp}\langle \sigma^\dagger(t)C^{(r|p)}(t+\tau) \rangle \\ &+ \sum_{rp} G_{ijvv}^{nm,rp}\langle \sigma^\dagger(t)V^{(r|p)}(t+\tau) \rangle \\ &+ \sum_{rp} G_{ijvc}^{nm,rp}\langle \sigma^\dagger(t)P^{(r|p)}(t+\tau) \rangle \\ &+ \sum_{rp} G_{ijcv}^{nm,rp}\langle \sigma^\dagger(t)\bar{P}^{(r|p)}(t+\tau) \rangle. \end{aligned} \quad (\text{A.11})$$

The only non vanishing elements of the regression matrix are given by:

$$\begin{aligned} G_{vv,vv}^{nm,nm} &= \chi_N^{(n|m)}, \quad G_{cc,cc}^{nm,nm} = \chi_C^{(n|m)}, \quad G_{vc,vc}^{nm,nm} = \chi_P^{(n|m)}, \\ G_{cv,cv}^{nm,nm} &= \chi_P^{(m|n)*}, \quad G_{vv,cc}^{nm,nm} = 2\Gamma_r, \\ G_{vv,vc}^{nm,nm} &= i\Omega, \quad G_{vv,cv}^{nm,nm} = -i\Omega, \quad G_{cc,vc}^{nm,nm} = -i\Omega, \quad G_{vv,cv}^{nm,nm} = i\Omega, \\ G_{vc,vv}^{nm,nm} &= i\Omega, \quad G_{vc,cc}^{nm,nm} = -i\Omega, \quad G_{cv,vv}^{nm,nm} = -i\Omega, \quad G_{cv,cc}^{nm,nm} = i\Omega, \\ G_{cc,cc}^{nm,n-1m} &= ing, \quad G_{cc,cc}^{nm,nm-1} = -img, \quad G_{vc,vc}^{nm,nm-1} = -img, \\ G_{cv,cv}^{nm,n-1m} &= ing, \quad G_{vc,vc}^{nm,nm+1} = -ig, \quad G_{vc,vc}^{nm,n+1m} = -ig, \end{aligned} \quad (\text{A.12})$$

with the prefactors  $\chi$  defined as in (3.29)-(3.32).

## A.5. Coherent population transfer

For a  $\Lambda$ -system interacting with two classical external laser fields

$$H_0 = \hbar\omega_a|a\rangle\langle a| + \hbar\omega_b|b\rangle\langle b| + \hbar\omega_c|c\rangle\langle c|, \quad (\text{A.13})$$

$$H_I = \hbar[\Omega_1(t)|b\rangle\langle a|e^{i\omega_1 t} + \Omega_2(t)|c\rangle\langle a|e^{i\omega_2 t}] + H.c., \quad (\text{A.14})$$

a coherence between the lower levels  $|b\rangle \rightarrow |a\rangle$  can be created for a coherent population transfer [SZ97]:

$$\dot{\rho}_{cb} = -(i\omega_{cb} + \gamma_{cb})\rho_{cb} - \Omega_1 e^{-i\omega_1 t} \rho_{ca} + \Omega_2 e^{i\omega_2 t} \rho_{ab}, \quad (\text{A.15})$$

$$\dot{\rho}_{ac} = -(i\omega_{ac} + \gamma_{ac})\rho_{ac} - \Omega_2 e^{i\omega_2 t} [\rho_{aa} - \rho_{cc}] + \Omega_1 e^{-i\omega_1 t} \rho_{bc}, \quad (\text{A.16})$$

$$\dot{\rho}_{ab} = -(i\omega_{ab} + \gamma_{ab})\rho_{ab} - \Omega_1 e^{-i\omega_1 t} [\rho_{aa} - \rho_{bb}] + \Omega_2 e^{-\omega_2 t} \rho_{cb}, \quad (\text{A.17})$$

$$\dot{\rho}_{bb} = -\gamma_b \rho_{bb} - i\Omega_1 \rho_{ab} e^{-i\omega_1 t} + i\Omega_1 \rho_{ba}^{i\omega_1 t}, \quad (\text{A.18})$$

$$\dot{\rho}_{cc} = -\gamma_c \rho_{cc} - i\Omega_2 \rho_{ac}^{-i\omega_2 t} + i\Omega_2 \rho_{ca}^{i\omega_2 t}, \quad (\text{A.19})$$

$$\dot{\rho}_{aa} = -\gamma_a \rho_{aa} - i\Omega_2 \rho_{ac}^{-i\omega_2 t} + i\Omega_2 \rho_{ca}^{i\omega_2 t} - i\Omega_1 \rho_{ab} e^{-i\omega_1 t} + i\Omega_1 \rho_{ba}^{i\omega_1 t} \quad (\text{A.20})$$

In contrast to Eqs. (6.5)-(6.10), these equations are symmetric with respect to the two interactions.

## A.6. Effective coupling between two $\Lambda$ -systems

In Fig. 6.11, the interaction time for a population switch between two  $\Lambda$ -systems is depicted for the findings of Eq. (6.48), reviewing the analytical results of Ref. [IAB<sup>+</sup>99]:

$$g_{\text{eff}}^{1-2} = \frac{g_{\text{eff}}^1 g_{\text{eff}}^2}{\Delta_{ab}^1 - \Delta_{ac}^2}, \quad (\text{A.21})$$

$$\text{with } g_{\text{eff}}^i = \frac{g_{\text{cav}}^i \Omega^i}{2(\Delta_{ab}^i + \Delta_{ac}^i)}. \quad (\text{A.22})$$

Similar to Eq. (6.48), the effective coupling is sensitive to the Raman resonance  $\Delta_{ab}^1 - \Delta_{ac}^2$ . For the coherent population switch, this process has to be inhibited. However, it predicts an equal sensitivity towards the laser- and the cavity detuning. This is not the case in Eq. (6.48), where the cavity detuning alone is not important to the process.

### A.6.1. Cavity-coupling

The cavity-emitter coupling for the NV center sitting at a field maximum of a photonic crystal cavity is calculated as:

$$g_{\text{cav}} = \sqrt{\frac{d\omega F}{4Q\tau}} = 19.1 \text{ ns}^{-1}, \quad (\text{A.23})$$

## A.6. EFFECTIVE COUPLING BETWEEN TWO $\Lambda$ -SYSTEMS

---

where  $Q$  is the quality-,  $F$  the Purcell factor,  $\tau$  the lifetime of excited state density and  $d$  the Debye-Waller factor.  $\omega$  is the frequency of the NV centers optical transition frequency.



# Bibliography

- [ADG90] AGARWAL, G. S. ; DUTTA GUPTA, S.: Steady states in cavity QED due to incoherent pumping. In: *Phys. Rev. A* 42 (1990), Aug, S. 1737–1741
- [AE75] ALLEN, L. ; EBERLY, J.H.: *Optical resonance and two level atoms*. Dover, 1975
- [AGR<sup>+</sup>82] ASPECT, Alain ; GRANGIER, Philippe ; ROGER, Gerard u. a.: Experimental realization of Einstein-Podolsky-Rosen-Bohm Gedankenexperiment: a new violation of Bell’s inequalities. In: *Physical review letters* 49 (1982), Nr. 2, S. 91–94
- [AHK99] AXT, V. M. ; HERBST, M. ; KUHN, T.: Coherent control of phonon quantum beats. In: *Superlattices and Microstructures* 26 (1999), Nr. 2, S. 117 – 128
- [AHR<sup>+</sup>11] ALBERT, Ferdinand ; HOPFMANN, Caspar ; REITZENSTEIN, Stephan ; SCHNEIDER, Christian ; HÖFLING, Sven ; WORSCHKECH, Lukas ; KAMP, Martin ; KINZEL, Wolfgang ; FORCHEL, Alfred ; KANTER, Ido: Observing chaos for quantum-dot microlasers with external feedback. In: *Nature Communications* 2 (2011), S. 366
- [AMK07] AHN, K. J. ; MILDE, F. ; KNORR, A.: Phonon-Wave-Induced Resonance Fluorescence in Semiconductor Nanostructures: Acoustoluminescence in the Terahertz Range. In: *Phys. Rev. Lett.* 98 (2007), Nr. 2, S. 027401
- [AR13] AUFFEVES, Alexia ; RICHARD, Maxime: Single shot quantum non-demolition readout with a hybrid opto-mechanical transducer. In: *arXiv preprint arXiv:1305.4252* (2013)
- [BAHK10] BEARDSLEY, R. P. ; AKIMOV, A. V. ; HENINI, M. ; KENT, A. J.: Coherent Terahertz Sound Amplification and Spectral Line Narrowing in a Stark Ladder Superlattice. In: *Phys. Rev. Lett.* 104 (2010), Feb, S. 085501
- [BCFM88] BUFFA, R. ; CAVALIERI, S. ; FINI, L ; MATERA, M: Resonance Fluorescence of a two-level atom driven by short laser pulse: extension to the off-resonance excitation. In: *J. Phys. B* 21 (1988), Jul, S. 329
- [BCR<sup>+</sup>12] BERNIEN, Hannes ; CHILDRESS, Lilian ; ROBLEDO, Lucio ; MARKHAM, Matthew ; TWITCHEN, Daniel ; HANSON, Ronald: Two-Photon Quantum Interference from Separate Nitrogen Vacancy Centers in Diamond. In: *Phys. Rev. Lett.* 108 (2012), Jan, S. 043604

- 
- [BHP<sup>+</sup>13] BERNIEN, H ; HENSEN, B ; PFAFF, W ; KOOLSTRA, G ; BLOK, MS ; ROBLED0, L ; TAMINIAU, TH ; MARKHAM, M ; TWITCHEN, DJ ; CHILDRESS, L u. a.: Heralded entanglement between solid-state qubits separated by three metres. In: *Nature* 497 (2013), Nr. 7447, S. 86–90
- [BIZR00] BIOLATTI, E. ; IOTTI, R. C. ; ZANARDI, P. ; ROSSI, F.: Quantum Information Processing with Semiconductor Macroatoms. In: *Phys. Rev. Lett* 85 (2000), Nr. 26, S. 5647
- [BJS<sup>+</sup>07] BEAUD, P. ; JOHNSON, S. L. ; STREUN, A. ; ABELA, R. ; ABRAMSOHN, D. ; GROLIMUND, D. ; KRASNIQI, F. ; SCHMIDT, T. ; SCHLOTT, V. ; INGOLD, G.: Spatiotemporal Stability of a Femtosecond Hard–X-Ray Undulator Source Studied by Control of Coherent Optical Phonons. In: *Phys. Rev. Lett.* 99 (2007), Oct, Nr. 17, S. 174801
- [BLS<sup>+</sup>01] BORRI, Paola ; LANGBEIN, Wolfgang ; SCHNEIDER, Stephan ; WOGGON, Ulrike ; SELLIN, Roman L. ; OUYANG, Dongxun ; BIMBERG, Dieter: Ultralong Dephasing Time in InGaAs Quantum Dots. In: *Phys. Rev. Lett.* 87 (2001), Sep, Nr. 15, S. 157401
- [BNT<sup>+</sup>09] BALASUBRAMANIAN, Gopalakrishnan ; NEUMANN, Philipp ; TWITCHEN, Daniel ; MARKHAM, Matthew ; KOLESOV, Roman ; MIZUOCHI, Norikazu ; ISOYA, Junichi ; ACHARD, Jocelyn ; BECK, Johannes ; TISSLER, Julia u. a.: Ultralong spin coherence time in isotopically engineered diamond. In: *Nature materials* 8 (2009), Nr. 5, S. 383–387
- [BP02] BREUER, H.-P. ; PETRUCCIONE, F.: *The Theory of Open Quantum Systems*. Oxford : Oxford University Press, 2002
- [BPM07] BRION, E ; PEDERSEN, L H. ; MÄÄLMEER, K: Adiabatic elimination in a lambda system. In: *Journal of Physics A: Mathematical and Theoretical* 40 (2007), Nr. 5, S. 1033
- [BR12] BLATT, Rainer ; ROOS, CF: Quantum simulations with trapped ions. In: *Nature Physics* 8 (2012), Nr. 4, S. 277–284
- [BSL<sup>+</sup>09] BIMBERG, D. ; STOCK, E. ; LOCHMANN, A. ; SCHLIWA, A. ; TOFFLINGER, J.A. ; UNRAU, W. ; MUNNIX, M. ; RODT, S. ; HAISLER, V.A. ; TOROPOV, A.I. ; BAKAROV, A. ; KALAGIN, A.K.: Quantum Dots for Single- and Entangled-Photon Emitters. In: *IEEE Photonics J.* 1 (2009), June, Nr. 1, S. 58–68
- [BTS98] BERGMANN, K. ; THEUER, H. ; SHORE, B. W.: Coherent population transfer among quantum states of atoms and molecules. In: *Rev. Mod. Phys.* 70 (1998), Jul, Nr. 3, S. 1003–1025
- [C. 93] C. GINZEL, H.J. BRIEGEL, U. MARTININ, B.-G. ENGLERT, AND A. SCHENZLE: In: *Phys. Rev. A* 48 (1993), 732 S.

- [Car99] CARMICHAEL, H.J.: *Statistical Methods in Quantum Optics 1 - Master Equation and Fokker-Planck Equations*. Springer, Berlin Heidelberg New York, 1999
- [Car02] CARMICHAEL, H.J.: *Statistical Methods in Quantum Optics 1 - Master Equation and Fokker-Planck Equations*. Springer, Berlin Heidelberg New York, 2002
- [CFC<sup>+</sup>10] CHERNIKOV, Alexej ; FELDTMANN, Thomas ; CHATTERJEE, Sangam ; KOCH, Martin ; KIRA, Mackillo ; KOCH, Stephan W.: Time-resolved phonon-sideband spectroscopy. In: *Solid State Communications* 150 (2010), Nr. 37-38, S. 1733 – 1736
- [CK03] CHEN, Jing ; KHURGIN, J.B.: Feasibility analysis of phonon lasers. In: *IEEE* 39 (2003), Apr, Nr. 4, S. 600
- [CKJ<sup>+</sup>11] CAMERER, Stephan ; KORPPI, Maria ; JÖCKEL, Andreas ; HUNGER, David ; HÄNSCH, Theodor W. ; TREUTLEIN, Philipp: Realization of an optomechanical interface between ultracold atoms and a membrane. In: *Physical Review Letters* 107 (2011), Nr. 22, S. 223001
- [CKM02] CHEN, J. ; KHURGIN, B. ; MERLIN, R.: Stimulated-emission-induced enhancement of the decay rate of longitudinal optical phonons in iii-v semiconductors. In: *Appl. Phys. Lett.* 80 (2002), S. 233
- [CKR09] CARMELE, A. ; KNORR, A. ; RICHTER, M.: Photon statistics as a probe for exciton correlations in coupled nanostructures. In: *Phys. Rev. B* 79 (2009), Jan, Nr. 3, S. 035316
- [CKS<sup>+</sup>13] CARMELE, Alexander ; KABUSS, Julia ; SCHULZE, Franz ; REITZENSTEIN, Stephan ; KNORR, Andreas: Single Photon Delayed Feedback: A Way to Stabilize Intrinsic Quantum Cavity Electrodynamics. In: *Phys. Rev. Lett.* 110 (2013), Jan, S. 013601
- [CM87] COOK, R. J. ; MILONNI, P. W.: Quantum theory of an atom near partially reflecting walls. In: *Phys. Rev. A* 35 (1987), Jun, S. 5081–5087
- [CMPFT01] CAMPS, I. ; MAKLER, S. S. ; PASTAWSKI, H. M. ; FOA TORRES, L. E. F.: GaAs–Al<sub>x</sub>Ga<sub>1-x</sub>As double-barrier heterostructure phonon laser: A full quantum treatment. In: *Phys. Rev. B* 64 (2001), Sep, S. 125311
- [CRCK10] CARMELE, Alexander ; RICHTER, Marten ; CHOW, Weng W. ; KNORR, Andreas: Antibunching of Thermal Radiation by a Room-Temperature Phonon Bath: A Numerically Solvable Model for a Strongly Interacting Light-Matter-Reservoir System. In: *Phys. Rev. Lett.* 104 (2010), Apr, Nr. 15, S. 156801
- [CT92] COHEN-TANNOUJDI, C.: *Atom-Photon-Interactions*. John Wiley & Sons, Inc., 1992

- 
- [Czy00] CZYCHOLL, Gerd: *Theoretische Festkörperphysik*. Vieweg, 2000
- [DMR<sup>+</sup>10] DACHNER, Matthias-René ; MALIC, Ermin ; RICHTER, Marten ; CARMELE, Alexander ; KABUSS, Julia ; WILMS, Alexander ; KIM, Jeong-Eun ; HARTMANN, Gregor ; WOLTERS, Janik ; BANDELOW, Uwe ; KNORR, Andreas: Theory of carrier and photon dynamics in quantum dot light emitters. In: *Phys. Status Solidi B* 247 (2010), Nr. 4, S. 809–828
- [DRB<sup>+</sup>10] DUBIN, F. ; RUSSO, C. ; BARROS, H. G. ; STUTE, A. ; BECHER, C. ; SCHMIDT, P. O. ; BLATT, R.: Quantum to classical transition in a single-ion laser. In: *Nature Phys.* 6 (2010), May, S. 350
- [DZ02] DORNER, U ; ZOLLER, P: Laser-driven atoms in half-cavities. In: *Physical Review A* 66 (2002), Nr. 2, S. 023816
- [EW77] EBERLY, J. H. ; WODKIEWICZ, K.: The time-dependent physical spectrum of light. In: *J. Opt. Soc. A.* 67 (1977), S. 1252
- [FL02] FLEISCHHAUER, M. ; LUKIN, M. D.: Quantum memory for photons: Dark-state polaritons. In: *Phys. Rev. A* 65 (2002), Jan, S. 022314
- [FLKJP13] FAINSTEIN, A. ; LANZILLOTTI-KIMURA, N. D. ; JUSSERAND, B. ; PERRIN, B.: Strong Optical-Mechanical Coupling in a Vertical GaAs/AlAs Microcavity for Subterahertz Phonons and Near-Infrared Light. In: *Phys. Rev. Lett.* 110 (2013), Jan, S. 037403
- [Fri96] FRICKE, Jens: Transport Equations Including Many-Particle Correlations for an Arbitrary Quantum System: A General Formalism. In: *Ann. Phys.* 252 (1996), S. 479–498
- [FRZ85] FLORJACZYK, Mirosław ; RZAEWSKI, Kazimierz ; ZAKRZEWSKI, Jakub: Resonance scattering of a short laser pulse on a two-level system: Time-dependent approach. In: *Phys. Rev. A* 31 (1985), Mar, S. 1558–1562
- [FSH<sup>+</sup>12] FARAON, Andrei ; SANTORI, Charles ; HUANG, Zhihong ; ACOSTA, Victor M. ; BEAUSOLEIL, Raymond G.: Coupling of nitrogen-vacancy centers to photonic crystal cavities in monocrystalline diamond. In: *Physical Review Letters* 109 (2012), Nr. 3, S. 033604
- [FWDK03] FÖRSTNER, J. ; WEBER, C. ; DANCKWERTS, J. ; KNORR, A.: Phonon-Assisted Damping of Rabi Oscillations in Semiconductor Quantum Dots. In: *Phys. Rev. Lett.* 91 (2003), Sep, Nr. 12, S. 127401
- [Gar11] GARTNER, Paul: Two-level laser: Analytical results and the laser transition. In: *Phys. Rev. A* 84 (2011), Nov, S. 053804
- [GHV<sup>+</sup>09] GRÖBLACHER, Simon ; HERTZBERG, Jared B. ; VANNER, Michael R. ; COLE, Garrett D. ; GIGAN, Sylvain ; SCHWAB, KC ; ASPELMEYER, Markus: Demonstration of an ultracold micro-optomechanical oscillator in a cryogenic cavity. In: *Nature Physics* 5 (2009), Nr. 7, S. 485–488

- [Gla63] GLAUBER, R.J.: The Quantum Theory of Optical Coherence. In: *Phys.Rev.* 130 (1963), Nr. 6, S. 2529–2539
- [GLPV10] GRUDININ, Ivan S. ; LEE, Hansuek ; PAINTER, O. ; VAHALA, Kerry J.: Phonon Laser Action in a Tunable Two-Level System. In: *Phys. Rev. Lett.* 104 (2010), Feb, Nr. 8, S. 083901
- [GMM<sup>+</sup>06] GAMBETTA, A ; MANZONI, C ; MENNA, E ; MENEGHETTI, M ; CERULLO, G ; LANZANI, G ; TRETIAK, S ; PIRYATINSKI, A ; SAXENA, A ; MARTIN, RL u. a.: Real-time observation of nonlinear coherent phonon dynamics in single-walled carbon nanotubes. In: *Nature Physics* 2 (2006), Nr. 8, S. 515–520
- [GTVC<sup>+</sup>10] GONZALEZ-TULEDA, A. ; VALLE, E. del ; CANCELLIERI, E. ; TEJEDOR, C. ; SANVITTO, D. ; LAUSSY, F. P.: Resonance fluorescence of semiconductor quantum dots: Signatures of the electron-phonon interaction. In: *Phys. Rev. B* 71 (2010), Nr. 15, S. 153309
- [HA08] HANSON, Ronald ; AWSCHALOM, David D.: Coherent manipulation of single spins in semiconductors. In: *Nature* 453 (2008), Nr. 7198, S. 1043–1049
- [Hak79] HAKEN, Hermann: *Licht und Materie*. Bd. 1. Mannheim : B.I. Wissenschaftsverlag, 1979
- [Hak93] HAKEN, Hermann: *Quantenfeldtheorie des Festkörpers*. Teubner, 1993
- [Hak94] HAKEN, Hermann: *Licht und Materie*. Bd. 2. 2. Auflage. Mannheim : B.I. Wissenschaftsverlag, 1994
- [Hau70] HAUG, Albert: *Theoretische Festkörperphysik II*. Vienna : Franz Deuticke, 1970
- [Hau04] HAUG, Albert: *Quantum Theory of the Optical and Electronic Properties of Semiconductors*. Bd. 4. World Scientific, Singapore, 2004
- [HBG<sup>+</sup>01] HEITZ, R. ; BORN, H. ; GUFFARTH, F. ; STIER, O. ; SCHLIWA, A. ; HOFFMANN, A. ; BIMBERG, D.: Existence of a phonon bottleneck for excitons in quantum dots. In: *Phys. Rev. B* 64 (2001), Nov, Nr. 24, S. 241305
- [HBW<sup>+</sup>07] HENNESSY, K. ; BADOLATO, A. ; WINGER, M. ; GERACE, D. ; ATATURE, M. ; GULDE, S. ; FALT, S. ; HU, E. L. ; IMAMOGLU, A.: Quantum nature of a strongly coupled single quantum dot-cavity system. In: *Nature* 445 (2007), feb, Nr. 7130, S. 896–899
- [HDY<sup>+</sup>11] HEILIGENTHAL, Sven ; DAHMS, Thomas ; YANCHUK, Serhiy ; JÜNGLING, Thomas ; FLUNKERT, Valentin ; KANTER, Ido ; SCHÖLL, Eckehard ; KINZEL, Wolfgang: Strong and Weak Chaos in Nonlinear Networks with Time-Delayed Couplings. In: *Phys. Rev. Lett.* 107 (2011), Nov, S. 234102

- 
- [HGL<sup>+</sup>95] HEITZ, R. ; GRUNDMANN, M. ; LEDENTSOV, N. N. ; ECKEY, L. ; VEIT, M. ; BIMBERG, D. ; USTINOV, V. M. ; EGOROV, A. Y. ; ZHUKOV, A. E. ; KOPEV, P. S. ; ; ALFEROV, Zh. I.: Multiphonon-relaxation processes in self-organized InAs/GaAs quantum dots. In: *Appl. Phys. Lett* 62 (1995), S. 116716
- [HK94] HAUG, Hartmut ; KOCH, Stephan W.: *Quantum Theory of the Optical and Electronic Properties of Semiconductors*. Singapore : World Scientific, 1994
- [HMS<sup>+</sup>99] HEITZ, R. ; MUKHAMETZHANOV, I. ; STIER, O. ; MADHUKAR, A. ; BIMBERG, D.: Enhanced Polar Exciton-LO-Phonon Interaction in Quantum Dots. In: *Phys. Rev. Lett.* 83 (1999), Nr. 22, S. 4654–4657
- [Hoh10] HOHENESTER, Ulrich: Cavity quantum electrodynamics with semiconductor quantum dots: Role of phonon-assisted cavity feeding. In: *Phys. Rev. B* 81 (2010), Apr, Nr. 15, S. 155303
- [HR50] HUANG, Kun ; RHYS, Avril: Theory of Light Absorption and Non-Radiative Transitions in F- Centres. In: *Proc R Soc A* 204 (1950), Dec, S. 1078
- [HSM<sup>+</sup>00] HEITZ, R. ; STIER, O. ; MUKHAMETZHANOV, I. ; MADHUKAR, A. ; BIMBERG, D.: Quantum size effect in self-organized InAs/GaAs quantum dots. In: *Phys. Rev. B* 62 (2000), Nr. 16, S. 11017
- [IAB<sup>+</sup>99] IMAMOGLU, A. ; AWSCHALOM, D. D. ; BURKARD, G. ; DIVINCENZO, D. P. ; LOSS, D. ; SHERWIN, M. ; SMALL, A.: Quantum Information Processing Using Quantum Dot Spins and Cavity QED. In: *Phys. Rev. Lett.* 83 (1999), Nov, S. 4204–4207
- [JH11] JARITZ, G. ; HOHENESTER, U.: Controlled cavity-assisted generation of single and entangled photons in semiconductor quantum dots. In: *The European Physical Journal B* 82 (2011), Nr. 1, S. 29–35
- [JLR<sup>+</sup>09] JIANG, Xiaoshun ; LIN, Qiang ; ROSENBERG, Jessie ; VAHALA, Kerry ; PAINTER, Oskar: High-Q double-disk microcavities for cavity optomechanics. In: *Optics Express* 17 (2009), Nr. 23, S. 20911–20919
- [KAK02] KRUMMHEUER, B. ; AXT, V. M. ; KUHN, T.: Theory of pure dephasing and the resulting absorption line shape in semiconductor quantum dots. In: *Phys. Rev. B* 65 (2002), Nr. 19, S. 195313
- [KBP<sup>+</sup>13] KEPESIDIS, KV ; BENNETT, SD ; PORTOLAN, S ; LUKIN, MD ; RABL, P.: Phonon cooling and lasing with nitrogen-vacancy centers in diamond. In: *Physical Review B* 88 (2013), Nr. 6, S. 064105
- [KCBK12] KABUSS, Julia ; CARMELE, Alexander ; BRANDES, Tobias ; KNORR, Andreas: Optically Driven Quantum Dots as Source of Coherent Cavity Phonons: A Proposal for a Phonon Laser Scheme. In: *Phys. Rev. Lett.* 109 (2012), Jul, S. 054301

- [KCK13] KABUSS, Julia ; CARMELE, Alexander ; KNORR, Andreas: Threshold behavior and operating regimes of an optically driven phonon laser: Semiclassical theory. In: *Phys. Rev. B* 88 (2013), Aug, S. 064305
- [KCR<sup>+</sup>11] KABUSS, Julia ; CARMELE, Alexander ; RICHTER, Marten ; CHOW, Weng W. ; KNORR: Inductive equation of motion approach for a semiconductor QD-QED: Coherence induced control of photon statistics. In: *Phys. Status Solidi b* 248 (2011), Apr, Nr. 4, S. 872–878
- [KCRK11] KABUSS, Julia ; CARMELE, Alexander ; RICHTER, Marten ; KNORR, Andreas: Microscopic equation-of-motion approach to the multiphonon assisted quantum emission of a semiconductor quantum dot. In: *Phys. Rev. B* 84 (2011), Sep, S. 125324
- [KGG<sup>+</sup>06] KHITROVA, G. ; GIBBS, H. M. ; KIRA, M. ; KOCH, S. W. ; SCHERER, A.: Vacuum Rabi splitting in semiconductors. In: *Nat. Phys.* 2 (2006), S. 81–90
- [KJHK99] KIRA, M. ; JAHNKE, F. ; HOYER, W. ; KOCH, S. W.: Quantum theory of spontaneous emission and coherent effects in semiconductor microstructures. In: *Prog. Quantum Electron.* 23 (1999), S. 189–279
- [KK06] KIRA, M. ; KOCH, S.W.: Many-body correlations and excitonic effects in semiconductor spectroscopy. In: *Prog. Quantum Electron.* 30 (2006), Nr. 5, S. 155–296
- [KK08] KIRA, M. ; KOCH, S.W.: Cluster-expansion representation in quantum optics. In: *Phys. Rev. A* 78 (2008), S. 022102
- [KK11] KIRA, Mackillo ; KOCH, Stephan W.: *Semiconductor quantum optics*. Cambridge University Press, 2011
- [KPSR12] KHURGIN, J. B. ; PRUESSNER, M. W. ; STIEVATER, T. H. ; RABINOVICH, W. S.: Laser-Rate-Equation Description of Optomechanical Oscillators. In: *Phys. Rev. Lett.* 108 (2012), May, S. 223904
- [KR10] KABUSS, J. ; RICHTER, M.: Theory of light scattering from semiconductor quantum dots: Excitation frequency dependent emission dynamics. In: *Phys. Rev. B* 81 (2010), Feb, Nr. 7, S. 075314
- [KV07] KIPPENBERG, Tobias J. ; VAHALA, Kerry J.: Cavity opto-mechanics. In: *Optics Express* 15 (2007), Nr. 25, S. 17172–17205
- [KV08] KIPPENBERG, TJ ; VAHALA, KJ: Cavity optomechanics: back-action at the mesoscale. In: *science* 321 (2008), Nr. 5893, S. 1172–1176
- [KWH<sup>+</sup>10] KABUSS, Julia ; WERNER, Stefan ; HOFFMANN, Axel ; HILDEBRANDT, Peter ; KNORR, Andreas ; RICHTER, Marten: Theory of time-resolved Raman scattering and fluorescence emission from semiconductor quantum dots. In: *Phys. Rev. B* 81 (2010), Feb, Nr. 7, S. 075314

- 
- [LFJTM04] LACHARMOISE, P. ; FAINSTEIN, A. ; JUSSERAND, B. ; THIERRY-MIEG, V.: Optical cavity enhancement of light-sound interaction in acoustic phonon cavities. In: *Appl. Phys. Lett.* 84 (2004), April, Nr. 17, S. 3274
- [LHVB<sup>+</sup>09] LAUCHT, A. ; HAUKE, N. ; VILLAS-BÔAS, J. M. ; HOFBAUER, F. ; BÖHM, G. ; KANIBER, M. ; FINLEY, J. J.: Dephasing of Exciton Polaritons in Photoexcited InGaAs Quantum Dots in GaAs Nanocavities. In: *Phys. Rev. Lett.* 103 (2009), Aug, S. 087405
- [LK80] LANG, Roy ; KOBAYASHI, Kohroh: External optical feedback effects on semiconductor injection laser properties. In: *Quantum Electronics, IEEE Journal of* 16 (1980), Nr. 3, S. 347–355
- [LKFBJ07] LANZILLOTTI-KIMURA, N. D. ; FAINSTEIN, A. ; BALSEIRO, C. A. ; JUSSERAND, B.: Phonon engineering with acoustic nanocavities: Theoretical considerations on phonon molecules, band structures, and acoustic Bloch oscillations. In: *Phys. Rev. B* 75 (2007), Jan, S. 024301
- [Lou73] LOUISELL, W. H.: *Quantum Statistical Properties of Radiation*. Wiley, 1973
- [Lou90] LOUISELL, W. H.: *Quantum Statistical Properties of Radiation*. Wiley, 1990
- [LSW<sup>+</sup>03] LIU, HC ; SONG, CY ; WASILEWSKI, ZR ; SPRINGTHORPE, AJ ; CAO, JC ; DHARMA-WARDANA, C ; AERS, GC ; LOCKWOOD, DJ ; GUPTA, JA: Coupled electron-phonon modes in optically pumped resonant intersubband lasers. In: *Physical review letters* 90 (2003), Nr. 7, S. 077402
- [LVT08] LAUSSY, F.P. ; VALLE, E. del ; TEJEDOR, C.: Strong Coupling of Quantum Dots in Microcavities. In: *Phys. Rev. Lett.* 101 (2008), Nr. 8, S. 083601
- [LWWK07] LINDWALL, Greta ; WACKER, Andreas ; WEBER, Carsten ; KNORR, Andreas: Zero-Phonon Linewidth and Phonon Satellites in the Optical Absorption of Nanowire-Based Quantum Dots. In: *Phys. Rev. Lett.* 99 (2007), Nr. 8, S. 087401
- [Mad78] MADELUNG, O.: *Introduction to Solid-State Theory*. Berlin : Springer-Verlag, 1978
- [Mah81] MAHAN, G.D.: *Many-Particle Physics*. New York : Plenum, 1981
- [Mah00] MAHAN, G. D.: *Many-Particle Physics*. New York : Kluwer Academic/Plenum Publishers, 2000
- [MBB<sup>+</sup>03] MCKEEVER, Jason ; BOCA, Andreea ; BOOZER, A D. ; BUCK, Joseph R. ; KIMBLE, H J.: Experimental realization of a one-atom laser in the regime of strong coupling. In: *Nature* 425 (2003), Nr. 6955, S. 268–271
- [MBW97] MEYER, C. M. ; BRIEGEL, H.-J. ; WALTHER, H.: Ion-trap laser. In: *Europhys. Lett.* 37 (1997), Feb, Nr. 5, S. 317–322

- [MGT<sup>+</sup>11] MAZE, JR ; GALI, Adam ; TOGAN, Emre ; CHU, Yiwen ; TRIFONOV, Alexei ; KAXIRAS, Efthimios ; LUKIN, MD: Properties of nitrogen-vacancy centers in diamond: the group theoretic approach. In: *New Journal of Physics* 13 (2011), Nr. 2, S. 025025
- [MIM<sup>+</sup>00] MICHLER, P. ; IMAMOGLU, A. ; MASON, M. D. ; CARSON, P. J. ; STROUSE, G. F. ; BURATTO, S. K.: quantum correlation among photons from a single quantum dot at room temperature. In: *Nature* 406 (2000), S. 968–970
- [MK04] METZGER, Constanze H. ; KARRAI, Khaled: Cavity cooling of a microlever. In: *Nature* 432 (2004), Nr. 7020, S. 1002–1005
- [MKB<sup>+</sup>00] MICHLER, P. ; KIRAZ, A. ; BECHER, C. ; SCHOENFELD, W. V. ; PETROFF, P. M. ; ZHANG, Lidong ; HU, E. ; IMAMOGLU, A.: A Quantum Dot Single-Photon Turnstile Device. In: *Science* 290 (2000), Nr. 5500, S. 2282–2285
- [MKH08] MILDE, F. ; KNORR, A. ; HUGHES, S.: Role of electron-phonon scattering on the vacuum Rabi splitting of a single quantum dot and a photonic crystal nanocavity. In: *Phys. Rev. B* 78 (2008), S. 035330
- [MKLM12] MOELBJERG, Anders ; KAER, Per ; LORKE, Michael ; MØRK, Jesper: Resonance Fluorescence from Semiconductor Quantum Dots: Beyond the Mollow Triplet. In: *Phys. Rev. Lett.* 108 (2012), Jan, S. 017401
- [ML08] MCCUTCHEON, Murray W. ; LONCAR, Marko: Design of a silicon nitride photonic crystal nanocavity with a Quality factor of one million for coupling to a diamond nanocrystal. In: *Optics Express* 16 (2008), Nr. 23, S. 19136–19145
- [MMT90] MØRK, J ; MARK, J ; TROMBORG, B: Route to chaos and competition between relaxation oscillations for a semiconductor laser with optical feedback. In: *Physical review letters* 65 (1990), Nr. 16, S. 1999
- [Mol69] MOLLOW, B. R.: Power Spectrum of Light Scattered by Two-Level Systems. In: *Phys. Rev.* 188 (1969), Dec, Nr. 5, S. 1969–1975
- [MS92] MU, Yi ; SAVAGE, C.M: One-atom lasers. In: *Phys. Rev. A* 46 (1992), Nov, Nr. 9, S. 5944
- [Muk95] MUKAMEL, Shaul: *Principles of nonlinear optical spectroscopy*. New York : Oxford University Press, 1995
- [MVA12] MATTHIESEN, Clemens ; VAMIVAKAS, Anthony N. ; ATATÜRE, Mete: Sub-natural Linewidth Single Photons from a Quantum Dot. In: *Phys. Rev. Lett.* 108 (2012), Feb, S. 093602
- [MVTG06] MIRANDA, Rafael P. ; VASILEVSKIY, Mikhail I. ; TRALLERO-GINER, Carlos: Nonperturbative approach to the calculation of multiphonon Raman scattering in semiconductor quantum dots: Polaron effect. In: *Phys. Rev. B* 74 (2006), Sep, Nr. 11, S. 115317

- 
- [MW95] MANDEL, L. ; WOLF, E.: *Optical coherence and quantum optics*. Cambridge : Cambridge University Press, 1995
- [MZ07] MULJAROV, E. A. ; ZIMMERMANN, R.: Exciton Dephasing in Quantum Dots due to LO-Phonon Coupling: An Exactly Solvable Model. In: *Phys. Rev. Lett.* 98 (2007), May, Nr. 18, S. 187401
- [NKI<sup>+</sup>10] NOMURA, M ; KUMAGAI, N ; IWAMOTO, S ; OTA, Y ; ARAKAWA, Y: Laser oscillation in a strongly coupled single-quantum-dot–nanocavity system. In: *Nature Physics* 6 (2010), Nr. 4, S. 279–283
- [OLS10] OTTO, Christian ; LÜDGE, Kathy ; SCHÖLL, Eckehard: Modeling quantum dot lasers with optical feedback: sensitivity of bifurcation scenarios. In: *physica status solidi (b)* 247 (2010), Nr. 4, S. 829–845
- [PGR<sup>+</sup>07] PRESS, D. ; GOETZINGER, S. ; REITZENSTEIN, S. ; HOFMANN, C. ; LOEFFLER, A. ; KAMP, M. ; FORCHEL, A. ; YAMAMOTO, Y.: Photon Antibunching from a Single Quantum-Dot-Microcavity System in the Strong Coupling Regime. In: *Phys. Rev. Lett.* 98 (2007), S. 117402
- [PMOaU<sup>+</sup>] PIEGDON, K. A. ; M. OFFER AND, A. L. ; URBANSKI, M. ; HOISCHEN, A. ; KITZEROW, H.-S. ; S.DECLAIR ; FÖRSTNER, J. ; MEIER, T. ; REUTER, D. ; WIECK, A. D. ; MEIER, C.: Self-assembled quantum dots in a liquid-crystal-tunable microdisk resonator. In: *Physica E*
- [RCSK09] RICHTER, Marten ; CARMELE, Alexander ; SITEK, Anna ; KNORR, Andreas: Few-Photon Model of the Optical Emission of Semiconductor Quantum Dots. In: *Phys. Rev. Lett.* 103 (2009), Nr. 8, S. 087407
- [RGGJ10] RITTER, S. ; GARTNER, P. ; GIES, C. ; JAHNKE, F.: Emission properties and photon statistics of a single quantum dot laser. In: *Opt. Express* 18 (2010), S. 9909–9921
- [RH11] ROY, C. ; HUGHES, S.: Phonon-Dressed Mollow Triplet in the Regime of Cavity Quantum Electrodynamics: Excitation-Induced Dephasing and Non-perturbative Cavity Feeding Effects. In: *Phys. Rev. Lett.* 106 (2011), Jun, S. 247403
- [RH13] RIPS, Simon ; HARTMANN, Michael J.: Quantum Information Processing with Nanomechanical Qubits. In: *Phys. Rev. Lett.* 110 (2013), Mar, S. 120503
- [RWJ<sup>+</sup>09] ROZAS, G. ; WINTER, M. F. P. ; JUSSERAND, B. ; FAIRSTEIN, A. ; PERRIN, B. ; SEMENOVA, E. ; LEMAÎTRE, A.: Lifetime of THz Acoustic Nanocavity Modes. In: *Phys. Rev. Lett.* 102 (2009), Jan, Nr. 1, S. 015502
- [RWK87] REMPE, G. ; WALTHER, H. ; KLEIN, N.: Observation of Quantum Collapse and Revival in a One-Atom Maser. In: *Phys. Rev. Lett.* 58 (1987), Nr. 4, S. 353 – 356

- [SDR<sup>+</sup>10] SAUER, S. ; DANIELS, J. M. ; REITER, D. E. ; KUHN, T. ; VAGOV, A. ; AXT, V. M.: Lattice Fluctuations at a Double Phonon Frequency with and without Squeezing: An Exactly Solvable Model of an Optically Excited Quantum Dot. In: *Phys. Rev. Lett.* 105 (2010), Oct, Nr. 15, S. 157401
- [SDW<sup>+</sup>11] STOCK, Erik ; DACHNER, Matthias-Rene ; WARMING, Till ; SCHLIWA, Andrei ; LOCHMANN, Anatol ; HOFFMANN, Axel ; TOROPOV, Aleksandr I. ; BAKAROV, Askhat K. ; DEREBEZOV, Ilya A. ; RICHTER, Marten ; HAISLER, Vladimir A. ; KNORR, Andreas ; BIMBERG, Dieter: Acoustic and optical phonon scattering in a single In(Ga)As quantum dot. In: *Phys. Rev. B* 83 (2011), Jan, Nr. 4, S. 041304
- [SGB99] STIER, O. ; GRUNDMANN, M. ; BIMBERG, D.: Electronic and optical properties of strained quantum dots modeled by 8-band kp theory. In: *Phys. Rev. B* 59 (1999), Feb, Nr. 8, S. 5688–5701
- [SKH<sup>+</sup>12] STANNIGEL, K. ; KOMAR, P. ; HABRAKEN, S. J. M. ; BENNETT, S. D. ; LUKIN, M. D. ; ZOLLER, P. ; RABL, P.: Optomechanical Quantum Information Processing with Photons and Phonons. In: *Phys. Rev. Lett.* 109 (2012), Jul, S. 013603
- [SNCH<sup>+</sup>12] SAFAVI-NAEINI, Amir H. ; CHAN, Jasper ; HILL, Jeff T. ; ALEGRE, Thiago P. M. ; KRAUSE, Alex ; PAINTER, Oskar: Observation of Quantum Motion of a Nanomechanical Resonator. In: *Phys. Rev. Lett.* 108 (2012), Jan, S. 033602
- [SRA<sup>+</sup>08] SCHLIESSER, Albert ; RIVIÈRE, Rémi ; ANETSBERGER, Georg ; ARCIZET, Olivier ; KIPPENBERG, Tobias J.: Resolved-sideband cooling of a micromechanical oscillator. In: *Nature Physics* 4 (2008), Nr. 5, S. 415–419
- [SRT11] SOYKAL, Ö. O. ; RUSKOV, Rusko ; TAHAN, Charles: Sound-Based Analogue of Cavity Quantum Electrodynamics in Silicon. In: *Phys. Rev. Lett.* 107 (2011), Nov, S. 235502
- [SRX<sup>+</sup>10] SHI, Fazhan ; RONG, Xing ; XU, Nanyang ; WANG, Ya ; WU, Jie ; CHONG, Bo ; PENG, Xinhua ; KNIEPERT, Juliane ; SCHOENFELD, Rolf-Simon ; HARNEIT, Wolfgang ; FENG, Mang ; DU, Jiangfeng: Room-Temperature Implementation of the Deutsch-Jozsa Algorithm with a Single Electronic Spin in Diamond. In: *Phys. Rev. Lett.* 105 (2010), Jul, S. 040504
- [STN<sup>+</sup>06] SANTORI, Charles ; TAMARAT, Philippe ; NEUMANN, Philipp ; WRACHTRUP, Jörg ; FATTAL, David ; BEAUSOLEIL, Raymond G. ; RABEAU, James ; OLIVERO, Paolo ; GREENTREE, Andrew D. ; PRAWER, Steven ; JELEZKO, Fedor ; HEMMER, Philip: Coherent Population Trapping of Single Spins in Diamond under Optical Excitation. In: *Phys. Rev. Lett.* 97 (2006), Dec, S. 247401
- [Sto94] STOLZ, Heinrich: *Springer Tracts in Modern Physics*. Bd. 130: *Time-Resolved Light Scattering from Excitons*. Springer-Verlag, Berlin, 1994

- 
- [SWB07] SCHLIWA, Andrei ; WINKELNKEMPER, Momme ; BIMBERG, Dieter: Impact of size, shape, and composition on piezoelectric effects and electronic properties of In(Ga)As/GaAs quantum dots. In: *Phys. Rev. B* 76 (2007), Nr. 20, S. 205324
- [SWL<sup>+</sup>09] SCHLIWA, Andrei ; WINKELNKEMPER, Momme ; LOCHMANN, Anatol ; STOCK, Erik ; BIMBERG, Dieter: In(Ga)As/GaAs quantum dots grown on a (111) surface as ideal sources of entangled photon pairs. In: *Phys. Rev. B* 80 (2009), Oct, Nr. 16, S. 161307
- [SZ97] SCULLY, M. O. ; ZUBAIRY, M. S.: *Quantum Optics*. Cambridge : Cambridge University Press, 1997
- [TBF<sup>+</sup>02] TRIGO, M. ; BRUCHHAUSEN, A. ; FAINSTEIN, A. ; JUSSERAND, B. ; THIERRY-MIEG, V.: Confinement of Acoustical Vibrations in a Semiconductor Planar Phonon Cavity. In: *Phys. Rev. Lett.* 89 (2002), Nov, S. 227402
- [TBMD12] TAO, Y ; BOSS, JM ; MOORES, BA ; DEGEN, CL: Single-crystal diamond nanomechanical resonators with quality factors exceeding one million. In: *arXiv preprint arXiv:1212.1347* (2012)
- [TCT<sup>+</sup>10] TOGAN, E ; CHU, Y ; TRIFONOV, AS ; JIANG, L ; MAZE, J ; CHILDRESS, L ; DUTT, MVG ; SØRENSEN, AS ; HEMMER, AS: PR and Zibrov, and MD Lukin. In: *Nature* 466 (2010), S. 730
- [TS10] TAREL, G. ; SAVONA, V.: Linear spectrum of a quantum dot coupled to a nanocavity. In: *Phys. Rev. B* 81 (2010), Feb, Nr. 7, S. 075305
- [UAR<sup>+</sup>11] ULRICH, SM ; ATEs, S ; REITZENSTEIN, S ; LÖFFLER, A ; FORCHEL, A ; MICHLER, P: Dephasing of triplet-sideband optical emission of a resonantly driven InAs/GaAs quantum dot inside a microcavity. In: *Physical Review Letters* 106 (2011), Nr. 24, S. 247402
- [UWU<sup>+</sup>12] ULHAQ, A ; WEILER, S ; ULRICH, SM ; ROSSBACH, R ; JETTER, M ; MICHLER, P: Cascaded single-photon emission from the Mollow triplet sidebands of a quantum dot. In: *Nature Photonics* 6 (2012), Nr. 4, S. 238–242
- [VAK02] VAGOV, A. ; AXT, V. M. ; KUHN, T.: Electron-phonon dynamics in optically excited quantum dots: Exact solution for multiple ultrashort laser pulses. In: *Phys. Rev. B* 66 (2002), Oct, Nr. 16, S. 165312
- [VHK<sup>+</sup>09] VAHALA, K. ; HERMANN, M. ; KNÜNZ, S. ; BATTEIGNER, V. ; SAATHOFF, G. ; HÄNSCH, T. W. ; UDEM, Th.: A phonon laser. In: *Nature Phys.* 5 (2009), Aug, S. 682–686
- [VLT09] VALLE, Elena del ; LAUSSY, Fabrice P. ; TEJEDOR, Carlos: Luminescence spectra of quantum dots in microcavities. II. Fermions. In: *Phys. Rev. B* 79 (2009), Jun, Nr. 23, S. 235326

- [VMS<sup>+</sup>12] VIJAY, R ; MACKLIN, Chris ; SLICHTER, DH ; WEBER, SJ ; MURCH, KW ; NAIK, R ; KOROTKOV, Alexander N. ; SIDDIQI, I: Stabilizing Rabi oscillations in a superconducting qubit using quantum feedback. In: *Nature* 490 (2012), Nr. 7418, S. 77–80
- [VW94] VOGEL, Werner ; WELSCH, Dirk-Gunnar: *Lectures on Quantum Optics*. Akademie Verlag, Berlin, 1994
- [Web02] WEBER, Carsten: *On the Theory of Electron-Phonon Coupling and the Optical Linewidth in Semiconductor Quantum Dots*, Technische Universität Berlin, Diplomarbeit, 2002
- [WM08] WALLS, Daniel F. ; MILBURN, G Gerard J.: *Quantum optics*. Springer, 2008
- [WM10] WISEMAN, Howard M. ; MILBURN, Gerard J.: *Quantum measurement and control*. Cambridge University Press, 2010
- [Woo98] WOOTTERS, William K.: Entanglement of Formation of an Arbitrary State of Two Qubits. In: *Phys. Rev. Lett.* 80 (1998), Mar, Nr. 10, S. 2245–2248
- [WRI02] WILSON-RAE, I. ; IMAMOGLU, A.: Quantum dot cavity-QED in the presence of strong electron-phonon interactions. In: *Phys. Rev. B* 65 (2002), May, Nr. 23, S. 235311
- [WRW<sup>+</sup>11] WERNER, S. ; REPARAZ, J. S. ; WAGNER, M. R. ; ZIMMER, P. ; LEDENTSOV, N. N. ; KABUSS, J. ; DACHNER, M. R. ; RICHTER, M. ; KNORR, A. ; THOMSEN, C. ; HOFFMANN, A.: Decay dynamics of excitonic polarons in InAs/GaAs quantum dots. In: *J. Appl. Phys.* 110 (2011), Aug, S. 074303
- [WRZI04] WILSON-RAE, I. ; ZOLLER, P. ; IMAMOGLU, A.: Laser Cooling of a Nanomechanical Resonator Mode to its Quantum Ground State. In: *Phys. Rev. Lett.* 92 (2004), Feb, Nr. 7, S. 075507
- [WSK<sup>+</sup>10] WOLTERS, Janik ; SCHELL, Andreas W. ; KEWES, Gunter ; NUSSE, Nils ; SCHOENGEN, Max ; DOSCHER, Henning ; HANNAPPEL, Thomas ; LOCHEL, Bernd ; BARTH, Michael ; BENSON, Oliver: Enhancement of the zero phonon line emission from a single nitrogen vacancy center in a nanodiamond via coupling to a photonic crystal cavity. In: *Applied Physics Letters* 97 (2010), Nr. 14, S. 141108–141108
- [WSSB13] WOLTERS, Janik ; STRAUSS, Max ; SCHOENFELD, Rolf S. ; BENSON, Oliver: Quantum Zeno phenomenon on a single solid-state spin. In: *Phys. Rev. A* 88 (2013), Aug, S. 020101
- [WVT<sup>+</sup>09] WINGER, Martin ; VOLZ, Thomas ; TAREL, Guillaume ; PORTOLAN, Stefano ; BADOLATO, Antonio ; HENNESSY, Kevin J. ; HU, Evelyn L. ; BEVERATOS, Alexios ; FINLEY, Jonathan ; SAVONA, Vincenzo ; IMAMOLU, Atac: Explanation of Photon Correlations in the Far-Off-Resonance Optical Emission from

- a Quantum-Dot-Cavity System. In: *Phys. Rev. Lett.* 103 (2009), Nr. 20, S. 207403
- [YTC00] YAMAMOTO, Yoshihisa ; TASSONE, Francesco ; CAO, Hui: *Semiconductor cavity quantum electrodynamics*. Springer, 2000 (169)
- [YXFD10] YANG, Wanli ; XU, Zhenyu ; FENG, Mang ; DU, Jiangfeng: Entanglement of separate nitrogen-vacancy centers coupled to a whispering-gallery mode cavity. In: *New Journal of Physics* 12 (2010), Nr. 11, S. 113039
- [ZDP<sup>+</sup>12] ZHOU, X. ; DOTSENKO, I. ; PEAUDECERF, B. ; RYBARCZYK, T. ; SAYRIN, C. ; GLEYZES, S. ; RAIMOND, J. M. ; BRUNE, M. ; HAROCHE, S.: Field Locked to a Fock State by Quantum Feedback with Single Photon Corrections. In: *Phys. Rev. Lett.* 108 (2012), Jun, S. 243602

## BIBLIOGRAPHY

---



# Danksagung

Ich danke Prof. Andreas Knorr für die wundervolle Betreuung meiner Doktorarbeit und generell für seine freundliche und inspirierende Unterstützung meiner Forschung.

Mein Dank geht auch an Prof. Oliver Benson für die Übernahme des Zweitgutachters sowie an Prof. Birgit Kanngießer, für die Übernahme des Prüfungsvorsitzes.

Ich danke den Mitgliedern der Arbeitsgruppe für die schöne Zeit, im speziellen meinen Kollegen im 7. Stock, Marten Richter, Frank Milde, Ermin Malic, Matthias-Rene-Dachner, Mario Schoth, Thi Uyen-Khanh Dang und Alexander Carmele. Ich danke Marten für die Betreuung in den Anfängen meiner Doktorandenzeit und das Vertrauen, das er in mich setzte. Matthias-Rene danke ich für seine enorme Bereitschaft zu wissenschaftlichem Austausch. Ich danke Marten Richter, Mario Schoth und Peter Orłowski für Ihre große Hilfsbereitschaft als Netzwerkadministratoren. Des Weiteren danke ich Frank Milde, Matthias-Rene Dachner und Marten Richter für das Korrekturlesen meiner Arbeit und insbesondere Alex dafür, dass er die komplette Arbeit gelesen hat. Ich danke darüber hinaus Kristina Ludwig für die freundlich Unterstützung in allen administrativen Angelegenheiten und Dokumentendschungel.

Des Weiteren danke ich Alex für zahlreiche und inspirierende Zusammenarbeiten in meiner Zeit bei der AG Knorr.

Ich danke Prof. Weng W. Chow dafür, dass er zusammen mit Prof. Andreas Knorr es mir ermöglicht hat einen einmonatigen Forschungsaufenthalt in Albuquerque zu verbringen, und für die darauf folgenden Kollaborationen und fruchtbaren wissenschaftlichen Diskussionen.

Für wissenschaftliche Kollaboration und Austausch danke ich Stefan Werner und Axel Hoffmann, sowie Tobias Brandes und Christina Pörtl. Diesbezüglich danke ich auch Christopher Köhler, Felix Schlosser und Mario Schoth sowie Janik Wolters für das tolle Projekt über Verschränkung in fehlerhaften Diamantstrukturen.

Ich möchte meinem Vater sehr herzlich dafür danken, dass er an mich geglaubt hat. Meiner Mutter danke ich für Ihre Unterstützung in den letzten Jahren und die Sicherheit, die Sie mir in einer für Sie selbst schweren Zeit dennoch gegeben hat. Ich danke meinem großen Bruder Wolfgang dafür, dass er mich zum Physikstudium ermutigt hat und meiner kleinen Schwester Caroline für ihre Freundschaft. Zuletzt und im Besonderen danke ich meinem geliebten Alex, mit Ihm ist die Welt und die Wissenschaft ein Universum voller Totoros.